Open access • Dissertation • DOI:10.14264/UQL.2019.342

Free-jet testing of a Mach 12 scramjet in an expansion tube

Pierpaolo Toniato

Published on: 12 Apr 2019

Topics: Expansion tunnel, Mach number, Scramjet, Hypersonic speed and Combustor

THE UNIVERSITY OF QUEENSLAND

AUSTRALIA

Free-jet testing of a Mach 12 scramjet in an expansion tube

Pierpaolo Toniato

Diplôme d'Ingénieur
M.Sc (Aerospace Engineering) *with honours*

A thesis submitted for the degree of Doctor of Philosophy at
The University of Queensland in 2019

School of Mechanical & Mining Engineering
Centre for Hypersonics

Abstract

Scramjet technology has the theoretical potential to provide air-breathing propulsion as a more efficient alternative to conventional rocket propulsion. Since the vehicle captures its oxidiser from the atmosphere — as opposed to carrying it like a rocket — the specific impulse can theoretically be increased by an order of magnitude, thereby increasing payload mass fractions. In this context, three-stage hybrid rocket-scramjet-rocket launch systems have shown to potentially provide a cost-effective and flexible solution for satisfying the requirements of the small-satellites market. However, to be economically feasible, the proposed scramjet-powered second stage would be reusable.

Rectangular-to-Elliptical-Shape-Transitioning (REST) engines have shown to be a viable concept that can be integrated into access-to-space vehicles operating between Mach 5 and 12. The half-scale Mach 12 REST engine is a research scramjet specifically designed to operate in the last part of the ascent trajectory. Previous studies have demonstrated the ability of this design to successfully operate at equivalent flight conditions of Mach 11.6, 30 kPa dynamic pressure. However, tests have never been performed in freejet mode at the design conditions, as the facility which was used — the T4 reflected shock tunnel — was limited, like all RSTs by the extreme total pressure requirements of a Mach 12 flight. These limitations are aggravated by the even higher pressure necessary for pressure-length scaling, used to conserve the flow similarity between the half-scale experimental model and the flight engine.

To overcome these limitations and allow freejet testing with pressure-length scaling, the use of expansion tubes has been proposed. These are currently the only kind of facility capable of producing these high-pressure requirements. Currently, the University of Queensland operates the X3 expansion tube, which is one of the few facilities worldwide with the potential to produce both the required total pressures and sufficiently long test times (up to 1.5 ms) to test an engine such as the Mach 12 REST engine.

The goal of this thesis is to investigate and test *for the first time*, the Mach 12 REST engine in freejet mode, at fully replicated flight conditions. The study proposed using the X3 expansion tube, however, prior to this study the fastest scramjet test flow produced by X3 was Mach 10. Therefore, a significant part of this work tackles the extension of the X3 tunnel capabilities.

A major element of the upgrade to X3 is a new hypersonic Mach 12 nozzle, which has been developed to allow higher Mach number flows and bigger core flow sizes. The nozzle profile has been designed via a parallel implementation of the Nelder-Mead optimiser coupled with a RANS flow solver. The designed, fully contoured nozzle is 2.8 m long with an exit diameter of 573 mm.

A Mach 12 operating condition for the facility has also been developed and tested, replicating the flight condition at Mach 12 and 50 kPa dynamic pressure. Experimental measurements and computation have revealed that the new test condition has a Mach number of 11.1 ± 0.9, 52.2 kPa dynamic pressure across a useful test time of 1.3 ms. The discrepancy to the target Mach number was due to an excessively thick boundary layer in the acceleration tube, which could only be addressed by

shortening the X3 acceleration tube. This hardware modification was not feasible within the thesis timeline.

Using the new nozzle and operating conditions in X3, the engine was first tested without pressure-length scaling to match previous experiments in the T4 facility, at a total enthalpy of $6\,\mathrm{MJ\,kg^{-1}}$ and a total pressure of $223\,\mathrm{MPa}$. These experiments, the first under full freestream conditions, have demonstrated successful and robust combustion. The engine has been tested with two fuelling configurations, combustor-only and inlet-combustor injection. The results confirmed that the latter was able to produce a significant increase in combustion. The engine was finally tested at the pressure-length scaled condition (for a total pressure of $450\,\mathrm{MPa}$), where experiments indicated a reduced amount of combustion. A comparison with previous experimental data has shown similar flow structures and pressure levels, although discrepancies were noted in the position of the shock inside the combustor.

The combined-injection scheme experiments initially produced engine unstarts. It was postulated that the acceleration tube air gas was igniting the inlet pre-fuelled hydrogen, thus unstarting the engine. A new accelerator gas substitution — replacing air with helium — was proposed and tested with successful and reliable results. This substitution was shown to facilitate the flow starting process during scramjet testing in expansion tube facilities.

Expansion tubes have been shown to be able to carry out scramjet testing, however, they present several challenges such as a steady gradient in the freestream properties during the test time, unsteady disturbances, and the flow conditions are harsh on models. Nonetheless, comparisons to RST experiments steady numerical data indicate good agreement, showing that the data is still representative of the target steady conditions.

In summary, this thesis demonstrates the potential of expansion tubes for high Mach number scramjet freejet testing, which addresses the limitations of reflected shock tubes, thus providing experimental data for conditions that were previously only achievable numerically or in flight. Furthermore, it provides the first data on the Mach 12 REST engine at design pressure and pressure-length scaled freestream conditions, showing robust combustion.

Declaration by author

This thesis is composed of my original work, and contains no material previously published or written by another person except where due reference has been made in the text. I have clearly stated the contribution by others to jointly-authored works that I have included in my thesis.

I have clearly stated the contribution of others to my thesis as a whole, including statistical assistance, survey design, data analysis, significant technical procedures, professional editorial advice, financial support and any other original research work used or reported in my thesis. The content of my thesis is the result of work I have carried out since the commencement of my higher degree by research candidature and does not include a substantial part of work that has been submitted to qualify for the award of any other degree or diploma in any university or other tertiary institution. I have clearly stated which parts of my thesis, if any, have been submitted to qualify for another award.

I acknowledge that an electronic copy of my thesis must be lodged with the University Library and, subject to the policy and procedures of The University of Queensland, the thesis be made available for research and study in accordance with the Copyright Act 1968 unless a period of embargo has been approved by the Dean of the Graduate School.

I acknowledge that copyright of all material contained in my thesis resides with the copyright holder(s) of that material. Where appropriate I have obtained copyright permission from the copyright holder to reproduce material in this thesis and have sought permission from co-authors for any jointly authored works included in the thesis.

Publications included in this thesis

No publications included

Submitted manuscripts included in this thesis

No manuscripts submitted for publication included

Other publications during candidature

Journal papers

D. E. Gildfind, C. M. James, P. Toniato, and R. G. Morgan. "Performance considerations for expansion tube operation with a shock-heated secondary driver". In: *Journal of Fluid Mechanics* 777 (July 2015), pp. 364–407. DOI: 10.1017/jfm.2015.349

Peer-reviewed conference papers

P. Toniato, D. Gildfind, P. A. Jacobs, and R. G. Morgan. "Extension of the X3 expansion tube capabilities for Mach 12 scramjet testing: flow condition development and nozzle optimization". In: *20th Australasian Fluid Mechanics Conference*. Australasian Fluid Mechanics Society. Perth, Western Australia, Australia, 2016

P. Toniato, D. Gildfind, P. A. Jacobs, and R. G. Morgan. "Optimisation and design of a fully instrumented Mach 12 nozzle for the X3 expansion tube". In: *31th International Symposium on Shock Waves*. Nagoya, Japan: Springer, July 10, 2017

Conference papers

P. Toniato, D. E. Gildfind, C. M. Jacobs, and R. Morgan. "Development of a new Mach 12 scramjet operating capability in the X3 expansion tube". In: *7th Asia-Pacific International Symposium on Aerospace Technology (APISAT)* (Cairns). Nov. 26–29, 2015

P. Toniato, D. E. Gildfind, A. Andrianatos, and R. G. Morgan. "Full Free-stream Mach 12 Scramjet Testing in Expansion Tubes". In: *2018 Applied Aerodynamics Conference*. American Institute of Aeronautics and Astronautics, June 2018. DOI: 10.2514/6.2018-3818

C. M. James, D. R. Smith, C. McLean, R. G. Morgan, S. W. Lewis, and P. Toniato. “Improving High Enthalpy Expansion Tube Condition Characterisation Using High Speed Imagery”. In: *2018 Aerodynamic Measurement Technology and Ground Testing Conference*. American Institute of Aeronautics and Astronautics, June 2018. DOI: 10.2514/6.2018-3805

Contributions by others to the thesis

Andreas Andrianatos developed the operating piston conditions and related L1D numerical model used in this thesis. Juan Ramon Llobet helped in the development of the computational grid of the nozzle inlet rake.

Statement of parts of the thesis submitted to qualify for the award of another degree

No works submitted towards another degree have been included in this thesis.

Research Involving Human or Animal Subjects

No animal or human subjects were involved in this research.

Acknowledgements

First and foremost, I would like to thank my supervisor Dr. David Gildfind, for providing support, encouragement and advice through all of this PhD. Thank you for sharing your enthusiasm and expertise for the field, but also for listening and helping when nothing was working. Thank you for carefully checking all of my work, I hope my writing is a bit better than when I started.

My sincere thanks goes to my associate supervisor, Prof. Richard Morgan. Your insights on hypersonics, scramjet and expansion tube never cease to amaze me. Your knowledge was an invaluable contribution to this thesis. Thank you for believing in this project and make it happen.

A special thanks to Dr. Peter Jacobs, who supported me with great advice, kind words and optimism through these years. Many thanks to the technicians that helped along the way: Frans, Neil, Keith and Barry.

To all the people that has worked in the xLabs during these years, thank you for your company and help. A special mention to my X3 operators, Andreas, Sam, Daniel and Nils, your sweat was not wasted in vain. Many thanks to the T4 gang, because I literally took all of your instrumentation and you were cool about it. Many thanks to Will, who taught me all the magic tricks of the engine.

Juan, Augusto and Andreas: thank you guys for helping out in so many ways that a whole page would not be enough to describe. Most especially, thank you for bearing my bitterness and complains. I still do not know how you managed to do it, but you truly are great friends. Jeremy, a special “cacedédi” goes to you as well. Thank you for being my first mate in Australia even though it is 4 years you want to go surfing and we have not yet gone together. To all the other friends I did not mention, thank you all, these years have been difficult but rewarding, thank you for being part of this journey.

Thank you to my family, Mamma, Papà, Eleo, Betta, even from far away you have never stopped loving me.

Finally, but most importantly, thank you Lisa, because not only you decided to follow me in this crazy adventure on the other side of the world, but also you gave me a never-ending support, even when I wanted to give up. The biggest achievement of these years was not finishing my PhD, but rather realising the amazing person you are. You truly are the sun of my life, and you always will be.

Financial support

This research is supported by an Australian Government Research Training Program (RTP) Scholarship and the Cooperative Research Centre for Space Environment Management (SERC Limited) through the Australian Governments Cooperative Research Centre Program. This research was undertaken with support and funding of the Australian Research Council.

Keywords

Mach 12, scramjet, hypersonics, air-breathing propulsion, access-to-space, ground testing, expansion tube, numerical simulation, optimisation

Australian and New Zealand Standard Research Classification (ANZSRC)

ANZSRC code: 090107, Hypersonic Propulsion and Hypersonic Aerodynamics, 100%

Fields of Research (FoR) Classification

FoR code: 0901, Aerospace Engineering, 100%

To Lisa,
for your unwavering support and love.
Without you, I wouldn't have made it.

CONTENTS

LIST OF FIGURES

LIST OF TABLES

1 INTRODUCTION

We live in an era where space has never been so important: space-technology permeates every aspect of our lives. Every time we listen to weather forecasts, we look at maps on our phones, we watch movies or live events on the other side of the world, we are using satellites. In this globalised and always-connected world, they are the essential links of our society. Hand-in-hand with space technology, access-to-space capabilities are equally fundamental. However, conventional rocket launching systems are exceedingly complex and expensive, with cost estimates above $20 000 per kilogram, so that only a handful of countries and companies can afford such launching capabilities.

At the same time, although the advancements in electronics and satellite instrumentation technologies have led to satellites that are becoming smaller while gaining in capabilities, launch systems have not changed and rockets that are currently available were designed to launch massive payloads. This forces the new generation of small-scale satellites to share launches and orbits, resulting in lack of flexibility and increased waiting times [7]. In this context there is a push for a new generation of access-to-space technology: cheaper, more flexible and more efficient launch systems tailored for small payloads. A new market answering these needs is opening up in this decade and companies are pushing for new solutions such as reusable rockets (spaceX), or rocket engines with battery-powered pumps (RocketLab). However, these rocket-based launch systems are based on a mature technology, and they are close to the theoretical performance limits. Therefore, there is little margin for disruption of the current sector leaders. A new radical technology shift is required, both to fully answer the newly-arisen market needs, and to be able to compete in a sector where development costs and elevated risks are an enormous entry barrier [8, 9].

Rocket propulsion has managed to reach those highly optimised efficiency levels by being conceptually relatively simple, carrying both fuel and oxidiser (i.e. oxygen) in their tanks. This requires more than half of the whole weight of the system to be just propellant [10]. This is an important drawback; for this reason, in contrast to the recent push for more efficient rockets, more and more concepts exploring the possibility of instead using the oxygen already present in the atmosphere, which aeroplanes turbofan engines do, have been proposed. One of the most promising concepts that take advantage of this idea are scramjets, or supersonic combustion ramjets.

Ramjets are air-breathing engines capable of flying at supersonic speeds. At these velocities the ramjet has enough speed and momentum to be able to compress the flow without the use of a compressor, just using the shock waves generated at its inlet. At low and medium supersonic speeds (below

what is considered hypersonic speed), a compression down to subsonic conditions is possible at the inlet, allowing subsonic combustion [11]. However, at Mach numbers above approximately 5 the pressure and temperature loads produced by decelerating the flow to subsonic speeds would be structurally impractical to withstand, total pressure losses become prohibitive, and the exceedingly high temperatures cause dissociation of combustion products precluding the required heat release. At these speeds, a ramjet is not operable and the scramjet is considered the only viable option, in which the flow remains supersonic all along the internal flow path of the engine [12, 13].

1.1 SCRAMJETS

The scramjet concept is, in principle, quite simple. It consists of a carefully contoured hollow tube whose shape generates shock waves able to produce the right amount of compression to achieve sustained and efficient combustion. A schematic of a generic two-dimensional scramjet is shown in Fig. 1.1. Scramjets are usually heavily integrated to the airframe, taking advantage of the vehicle shape to perform the first part of the compression [10]. After the forebody-compressed flow reaches the intake, the inlet continues the now internal compression process. The isolator is an important component to stabilise the shock system and avoid high pressure in the combustor affecting the inlet flow. At the combustor entrance, fuel is injected. Due to the high pressure and temperatures, the mixture is able to spontaneously ignite and burn throughout the combustor. Finally, to achieve thrust the flow is expanded, initially internally in the nozzle, and finally externally in the vehicle afterbody.

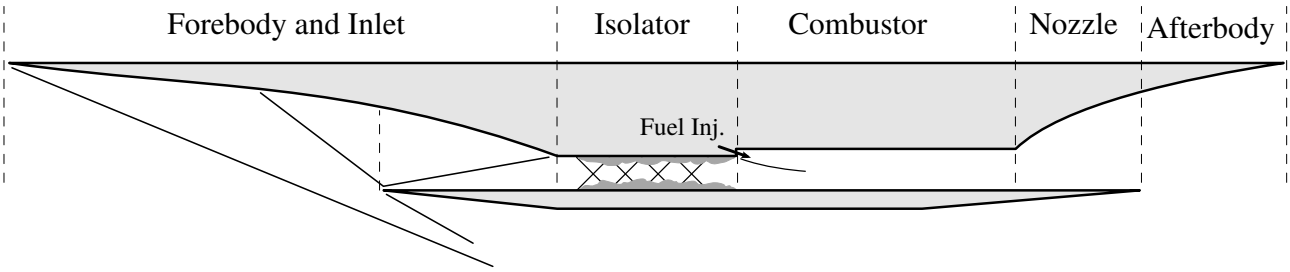

Figure 1.1: Schematic of a generic 2D scramjet engine. Adapted from [14].

Despite the conceptual simplicity, in practice, design of such an engine is complex. Numerous scramjet engines have been proposed over the years, but only a handful of them have been tested in flight (as discussed later in Section 2.4). This is due to the technical complexities associated with hypersonic flight and supersonic combustion. Among these complexities, the most relevant are high thermal and structural loads, short fuel residence times and high viscous drag [10]. These are fundamental aspects that need to be understood and evaluated. To investigate these issues, flight tests are the ultimate requirement, but not an efficient or feasible way to do preliminary engine development, as they are extremely costly in terms of time and required investment. For this reason, ground testing is a fundamental tool for scramjet research. However, the ability to accurately replicate the real flight conditions

is a complex challenge, and developing improved methods to obtain high fidelity test conditions is important to move forward in the development of scramjet engines. On the other hand, considering that test times in impulsive facilities are really short, the cost per second of flight-experiments can be lower than ground tests if designed with affordability in mind [15].

Scramjets, although unable to operate at supersonic speeds (below Mach 5) or outside the atmosphere, are theoretically able to produce higher specific impulse — that is the amount of thrust per amount of propellant burned per unit time per g — than rockets, and therefore represent a viable alternative to rockets during much of the trajectories of a launch to space.

1.2 SCRAMJET FOR ACCESS TO SPACE

Historically, the scramjet engines that have been proposed were either designed to fly at a fixed cruise speed, or designed for acceleration [16]. Engines designed for defence purposes fall for the most part into the first category, i.e. they are designed to be an alternative to cruise missiles and interceptor systems. All the engines that could replace the mission profiles of rocket-based access-to-space systems fall into the second category of "accelerators".

Single-stage-to-orbit and multiple-stage-to-orbit systems have been explored over the years. This includes vehicles such as the NASP SSTO concept from NASA [17] or the two-stage-to-orbit concept by Bowcutt and Smith [7], however, those programs never went past the conceptual phases.

In the wake of the recent push for cheaper access-to-space for small-scale satellites, Smart and Tetlow [8] and Preller and Smart [18] proposed a hybrid three-stage rocket-scramjet-rocket system that could theoretically achieve an increased payload mass fraction up to 1.8 %, compared with the 0.9 % payload mass fraction that can be obtained with current multi-stage systems dedicated to small-scale payloads. Along with increased payload mass-fractions, scramjets would allow for higher flexibility in launch windows and target orbits. Most importantly, increased payload mass fractions and higher specific impulse makes reusability much easier to achieve [19], with a scramjet-powered vehicle able to fly back to the base. Reusability is essential for reduced costs. Yet, an access-to-space scramjet engine would require tighter vehicle integration, as to satisfy the performance requirements the engine would need to take full advantage of the vehicle compression field [16]. In addition, a large operating window is required for the engine, spanning from Mach 6 to as high as Mach 12 flight speed (for a flight speed at the upper bound of $4\,\mathrm{km\,s^{-1}}$).

Amongst the handful of flights tests that have been carried out, only one, the X43 scramjet by NASA, has managed to successfully fly in the high Mach number regime, cruising at Mach 9.68 [20]. However, data from this flight still remains highly classified. Currently, no air-breathing engine has ever flown at speeds above Mach 10.

1.3 RESEARCH CONTEXT: MACH 12 REST ENGINE

With access-to-space in mind, Smart [21] proposed the REST (Rectangular to Elliptical Shape Transition) inlet design methodology, to create a scramjet inlet for tightly vehicle-integrated scramjet designs. The initially rectangular inlet allows the required vehicle integration, and an elliptical combustor allows higher mixing and combustion efficiencies, increased structural strength, and reduced heat losses [21]. This inlet design also allows flow spillage below the cowl closure, and thus, it is able to start and operate at off-design conditions; an essential requirement for accelerating engines.

In particular, an engine with a target Mach number of 12 — the highest Mach number at which an access-to-space engine is expected to fly [22] — has been developed at the University of Queensland (UQ). This engine, called the Mach 12 REST engine, or M12REST, has been demonstrated to work in a variety of off-design, low Mach number, conditions [23], satisfying the accelerator requirements, and proving to be a promising design for integration into a rocket-scramjet-rocket system. The engine is shown in Fig. 1.2

Figure 1.2: Mach 12 REST engine [24].

The Scramjet operating envelope is limited at high altitude by low oxygen densities and combustion efficiency. At low altitude it is limited by structural and thermal loads. Both these limits closely depend on Mach number, so that it is imperative to reproduce the design Mach number during the experiments. The high total pressure requirements at high Mach number can only be achieved by expansion tubes, and this is the fundamental motivation for the present study.

1.4 RESEARCH CONTEXT: GROUND TESTING LIMITS

Air-breathing propulsion for access to space is still in its infancy. The high level of integration necessary for these engines requires a multi-disciplinary approach, where design in different areas is closely interrelated. This complexity along with the extremely high costs of flight experiments make

ground testing fundamental for advancing scramjet technology. On the other hand, the capabilities of computational predictive tools are still limited, especially in combustion modelling, where supersonic combustion simulations still largely rely on models designed for subsonic or low supersonic flows [25, 26]. Moreover, a high computational cost is associated with simulating realistic engine sizes. For these reasons, CFD tools are not yet able to replace physical testing of scramjet engines.

High Mach number scramjets are especially complex, as there are a number of key phenomena that cannot be extrapolated from lower Mach number experiments (below Mach 8): fuel penetration, turbulent mixing rates, combustion efficiencies, and internal losses [27]. For this reason, reliable testing requires facilities capable of generating flow conditions as representative as possible of the actual flight conditions.

In this context, it is clear that reliable and accurate ground testing of a high Mach number scramjet is an essential part in the advancement towards the goal of successfully using these engines for access-to-space. However, achieving the required capabilities to produce the necessary high Mach number flows in wind tunnels is exceedingly difficult. The required total pressure and total enthalpies to replicate the access-to-space flight altitude and speeds are extremely high and only a handful of impulsive facilities in the world are able to produce such flows above Mach 10.

Compared to *full freestream* or *freejet* testing, where the actual freestream flight flow properties are replicated, various testing methodologies that reduce the test flow requirement, have been proposed over the years:

- *direct connect* testing, where the facility reproduces the equivalent conditions at the combustor entrance.
- *semi-freejet* testing, where the facility reproduces the flow behind the forebody shock.

These reduce the total pressure requirements because they aim to simulate the flow after one or more significant shock waves after which, indeed, the total pressure is significantly reduced. Direct connect and semi-freejet, although able to provide great insight into scramjet behaviour, and able to increase our modelling capabilities, intrinsically neglect phenomena that happen in the earlier part of the engine, such as the formation and ingestion of the hypersonic boundary layer at the flight Mach number, transition to turbulence, influence of the forebody shock, and forebody flow spillage.

Reflected shock tunnels, one of the most used type of facility to produce scramjet flows in the Mach range between 4 to 10, are structurally limited in terms of total pressure, and suffer from high levels of chemical dissociation in the freestream due to the extremely high temperature created in the stagnation process, and the subsequent rapid expansion which does not allow recombination of the dissociated chemical species. This reduces the reliability of the data obtained on combustion testing, as significant mass fractions of oxygen and nitrogen oxides have been shown to enhance combustion [28] and can lead to results which are unrepresentative of the flight.

Contrary to RSTs, expansion tubes are able to produce extremely high total pressures thanks to the unsteady expansion mechanism. Additionally, they do not stagnate the flow at any time, while also avoiding the dissociation problem. On the other hand, test times in expansion tubes are much shorter compared to compatible size reflected shock tunnels. However, the Centre for Hypersonics at the University of Queensland currently operates X3, which at 70 m long is one of the biggest expansion tubes in the world, and is therefore potentially able to produce test times sufficiently long to test a full-scale scramjet engine at high Mach number.

The use of the X3 facility can significantly build upon previous ground testing research. Taking as an example the thoroughly studied Mach 12 REST engine, due to the operation and size limitations of the T4 RST at UQ, previous testing has been performed at off-design or in semi-freejet mode at Mach 10. These tests are also influenced by the altered chemistry of the test gas, and furthermore, binary scaling could not be applied to total pressure limits of T4, despite it being a world-class RST. For these reasons, the use of the X3 expansion tunnel can potentially provide very valuable data for high Mach number scramjet engines, which, at the moment, cannot be obtained. This is the motivation behind this thesis, which focuses on performing the necessary modifications and developing scramjet testing capability in X3, as well as for the first time testing a scramjet engine in these conditions.

1.5 THESIS OBJECTIVES

This thesis aims to perform ground testing of a high Mach number scramjet at Mach 12 full freestream flight conditions.

To achieve this, the access-to-space Mach 12 REST engine is tested in the X3 expansion tube, as it is theoretically able to produce chemically correct test flows at the required total pressure and for sufficient test time to achieve steady operation. In pursuing this objective, a number of research questions needed to be addressed:

- *Can the X3 expansion tunnel produce the required flow in terms of Mach number, enthalpy, and core flow size and quality?* This facility had never been operated before at the required Mach 12 conditions. While expansion tubes are able to produce exceedingly high total pressure and enthalpy, they suffer from several drawbacks, such as short test times and test flow disturbances, which are intensified in the operating conditions required for scramjet testing. Thus, a new condition, which allows the required operation of this facility, had to be investigated and developed. This included the design and optimisation of a new nozzle to enlarge and regulate the test flow and its quality.

- *Can the engine successfully and reliably achieve combustion at the theoretically more realistic test conditions produced in the X3 expansion tube?* Previous ground testing research in reflected shock tunnels has shown the ability of scramjet engines to achieve significant combustion. However, these tests have varying degrees of dissociated molecules in the test gas from the stagnation process.

  Moreover, full freestream conditions at Mach 12 have never been tested before for any Mach 12 engine. For these reasons, it remains unproven that these engines can reliably ignite and sustain combustion at the target flight. The tests performed during this work can supplement existing data on scramjet combustion at Mach 12 conditions.
- *If pressure-length scaling is applied, does the engine perform differently?* The Mach 12 REST engine is nominally a half-scale engine and pressure-length scaling to fully replicate the nominal vehicle flight conditions has not been experimentally verified prior to this study. This work aims to demonstrate that it is feasible to carry out these experiments and produce meaningful comparisons.
- *How does the newly gathered data compare to previous research?* There is a large pool of data generated by testing the engine in off-design conditions. The data generated at full freestream, large scale, high chemical fidelity conditions in X3 allow evaluation and comparison with results of previous research on this engine, and which is carried out in the last part of this thesis.

1.6 THESIS OUTLINE

This work is organised as follows:

THE SECOND CHAPTER introduces the topic of scramjets for access-to-space. Moreover, the engine used for this thesis, a three-dimensional airframe-integrated M12REST engine, is presented. Scramjet ground test requirements and available test facilities are then discussed, and their capabilities to test high Mach number scramjets are analysed. Expansion tubes advancements and UQ's X3 facility are presented. Finally, it is shown that X3 is one of the few facilities in the world able to satisfy the total pressure and total enthalpy required to test a scramjet engine at Mach 12 and above at full flight conditions.

THE THIRD CHAPTER details the process for the development of a new operating condition to produce the required Mach 12 test flow. A series of experiments carried out to evaluate the best possible configuration of the facility are discussed, and finally, the details and characteristics of the selected condition are listed.

THE FOURTH CHAPTER considers the design and the manufacture of a new hypersonic nozzle, required to produce the target Mach number along with a core flow of a significant size. The new design process, coupling an optimisation algorithm with parallel computation of CFD simulations, is discussed and the obtained and subsequently manufactured nozzle profile is presented.

THE FIFTH CHAPTER analyses the performance of the newly built Mach 12 nozzle, and the capability of the facility to produce the targeted high Mach number flow is assessed. In the second part of the chapter, a hybrid numerical model of the facility, required to estimate the experimental flow properties, is introduced and then compared to the experimental results.

IN THE SIXTH CHAPTER the experimental techniques used for the scramjet tests are introduced. The experimental model, boundary layer trips, hydrogen fuel system, pressure sensors, and heat transfers gauges are presented. The methodology to experimentally verify successful combustion is described.

THE SEVENTH CHAPTER examines in detail the Mach 12 scramjet's experimental results that have been carried out in the X3 expansion tube, comparing the measured performance to numerical data. Finally, a comparison with experimental data from UQ T4 RST facility is presented.

THE FINAL CHAPTER of this thesis summarises the most important achievements and findings from the previous chapters. A section on recommendations for future work is also included.

2 LITERATURE REVIEW

2.1 PREAMBLE

Sections 2.9 and 2.10.1 are an extended version of parts of the paper: P. Toniato et al. "Development of a new Mach 12 scramjet operating capability in the X3 expansion tube". In: *7th Asia-Pacific International Symposium on Aerospace Technology (APISAT)* (Cairns). Nov. 26–29, 2015

2.2 INTRODUCTION

This chapter can be broadly divided in two parts. The first part is centred on scramjet engines. Scramjets for access-to-space are presented, followed by a discussion of the different aspects that are of importance to high Mach number scramjets. Then, the REST inlet design methodology is introduced and the Mach 12 REST engine is presented. A detailed literature review on the experiments carried out with this engine is discussed and important remaining scientific questions that can be answered with this thesis are identified. Finally, the chosen engine configuration is presented.

The second part of this chapter is centred on ground testing facilities for high Mach number scramjets. A literature review on impulsive facilities is presented, and advantages and disadvantages of the different types are noted. Expansion tube capabilities and their operation are introduced. It is shown that these facilities have the capability to achieve the required total pressure and total enthalpy. The peculiarities that characterise scramjet testing in expansion tubes are also discussed. Finally, the chapter will conclude with the previous scramjet testing experiments carried in expansion tubes, and the selected facility for this study, X3, is introduced.

2.3 SCRAMJETS

Supersonic combusting ramjets, or scramjets are a class of air-breathing propulsion system for hypersonic aircraft designed for operation above Mach 5 [29]. Scramjets, as shown in Fig. 2.1, which essentially are carefully designed hollow tubes, operate on an approximate Brayton cycle, similarly to most of the other air-breathing engines. They distinguish themselves by the fact that thrust is achieved by supersonic combustion of the oxygen contained in the air. The compression phase of the cycle (in Fig. 2.1, 0–2) is done by compression-surfaces — rams — that, in the case of airframe integrated engines, consists of the actual vehicle forebody surfaces and inlet surfaces. Heat addition (3–4) is achieved by the combustion of the fuel injected at the combustor inlet. Finally, the flow is expanded to the external pressure through a nozzle and the expansion surfaces of the vehicle to produce thrust (4–9).

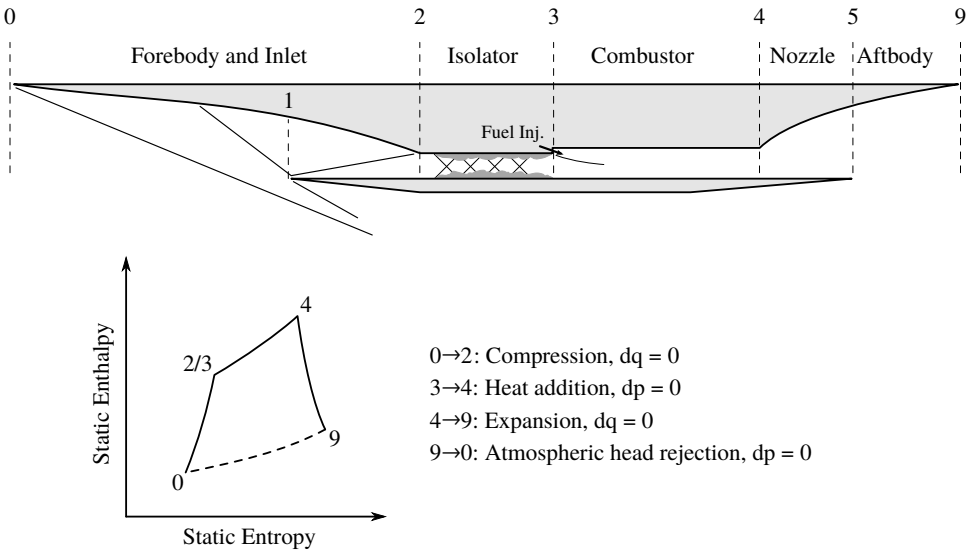

Figure 2.1: Schematic of a generic 2D scramjet engine and operating Brayton cycle. Adapted from [14].

In contrast to rockets engines, which need to carry oxidiser on board, the differentiating characteristic of a scramjet is the capability to use atmospheric oxygen as the oxidiser. Indeed, in what is often referred as "the tyranny of the rocket equation", for increasing payload masses, more fuel is required, but as the fuel increases the total mass, even more fuel is required, in an exponential loop that fundamentally limits the amount of payload that can be put in space. Therefore, payload mass fractions for rockets are often below or around 1 % [9].

A significant metric for space launch systems is the specific impulse, defined as $I_{sp} = \frac{T}{\dot{m} g}$, i.e. the ratio of thrust to the mass of fuel burned multiplied by g, the gravitational constant. Removing the need to carry the oxidiser allows vehicle mass and size reduction, and therefore an increase in the specific impulse of the system, as can be seen in Fig. 2.2.

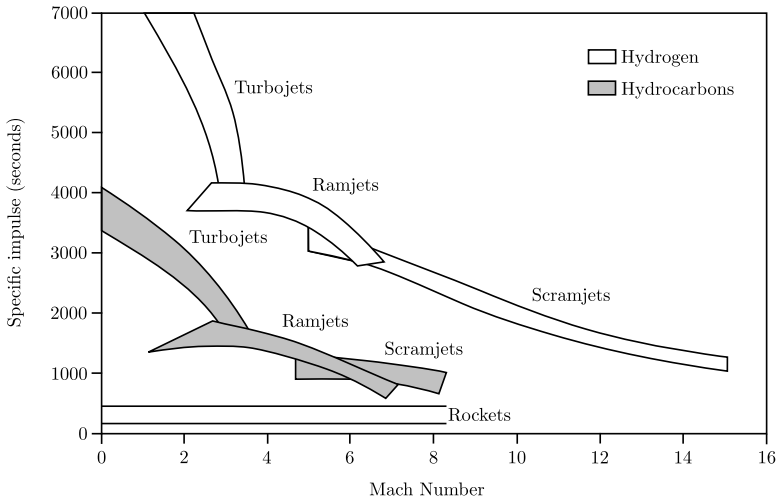

Figure 2.2: Specific impulse versus Mach for various engines. Adapted from [30, 31].

2.3.1 Scramjets for access to space

Recent studies, well summarised in the FAA report [32], of the space launch market indicate that the launch of non-geosynchronous orbit satellites (low-earth and middle earth orbits, i.e. 100 km to 20 000 km) during the next 10 years will be considerably more frequent than in the previous decade. This is driven by an increase in commercial transportation and telecommunications, and is forecast to increase by 5 % in the next two years alone [32]. Due to the rapid development of technology in this sector, reduced design cycles and increased responsiveness, a shift from large scale to smaller scale, cheaper, lighter (<500 kg) satellites is occurring [18]. However, the current cost per kilogram of launching small payloads is three times higher than that for large payloads due to the reduced efficiency of small rockets [18]. The FAA report, [32] it is reported that there is a forecast of more than 400 rocket launches in the next decade which will put an estimated 1000 payloads into orbit. Across these 400 rocket launches, less than 20 % will be small-scale or dedicated to small systems. In this context, small payloads are necessarily grouped together, sharing orbit and launch windows and most importantly, having to adapt to the requirements of the primary launch payload. This also introduces a significant increase in waiting times and limits operational capabilities. The significant lack in flexibility and responsiveness of traditional launch systems is such that a new technology shift is required to meet the small-scale satellites requirements, while being economically viable for both launch systems and satellites companies [7].

In this perspective, in the 1980s and 90s under the NASP (National Aero-Space Plane) program SSTO vehicles (single stage to orbit) were proposed. Moses et al. [33] proposed an integrated lifting vehicle concept working on a turbojet/ramjet up to Mach 4, followed by a scramjet operation mode up to Mach 15. However, it was found that such a concept was well beyond the available technology of the time, and this still remains true today. Indeed, up to the present day, the longest scramjet flight was carried out by the X-51A program for a length of 200 s [34]. Additionally, more recent studies show that high payload mass fractions can be obtained only with multi-stage launch systems [8].

Traditional launch systems are based on two or three stage rocket systems. As an alternative, a rocket-scramjet-rocket system has been recently proposed, in which both first and second stage would be reusable and able to flight back to the launch base [18, 22]. The second stage vehicle, named SPARTAN, would be a high lift-to-drag vehicle, powered by multiple airframe integrated scramjet engines [9], and the vehicle is depicted in Fig. 2.3. It has been shown [9] that this launch system would be able to increase payload mass fractions up to 1.8 %, from the $<$1 % of traditional small rocket systems, corresponding to about 500 kg into a sun-synchronous orbit.

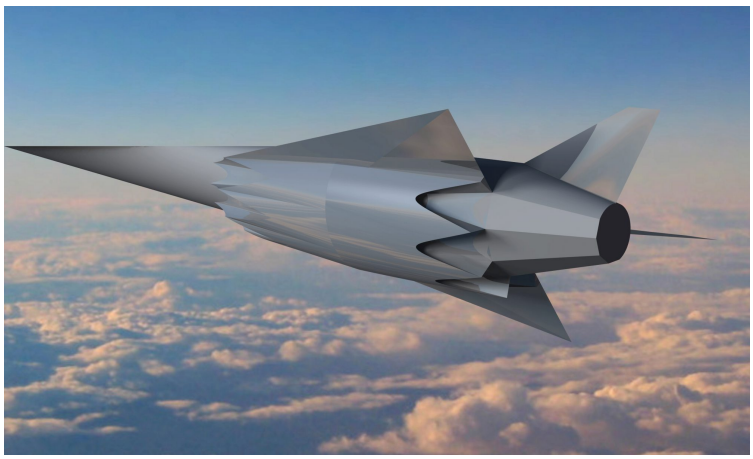

Figure 2.3: Proposed scramjet-powered second stage vehicle [9]. Picture courtesy of Dawid Preller.

It has been argued that the scramjet stage should be expendable [35], because that would allow the use of ablative cooling systems and simplify the design of the engine. However, it has been shown [36, 37] that, given an expendable rocket and an equivalent expendable scramjet, the scramjet would have higher structural mass than the rocket, which would have a higher propellant mass fraction. Therefore, it would not be economically feasible to build and use an expendable scramjet stage, as the propellant cost is lower than the structural cost of the scramjet [37]. The same authors argue that a reusable scramjet would be more practical than rockets because of fewer moving parts [37].

Several authors have elaborated on the above considerations, following in-depth analysis of the advantages of scramjet powered vehicles over rocket systems, which have been summarised by Kumar et al. [38]:

FLEXIBILITY The use of a high lift-to-drag ratio vehicle would permit changing trajectory and/or orbit on demand and allow horizontal landing. Additionally, it would require a shorter time to rendezvous with a target spacecraft and provide a larger launch window and higher number of rendezvous opportunities [19].

SAFETY Abort and return to base would be possible, saving the payload (and greatly reducing insurance costs, which are currently the third most expensive item for a satellite launch [32])

RELIABILITY It is expected that scramjet-powered vehicles would be more reliable because of lower thermal loads and lower pressure and mass flow requirements for the fuel pumps. Additionally, there would be fewer moving parts in a scramjet than in a rocket.

COSTS These could be potentially reduced because the use of scramjets could allow for reusable vehicles and reduced use of propellant.

On the other hand, scramjet operation will require tight engine-vehicle integration, inherently more complex than a standard rocket system [18]. Additionally, decades of experience on rocket-only systems have greatly pushed the rocket operational envelope and reached performance close to theoretical limits. Scramjet development significantly lag behind rockets because only a handful of flight experiments have been carried out [22].

2.4 SCRAMJET FLIGHT TEST HISTORY

Gildfind [30] provides a review of some of the scramjets that have been flight tested. Amongst these, Hyshot II was the first scramjet to demonstrate positive supersonic combustion during a flight at Mach 8 in July 2002.

Prior to Hyshot, a joint Russian/American project, attempted to flight a scramjet at Mach 6.4. Although the flight was successful, the results indicated that the engine operated in subsonic combustion mode, which was itself caused by a defective injector and manufacturing modifications to the inlet [39].

With the NASA Hyper-X program, the X-43 vehicle achieved two successful flights at Mach 6.9 and 9.6 in 2004. Both included a hydrogen-powered flight of more than 5 seconds [20, 40].

On March 2006, a collaboration between University of Queensland and British company Qinetic lead to the launch of Hyshot III, which sustained Mach 7.6 hypersonic flight during its free fall for about 6 seconds [41, 42].

Some days later, Hyshot IV was launched, carrying a scramjet payload designed and built by JAXA (Japanese Space Agency), but the nose cone did not deploy and the experiment failed [43].

On June 2007, the HyCAUSE scramjet was launched. However, a failure in the exo-atmospheric re-orientation manoeuvre caused the vehicle to enter into a complex spinning-coning motion, and it did not achieve all the scientific objectives [44].

HIFIRE was one of the largest collaborative research programs between Australia and the USA (US $54 million) [45]. Its purpose was to develop and validate technologies critical to hypersonic aerospace systems, through flight tests, allowing for the gathering of system-level performance data that cannot be obtained through ground testing [46]. These experiments included testing of full scramjet engines. HIFIRE 2 was launched in May 2012. A hydrocarbon-fuelled scramjet, it flew on a constant dynamic pressure trajectory from Mach 5.4 to Mach 8. It successfully completed the first scramjet combustion transition mode from subsonic to supersonic. Additionally, a TDLAS (Tunable Diode Laser Absorption Spectroscopy) system to monitor in-flight water production in the combustion products

was integrated into the payload and worked successfully [45]. The HIFIRE 3 payload consisted of a hydrogen-fuelled "radical farming" scramjet. Launched in September 2012, it flew successfully and all scientific objectives were met [15]. The goal of HIFIRE 7 was to test an ethylene-fuelled REST inlet scramjet at Mach 7.8 on a ballistic re-entry. Launched in April 2015, the payload lost its telemetry before the experiment [47].

The most successful experiment so far (in term of flight duration) is the Boeing / US Air Force X-51A [48], a hydrocarbon-fuelled scramjet that achieved about 40 seconds of scramjet operation on May 2010 at Mach 5, in its first flight. The vehicle did not reach its target speed and operation time (Mach 6 and 300 seconds) but the test is considered to have met the scientific objectives [48].

The second and third flights of the X-51A, done in June 2011 and August 2012, failed [49, 50]. In its fourth attempt, the X-51 successfully flew for 210 seconds up to Mach 5.1 for over six minutes of flight, being the longest air-breathing hypersonic flight [34].

Scramspace was a three year, AUD $14 million research program with the objective of launching a Mach 8 scramjet. Launched in September 2013, the sounding rocket failed shortly after launch because of faulty graphite in the nozzle, therefore never achieving desired speed and trajectory to test the scramjet [51].

2.5 SCRAMJET PROCESSES AND CHARACTERISTICS

In the following section a short literature review of different scramjet design topics is given, with the goal of introducing the complexities of this kind of engine, with a special focus on high Mach number scramjets. The complexities of a scramjet system are several, and a variety of disciplines are involved. The interactions between each subsystem are not yet fully understood, and the behaviour of the engine as a whole needs to be investigated, making ground testing (or flight testing) of full-vehicles (including the forebody) still important.

SCRAMJET FLOW-PATH The critical role of an optimised scramjet flow-path at high Mach number becomes evident if Eq. (2.1), a *rule of thumb* given by Anderson [52] is considered:

$$\left[\frac{\text{heat release}}{\text{kinetic energy of airstream}}\right] \simeq \frac{69}{M_\infty^2} \tag{2.1}$$

The formula, which compares the ideal heat release over the kinetic energy of the incoming air-stream, shows that at Mach 6, the ratio is ~2. At Mach 12 the ratio decreases to 0.5. That means that at higher Mach numbers adding a given amount of energy to the flow provides a smaller and smaller change

in velocity. Finally, as energy is proportional to the square of velocity, it can be seen that following Anderson's rule of thumb, thrust per unit mass is proportional to $\frac{1}{M}$.

The actual heat release at high speed diminishes because of the difficulty in obtaining adequate mixing without high losses [53]. Additionally, a fixed geometry inlet scramjet (the most likely flight configuration) would encounter a variety of operating conditions during the flight, including a pressure decrease (higher altitude) and a post-forebody-shock temperature increase (higher Mach number), as the vehicle is accelerated to high Mach. Kutschenreuter [53] observed that lower pressure and high post-combustion temperature both decrease the amount of heat release due to an increased rate of endothermic reactions. Higher fuel-to-air ratios would be necessary to cool the flow and prevent endothermic reactions from occurring.

FUEL The residence time and ignition mechanism of the fuel are extremely critical for scramjet performance. As an example, for Mach > 7 the residence time is in the order of $1\,\mathrm{ms}$ for an engine of about $1\,\mathrm{m}$ to $2\,\mathrm{m}$. A fuel with short ignition delay time is required, while it is also desirable that it has a high specific energy to maximise specific impulse [54]. Hydrogen exhibits a much higher specific energy ($116.7\,\mathrm{MJ\,kg^{-1}}$) compared to hydrocarbon fuels (for example CH_4 with $50.0\,\mathrm{MJ\,kg^{-1}}$), but at the same time the energy density is lower ($8285\,\mathrm{MJ\,m^{-3}}$ vs $21\,200\,\mathrm{MJ\,m^{-3}}$) so that net density is higher ($71\,\mathrm{kg\,m^{-3}}$ vs $424\,\mathrm{kg\,m^{-3}}$) [54]. However, the heat release per kilogram of air is similar between the two kinds of fuels, so that they develop similar levels of thrust. Additionally, the use of hydrogen as a fuel in flight experiments is limited by the additional storage requirements, due to its volatility and permeability, which do not characterise hydrocarbon fuels. For example, the X43 vehicle had to pressurize the internal cavities with nitrogen, to avoid hydrogen leaks reacting with the atmospheric oxygen [20].

Hydrocarbon fuels therefore have the overall advantage of higher energy density with additional advantages, such as simpler handling and storage requirements due to the fuel of being a liquid at room temperature. Military operations, as an example, would require the fuel to be stored in the scramjet for long periods, ready to be launched. However, Lewis [54] predicts that useful range for hydrocarbon powered scramjets is limited to flights below Mach 10. Tetlow and Doolan [37] analysed a three-stage vehicle (rocket-scramjet-rocket) and concluded that a hydrogen-fuelled scramjet would outperform a hydrocarbon one in this configuration.

Hydrocarbon fuel ignition delays are prohibitively large above Mach 7, as they become of the same order of magnitude of the fuel residence times. The difference is over one order of magnitude with respect to hydrogen [55, 56]. As a consequence, the use of hydrocarbon fuels for scramjet powered vehicles is linked to the development of new injection, mixing and ignition systems that can enhance the combustion efficiencies over the scramjet's short residence times. Denman [57] showed supersonic combustion of hydrocarbon fuels in a Mach 7 scramjet engine, with a cavity flame-holder.

Finally, it is important to note that the fuel can also be used as a cooling fluid (as a heat sink) to reduce the heat load over the vehicle structure and increase the overall fuel combustion efficiency. Heiser

and Pratt [10] observed that hydrogen would be the only fuel able to satisfy the cooling requirements above Mach 10. Jazra et al. [22] noted that the engine-vehicle integration is a critical aspect of the vehicle's performance, and that a multidisciplinary optimisation process is necessary as a part of the design process to establish optimal fuel selection. Indeed, the choice of the fuel system is related in an inter-dependent way to the whole vehicle design, and not only to energy or cooling requirements.

INLET AND COMPRESSION A hypersonic inlet contracts the incoming freestream flow into the combustion section of the scramjet. From a thermodynamic point of view, a higher compression ratio increases the efficiency of the Brayton cycle of the engine [58]. Contrary to subsonic engines (turbojet), the compression can occur without the use of mechanical parts, but rather through oblique shock waves generated by the carefully designed shape of the inlet itself. The compression generated by the oblique wave emanating from the vehicle forebody is also taken advantage of by the inlet, reducing the compression that the intake itself has to create.

Existing inlet designs include 2D planar, 2D axisymmetric (Oswatitsch and Busemann [59, 60]), and 3D (inward turning, REST [21] and side-wall compression [58]). Shape-transition inlets are an effective option for airframe-integrated scramjet engines. The REST (rectangular to elliptical shape transition) inlet uses shape transition to achieve good vehicle integration, and it has been shown to work in a wide range of conditions [21], taking advantage of its shape to allow spillage to help start the inlet, while being efficient during operation at the nominal Mach number. Shape transition engines are designed to take advantage of the initial vehicle compression field generated by the leading-edge shock, ensuring that the actual inlet shape blends nicely around the vehicle and, finally, guaranteeing that the inlet transitions to an efficient shape for a combustor (i.e. circular or elliptical).

The amount of compression that an inlet should provide is highly dependent on the Mach number range of operation and the method of integration with the vehicle [61]. A rule of thumb, proposed by Kutschenreuter [53], suggests that the pressure at the combustor entrance should be ~50 kPa. The same value is confirmed by Smart [61], which also suggests that for various Mach flight speeds between 6 to 12, inlets with compression ratios between 50 and 100 would allow for optimum cycle efficiency.

Inlet unstarting is a critical issue that could prevent successful operation of scramjets. This is generally caused by the inability of the combustor sections to "process" the flow captured by the intake. This issue is caused because, for many scramjet geometries, both a supersonic and subsonic flow solution exists for much of the flight regime. Upper and lower bounds for a starting inlet have been identified in terms of the contraction ratio, i.e. capture area vs throat area. The upper bound corresponds to the compression ratio that an isentropic compression would achieve for a given inlet Mach number (even if the actual limit is higher, because of viscous losses and shock waves) [58]. The lower bound is determined by assuming a normal shock at the beginning of the combustor and calculating the isentropic flow process for which the flow will again be sonic at the throat (Kantrowitz

limit) [62]. However, the limit is conservative for high Mach numbers, and started inlets in conditions lower than Kantrowitz limit have been observed [58].

The starting process in impulsive facilities (and specifically in expansion tubes) is different to in-flight conditions. The initially low-pressure nozzle fill gas (or for expansion tubes, shock-processed accelerator gas) has a lower density, making it, at least in theory, easier to start the inlet, as the mass flow is proportional to the density [58]. The presence of O and NO radicals have also been shown to enhance combustion [28].

Viscous dissipation plays a fundamental role, given the high increase in temperature and gas density. The interaction of the boundary layer with the outer flow (outer with respect to the boundary layer) is strongly coupled, such that the outer flow sees a substantially different "equivalent geometry" of the wall, having a significant effect on the inlet effective capture area [63].

Boundary layer transition on an inlet can potentially influence performance and operability of the engine [58]. Transition to turbulent flow and boundary layer separation are responsible for an increase in friction losses and heat flux loads. Therefore, it is fundamental to predict separation regions in the engine, and take them into account within the design process. While this is an extremely complex phenomenon, some correlations exist depending on the transition mechanism (see [58]). If the boundary layer transition cannot be predicted accurately, it is important then to put in place mechanisms to force the laminar boundary layer transition to turbulent, as the separation regions created by adverse pressure gradients can potentially unstart the engines [24].

Returning to the goals of this thesis, testing a nose-to-tail engine, i.e. an engine including the vehicle forebody through to the nozzle exit in freejet mode, allows analysis of the global interactions between the different mechanisms in play, especially boundary layer development and transition in the inlet, which usually are not taken into account because of the necessity of studying scaled model or direct-connected (or semi-direct) engines.

INJECTION AND MIXING The issue of the mixing of fuel and air is fundamental for supersonic combustion, and it becomes increasingly difficult as the Mach number increases. The momentum in the axial direction dominates all the mixing phenomena, and extremely careful and studied methods are required to increase mixing without introducing the side effects of total pressure losses that result directly in a reduction on net thrust [64]. Ideally, an effective injection would be able to provide a high mixing rate minimising the thermodynamic losses occurring in these processes.

The different techniques that have been used so far can be divided into three categories: strut based, flush wall injection, and injection from ramps [65]. The first category provides high mixing rates by adding fuel to the middle of the combustor duct, but also creates a large disturbance to the flow. Additional drawbacks are increased cooling requirements on the struts and strong shock interactions. Struct-based techniques are used in the lower part of the scramjet flight envelope [66]. Flush wall

injectors do not block the flow in any way, but they suffer from greater mixing length [67] than the other injection types. Ramp injection [68] uses a ramp to inject tangentially to the flow, with the injectors located in the trailing edge of the ramp. The flow over the ramp creates some vortices that increase mixing. Inlet injection (or upstream injection) attempts to solve both the strut flow blockage and the mixing length problems by injecting at the inlet, before the combustor, and allowing for partial fuel/air mixing before entry into the combustor [69, 70]. Several geometries have been studied, with the focus being on streamwise fuel injection in order to benefit from the thrust increase given by the fuel momentum [71].

Fuel injection in ground testing facilities has some differences compared to flight: it has been observed that there is a mixing rate reduction in flight compared to ground testing due to lower turbulence levels present in the atmosphere compared to wind tunnels [72]. Additionally, it is expected that the fuel will be heated and used as a heat sink to reduce the temperature of the structure and improve performance [73].

COMBUSTOR The combustor is one of the key elements of a scramjet engine, and its design presents many challenges: large and localised peak heating, wall cooling requirements, minimisation of losses and increased mixing efficiencies. These design issues have an increased importance when considering high Mach number scramjets. With increasing Mach number, the overall heat release from the combustion process is proportionally lower with higher Rayleigh losses in the combustor [10]. Another key characteristic that differentiates high Mach number scramjets is that for Mach >8 the increased kinetic energy of the airflow tends to suppress the localised combustion pressure rise (which would, at lower Mach number, cause boundary layer separation), so that the flow remains attached through the whole combustor [65].

The shape of the combustor has a fundamental role on engine performance, and it depends on several factors: weight per unit length, combustor length over combustor height, boundary layer effects, and the ratio of wetted surface area to flow-path area [66]. Small ratios of wetted area to flow-path area reduce skin friction drag and heat transfer. The length to height ratio is important because mixing and combustion efficiencies are related to this ratio, due to reduced penetration and mixing distance requirement for the fuel. Rectangular shaped combustors suffer from corner effects and a complex interaction with the boundary layer [74]. Elliptical and circular shapes have been investigated and compared [66]. While circular combustors offer less structural weight and a higher ratio of wetted area over flow-path area, elliptical shapes offer higher length-to-height ratios, allowing for a more efficient injection. It is considered that elliptical shapes with aspect ratios up to 1.6 do not require additional structural reinforcements to withstand the load compared to an equivalent circular combustor, and therefore might be preferred [74].

The length of the combustor is a trade-off between the level of mixing and combustion achieved, and the viscous drag and heat transfer that are generated. The hypersonic boundary layer that develops in the internal flow path of the engine makes up for a significant part of the overall engine drag. Tanimizu et al. [75] observed that the supersonic flow passing through the combustor of an axisymmetric engine created more than 60 % of the total skin fraction drag. It has been shown that the optimal configuration

length in terms of thrust often does not correspond to maximum combustion: the heat released obtained in a longer combustor can be offset by the increased skin friction losses [76].

The cooling requirements for flight vehicles, especially for high Mach numbers, might be the design limiting factor, because of the necessity of withstanding the high peak localised heating loads [77]. It has been suggested that the fuel could be used as a thermal sink to absorb a large portion of the heat load [74]. Another solution that has been proposed is the use of film cooling, or hydrogen boundary layer combustion that might be able to transfer a lower amount of heat to the walls [78]. The interaction between inlet and combustor is extremely critical to the engine's performance. Anderson et al. [77] suggests that all shock waves generated in the inlet should be prevented from entering the combustor to minimise losses, but satisfying this criterion, especially in the off-design conditions, is very difficult. An isolator, which is an intermediate duct between inlet and combustor, is often proposed as a means to adapt the fluctuating pressure in the combustor to the inlet pressure, through a complex shock train that is generated [10].

Contrary to the thoughts of Anderson et al. [77], Odam and Paull [70] proposed a new technique, radical farming, in which the inlet is designed to allow the shock to pass through the combustor, and is arranged to form localised regions of elevated pressure and temperature. These discrete areas of non-uniform flow promote rapid reaction rates and increase the combustion efficiency. As strong waves are present throughout the combustor, much more thorough considerations of flow interactions and friction losses are necessary. The HIFIRE 3 flight experiment showed the operability of an axisymmetric, high contraction ratio radical farming scramjet, following on from a design developed by Hunt [79] for his doctoral dissertation, which in ground test experiments showed high reliability and robust combustion.

THRUST NOZZLE The use of a nozzle is necessary in order to maximise the thrust obtainable by the engine. While it is generally easier to design a scramjet nozzle than a ramjet one (with the flow being already supersonic it is not necessary to consider the difficult subsonic to supersonic transition), the exit flow from the combustor might be non-uniform, requiring relatively complex designs [10]. Additionally, non-equilibrium effects (i.e. recombining flows) occur in the rapid expansion, and they should be considered for an optimised nozzle. If high levels of dissociated molecules are present in the flow exiting the combustor, then the nozzle expansion might be too fast to reach equilibrium state, such that all the energy associated with dissociated and excited molecules is not recovered, reducing the overall efficiency [80].

The cross-sectional area of a nozzle is likely to be higher than that of the engine itself, increasing inviscid and viscous drag of the vehicle. In addition, skin friction (both internal and external) is not negligible. A compromise is therefore necessary between the thrust generated by the nozzle and the drag associated with a larger nozzle [10]. Particularly at higher Mach numbers, where the thrust available is low, this compromise is critical [53].

2.6 THE REST ENGINES

In the previous section, it has been observed that a promising candidate shape for a scramjet combustor is elliptical. However, the question of how to design an efficient inlet connecting a sharp inlet cornered surface to a quasi-circular combustor is of fundamental importance. Busemann inlets are one of the most efficient in terms of contraction ratio [58], but with their axisymmetric shape they would not be able to provide an efficient integration into the airframe. Additionally, they cannot be started under steady flow conditions. Indeed, it is difficult to envision a Busemann inlet, or any other axisymmetric inlet that could integrate into a payload-holding vehicle [58].

The "rectangular to elliptical shape transition" (REST) methodology was developed by Smart [21] to overcome this problem. This methodology is based on a streamline tracing technique in which the capture area of the inlet and the throat geometry are specified a priori. The resultant capture shape has a flat top and side and a V-shaped cowl to provide for highly swept leading edges that terminate in a sharp cowl connection point, as in Fig. 2.4 [11]. This configuration allows for 3D inlets that do not suffer from boundary layer spillage, with the capability to operate over a wide range of flight Mach numbers and to self-start. Details of the procedure can be found in Smart [21]. The upper surface is designed to facilitate integration with the vehicle. For ground-testing engines, this surface is considered flat, although integration with other shapes, such as conical surfaces, is still possible [9].

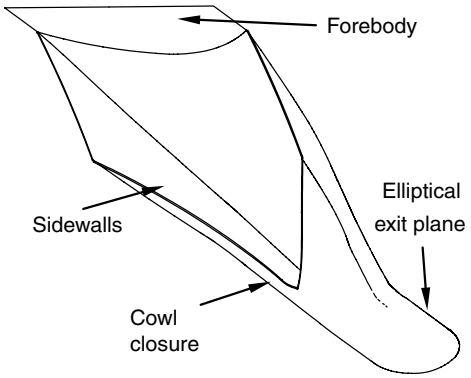

Figure 2.4: REST inlet surface. From [11].

2.6.1 Mach 12 REST engine

A total of four different engines have been designed, built, and tested, by the research group of Smart at the University of Queensland. These engines were designed with access-to-space in mind, and as such, they were candidates for use in this work. The last and most current of those engines — at the time of writing — and the one of most interest in this thesis is the M12REST engine, shown in Fig. 2.5. The combustor and nozzle are inclined 6° with respect to the inlet to realign the flow with the nominal

flight direction. The combustor is divided into two sections, with the first one having a constant internal area section and the second diverging to maintain constant temperature in the combustion region. Finally, a generic conical divergent nozzle with an area ratio of 4.0 (not specifically optimised for thrust) is located at the end of the combustor.

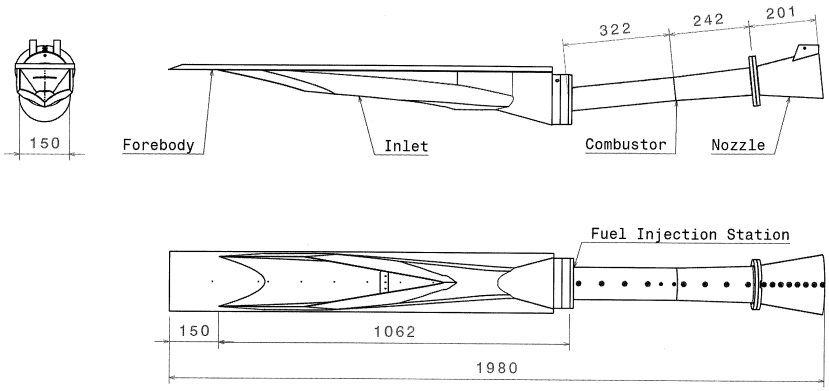

Figure 2.5: Schematics of Mach 12 REST engine model. From [65].

Fuel can be supplied to the engine at two stations: the first one is located along the inlet at the combustor entry, consisting of 3 portholes 4 mm in diameter and angled at 45° with respect to the local flow. These injectors have been sized to allow the fuel to penetrate the inlet boundary layer in order to increase mixing with the airflow captured by the engine. The second station, at the entry of the combustor, consists of 48 "boundary layer" portholes, 1.5 mm diameter angled at 10° [23]. The goal of such a configuration is to benefit from skin friction reduction through boundary layer combustion [81]. Suraweera and Smart [23] tested the engine in semi-direct connected mode (semi-freejet), in UQ's T4 reflected shock tunnel (RST) at conditions equivalent to freestream Mach 8.4 (Mach 7.14 at the engine inlet after forebody shock processing). In that T4 campaign, it was observed that the failure of the boundary layer to transition to turbulent was responsible for the flow separation and mismatch with expected performance from the CFD.

Wise [82] tested a half scale M12REST engine with a forebody plate in semi-freejet mode. This campaign investigated how to assure a fully transitioned boundary layer with the use of boundary layer trips. Thin-film heat transfer gauges were used to measure the heat flux and the state (laminar or turbulent) of the boundary layer. For these experiments, the necessity of including a 500 mm long flat plate to insure a fully transitioned boundary layer, along with space and test time constraints given by the facility, limited the maximum size for the engine. The injectors at the second station for this configuration were modified and consisted of 36 injectors, 0.9 mm in diameter, angled at 10° injecting on a backward facing step (details of that configuration are shown in [82, Fig. 6.6]).

The Wise campaign [82] was conducted in the T4 RST, with a Mach 12 equivalent enthalpy, but with a Mach 10 flow (semi free-jet). This was carried out to recreate the flow created behind a shock generated by a forebody at 6°. The performance of the facility, however, was slightly higher than desired. For this reason, the model was inclined at 1.6° angle of attack in order to match the target

Mach number at the engine inlet. The calculated equivalent flight dynamic pressure for these tests was 27 kPa to 32 kPa (compared with the target inlet design of 50 kPa dynamic pressure).

The results showed that robust combustion could be achieved for a variety of equivalence ratios, ranging from 0.60 to 0.76 for inlet-only fuelled shots. Combustor-only injection, however, failed to demonstrate stable supersonic combustion, indicating that the radicals produced by the inlet injection were fundamental for ignition, even considering the high temperatures created in the combustor. Combined injection was also investigated at different fuel ratios between the two combustors. An optimal configuration was found at the fuel ratio (inlet: combustor) 31 : 69 with an equivalence ratio of 1.0. Higher equivalence ratios did not increase the performance of the engine.

In parallel to the work of Wise, Barth [83] numerically investigated the flow dynamics of the engine. The key observation was that fuel is pushed toward the side walls due to the presence of streamwise vortices, failing in the goal of achieving boundary layer combustion, which in theory allows for a reduction in viscous drag [84] and which was the goals of the original combustor of Wise [82].

Barth also proposed a different injection scheme, shown in Fig. 2.6. While the inlet injectors were kept, a new injection station at the combustor entry was proposed. It was longitudinally located at the same position as the preceding one, and it consists of injectors, 0.8 mm in diameter, angled at 45° in the flow direction. The rationale for this configuration is detailed in [83] but is briefly illustrated here. The central injector in the cowl-side was placed to take advantage of the pair of streamwise vortices that are specific to this engine. The off-centre cowl-side injectors have been placed to evenly distribute the fuel through the high-density air flow of the cowl-side. CFD simulations results informed the placement of the side-wall injectors, which were located to take advantage of an oxygen rich zone that previously did not interact with cowl-side fuel.

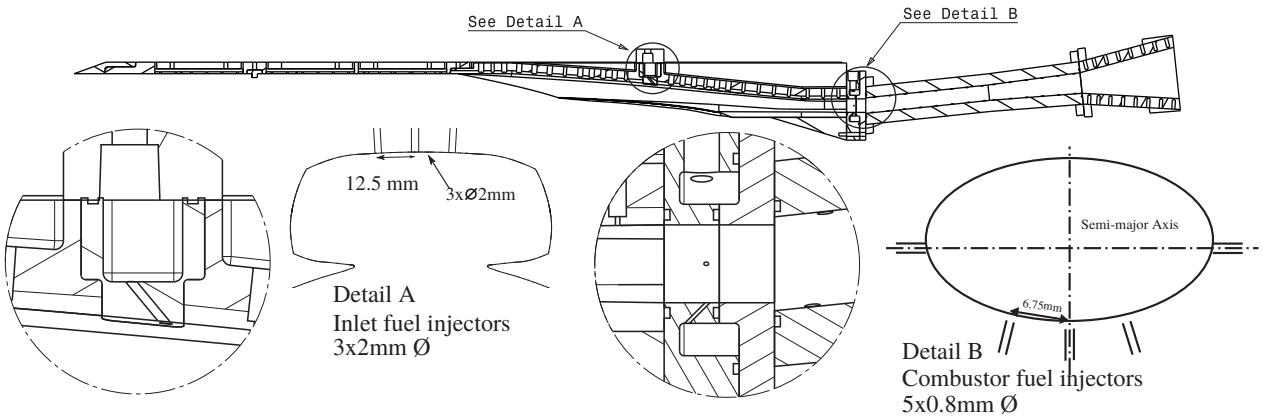

Figure 2.6: Mach 12 REST engine in the configuration of Barth [83].

This injector configuration was tested with the same model and conditions of Wise [82]. The results have shown that the estimated combustion efficiency improved by 2 % when using the improved injection scheme, while using 6 % less fuel. However, according to the simulations, it was observed

that the fuel failed to penetrate the core flow rich in oxygen, and further optimisation remains an ongoing research area [83].

Barth [83] also conducted a CFD study simulating the engine at the experimentally produced flow conditions — in which there is a non-negligible amount of nitric oxide (NO) — and at the design atmospheric condition. It was observed that there was an 11 % difference in the capture area of the engine, due to spillage and changed shock angles. Considering the different chemical composition, the results showed that the flight equivalence ratio is 27 % smaller than the one calculated in the facility.

Doherty et al. [85] developed a streamlined, airframe integrated M12REST engine at 32 % scale compared to the one designed by Suraweera and Smart [23], in order to fit the whole engine (including forebody) into the core-flow of the T4 testing facility. The goal of the authors was to use a multi-component force balance [86] to measure the thrust provided by the engine. For this configuration, the inlet station consisted of 3 injectors, 1.3 mm in diameter. The second station was similar to the original used by Suraweera [47], with 24 portholes, each 0.65 mm in diameter.

The model included a 6° wedge as a forebody, with a boundary layer trip to ensure transition, similar to Wise [82]. Finally, the nozzle was modified and rotated to take advantage of available space and to facilitate a more streamlined external geometry. That work represents the first attempt at testing a REST-class engine integrated within an airframe, in freejet mode, although at off-design conditions.

Similarly to all the previous tests, that model was tested without applying any binary scaling, due to operating limitations of the T4 RST in terms of total pressure. The engine has been tested at Mach ~10 condition, for an equivalent dynamic pressure of 27.9 kPa and 48.0 kPa. The authors showed that REST class engines can be integrated within an airframe and operate in freejet mode. As observed previously, inlet injection was again found to be fundamental to achieving supersonic combustion. Additionally, many technical difficulties were also encountered with the use of a force balance due to the interaction of the facility with its shielding which caused blockage and flow separation in the nozzle.

More recently, Landsberg [87] carried out a mixed experimental and numerical study on the M12REST engine, investigating several techniques to increase combustion and mixing efficiency in the engine. He proposed a reduced-length combustor, using the injection scheme of Barth, although removing the backward facing step. Net system improvements were achieved thanks to a reduction of 22 % in viscous drag, and an overall combustion efficiency above 80 %. The 68 % shorter combustor produced an estimated improvement in gross thrust coefficient within the range 10 % to 25 %.

2.6.2 Engine choice and flight conditions

The previous sections of the literature review illustrated how high Mach number scramjets have an important role for new access-to-space scramjet vehicles. At the same time, only a handful of flight-experiments have been carried out, and their data is often still classified.

The M12REST is a promising concept to explore the high Mach number regime of scramjet operation. The engine has been designed for flight at Mach 12 at 50 kPa dynamic pressure, at an altitude of 36 km, and it is meant to be attached to a vehicle with a 6° angle of attack forebody. The design flow condition is indicated in Table 2.1.

Table 2.1: Target flow conditions on a 50 kPa dynamic pressure.

	Units	Full scale	1:2 Scale model
Altitude	km	36	36
p	Pa	496	992
p_0	MPa	310	620
H	$MJ\,kg^{-1}$	7.2	7.2
T	K	239	239
u	$m\,s^{-1}$	3722	3722
M		12	12
q	kPa	50	100

This engine was tested in a variety of conditions and configurations, but, all of them were at off-design condition, and/or in semi-freejet mode, i.e. such that the facility produces the equivalent flow behind the forebody shock. The interactions of the boundary layer developed by the forebody ingested by the inlet and combustor at the design Mach number have been not investigated before. Additionally, notwithstanding the fact the engines of Wise, Barth, Doherty and Landsberg [14, 82, 83, 87] were scaled down version of the original ideal flight engine, no pressure-length scaling was applied, and similarity with flight was not achieved.

For these reasons, the engine in the optimised-configuration by Barth [83] (depicted in Fig. 2.6) was chosen and adopted for this thesis, with the goal of carrying out ground-testing in full-freestream conditions.

2.7 GROUND TESTING

In this final part of the chapter the focus will be on ground testing facilities and their associated capabilities. This will contribute to the understanding of how expansion tubes can and should be used for high Mach number scramjet testing.

2.7.1 The case for ground-testing

Ground testing for any kind of air-breathing engine is essential due to the much higher costs and risks associated with flight testing [88]. Yet, one might argue that the continuing advances in Computational

Fluid Dynamics (CFD) would decrease the importance of experimental testing. However, while CFD codes are extremely useful to provide insight into many processes that are not normally easily accessible to the experimentalist, and allowing parametric studies with (relatively) rapid and low-cost turnaround, the codes must be validated against experimental data. Especially difficult to appropriately model in CFD are phenomena like combustion and turbulence, which take place down to a molecular level. These phenomena can be only approximated by CFD tools, which fundamentally rely on a continuum description of the fluids and requires simplified reaction schemes to make solutions feasible [73].

Additionally, a scramjet-powered vehicle requires a multidisciplinary approach, as a tight integration between the engine and the vehicle is required, and also between the engine subsystems. The interactions are not yet fully understood, making both ground and flight testing still a continuing important requirement.

Having ground testing capabilities is therefore fundamental to the future developments of scramjets. The range of required scramjet ground testing can vary and could include structure, external/internal aerodynamics, thermal, and propulsive testing [74].

2.7.2 Pressure-length scaling

For aeropropulsion tests, the chemical composition of the gas and the flow features must be preserved [89]. As described in [52], the primitive variables involved in the flow characterisation of hypersonic combustion processes are: pressure P, temperature T, velocity $\mathbf{u}$, model characteristic length L and gas composition ν_i. The (classical) dimensionless groups that can be produced from these quantities are: Mach number M, Reynolds Number Re, Stanton number C_H, and Damköhler first and second numbers D_1 and D_2. The interpretation of the last two parameters is specific to hypersonic reacting flows, and correspond to the ratio of flow transit time through the combustor to chemical reaction time (D_1), and the ratio of heat added by reactions to the stagnation enthalpy of the inviscid flow (D_2). To correctly reproduce the flow features conservation of all these numbers is necessary [52].

As shown in [90–92], binary scaling (otherwise known as density-length scaling), if applied at constant temperature, is called pressure-length scaling (pL) and is able to theoretically replicate most (but not all) the dimensionless numbers defined previously. As an example, mixing and viscous effects may be matched, but the combustion pressure rise is underestimated [90, 91].

Pressure-length scaling allows reduction of the test model size, which is often unavoidable for ground testing, but comes at the cost of increasing the pressure p by the inverse of length, to ensure the product pL remains constant. Additionally, as it will be shown later in Section 2.8, reproducing the high Mach number scramjet flow conditions for access to space is very challenging. The ability of the facility to produce the absolute total pressure and enthalpy becomes a fundamental consideration [28].

2.7.3 Total pressure requirements and ground testing methods

Figure 2.7 provides an approximate overview of the various hypersonic facilities and their performance in terms of Mach number and total pressure. The pressure requirements increase on a logarithmic scale [28] with flight test Mach number reaching values of the order of GPa. Those requirements are out of the range of most current facilities, and so far, this problem has been solved in two different ways. The first possibility consists of studying only scramjets designed to operate at low dynamic pressures or studying high-Mach scramjet operating at off-design conditions.

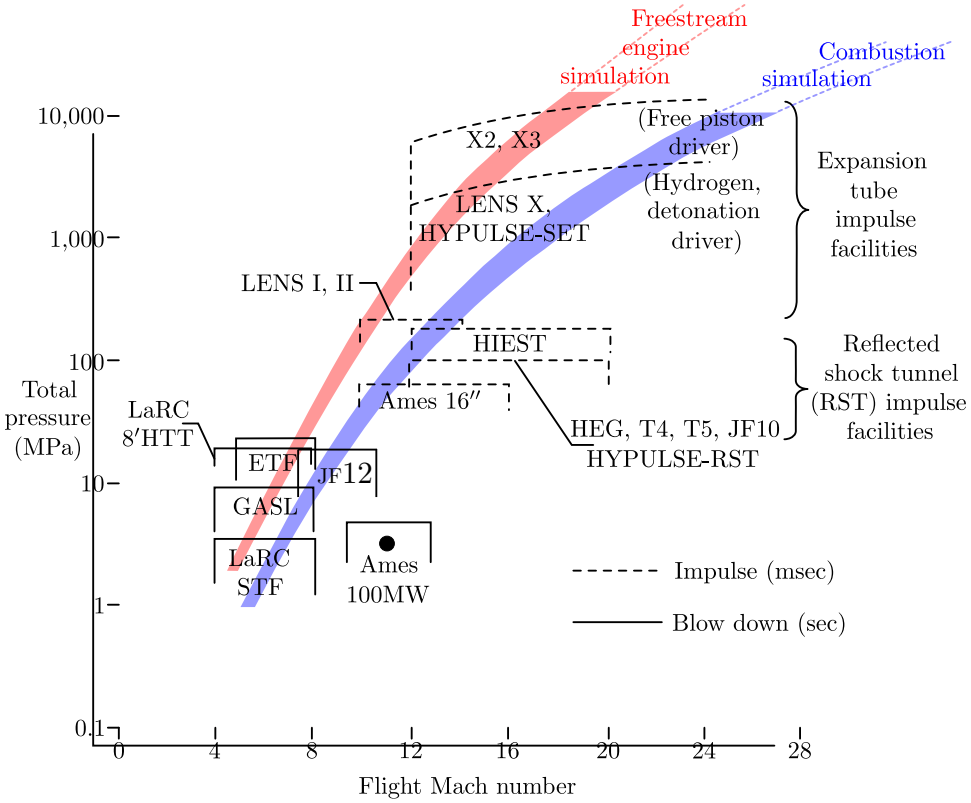

Figure 2.7: Total pressure vs flight Mach number for different hypersonic facilities for scramjet testing [30]

On the other hand, it is possible to reduce the total pressure requirements by simplifying the scramjet flow path in two different ways:

- *Direct connect* simulation, which reproduces conditions at the combustor entrance where the flow has already been compressed and slowed down by the vehicle and inlet shocks.
- *Semi-direct or semi-freejet* scramjet testing, which reproduces conditions at the cowl tip or simply the flow behind the forebody.

The total pressure requirements for these studies can be lower by up to an order of magnitude [28] since the flow total pressure is significantly reduced by the vehicle forebody shock. Another advantage of this technique is the shorter required model length. This is advantageous as the reduced length reduces the required test time to establish the flow, or because it can allow for a larger scale engine for a given

facility. However, the drawback of this technique is that it does not reproduce all the flow features that are generated by the interaction with the vehicle and the inlet, such as boundary layer development and flow non-uniformities. Most importantly, the effects at high Mach number of the ingestion of the boundary layer developed in the forebody into the inlet and then combustor are not reproduced.

Freejet engine simulation, (or full freestream) which aims to reproduce the full freestream flow conditions, would allow an in-depth evaluation of the scramjet operation, including the effects of the vehicle/engine integration. Considering the size of the current facilities, and their capability in terms of test time (and therefore in terms of flow length), nose-to-tail scramjets can normally be tested only if scaled models are employed. However, the necessary high freestream pressures to maintain pL product makes free-jet testing impractical for most, but not all, facilities.

2.8 COMMON FACILITIES FOR SCRAMJETS GROUND TESTING

All the requirements of total pressure, total enthalpy (temperature), gas composition, flight-equivalent flow features and test time cannot be simultaneously satisfied by any hypersonic wind tunnel for scramjet testing, as discussed by Lu and Marren [93]. Different types of facility offer the possibility of exploring different parts of the scramjet performance envelope. As an example, blowdown facilities allow for a relatively long test time (in the order of seconds), but at low Mach numbers (up to eight), and only being able to test scramjet combustors (direct-connect) at higher Mach numbers. On the other hand, reflected shock tunnels (RST) can reach higher enthalpies, up to $30\,\mathrm{MJ\,kg^{-1}}$, and test full engines, with the trade-off of much short test times (in the order of milliseconds [94]). In the following section a description of the different types of facilities is presented, with particular emphasis on high Mach number (i.e. Mach above 8) scramjet testing.

2.8.1 Blowdown facilities

Blowdown facilities operate by isentropically expanding a high-pressure reservoir of test gas through a nozzle into a low-pressure section [95]. Heat can be added to the high-pressure gas to increase the total enthalpy, which increases performance and is required to prevent liquefaction of the gas at high Mach after expansion [93]. Possible heating methods are combustion, electric arc and electro resistive heating [74]. These facilities, while useful for low hypersonic Mach number scramjet testing (under Mach 8), are unable to simulate higher Mach numbers for several reasons [30]:

- Total pressure is limited by the necessity of structurally containing the stagnated gas.

- Flow contamination and dissociation, which can occur due to heating of the test gas, is an issue that has been widely reported for these types of wind tunnel [52, 96, 97]. Dissociation of oxygen and nitrogen can lead to an apparent non-negligible scramjet performance increase, and would be amplified at higher Mach numbers and total pressures [96]. Similarly, the effects of different heating systems are technology and fuel dependent, and their specific effects are unknown. On the other hand, there are facilities that use a specific mechanism to create non-vitiated air. For example, the NASA HTF uses a 3MW graphite core storage heater to heat some nitrogen, then mixed with oxygen to obtain a flow of synthetic air [98].
- The power requirements for this kind of facility become impractically high at large scale and high Mach [95].
- Total temperature is limited by materials required to contain the gas at high temperature for relatively long periods of times. Regenerative cooling system would be necessary, further increasing the power required to operate this kind of wind tunnel [95].

2.8.2 Shock tube

The first and simplest kind of impulse facility is the non-reflected shock tube. It consists of a tube divided into two sections by a diaphragm. A high-pressure driver gas is enclosed in the first section, separated from a low-pressure test gas by the diaphragm. When the diaphragm is ruptured a shock wave is generated and propagates into the test gas, increasing its temperature and pressure, while also inducing a motion of gas behind the shock wave that is eventually used as the test flow [99].

This kind of facility is unable to produce high Mach number flows, and therefore cannot be used for scramjet testing. This is because, in shock tubes, a velocity increase is associated with a test gas temperature rise such that Mach number of the test flow is fundamentally limited to around ~3.0, when real gas effects are accounted for [100]. In other words, it is impossible to generate hypersonic flows with this kind of device. Furthermore, the post shock temperature is too high for realistic combustion studies. Test times are usually in the order of tens of microseconds [101]. Total enthalpy of the test gas is limited by radiation effects and by the fact that even if extremely high shock speeds were obtainable, those would create a highly dissociated gas that would not have the proper chemical composition to reproduce flight conditions [102]. Finally, it is possible to attach a nozzle to generate the required high Mach, but the startup time of the nozzle severely reduces the available test flow [103]. While not useful for the scope of this study, it represents the starting point for all the following, more sophisticated facilities.

2.8.3 Reflected shock tunnel

The reflected shock tunnel (RST) is a facility derived from the basic shock tube, which operates by processing the test gas with two shocks. A first shock propagates into the test gas like in a shock tube, but, when it reaches the end of the tube, it is reflected, processing the gas a second time and stagnating it. Then, the hypersonic flow is produced by expanding the stagnated gas through a steady expansion nozzle to the desired condition. This technique allows test gas to be cooled to realistic freestream temperatures and expanded to hypersonic Mach numbers. The Mach number is then a specifiable variable, upon use of suitable supersonic nozzle [104]. The total (stagnation) enthalpy of the test gas depends on the temperature, pressure and composition of the driver gas, diaphragm rupture pressure, and filling pressure of the test gas [105]. Test time for this kind of facility is in the order of milliseconds [94], because the gradual release of test gas through a choked throat extends the running time compared to a basic, non-reflected, shock tube.

The invention of the original reflected shock tunnel is attributed to Hertzberg [103]. Ray Stalker proposed and developed the free-piston reflected shock tunnel [106], in which a free piston is used to compress the flow, and to generate the primary shock in the shock tube. These modifications allow to generate the required enthalpies for scramjet testing. Under his supervision, the T1 to T5 series of free piston reflected shock tunnel were built, and most are still in use today. Free-piston driven reflected shock tunnels also being called as “Stalker tubes” [107].

Scramjet tests in reflected shock tunnels

Some existing facilities able to produce flows for high Mach number scramjets are: T4 at the University of Queensland, T5, LENS I/II in the United States, HEG in Germany and HIEST in Japan [94, 108]. This section, expanding the presentation of Marren and Lu [109], discusses high Mach number scramjet experiments carried out in these facilities.

T4 is a RST facility developed specifically for scramjet testing at the University of Queensland and was commissioned 1987. It has a free-piston driver, and is currently operated at total pressures of up to around $90\,\mathrm{MPa}$, with a maximum enthalpy of $15\,\mathrm{MJ\,kg^{-1}}$ [110, 111]. It was developed by Ray Stalker, after having developed T1, T2 and T3 at ANU in Canberra [107].

High Mach number scramjets have been tested in this facility. As an example, as previously discussed in Section 2.6, Suraweera and Smart [23] designed a Mach 12 REST engine that was tested at an off-design condition, Mach 7.5, in semi-direct mode. Doherty et al. [85] have tested an airframe-integrated $\sim \frac{1}{3}$ scaled version of the Mach 12 REST engine in T4, using a 6° wedge as a forebody. This engine was tested at a Mach 10, $48\,\mathrm{kPa}$ dynamic pressure flight equivalent condition, for a test time of around $1\,\mathrm{ms}$, which approximately represents the upper scramjet testing performance limit of T4, both in

terms of total pressure and Mach number. This facility has performed more scramjet tests than any other in the world, firing its 10000th shots in 2008 [112].

Currently, HIEST, in Kakuda, Japan, is one of the highest performance facilities amongst all the various reflected shock tunnels, with a maximum total pressure of around 150 MPa (although it is usually run at lower total pressures, around 50 MPa), a maximum total enthalpy of 30 $MJ\,kg^{-1}$, and a test time of 2 ms [113]. A semi-direct Mach 12 scramjet has been tested with Mach number varying between 9 to 14 at total enthalpies between 4 $MJ\,kg^{-1}$ to 9 $MJ\,kg^{-1}$, at a fixed total pressure of 30 MPa [114]. These experiments did not test a free-jet engine, and as such, albeit similar, they do not correspond to the goals of this thesis. In this facility, free flight aerodynamic tests of a full-scale model of the HiFIRE-5 payload were conducted at Mach 7.6 , total pressure 15 MPa, and total enthalpy 3.6 $MJ\,kg^{-1}$ [115].

HEG is a free piston driven reflected shock tunnel with similar scale and performance to HIEST, and is currently operated by DLR, in Göttingen, Germany. It is a 60 m long facility, and can drive total pressures up to 85 MPa and stagnation enthalpies up to 23 $MJ\,kg^{-1}$. Models in this facility can be up to 1.5 m long and 0.4 m wide [94].

The T5 RST at GALCIT, CalTech, is one of the free-piston driven facilities designed by Stalker [106] and still in use (along with T4). It is 42 m long and it has a capability to produce a stagnation enthalpy of 21 $MJ\,kg^{-1}$ and a total pressure up to 80 MPa for flow speeds in the range between 3 $km\,s^{-1}$ to 6 $km\,s^{-1}$, and test times in the order of 1 ms to 2 ms [94].

The LENS I/II facilities are able to produce flows up to 200 MPa and Mach 12 [108]. Test time up to 8 ms and Mach numbers up to 12 have been obtained. It has been reported that a generic two-dimensional scramjet has been tested between Mach 7 and 12; however, more detailed information was not presented [108]. The oxygen dissociation reported in the experiments was around 1 % which is less than the theoretical prediction [52]. However, it would also be expected that high levels of nitric oxide would be present in the test gas at those conditions due to the extremely high stagnation pressures.

In recent developments, China Academy of Aerospace Aerodynamic recently commissioned the free-piston driven reflected shock tunnel FD12, 100 m long, and with nozzle exit diameter of 1.2 m and 2 m [116]. Also, in China, the Chinese Academy of Science developed the detonation driver JF12 wind tunnel, which is, at a length of 265 m, by far, the longest and biggest reflected shock tunnel in the world (to date). It can reproduce Mach numbers in the range 5 to 9 at an equivalent altitude of 25 km to 50 km for test times of 100 ms [117].

Limits of reflected shock tunnels

RST facilities are limited by the necessity of containing the hot and high-pressure test gas prior to expansion through the nozzle [28]. Additionally, with increasing high total temperatures (necessary for high Mach number scramjet testing) nozzle throat erosion, throat melting and ablation of the tubes

become increasing problematic considerations [105]. Throats melting is exacerbated at high total pressure by the large test times associated with large facilities [118].

RSTs are limited by the balance of oxygen dissociation and recombination in the test gas between stagnation at the nozzle inlet and subsequent expansion through nozzle [73], a feature which also characterises the previously presented facilities relying on a steady expansion of the test gas. The formation of nitric oxide (NO) is of great relevance for this kind of facility. This is because the nitric oxide is stable through the expansion process and can be found in high proportions in the test gas. While the increase in total pressure reduces the dissociation of oxygen, it enhances the formation of NO [28, 74]. NO is problematic because it is a catalyst for radical formation and subsequent ignition, enhancing the heat release from the scramjet combustion process [74]. The consequence may be an over-estimation of the performance in RSTs experiments compared to flight tests.

Despite the ability to perform high quality scramjet testing in RSTs, the detrimental effects of the altered chemistry as well as the limited total pressure, which makes pressure-length scaling impossible in many cases, points to the use of expansion tubes as an attractive alternative at very high Mach numbers. Even at its highest performance, the total pressure of the RSTs facilities presented so far are still low compared to what has been achieved with expansion tubes. It will be shown in Section 2.9 that total pressures up to tens of gigapascal are achievable in expansion tubes [30, 119].

2.9 EXPANSION TUBE

The expansion tube is a shock tube with the addition of a low-pressure section — called an acceleration tube — downstream of the shock tube, with the two sections separated by a thin film secondary diaphragm. A schematic of an ideal expansion tube is shown in Fig. 2.8. The test gas, which is initially contained in the shock tube, is first processed by a normal shock wave generated by the rupture of the metallic primary diaphragm, which is typically made of steel and ruptures at high pressure. The secondary diaphragm is subsequently ruptured upon impact of the shock wave that has processed (i.e. accelerated and heated) the test gas. The incident shock wave continues on its path into the acceleration tube, where it “accelerates” as it processes the low-pressure gas towards the test section. Behind this shock wave the test gas expands into the acceleration tube by means of an unsteady expansion, which is the fundamental phenomenon involved in the generation of a hyper-velocity flow in an expansion tube. The test gas is finally expanded to the desired Mach through the use of a hypersonic (divergent only, as the flow is already supersonic) nozzle.

The fundamental advantages of an expansion tube compared to other facilities can be summarised as follows [120]:

- Higher total pressure and total enthalpy can be achieved for a given driver gas pressure and sound speed due to the final unsteady expansion (see in detail Section 2.9.2).
- Material degradation is avoided because of the absence of a sonic throat.
- The flow is never stagnated; therefore its total pressure and temperature are never fully statically attained by the test gas, alleviating thermal and structural requirements for the facility.

On the other hand, the unsteady expansion mechanism limits the amount of test time that can be achieved in the expansion tubes. For this reason, larger facilities are required to obtain equivalent test times to those achievable in reflected shock tunnels.

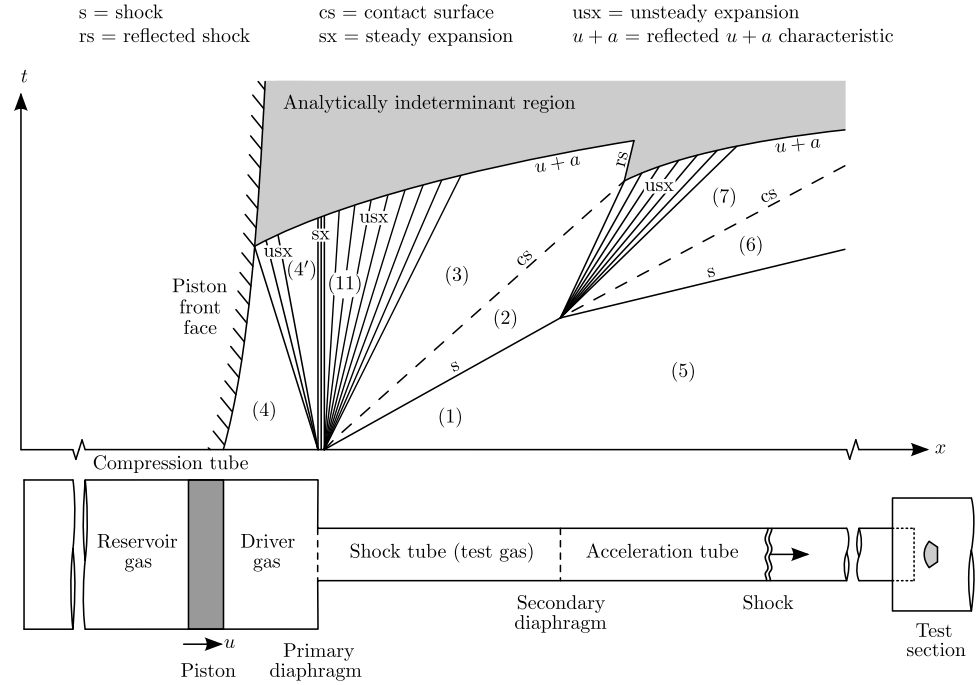

Figure 2.8: Basic expansion tube schematic and relative *x-t diagram* with key flow processes identified. Adapted from [1].

2.9.1 A minimal expansion tube abstraction

In Fig. 2.8, one can observe that the same basic structure repeats twice, in both the shock tube and acceleration tube. In these, an unsteady expansion drives a moving shock that processes the gas initially at rest. This is the minimal abstraction that allows understanding of the expansion tube flow processes.

In more detail, Fig. 2.9 illustrates the simplified model: *state 4* is the gas behind the unsteady expansion, which is coming from the previous section of the tube. In the case of the shock tube, this is the primary driver gas at rupture. In the case of the acceleration tube it is the shock-processed test gas in the shock tube. Upon diaphragm rupture, the gas undergoes an unsteady expansion to *state 3*. The diaphragm rupturing process generates a shock wave that is pushed forward by the unsteady expansion.

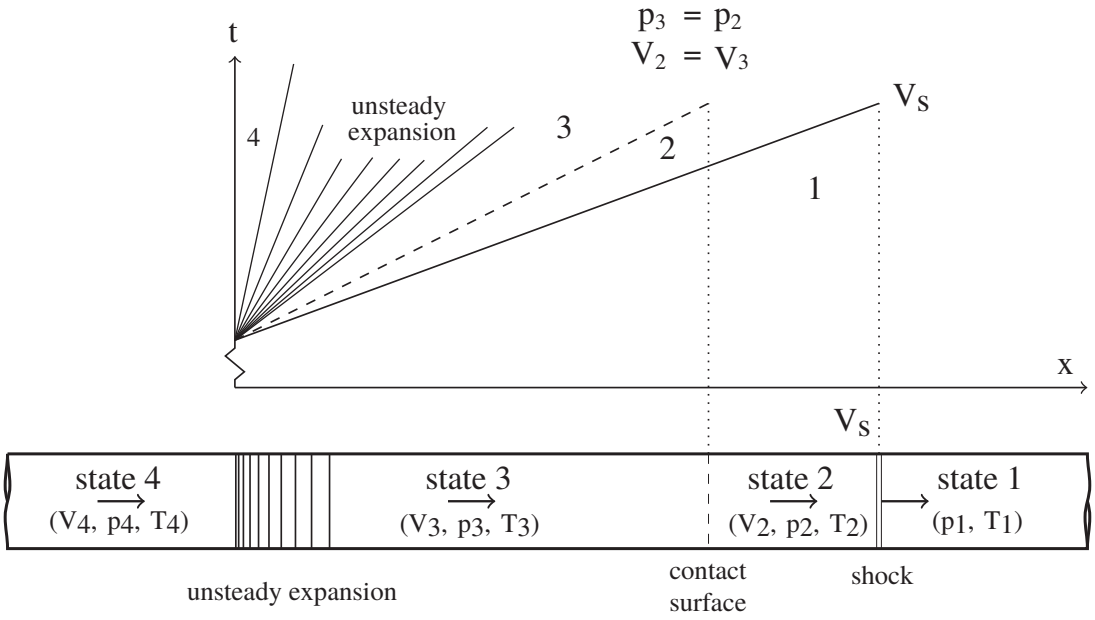

Figure 2.9: Minimal model of each section of an expansion tube and relative *x-t diagram* with flow processes. Adapted from [121].

This wave processes the gas in the tube initially at rest: *state 1* – to *state2*. The shock speed V_s is such that $P_3 = P_2$ and $V_3 = V_2$ across the contact surface. In other words, the shock wave speed is such that the flow behind it is at the same velocity and pressure as the unsteadily expanded flow. The same mechanism is also applicable to the secondary driver flow, as discussed later in this chapter.

Solving this model for each section of tube allows the flow processes in the expansion tube to be fully resolved. If a perfect gas is assumed, it is possible to derive a complete set of equations that can be solved numerically. If such an assumption is removed, however, it is still possible to solve expansion tube flow, by numerically solving the conservation equation of mass, momentum and enthalpy (see [99, p. 266]) that still holds for normal shocks (in a shock reference frame):

$$\rho_1 V_s = \rho_2 (V_s - u_2) \tag{2.2}$$

$$p_1 + \rho_1 {V_s}^2 = p_2 + \rho_2 (V_s - u_2)^2 \tag{2.3}$$

$$h_1 + \frac{V_s^2}{2} = h_2 + \frac{(V_s - u_2)^2}{2} \tag{2.4}$$

and numerically integrating the Riemann invariant of the expansion wave that can be written as:

$$u_3 = -\int_{p_4}^{p_3} \frac{dp}{\rho a} + u_4 \text{ or } p_3 = -\int_{u_4}^{u_3} \rho a \, du + p_4 \tag{2.5}$$

The problem can be solved analytically if a perfect gas is assumed [122] and iteratively if the equilibrium gas is assumed, as one has to find V_s to satisfy both $p_2 = p_3$ and $V_2 = V_3$. For further details the reader is referred to the discussion detailed in Gildfind [30] and [1].

2.9.2 Unsteady expansion process

As discussed previously, the unsteady expansion is the characteristic process of an expansion tube and can be compared with a steady expansion to better understand the underpinning mechanism. Following the dissertation of Trimpi [123], by definition, the total enthalpy of a thermally perfect gas is:

$$H = h + \frac{1}{2}u^2 \Rightarrow dH = dh + u\,du \tag{2.6}$$

where h and u are enthalpy and velocity of the gas. Since for a steady expansion the total enthalpy does not change (see [99, p. 198]), then $dH = 0$ and $du = -\left(\frac{dh}{u}\right)$. On the other hand, in an unsteady expansion the Riemann invariant along the characteristic line is conserved:

$$\frac{dJ_+}{dt} = 0 \text{ along } C_+ = \frac{dx}{dt} = u + a \tag{2.7}$$

with $J_+ = \frac{2}{\gamma-1}a + u$ for a thermally perfect gas. Differentiating we obtain:

$$\frac{2}{\gamma-1}\,da + du = 0 \tag{2.8}$$

Since for a calorically perfect gas $h = c_p T = \frac{\gamma R}{\gamma-1}T = \frac{1}{\gamma-1}a^2$, differentiating the first and last term yields:

$$dh = \frac{2}{\gamma-1}a\,da : \tag{2.9}$$

Then, replacing $\frac{2}{\gamma-1}\,da$ from Eq. (2.8) into Eq. (2.9):

$$du = -\frac{dh}{a} \tag{2.10}$$

That, together with Eq. (2.6) implies:

$$dH = -(M-1)\,dh \tag{2.11}$$

It is clear from Eq. (2.11) that if $M > 1$ and $dh < 0$ (i.e. flow is expanding) the total enthalpy increases proportionally to the Mach number, and the higher the Mach number, the larger the increase in total enthalpy. In the same mechanism, total pressure and temperature are also significantly increased. A conceptual explanation was given by Morgan [100] and shown in Fig. 2.10. A selected slug of shock heated test gas undergoes the unsteady expansion. This gas does work and transfers energy to the gas in front of it, equal to $W = \int pA\,dx$. The pressure differential is the same within the expansion fan for the gas slug. However, any planar surface crossing the unsteady expansion later in time (i.e. further away from the focus), as the unsteady expansion is growing, has a larger pressure-length integral and therefore does more work on the gas in front of it. In other words, there is a forward cascade of energy

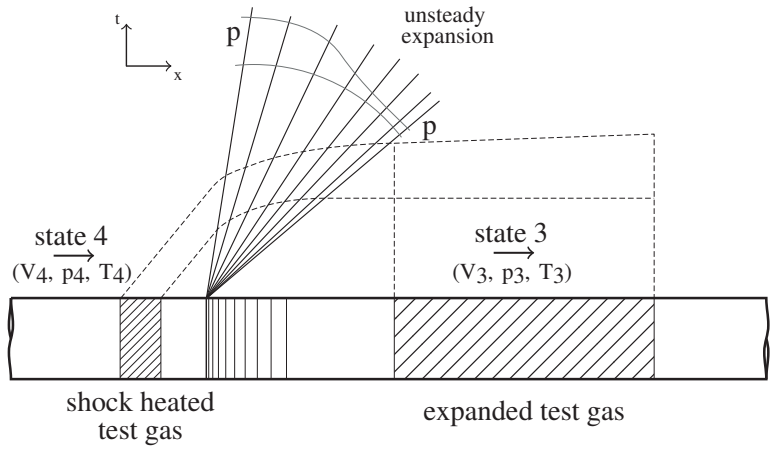

Figure 2.10: Schematic of the total enthalpy and pressure addition in an unsteady expansion. Adapted from [100].

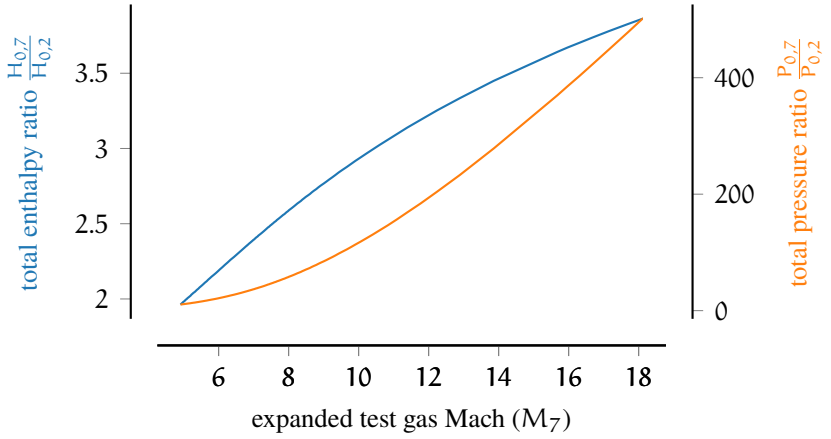

Figure 2.11: Total pressure and enthalpy multiplication across unsteady expansion for an generic Mach 12 scramjet condition. Shock tube post-shock properties $u_2 = 1616\,\mathrm{km\,s^{-1}}$, $T_2 = 1878\,\mathrm{K}$, $M_2 = 1.94$.

from the unexpanded gas to the expanded test gas. This means there is a net increase in both total enthalpy and associated total pressure. The drawback is that not all the test gas can be processed and a significant reduction of test time occurs. This mechanism, called enthalpy multiplication [100], explains the attractiveness of expansion tubes: the capability of obtaining high total enthalpies without the necessity of stagnating the gas, but rather by transforming static enthalpy into flow speed.

An example of the multiplication mechanism is shown in Fig. 2.11, where the calculated total pressure and total enthalpy ratios across an unsteady expansion are shown as a function of the expanded test gas Mach number. The figure, which has been obtained with the model of Section 2.9.1, refers to a generic Mach 12 scramjet condition, and clearly highlights the total pressure multiplier of the test gas, overcoming the stagnation pressure limitations of the other tunnels.

2.9.3 Mirels and viscous effects

An important phenomenon that limits shock and expansion tubes flow testing capability is the Mirels effect [124]. First identified by Duff [125], it consists of the boundary layer entrainment process acting behind the shock wave, where the boundary layer gradually captures mass between the shock wave and the contact surface. This slows down the former and accelerates the latter, until they eventually travel at the same speed, if the tube is long enough. This effect is especially noticeable at very low pressures, in the range 1 Pa to 100 Pa in the acceleration tube. The schematic of the flow process is shown in Fig. 2.12. Mirels derived an analytical model to estimate the effective test time for both laminar and turbulent boundary layers [126] and his predictions have been experimentally verified (see for example, [127, 128]).

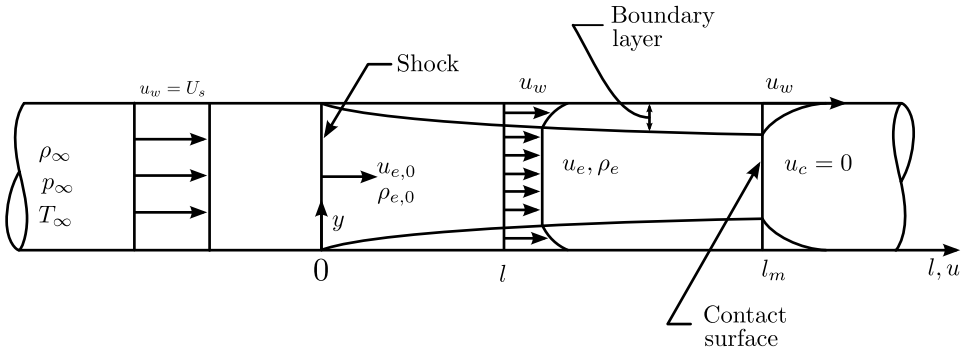

Figure 2.12: Mirels schematic of the flow between shock and contact surface in shock-stationary reference frame. Adapted from [30, 126].

The Mirels' effect sets a limit on the minimum allowable diameter for any given tube length to reduce the boundary layer effects to acceptable levels. It follows that to increase test times, it is required to increase the facility length, but also to increase the facility diameter.

More recently, Gildfind et al. [129] carried out full facility simulations, well-supported by experimental data, of the X3 expansion tube. It was observed that, unlike Mirels theory, if the acceleration tube is long enough (in that case an additional 10 m long section was added to the simulation), there is an eventual collapse of the test gas core flow, leading to no usable test time. This was an example where more complex viscous effects were present, coupled with the test gas unsteady expansion.

2.10 SCRAMJET TESTING IN EXPANSION TUBES

Expansion tube facilities have been used in the past to simulate scramjet conditions. In the HYPULSE facility, in the 1990s, Bakos at al. studied the quality of the flow for very high Mach numbers (15 to 20), but the achievable test time was very short (200 µs) [27, 130, 131]. Experiments have been carried out

in the same facility with a shock detonation driver to produce flow conditions at an equivalent dynamic pressure of 96 kPa, for a range of Mach numbers from 7 to 15 with total pressure up to 1.3 GPa [132].

Other studies have reported scramjet conditions in HYPULSE at Mach 7 to 12 with dynamic pressures of 28 kPa to 42 kPa, and enthalpies up to 22 MJ kg^{-1}, for estimated total pressure up to ~80 MPa [133, 134]. The Hyper-X scramjet model has been tested at Mach 7 and 10 in RST mode, and at Mach 13.5 freestream conditions in expansion tube mode with a largely off-design nozzle. Reported stagnation pressure and total enthalpies were respectively 10 MPa, 23 MPa and 300 MPa and 2.4 MJ kg^{-1}, 4.8 MJ kg^{-1} and 11.5 MJ kg^{-1}. For these tests, the scramjet was tested in semi-direct mode, assuming conditions equivalent to those behind a forebody [135]. A contoured nozzle was designed and built for a Mach 15 condition which has also been tested for a Mach 12 off-design condition with an enthalpy of 6.4 MJ kg^{-1}, and a test time of around 0.3 ms to 0.4 ms [136]. However, the tests at Mach 12 showed that the nozzle was not able to produce a suitable core flow [136]. This work done with the facility is the one most closely related to the objectives of this thesis. Unfortunately (to date) HYPULSE is no longer operational [137], and the available literature does not show they effectively carried out the planned Mach 12 semi-direct scramjet tests.

It is important to mention the work done at CUBRC led by Holden [138], who have developed LENS XX, a 70 m long expansion tube with an inner tube diameter of 60 cm using an electrically heated driver and heated test sections for enthalpies from 10 MJ kg^{-1} up to 90 MJ kg^{-1}, Mach numbers in the range 4 to 26, and test times of about 0.5 ms. Notwithstanding these capabilities, to the author's best knowledge, no explicit publication referring to high Mach number scramjet experiments carried out in this facility have been found in the literature.

At Stanford, some test conditions have been developed to study direct-connect scramjets, bypassing the inlet compression stage. With their facility named "Stanford Expansion tube", Mach 2.4 to 4.7 conditions have been tested for dynamic pressures of ~40 kPa with test times of 0.17 ms to 0.40 ms [127]. Additionally, a TDLAS (tunable diode laser absorption spectroscopy) system has been developed and used to characterise the facility and its unsteady gas flow process. The TDLAS system has enabled estimates of temperature, velocity and water fraction in the test gas [139].

The University of Illinois in 2007 developed a small, 10 m long, expansion tube, called "HET" [140], and successfully developed and tested a Mach 7, 95 kPa dynamic pressure flow condition for a test time of ~180 µs, albeit no engine has been tested.

The University of Michigan built the MHExT in 2015. The MHExT is a small-scale expansion tube used for reproducing combustion chamber conditions, for Mach between 1.7 to 2.7, total enthalpies of 0.3 MJ kg^{-1} to 2.3 MJ kg^{-1} and test times around 1.0 ms [141].

The University of Queensland has more than 30 years of experience developing, designing and working with free-piston driver facilities, and currently is operating two expansion tube facilities, X2 and X3. The former was used by McGilvray [74] for the first test of a nose-to-tail scramjet engine in

an expansion tube. For this study a Mach 10.1, 165 kPa dynamic pressure condition was developed for a test time of 550 µs and a total enthalpy of 5.3 MJ kg^{-1} [142]. The authors tested a $\frac{2}{5}$ scaled 2D hydrogen-fuelled scramjet derived from an existing scramjet tested in T4 [142], the large-scale RST facility operated by the University. The study compared the results obtained from the two facilities, and showed good agreement in comparison to the experimental uncertainties [142]. This was considered a validation of X2, and expansion tubes in general, for scramjet testing. The same author designed a Mach 10, 84 kPa dynamic pressure condition in X3 and performed detailed analysis of the condition, without any scramjet test [74]. Recently, Sancho [119] successfully completed full-scale crossover tests to X3, first overseeing test sections upgrades to permit scramjet testing, and secondly testing the full-scale T4 nose-to-tail scramjet which had been tested at subscale in X2, matching the condition developed in the RST (Mach 10, 65 kPa). Within the same study, he tested the same scramjet with a ~190 kPa dynamic pressure condition, with an estimated total pressure of more than 1 GPa [119].

The studies of Sancho and McGilvray showed that not only is ground testing of scramjets with combustion possible, but that expansion tubes currently represent a viable option to extend the envelope of ground testing to high dynamic pressures. In the following sections requirements and peculiarities of scramjet testing in expansion tubes will be described.

2.10.1 Expansion tube scramjet conditions

The unique features of scramjet test conditions, compared to normal expansion tube test flows, are higher density and lower speeds compared with the super-orbital conditions. Sometimes they are also called “low enthalpy” conditions, with reference to the enthalpy content with of super-orbital ones. In the rest of this thesis, unless otherwise specified, we will refer to scramjet condition as low enthalpy conditions, even though they are not really low enthalpy for other kind of facilities.

In such conditions, the flow processes behave differently, and some of these aspects are of high importance. In the following sections some of these novel features of scramjet testing in expansion tubes will be analysed. Specifically, the effect of using a shock heated secondary driver, and the issue of test gas quality will be described for these conditions.

Use of a shock heated secondary driver

A secondary driver is an additional section that can be interposed between driver and shock tube. Firstly proposed by Henshall [143], it has been tested experimentally for the first time by Stalker and Plumb [144] in a shock tube facility. Several years later, it was implemented in an expansion tube by Morgan and Stalker [122] to achieve super-orbital flows, up to 18.7 km s^{-1}. To enable this mode, an additional film diaphragm is inserted. The secondary driver is separated from the primary driver on

one side by the primary diaphragm, and from the shock tube on the other by the secondary diaphragm. This section, filled with helium, while being located in the driven tube, becomes the effective driver gas for the test gas in the shock tube. An expansion tube including a secondary driver and relative flow processes are presented in Fig. 2.13. The shock generated by the rupture of the primary diaphragm processes the secondary driver helium, increasing its temperature and flow speed. Indeed, it can be shown [1] that, given a low enough pressure helium gas, the shock-heating will raise the temperature so that the speed of sound of the shock-processed secondary driver is significantly higher than that of the primary driver. (Following notation in [1], $a_{sd2} > a_{sd3}$, and the secondary driver is said to be "over-tailored"). A stronger shock is achieved in the test gas because a higher speed of sound implies a "faster" transmission of energy into the test gas [30].

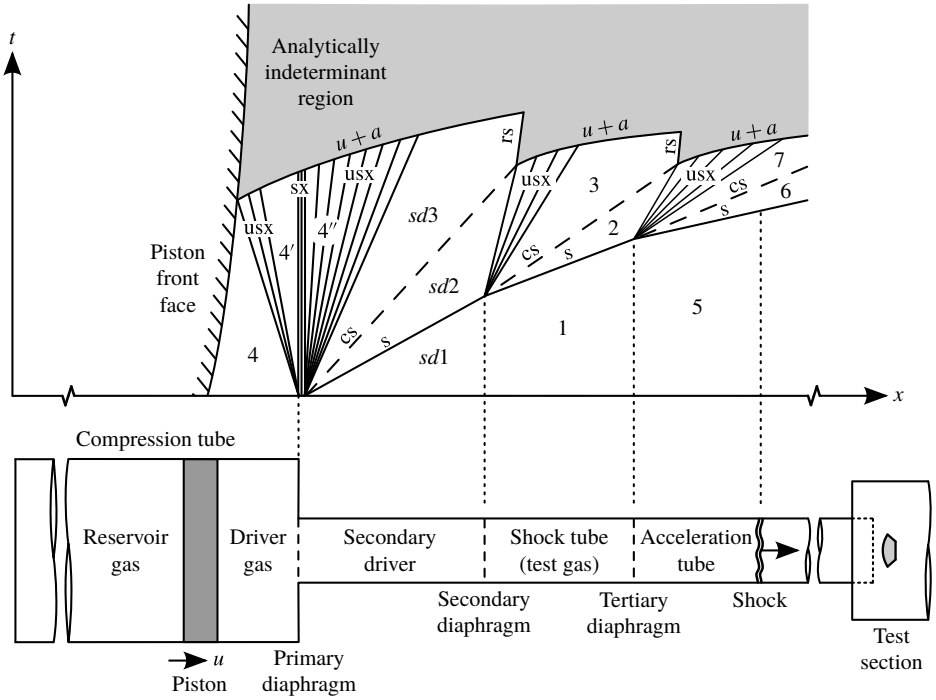

Figure 2.13: Expansion tube schematics operated with a secondary driver and relative *x-t diagram* with flow processes. Adapted from [1].

This results in the secondary driver being able to generate a stronger shock through the test gas compared with what could be achieved by the primary driver alone. This performance increase represented the motivation for the initial studies, as explained in detail in [100], where it was shown that the use of a shock heated secondary driver would allow simulation of test flows up to 20 km s^{-1}. These speeds would be sufficient, for example, to simulate entry to Earth's atmosphere returning from a far solar system mission, or entry to Neptune or Uranus' atmospheres — the smallest of the giants.

This performance increase, however, comes at the cost of reduced test time. This occurs for two reasons: the flow processes that this mechanism can support are reduced because of the reduced effective driver slug length, and second, for a fixed tube length, the presence of a secondary driver reduces the length of the shock and acceleration tubes, reducing the effective length of the driven tube.

Additionally, the use of a secondary driver implies the use of an additional diaphragm, which can reduce performance and increase noise, as discussed below. Finally, from an operational perspective, it is important to point out that having an additional driver to fill, and consequently, increasing total filling durations, allows an increased amount of air to leak in both shock tube and secondary driver, leading to higher uncertainties in the tube fill pressures and composition.

The required operating mode of a secondary driver produces an unsteady expansion at the secondary diaphragm [1]. This is the assumed operating mode of previous secondary driver studies targeting super-orbital test flows (see [122, 145]). However, if the test gas has a sufficiently high density compared to the secondary driver gas, which is normally the case for scramjet conditions (see for example [74, 119]), the shock-processed gas must slow-down instead of expand when hitting the test gas. Then, instead of the targeted unsteady expansion, a reflected shock originates at the secondary diaphragm.

Whether a reflected shock is created is a function of the fill pressures of the secondary driver p_{sd1} and p_1. Gildfind et al. [1] derived an analytical description for the above question to which the reader is referred for details, indicating that a reflected shock will occur for $rho_1 > 0.9\rho_{sd1}$.

Test flow disturbances in expansion tube

The first developments by Trimpi [123] indicated that expansion tubes would be able to simulate a wide range of conditions. However, many flow conditions had unacceptable level of noise, making the conditions useless, as found by Miller in the Langley Expansion tube [146]. Only a narrow range of suitable test flows could be achieved [147]. UQ was later contracted by NASA to study the reasons that prevented a number of flow conditions from being usable. Paull et al. [148] thoroughly investigated this issue. They determined that the unsteady expansion is responsible for the focus of the broadband noise from the driver into finite frequencies which can grow and become disruptive. Indeed, the unsteady expansion produces a large drop in the sound speed of the test gas, which has the effect of focusing the different components of the frequencies of lateral acoustic waves into a narrow band of frequencies, which later appear as disturbances in the test gas [149].

The same authors postulated that the main source of the noise (later manifested in the test flow) originates during the primary diaphragm rupturing process. Some other sources are present, but their origin was not identified. They subsequently found that penetration of the driver acoustic waves to the test gas can be inhibited by configuring the expansion tube in an over-tailored configuration ($a_2 > a_3$), i.e. such that the speed of sound of the expanded driver gas is lower than the speed of sound of the shock-processed test gas. They proposed an operating ratio of $\frac{a_2}{a_3} = 1.25$ to achieve an "acoustic buffer" and stop the noise from propagating through into the test flow. Such a value for this ratio has been supported experimentally in [100].

Jacobs [150] studied this very same problem with numerical simulations of the NASA Langley expansion tube. While he showed that those disturbances can propagate into the test gas, he also noted

that the condition having the smallest amount of noise was the one with the smaller speed of sound ratio. However, he suggested that this might be a result of the laminar model adopted for the simulation and possibly because of boundary layer transition. He proposed that the large amplitude noise origin is due to the arrival of the reflected head of the unsteady expansion, and that a solution would be to change the relative lengths of the different sections of the tube. This suggested that wave timing, and not just tailoring, were responsible for the observed noise.

Paull and Stalker [149] concluded that successful flow conditions would therefore only be possible for high enthalpy conditions where the test gas would be very hot, or as shown in [151], by reducing the sound speed of the driver gas. A driver speed reduction can be achieved using an Argon-Helium mixture. Finally, they observed that the required speed of sound drop was even more important to achieve for large-scale facilities, where the noise-focusing effect is amplified, by the increased area-change ratio at the diaphragm station.

Secondary driver as acoustic buffer

Scramjet conditions fit into the category of low enthalpy (from an expansion tube perspective, although they are high enthalpy from a hypersonic flight perspective) conditions because of their required high density and low speeds compared to super-orbital conditions, while ensuring high total pressure capabilities to apply pressure-length scaling. According to Paull and Stalker [149] those conditions cannot be simulated with satisfactory test quality due to the low sound speed ratio. Morgan [100], however, noted that the required sound speed increase could be obtained by using a helium secondary driver. Indeed, it could be easily configured in over-tailored mode to obtain a sound speed higher than that of the expanded driver gas. The disturbances generated at the primary diaphragm would then be theoretically suppressed by the shock-processed helium gas. However, the work performed by Morgan did not take into account the reflected shock waves that could arise at the secondary diaphragm with a dense test gas and the fact that the test gas would still be under-tailored with respect to the secondary driver gas. Indeed, the acoustic effects of these waves over the test gas are yet to be assessed, and further studies are necessary to characterise this mechanism.

Test flow unsteadiness

It has been noted by McGilvray [74] and Sancho Ponce [119] that scramjet conditions in expansion tubes are characterised by the undesirable feature of a steady pressure gradient that can be observed in the Pitot pressure traces (in addition to the flow disturbances already illustrated in the previous sections). The pressure is seen to gradually increase across the nominal test time, and CFD simulations confirm that static pressure, density, and temperature keep rising, while velocity and Mach number decrease [129]. As an example, this phenomenon can be observed in Fig. 2.14. McGilvray et al. elaborated and validated a technique, called “slug-tracking”, for analysing quasi-steady scramjet measurements [152],

including data from conditions presenting this steady pressure gradient. This approach relies on the fact that the spatial components of the total derivatives of flow properties are much higher than the temporal unsteadiness terms, and this approach is thought to work reasonably well [152].

The same phenomenon has been observed in the bigger facility, X3, as can be seen in Fig. 2.15. The cause of this behaviour has not yet been identified and together with flow unsteadiness, these represent the two major challenges of testing scramjets in expansion tubes. In the perspective of this thesis, these two phenomena are of significance, as combustion measurements are highly dependent on static pressure, but the aforementioned normalisation techniques have been proven to be adequate for previous experiments.

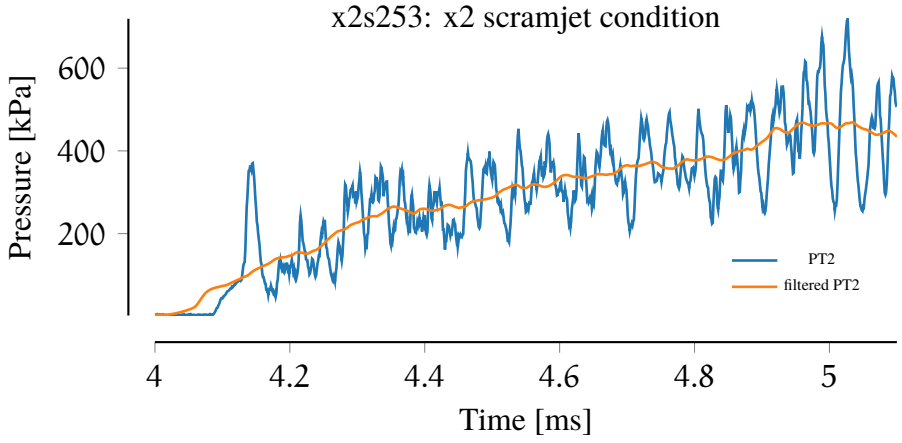

Figure 2.14: Example of flow unsteadiness in the X2 expansion tube, where a rising pressure, i.e. a steady pressure gradient can be observed. In the plot, Pitot pressure at nozzle exit on the tube axis. Mach 10 scramjet condition. Adapted from [74].

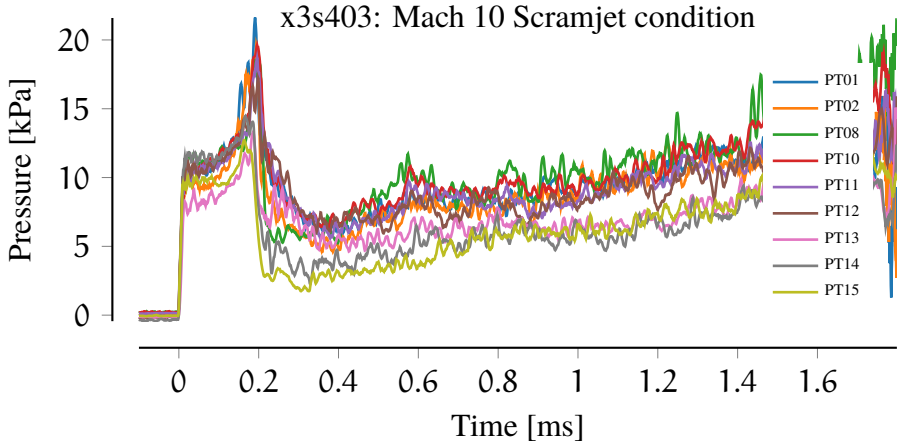

Figure 2.15: Example of flow unsteadiness in the X3 expansion tube, where a steady pressure gradient can be observed. PT10, PT8 respectively 40 mm above and below centreline. All probes are 20 mm equispaced. Test time between 0.4 ms and 1.4 ms. Mach 10 scramjet condition. Adapted from [119].

2.11 X3 FACILITY DESCRIPTION

Figure 2.16: X3 expansion tube inside the expansion tube laboratory. In the foreground the test section and dump tank.

X3 is a free piston driven expansion tube located at the University of Queensland. It is the largest impulsive facility at UQ, and one of the biggest expansion tubes in the world [153]. X3 has some of the highest potential performance by virtue of its free-piston driver, in terms of total pressure, total enthalpy, model size, and test time, amongst the major international impulse facilities. X3 is shown in Fig. 2.16.

X3 is part of the X-series of expansion tubes developed at UQ by Prof. Morgan and his research group. Schematics and relative sizes of the facilities are shown in Fig. 2.17. Design on X3 began in 1994, and manufacturing of the first configuration of the facility was completed in 2000 [154]. X3 was originally designed with a two-stage free-piston driver, with a 400 kg inner piston and a 100 kg outer piston. In its initial configuration, the first stage compression tube was 12 m long and 500 mm in diameter, and the second stage was 12 m long and 200 mm in diameter. The shock tube was originally 12.6 m long and 180.0 mm bore diameter. The acceleration tube was 24 m long and 182.6 mm in diameter. The dual piston arrangement was originally developed to contain costs and to capitalise on the previous experience with the smaller facility, X2, which at that time had a dual piston driver [155] — in fact, X2 was originally built as a prototype to test the expansion tube concept. This configuration was previously (both for X2 and X3) chosen mainly to reduce the cost of the high-pressure primary driver section, which increases greatly with diameter.

The first commissioning shots and subsequent experiments were conducted in the first part of 2001 [155]. The facility was used in this configuration for several aero-thermodynamic studies at high-enthalpy, super-orbital speeds [74]. However, this arrangement proved to be complex to operate and the operating conditions of the facility were limited by the requirement to decelerate and stop the heavy piston with a buffer system [74]. For this reason, a new single 200 kg piston driver was designed and installed in 2011 [156].

In its new configuration, the total length is 70 m, with a 14.5 m long compression tube. The second stage driver became part of the secondary/driver shock tube arrangement, while the existing shock tube and acceleration tube were kept unchanged. While initially operated without a nozzle, following the successful result of Scott [157] in developing a contoured nozzle for the X2 facility, X3 was modified to include a Mach 10 nozzle, which was directly scaled-up from the X2 one [158]. The use of a nozzle allows for a bigger core flow, a slight increase in test time [157], and reduction in viscous effects of the test flow [156]. The drop in static pressure and the corresponding pL product is often acceptable given the high total pressure performances of the X3 facility, and expansion tubes in general. The Mach 10 nozzle has an exit diameter of 440 mm. In Fig. 2.17 a schematic of the 2018 X3 facility is shown.

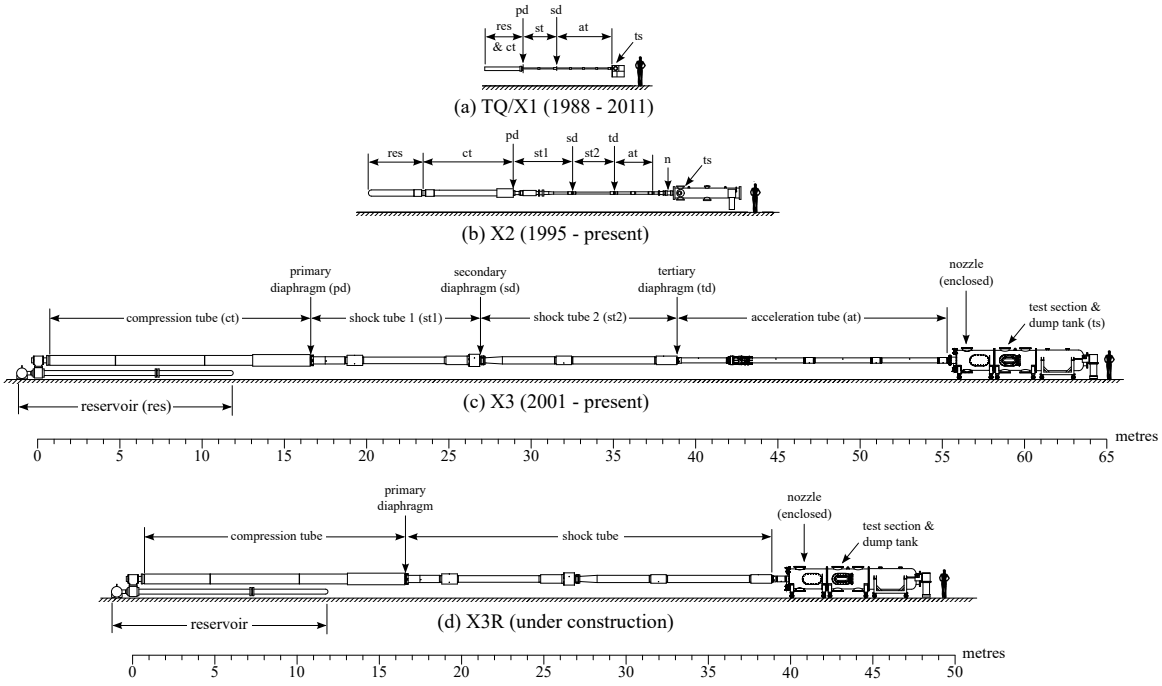

Figure 2.17: UQ's X-series of expansion tubes. X3 is the third from the top, in its 2018 configuration (with upgraded reservoir, test section extension and recoil joint. Support hardware is not presented. Picture courtesy of Gildfind, and updated by Stennet to include X3R configuration.

These upgrades successfully allowed development of new high total pressure, Mach 10 scramjet conditions, with test times of around 1 ms. Sancho tested a nose-to-tail Mach 10 scramjet in X3, completing crossover tests between T4, X2 and X3, providing experimental support to the proposition that expansion tubes can extend the envelope of existing facilities beyond RST total pressure limits. Indeed, the highest total pressure reached in his experiments was around 1 GPa, which is the highest total pressure at which a nose-to-tail scramjet has been ground tested in the literature [159].

Between 2014 and 2019, X3 has undergone a number of modifications to add a new operating mode as a reflected shock tunnel "X3R " that will allow low Mach number (up to 7) scramjet testing for over 10 ms test times. This includes a new test section extension, to allow the nozzle to be housed inside the vacuum chamber, thus reducing the vacuum load on it. Schematics of the new operating mode are also presented in Fig. 2.17.

To achieve the performance necessary for super-orbital conditions and also for higher Mach scramjet flows up to the limit of the envisaged scramjet flight envelope, lighter driver gas mixtures are required and a lightweight piston is necessary to achieve tuned operation. Following the introduction of a new lightweight piston for X2 after the work of Gildfind [30], another new and lightweight piston (100 kg) was developed and commissioned for X3 [160, 161]. This work is an integral part of the development of Mach 12 condition and will be discussed in detail in Section 3.5.1. Additionally, recent upgrades include a new recoil joint that allows the final part of the facility to be isolated from the vibrations induced by the piston driver, allowing for steadier measurements and fixing the position of the nozzle exit plane with respect to the model [162].

After these upgrades the X3 expansion tube is now able to reliably operate at a variety of conditions that are only achievable by a handful of ground testing facilities in the world. Moreover, it produces test times, in expansion tube mode, in the range of 1 ms to 1.5 ms, which few facilities of this type are able to match or surpass.

The X3 facility has total pressure and total enthalpy capabilities to produce freestream flows to test the Mach 12 REST engine at full freestream conditions, for a sufficiently long test time. However, no Mach 12 operating condition was available at the commencement of this project, so the development of such a condition became an integral part of this thesis. Finally, to satisfy the core flow size and exit Mach number requirements, a new nozzle was necessary, as the only available nozzle was designed to operate at Mach 10, with a core flow of 200 mm.

2.12 A FINAL OVERVIEW

In Section 2.6 a review of the M12REST engines previously experimentally tested has been discussed. It was noted that these experiments suffered from limitations due to testing in the T4 reflected shock tunnel, as follows:

- The presence of dissociated molecules like NO or atomic oxygen as a result of the rapid expansion of the test gas through the T4 nozzle. Specifically to M12REST tests, it has been observed that the chemical composition can influence engine performance.
- Inability to test at Mach 12. No engine has been tested in freejet mode at its design condition.
- Inability to attain the design flight dynamic pressure, 50 kPa.
- No binary or pressure-length scaling has been applied, meaning that the engine is treated as full scale, and cannot match Reynolds number or pressure-length product in flight.

These limitations potentially obscure the complex interactions that can take place when the engine is tested in freejet mode at high Mach number reproducing the design flight conditions.

The use of an expansion tube is of interest because it could potentially address the aforementioned issues. Indeed, the shock-processed test gas in an expansion tube is never stagnated, allowing for a cleaner (in terms of molecular oxygen and nitric oxide) inflow to the scramjet in the test section. The total pressure requirements necessary to match both the design dynamic pressure and eventual pressure-length scaling are within the capabilities of the X3 facility. However, test times are reduced compared to a RST of the same scale, and the use of a world-class facility is required. The X3 expansion tube can theoretically produce the required test-times and thus, this work has been developed around this facility.

A detailed literature review of scramjet experiments in expansion tubes has shown that some facilities (HYPULSE, LENS XX) are able to create high Mach number scramjet capability. However, to the author's best knowledge, full freestream experiments at Mach 12, or above, have not taken place or have not been published.

While it is clear, as illustrated in Section 2.10, that there are drawbacks in the use of expansion tubes for scramjet testing, it has also been argued that there is significant scientific value in test the Mach 12 REST engine in the X3 facility. This facility, indeed, should allow testing of the engine at its design condition, with pressure-length scaling applied for the first time.

In the next chapter, a new operating condition for the X3 expansion tube will be developed, and, an experimental study will be carried out in order to investigate the best configuration to use for the Mach 12 scramjet experiments.

3 MACH 12 CAPABILITY DEVELOPMENT IN THE X3 EXPANSION TUBE

3.1 RATIONALE

The development of a new flow condition for the facility is an integral and fundamental part of this thesis, as it is the underpinning requirement for enabling Mach 12 ground testing in X3.

In the previous chapter we discussed how expansion tubes operate and how they can achieve high enthalpy flows by means of the unsteady expansion mechanism. We also considered some peculiarities of scramjet testing in expansion tubes, whereby they operate at relatively low enthalpy (in relation to expansion tube super-orbital capabilities), and for which increased disturbances can disrupt the test flow. The first step to enable high Mach number scramjet testing in an expansion tube is to develop the baseline capabilities for the facility to produce the desired flow condition at the nozzle exit.

The target Mach 12 flow properties represented a departure from the conditions that were previously in use for the X3 expansion tube, and lie in a previously unexplored area of the performance envelope of the facility. As such, a significant amount of work was carried out to enable these experiments, using a combination of numerical modelling and experimental verification. This chapter details the work that has been accomplished in that direction.

3.2 INTRODUCTION

Achieving a new high Mach number capability for an expansion tube comes down to selecting an opportune combination of facility geometric configuration, piston mass, and fill pressures of the different internal tube sections. There are many phenomena that need to be considered to produce a successful test flow with the desired properties. Tuned piston operation, test flow disturbances, use of a secondary driver, and second order effects due to high density, all need to be carefully evaluated and accounted for during the condition design phase.

Additionally, X3 has only had limited use in the past [119] in its single driver piston configuration, and its performance is characterised by some peculiarities that have so far been neglected. For example, its aspect ratio (length/diameter) is particularly large and the shock tube is relatively long compared to the compression and acceleration tubes. It is also very important to realise that we are not yet

able to precisely achieve all the required flow parameters (speed, Mach number, pressure, and gas composition), and that a compromise is required. Indeed, the development of an operating condition, as shown in this chapter, is necessarily based upon simplified analytical models, that do not take into account all the phenomena occurring in an expansion tube experiment.

In this chapter we will take a look at the extensive work carried out to develop the new Mach 12 capability for the X3 expansion tube. The condition development process can be outlined as follows:

1. Identify the target flow properties.
2. Identify the available piston operating conditions.
3. Analytically estimate required fill pressures to achieve target condition and then choose piston operating condition.
4. Experimental validation, and if significant differences are found, adapt the operating condition.
5. Detailed characterisation with a hybrid 1D/2D numerical approach to fully establish flow properties.

This chapter will follow the same outline: in the first part the methodology, along with the analytical and numerical tools developed and used throughout this chapter, are presented. Then the target flow condition is examined, followed by a discussion on the tuned operating condition available to use in X3. The results of the condition development and the final operational parameters of the facility are then presented. A discussion of experimental results will follow, where different facility configurations have been tested considering the possible use of a secondary driver, and the ability to partition the driven tube at different locations (leading to different shock and acceleration tube lengths). Finally, the facility has been upgraded to operate with scored diaphragms, which has significantly reduced the amount of debris that can hit models placed in the test section.

This chapter focuses on the discussion of the final facility configuration. The last point of the list is not discussed here as the new hypersonic nozzle had to be designed in combination with the rest of the facility operating variables. The nozzle design is addressed in Chapter 4. Then, a detailed characterisation of the final flow properties will be presented in Chapter 5, which will include the commissioning of the Mach 12 nozzle.

3.3 METHODOLOGY

Accurate modelling requires the use of full-facility CFD. However, for a facility like X3, such a CFD model cannot be rapidly iterated to identify the required facility parameters for the target test condition. This is because fully resolved, time accurate, turbulent CFD of a 70 m long wind tunnel simply is not yet feasible with the computational resources at our disposal.

One-dimensional numerical codes are able to produce solutions in shorter times (on the order of 10 hours per simulation), but this is still too long for the preliminary design phase. Additionally, as discussed in Section 3.3.2, L1D requires the tuning of several empirical "loss factors" which can only be done through experimental comparison, and are not constant across the solution space. For this reason, the usefulness of L1D is relatively limited while exploring a diverse variety of parameters combinations.

Analytical models make several and significant assumptions on the flow physics, but, they are able to rapidly predict approximate facility performance. On the other hand, they fail to capture many of the phenomena that cannot be expressed analytically and therefore they are inherently limited. For example, Gildfind [30] initially used an analytical model to produce a theoretical Mach 13 condition in X2, only to find out that secondary wave processes from the driver were disrupting and slowing down the flow to the point that usable test time was not produced in the actual experiment. The designer can increase the complexity of the analytical model to better reproduce the expansion tube processes, but, in any case, experimental performance is the only metric to conclusively evaluate a flow condition and therefore needs to be included in the design loop. As such, a mixed experimental-analytical approach was adopted for this study, which is discussed in this section.

3.3.1 Analytical modelling

A simple state-to-state, zero-dimensional code has been developed following the expansion tube model presented in Section 2.9.1 to allow quick estimates of the exit flow properties.

The author implemented a quasi-0D code that uses classical isentropic and compressible flow relationships, coupled with the NASA Chemical Equilibrium with Applications code (CEA) [163] to take into account real gas and high temperature effects. Despite the improved chemistry, the accuracy of this simplified approach remains limited because of its inherent 0D nature: longitudinal and radial disturbances, and viscous and boundary layer effects (eventual laminar to turbulent transition and Mirels' effect [124, 126]) are not modelled. The code takes inspiration from Pitot, a tool for a rapid estimation of flow conditions for X2 expansion tube [164], which, however, could not take into account some X3 specificities, such as area-changes in different sections. Additionally, it could not work for scramjet, high-density conditions, where a reflected shock at the secondary driver (Section 2.10.1 on page 38) is typically generated. Those specificities have been integrated in this program.

Additionally, a new interface to CANTERA [165], a suite of tools for thermodynamic and combustion processes, has been developed. CANTERA allows for a more fine-tuned control of gas modelling, especially at low and high temperature, where CEA tends to fail. Most importantly it allows for much quicker calculation times, enabling faster parametric sweeps and the use of optimisation solvers.

The code purposefully does not try to take into account piston dynamics and the facility tuned operation, but rather it models the piston dynamics as an isentropic compression to target rupture

pressure. Although the isentropic compression assumption is used in X2 with satisfactory results, this is not the case in X3. It is proposed that, due to the significantly increased area of the compression tube and shock tube (X3 shock tube area is 5 times bigger than X2), and consequently non-ideal diaphragm opening processes, the opening losses are non-negligible. Adjustments to equivalent fill pressures are required to produce the experimentally obtained-shock speeds.

Code validation

The quasi-0D code has been validated against Pitot, faithfully reproducing high enthalpy (i.e. orbital re-entry condition at Mach numbers above 20) conditions. The new state-by-state program has then been used to analytically estimate the performance of a previous the Mach 10 operating condition of X3 expansion tube, as can be observed in Fig. 3.1. For details on the X3 Mach 10 operating condition the reader is referred to Gildfind et al. [166, Table 1].

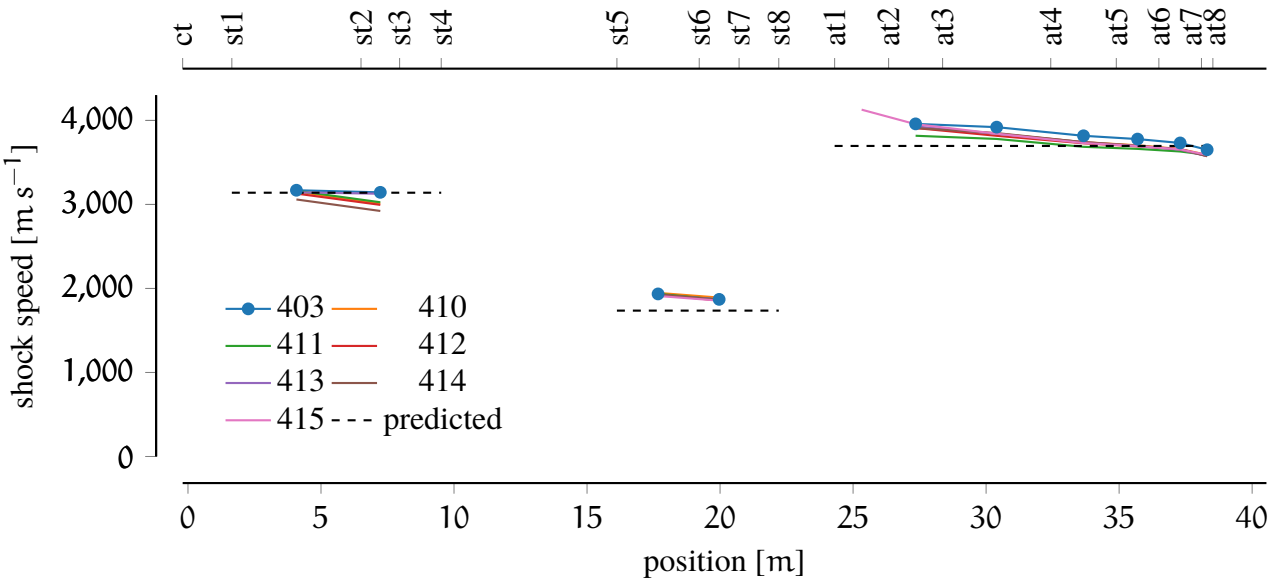

Figure 3.1: Comparison of the experimental shock speeds with the prediction of the state-by-state calculations. Each line indicates a different experiment. On the top axis positions of the experimental sensor is indicated (as presented in Fig. 3.2).

Considering shock speeds at the start of the shock and acceleration tubes, where viscous effects have minimal effect, the shock tube speeds are under-predicted by 10 % to 20 %. Consequently, this induces an underestimation of the shock speeds in the first part of the acceleration tube, but accuracy improves further down the tunnel.

This confirms the results found in [1], in which a similar 0D model showed reduced performance due to the presence of a reflected shock at the secondary diaphragm, which is in accordance with what is predicted by this code. The actual experimental shock tube speeds are higher than numerical estimates because of a reflected compression wave that accelerates the flow. To increase the accuracy

of the performance estimates of the facility it is necessary to switch to a higher order model, such as L1D (Section 3.3.2).

The presented tool has proven to behave as expected by the theory, and even if the prediction abilities are limited, it still remains useful in the preliminary phase of condition development.

Solving the inverse problem

As described above, the analytical tool is able to produce the exit flow conditions given a set of fill pressures. In our case we would like to solve the inverse problem, i.e. given a set of target flow properties, find the required fill pressures.

If tuned operation is disregarded, it can be shown that assuming a no-secondary-driver facility, and fixed gas compositions and fill temperatures, any triplet of fill pressures p_{CT}, p_{ST}, p_{AT} (i.e filling pressures for compression tube, shock tube and acceleration tube) produces a unique solution for the exit flow properties. In this case, to solve the inverse problem, the analytical model is then coupled with a Nelder-Mead optimiser. The optimiser in this case simply acts as a numerical solver, as there is only one solution to be found. The objective function for this problem is defined as:

$$f(p_{CT}, p_{ST}, p_{AT}) = \sqrt{\left(\frac{p - p_{target}}{p_{target}}\right)^2 + \left(\frac{T - T_{target}}{T_{target}}\right)^2 + \left(\frac{u - u_{target}}{u_{target}}\right)^2} \tag{3.1}$$

where p, u, T are the expanded test gas pressure, velocity and temperature in the acceleration tube and $p_{target}, u_{target}, T_{target}$ the corresponding target flow properties presented in Table 3.2.

The solutions found are then evaluated and validated for theoretical test time, and the acoustic buffer requirement (discussed in Section 2.10.1). As there is no prior experimental data, the obtained driver fill pressure cannot be adjusted to the equivalent tuned piston condition. In this case, the driver fill pressure was compared with the available tuned drivers as described in Section 3.5. Obtained target fill pressures are necessarily higher than the available tuned piston performance, because, as previously discussed, the code does not take into account the diaphragm losses. Thus, a more powerful driver condition is chosen, while maintaining the calculated p_{ST}, p_{AT}, to obtain the "combined" condition that will be tested experimentally.

Change in facility configurations or the use of a secondary driver were not explored analytically, but only experimentally, and will be presented in the following sections of this chapter.

3.3.2 L1D

To estimate the performance of a free-piston driven impulse facility, one has to model a variety of fluid and piston-dynamics phenomena that are intrinsically transient. Although CFD codes are getting more and more powerful and computational capabilities are increasingly faster, we are still far from achieving full-facility, high-fidelity simulation, particularly for a facility of the size of X3. Additionally, in the initial condition design phase, simulation times would be unacceptably high for parametric exploration. To answer this need, a reduced-dimensionality code named L1D was developed by Jacobs [167, 168] and has been used by many researchers over the years. In this section we will describe this code, which has been an essential part of the Mach 12 condition development. L1D is a numerical simulation tool and its principal characteristics are as follows:

- One-dimensional, axisymmetric model for the gas dynamics. One spatial parameter (axial) is defined, along with gradual variation in area.
- Lagrangian description of multiple gas slugs. As such, the grid moves and the size of cells varies in time, following the gas slugs in their trajectories.
- Second order accuracy in both space and time, with a shock-capturing scheme. This is required for shock-tube flows where multiple shock and expansion waves interact with each other.
- Capability to use different gas models for different gas slugs.
- Viscous effects are modelled using classical and/or empirical correlation factors.
- Pistons and diaphragms can be included and mass-dynamics equations are integrated into the system.

L1D cannot directly model 2D and 3D flow-processes, such as boundary layer development and flow through the launcher or across complex geometries, e.g. the primary diaphragm station. To simulate these effects, loss regions and loss factors are implemented based on classical pipe flow correlations. However, these parameters can only be deduced from experimental data.

The code allows for "rapid" ($\sim$ 10 hours) estimate of expansion tube flow processes, and to easily iterate design parameters. Although the code makes a great number of simplifying assumptions, it has shown to be extremely effective in modelling the axial wave processes which are the principal driver of expansion tube flow processes [30, 95, 155]. Its accuracy is reduced in the region were viscous effects dominate, which is usually the low-pressure acceleration tube [30, 95, 155]. An extensive discussion of the limitations of L1D, but also of the quasi 0D-models is carried out in Chapter 5, where the flow condition is numerically modelled.

This code, although not directly used for the condition design, was fundamental to the tuned piston condition development process, where it has shown to produce extremely accurate predictions of the piston dynamics [161]. It will be later used also in Chapter 5 to obtain a hybrid numerical model of the final experimental condition.

3.3.3 Experimental methodology

Once a theoretical condition was selected, experiments were carried out and flow properties were measured. In the following paragraphs we will briefly introduce the facility measurement capabilities that have been employed in this chapter.

The X3 expansion tube is equipped with several flush-mounted tube wall pressure sensors along the complete length of the facility. Figure 3.2 summarises the facility characteristics and the instrumentation locations. The sensors are installed in a custom-made mount flush to the wall, with the exception of driver pressure sensor CT, which is recessed. A variety of piezoelectric PCB pressure gauges are employed: model 111A22 (5000 psi — 34 MPa) for CT, model 113B24 (1000 psi — 7 MPa) for all the STx sensors and model 112A22 (50 psi — 344 kPa) for all ATx sensors in the acceleration tube. All of these are used to measure post-shock static pressure and shock speeds along the tube, and they are the primary metric to evaluate the facility performance.

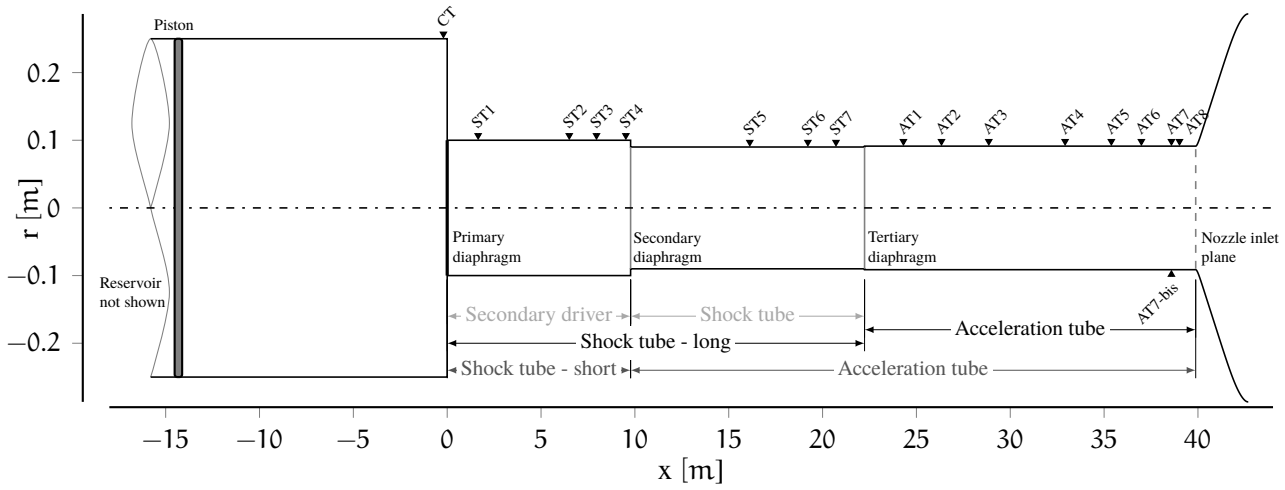

Figure 3.2: Geometrical layout and wall pressure probe locations in the X3 expansion tube. The different facility configurations, discussed later in this chapter, are also presented. X-axis origin corresponds to the primary diaphragm location.

The nozzle expansion process is complex and it is unclear how it interacts with the different facility configurations that are investigated in this chapter. It is, indeed, highly desirable to remove the nozzle influence from these measurements. To achieve that, a new rake at the nozzle inlet was developed. It was located just prior to the nozzle inlet and equipped with 8 pressure probes, as indicated in Fig. 3.3, where the probe P4 is located at the tube centreline. The probes are 15° cone-head pressure gauges, and not standard flat Pitot-pressure probes. This serves to improve survivability of the sensor, and has been used at UQ since 2012 [169]. The drawback is that cone-head probes have a slight Mach number dependency that needs to be taken into account when estimating flow properties. The probes are radially spaced 18.5 mm apart. Each cone-head probe is equipped with a PCB model 112A22 transducer (50 psi — 344 kPa). A detailed discussion of the inlet rake and the cone-head pressure

probes is provided in Sections 5.2.1 and 5.2.2. The inlet rake has been used because it allows radial evaluation of the flow within the acceleration tube, immediately prior to the nozzle.

All the transient pressure measurements presented in this chapter were filtered using a constrained equiripple finite impulse response (FIR) low-pass filter, with a cut-off frequency of 150 kHz — the resonant frequency of PCB pressure sensors — and the filter order was equal to 100 [170].

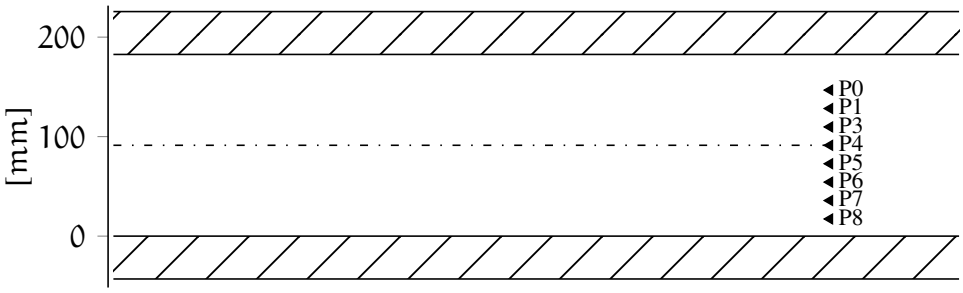

Figure 3.3: Vertical position of the nozzle inlet rake probes. See Fig. 5.2 and Table 5.1 for picture and description of the hardware. Flow is from left to right.

3.4 TARGET FLOW CONDITION

The main goal of this thesis was to test the M12REST engine reproducing as closely as possible its flight condition, i.e. examining the engine behaviour when mounted on a nominal vehicle flying at Mach 12 at 6° angle of attack, on a constant dynamic pressure trajectory of 50 kPa. However, as previously mentioned, the engine has been designed to be a 1:2 scaled version of the flight vehicle, and, as such, pressure-length (or binary scaling) is required to maintain most of the main flight parameters: Reynolds number, reaction rates, fuel mixing processes, and ignition times [90] (see Section 2.7.2 for a detailed discussion). The complete set of the required M12REST engine inflow properties is presented in Table 3.1 for both the nominal and the pressure-length scaled conditions. (The properties have been calculated assuming the US Standard Atmosphere model [171].)

Table 3.1: Target flow conditions on a 50 kPa dynamic pressure.

	Units	Full scale	1:2 Scale model
Altitude	km	36	36
p	Pa	496	992
p_0	MPa	310	620
H	$MJ\,kg^{-1}$	7.2	7.2
T	K	239	239
u	$m\,s^{-1}$	3722	3722
M		12	12
q	kPa	50	100

In the preliminary design phase, it was observed that the available Mach 10 nozzle would not have produced suitable Mach 12 flows and sufficiently large core flows. Therefore, the design and manufacture of a new Mach 12 nozzle was deemed necessary. For this reason, to solve the operating condition design problem the X3 expansion tube can be split in two independent parts, the facility, up to the end of the acceleration tube; and the nozzle inlet. This splitting allowed the author to undertake the two design problems independently, allowing the nozzle design in Chapter 4 to take place before the condition design presented in this chapter. New target flow conditions were defined for the nozzle inlet, serving at the same time as target exit flow conditions from the acceleration tube, and target inflow conditions for the nozzle design process. The target nozzle inlet properties, for both nominal and pressure-length scaled conditions, are outlined in Table 3.2.

Table 3.2: Target nozzle inlet flow properties.

(a) nominal condition

	Units	Value
p	Pa	10000
u	$m\,s^{-1}$	3650
T	K	600
M	[]	7.48

(b) pressure-length scaled condition

	Units	Value
p	Pa	20000
u	$m\,s^{-1}$	3650
T	K	600
M	[]	7.48

There is a spectrum of choices in determining the target nozzle inlet flow properties. For example, one can decide to drive a faster, colder flow in the facility and create a nozzle with a reduced expansion ratio or, vice-versa, produce a slower and hotter flow in the facility and design a nozzle with an increased expansion ratio. Temperature, pressure, and velocity have been estimated by exploring the expansion capabilities of a theoretical isentropic expansion with the area ratios calculated by assuming an exit nozzle diameter in the range 500 mm to 600 mm. Final values were then adjusted by verifying that the acceleration tube exit Mach number was in the range 6.5 to 7.5, which is well within the standard operating window of the X3 expansion tube.

3.5 THE LIGHTWEIGHT PISTON

X3 is a free-piston expansion tube. As such, the piston is crucial to successful experiments in this facility. Although not being an explicit part of this study, significant efforts to develop new piston capabilities took place in parallel. In this section those developments are briefly examined.

Prior to this study, the X3 expansion tube was equipped with a (relatively) heavyweight piston (200 kg) first commissioned in 2010 by Dann et al. [156]. This was a parallel project that was carried out, with the focus of investigating and expanding the capabilities of X3 for high enthalpy flows [161]. At the time, the available piston was not able to produce high enthalpy test flows (10 $km\,s^{-1}$ to 15 $km\,s^{-1}$) because tuned operation of that piston could not be achieved without the use of argon/helium driver

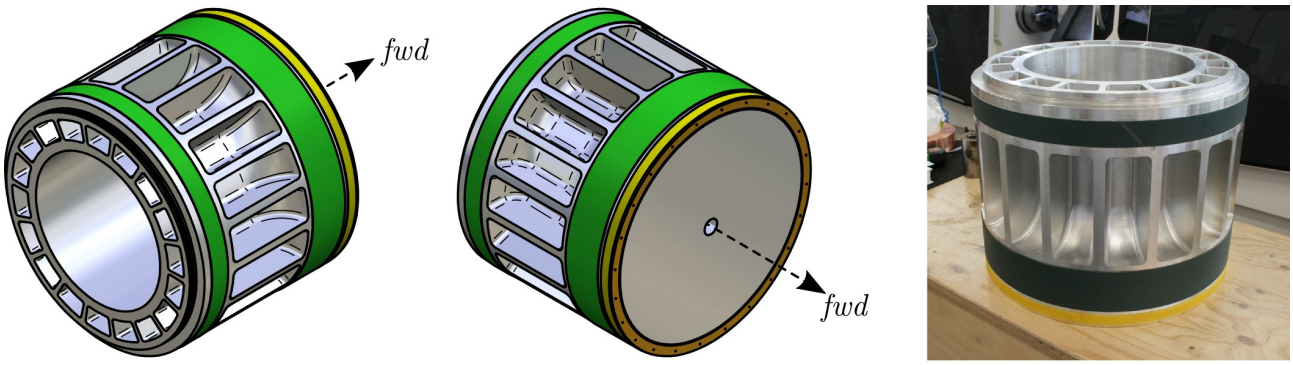

Figure 3.4: X3 new lightweight piston. First two images show the CAD model of the piston, the last one the manufactured piston. From [160].

gas mixtures. Argon driver gas allows tuned operation at lower speeds but reduces shock speeds. As discussed in [169] high driver gas sound speed requires high piston speed at rupture for tuned operation. This requires a (relatively) low mass piston that can be rapidly accelerated to the higher speed within the constraints of finite driver length and finite reservoir pressure (and also be rapidly slowed down again). For the purpose of such a project a new lightweight piston (100.8 kg), shown in Fig. 3.4, was developed for X3 (see [160]). Initial commissioning in 2013 indicated that the X3 reservoir was still not able to achieve sufficient piston speeds for tuned operation. Therefore, a new reservoir extension was manufactured to increase its total volume [161]. This allowed the lightweight piston to achieve the necessary higher speeds required for tuned operation, with higher mass fractions of helium in the primary driver, to increase the performance envelope of the expansion tube.

These upgrades inevitably modified the facility, such that the previous conditions for the heavy-weight piston could not be used any more. In parallel, Andrianatos et al. [161] developed a series of new operating conditions for the lightweight piston. The performance envelope of these conditions was such that target Mach 12 scramjet enthalpies were shown to be well within reach. For these reasons, the lightweight piston has been used for all of this work.

The targeted enthalpy and the total pressure are located in the lower part of the performance envelope of the lightweight piston, so that its use had also a series of important advantages. Firstly, as we will present later on, it becomes possible to easily apply pressure-length scaling to the scramjet experiment, doubling the total pressure by simply going to the next (in a performance-wise sense) available piston condition. Secondly, the condition is inherently less harsh on the facility, so that repeatability and day-to-day operations are simplified. Finally, this allows the use of a high mass fraction of Argon in the driver, reducing the effect of the flow disturbances as discussed in Section 2.10.1.

In other terms, the total pressure required at the desired enthalpy is easily achieved in X3 and this work confirmed that the required conditions for scramjet testing — out of reach of the highest performance RSTs — are achievable with the X3 expansion tube (although subject to other challenges, as described in Chapter 2).

3.5.1 Piston condition development

This section will cover the development of the new operating conditions for the lightweight piston. This is a brief summary of the work of Andrianatos et al. [161]. In a free-piston driven facility, the piston is driven by high-pressure gas in the reservoir to compress the driver gas in the compression tube. A steel diaphragm in front of the driver gas ruptures at a given pressure, which is a function of the steel properties and scoring characteristics. This mechanism creates an extremely high pressure and high temperature slug of driver gas able to drive the rest of the gas in the facility to hypersonic speeds.

The essential idea of tuned operation of a free-piston driver is that, unlike a constant volume driver, after diaphragm rupture the mass of driver gas swept by the piston motion continues to match or exceed the mass loss to the driver tube, such that the gas is maintained at high pressure for a longer duration. Thus, longer test times and higher performance are achieved. For a given piston mass, driver length and driver-shock tube area ratio, tuned-operation of a free-piston driver condition development consists in selecting the right combination of reservoir fill pressure, driver-gas composition and fill pressure, and diaphragm rupture pressure to achieve the high speed required to obtain, effectively, the 'ram' effect to drive up pressure, but equally importantly, to ensure a soft landing for the piston at the end of the stroke. The piston dynamics require a point of zero velocity and zero acceleration in the trajectory, at which point the piston can be 'caught' by an appropriate length of buffer, which in X3 comprises a set of energy absorbing nylon rods.

Hornung's analytical model

The first step in obtaining a new piston condition was to use the 0D model developed by Hornung [118]. This analysis, as a first approximation, produces a range of trajectories, and most importantly estimates the fill pressures and gas composition required for achieving soft landing. Reservoir fill pressures, on the other hand, cannot be accurately estimated this way, due to the fact that this model assumes an infinite reservoir and no pressure losses due to flow through channels.

For increased performance, a higher concentration of helium is desired (as this increases the speed of sound of the driver gas), however noting this, the high sound speed gas actually depletes the driver faster, so that lower compression ratio and higher fill driver pressures are required and the piston has to do more compression work on the driver gas. As a consequence, the piston needs to be driven faster to increase its kinetic energy, which requires high pressure initially, resulting in a feedback loop to a point where the required reservoir pressures become unrealistic.

Alternatively, if a tuned condition is already established for a driver gas comprised of a proportion of argon, helium can replace some or all of this argon, without changing the various fill pressures, if the exit area of the compression tube is restricted appropriately, as outlined in [172]. The contraction area

can be scaled by the square root of the gas constant ratios. This allows high-performance conditions to be reached without the need for unrealistic fill pressures for both the reservoir and driver. The performance-penalty comes down to a pressure loss of the driver gas, which undergoes a stronger steady expansion from the orifice plate diameter to the actual shock tube diameter. However, this performance reduction is often less than the one introduced by a reduced compression ratio with equivalent Helium percentage (required to maintain tuned operations), so that overall the use of an orifice plate can be beneficial. This is especially the case for high enthalpy conditions where driver gas sound speed is particularly important.

L1D model and experiments

Once theoretical fill pressure, gas composition, and orifice plate diameter had been determined, a numerical model of the compression tube was developed. As discussed in 3.3.2, this requires a simplification of the actual geometry and the introduction of loss factors to model various components of the facility to adequately reproduce the piston dynamics. The geometrical model is presented in Fig. 3.5, where the duct area changes along the length aims to represent the real-word three-dimensional volumetric features of the reservoir. To tune the loss factors and adjust the equivalent geometry of the model, "blank-off" experiments were carried out, whereby the steel diaphragm was replaced with a thick plate that would not break. The driver pressure was recorded and used to tune the L1D simulation, until good agreement was achieved.

With the tuned model, the theoretical conditions were then experimentally verified to obtain a set of final operating conditions as indicated in Table 3.3.

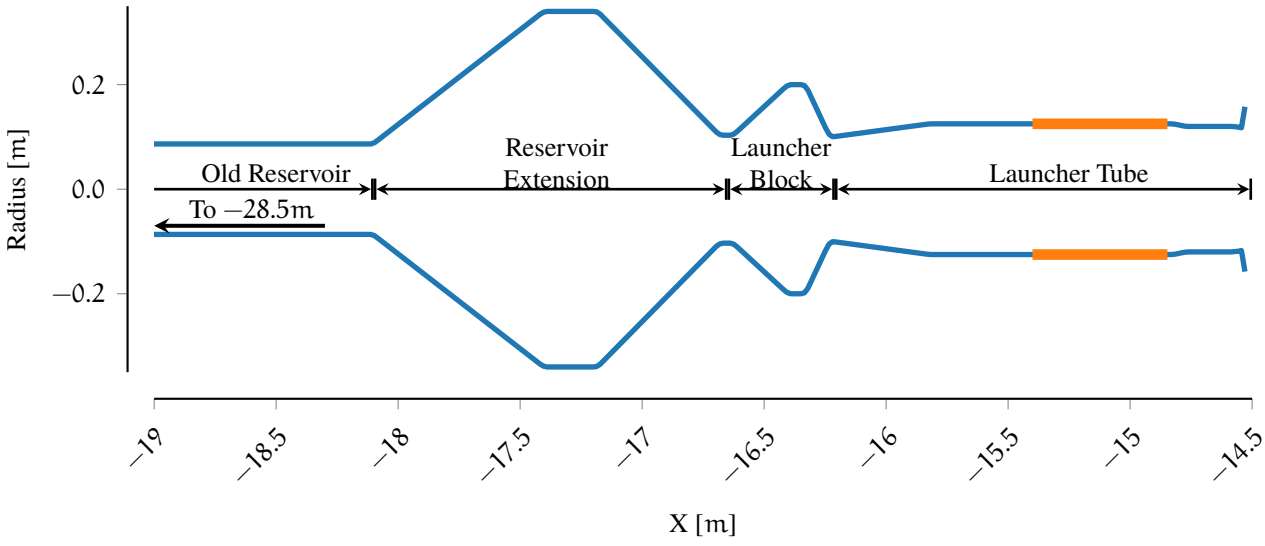

Figure 3.5: L1D model of the launcher and loss region in this section of the model. Courtesy of Andrianatos A.

Table 3.3: Lightweight piston tuned conditions: operating parameters.

(a) fill pressures, diaphragms and buffers

	flow condition	
diaphragm	2 mm	3 mm
driver gas fill pressure	149 kPa	46 kPa
reservoir pressure	6.7 MPa	8.8 MPa
buffer length	6 x 120 mm and 6 x 100 mm	12 x 50 mm

(b) gas mixtures and gas compositions

Orifice size	Argon	Helium
None	100 %	0 %
164.7 mm	40 %	60 %
149 mm	25 %	75 %
139.2 mm	15 %	85 %
112.5 mm	0 %	100 %

3.5.2 Experimental results

The aforementioned piston conditions were then tested in the facility. A short summary of their performance is given in Fig. 3.6, where the main performance estimator — shock speeds in the shock tube — is presented. Amongst those, as it will be discussed in Section 3.6, the 100 % Argon and the 60 % He conditions were selected to be used for the Mach 12 flow condition.

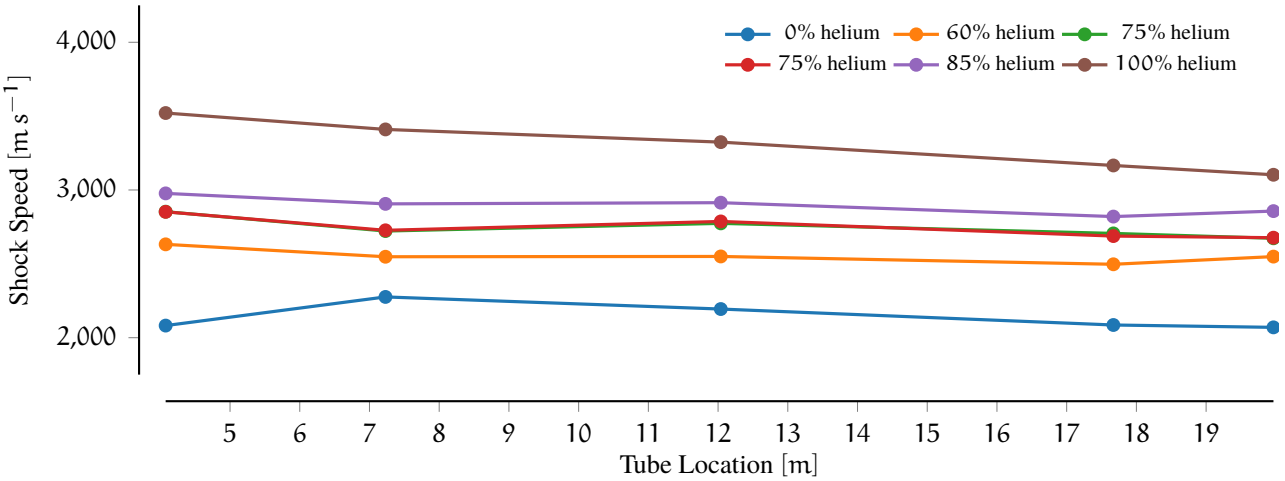

Figure 3.6: Shock speeds produced using a 2 mm diaphragm into 13.5 kPa air and the lightweight piston. Taken from [161].

3.6 CONDITION DEVELOPMENT: RESULTS AND EXPERIMENTAL VERIFICATION

The solution of the "analytical expansion tube problem", as presented in Section 3.3.1, and the tuned piston condition selected for actual testing, are indicated in Table 3.4. For the nominal, unscaled condition, the solution required a theoretical 149 kPa 100 % Argon driver, where the closest available tuned condition was at 49 kPa 100 % Argon, producing a compression ratio twice the analytically estimated compression ratio. Other theoretical fill pressures were calculated for other Helium-Argon gas mixtures, but they were discarded as using the 100 % Argon driver would, in theory, reduce test gas acoustic disturbances [151] and also because the available tuned driver at the equivalent gas composition, at 49 kPa, would have been too powerful, as shown by Fig. 3.6.

For the scaled condition, the 60 % He – 40 % Ar condition was chosen, as the compression ratio at 100 % Argon was evaluated to be too small, and therefore not expected to drive a fast-enough shock in 45.5 kPa test gas. It is important to note that the chosen piston driver is such that this condition is under-tailored and might require the use of a secondary driver to avoid test flow disturbances to propagate into the test gas. This, along with a thorough analysis of secondary drivers, is carried out in Section 3.8.

Table 3.4: Calculated fill conditions to obtain target flow properties indicated in Table 3.2. All initial gas temperature set to 300 K. Primary diaphragm rupture pressure: 17.5 MPa. The chosen tuned operating condition is indicated in bold.

(a) nominal/unscaled condition

driver gas composition	p_{CT} [Pa] estimate	p_{CT} [Pa] tuned condition	p_{ST} [Pa]	p_{AT} [Pa]
0 % He	149 276	49000		
60 % He	631 365	—		
75 % He	1 188 348	—	22 674.5	58.6
85 % He	2 087 959	—		
100 % He	10 370 423	—		

(b) pressure-length scaled condition

driver gas composition	p_{CT} [Pa] estimate	p_{CT} [Pa] tuned condition	p_{ST} [Pa]	p_{AT} [Pa]
0 % He	74 770	—		
60 % He	292 405	49000		
75 % He	528 618	—	45 451.0	117.0
85 % He	888 272	—		
100 % He	3 970 650	—		

Table 3.5: Nominal Mach 12 operating conditions.

Condition	Reservoir [MPa]	Diaphragm	Orifice plate	Primary driver	Sec. driver He [kPa]	Shock tube Air [kPa]	Acc. tube Air [Pa]
x3s506	6.7	2 mm	—	49 kPa 100 % Ar	—	22.7	58
x3s582	6.7	2 mm	165 mm	49 kPa 60 % He 40 % Ar	—	45.5	118

Table 3.5 shows a detailed summary of the two operating conditions that were both selected by the author for testing. For the rest of this work, they will be referred as CONDITION x3s506 and CONDITION x3s582, from the first experimental run at which they were initially fired.

In Fig. 3.7, experimental shock speeds for both conditions are presented, along with the analytical predictions. It can be observed that the experimentally obtained shock speeds are within 3.5 % of the analytically required shock speeds, notwithstanding a significant increase in compression ratio. The choice of the two drivers was proven correct and effective in making up for the losses at diaphragm rupture. The acceleration tube shock speeds show a significant slow-down along the acceleration tube, quantified at 7 %. The difference between measured shock speeds and target shock speeds at the end of the acceleration tube is within 12 %.

The shock speed attenuation is specific to X3 and exists for other different flow conditions (see for example Fig. 3.1, where the heavyweight piston condition was used and a comparable attenuation is noticeable). It is supposed that the attenuation is caused by the hypersonic viscous effects, boundary layer development and driver wave processes. It is noteworthy to observe that the shock speeds for

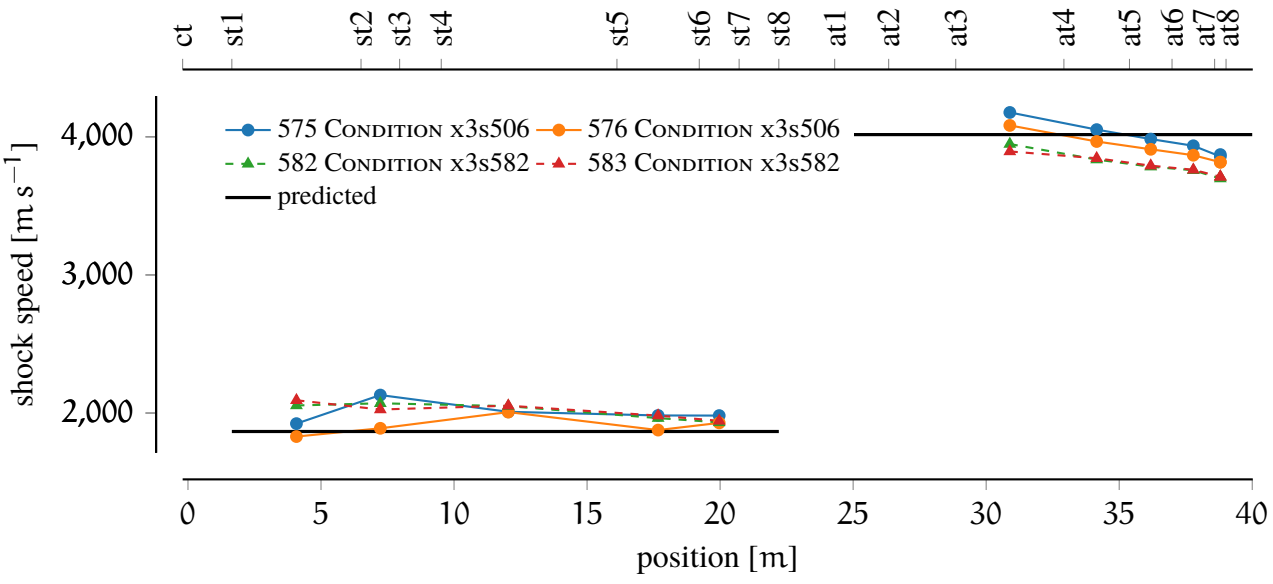

Figure 3.7: Shock speeds comparison for the reference CONDITION x3s506 and the scaled-pressure CONDITION x3s582. Predicted shock speeds are shown for both conditions, as (theoretically) they just differ in the pressure-length scaling done for CONDITION x3s582.

Condition x3s582 just after the secondary diaphragm are already lower than the shock speeds for Condition x3s506, notwithstanding a negligible difference in the shock tube.

Overall, despite some discrepancies, the mixed-experimental design approach produced two flow conditions that closely matched expectations. Therefore, these conditions were chosen for the rest of this project. In fact, although some differences from the theoretical flight condition arose, they were considered to have a negligible effect on the scramjet behaviour. In the remaining part of the chapter, an experimental analysis of the operating condition, carried out to verify the most opportune configuration to a produce steadier and longer test time, is discussed.

It is noted that the complete and detailed discussion of the nozzle exit flow parameters, coupled with hybrid CFD simulations carried out to reproduce the experimental conditions, is presented in Chapter 5.

3.7 SHOCK TUBE LENGTH/DIAPHRAGM LOCATION

The X3 expansion tube, after the reconfiguration to operate with a single piston driver, has three available diaphragm stations, as shown in Fig. 3.2. With the heavyweight piston, the only scramjet condition developed employed a secondary driver, so that the shock tube configuration became fixed. However, the newly proposed conditions in this thesis could theoretically run with or without a secondary driver. In that case, the shock and acceleration tubes could be configured in two different ways. As such, the question became where the diaphragm separating the acceleration tube and shock tube should be located. For the rest of the discussion, a *long shock tube* will refer to a facility configuration in which the diaphragm delimiting the shock tube is located at the nominal tertiary diaphragm station at x= 22.24 m (so that the shock tube is 22.24 m long and the acceleration tube is 18.07 m long). On the other hand, a *short shock tube* will refer to a facility configuration in which the diaphragm is located at the nominal secondary diaphragm station at x= 9.77 m (and the shock tube in this case is 9.77 m long and the acceleration tube is 30.54 m long). The two configurations are also shown in Fig. 3.2.

It is well-known that only a minor proportion of the test gas is processed by the unsteady expansion, so that adopting a shock tube twice as long does not necessarily mean that test times will double. Actually, a shorter acceleration tube might mean that the flow has less space and time to undergo the unsteady expansion. On the other hand, using a short shock tube has the consequence that the acceleration tube is more than 30 m long — without considering the nozzle — where the viscous interactions with the wall can become significant (as the length/diameter ratio is over 150), and might have unintended effects. X2, as an example, runs with an equivalent short shock tube mode, although the relative length of the acceleration tube is much smaller. Finally, it is noted that there are two area changes at the secondary and tertiary diaphragm stations. Although seemingly insignificant, their influence on the test times and the flow quality remains to be investigated.

Given the above considerations, and the fact that no study was done before for the X3 expansion tube, it was decided to undertake an experimental study to verify which of the two configurations appeared to be more effective in producing the desired flow conditions. In Table 3.6 the list of the experiments that have been carried out is presented.

Table 3.6: Facility operating parameters for facility-configuration tests.

Condition	Shot n.	Piston condition	Shock tube configuration	Shock tube Air [kPa]	Acc tube Air [Pa]
x3s506	575 576	49 kPa 100 % Ar	**Long**	22.7	58
x3s518	573 574	49 kPa 100 % Ar	**Short**	22.7	58

In Fig. 3.8, shock speeds along the tube for the series of experiments is shown. In the plot, the shock speed profiles are interrupted at different axial locations, which correspond to where the diaphragm was located. It is clear that, although there is a minor shot-to-shot variation, there is otherwise little difference in shock speeds produced by the two configurations. In other words, at a first approximation there are no performance penalties in running one or the other facility configurations.

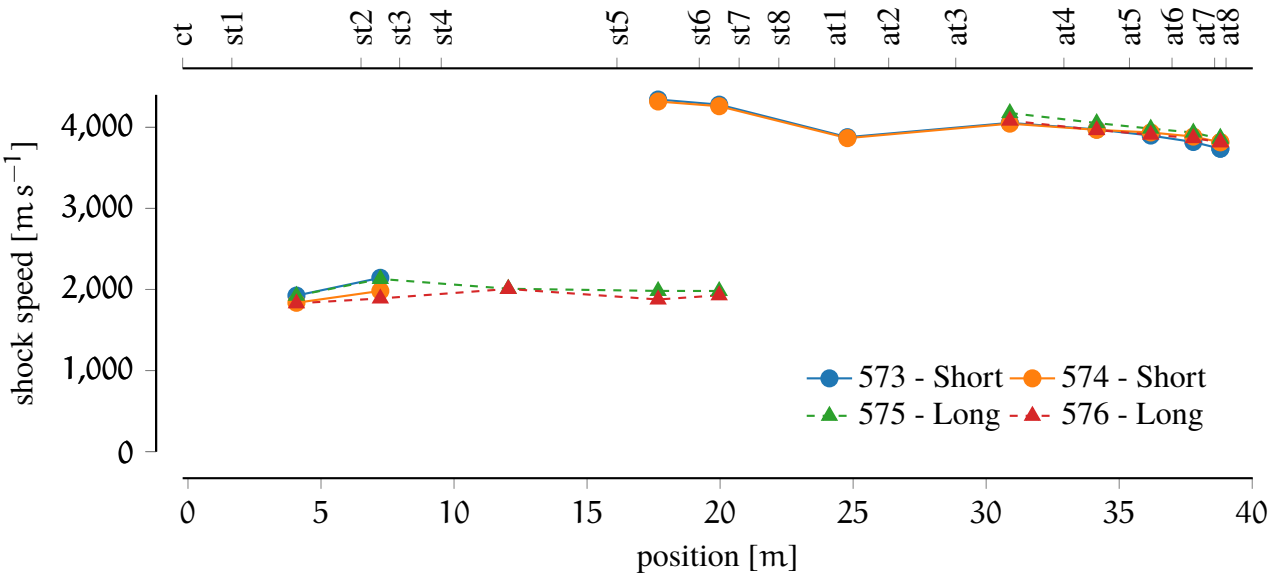

Figure 3.8: Shock speed variation for the series of facility-configuration experiments. Dashed lines/triangular markers indicate experiments in long-shock tube configuration. Solid lines/circles indicate experiments in short shock tube configuration. Lines are interrupted at the secondary diaphragm location, indicating where the shock tube ends and acceleration tube starts.

The wall pressure measurements taken at AT8, the last available sensor prior to the nozzle inlet rake, are presented in Fig. 3.9. The traces of the long shock tube experiments present a classic and relatively standard behaviour. The first flat part corresponds to the accelerator gas, followed by a dip in pressure that indicates the arrival of the test gas interface. Following the interface, the test gas presents a steady

pressure gradient. Conversely, the short shock tube traces show a significantly different and noteworthy behaviour. First, the pressure trace indicates that acceleration tube gas pressure is not constant, but gradually decreasing. The interface is not clearly identifiable and, most surprisingly, the apparent test gas is much steadier than for the long shock tube experiments.

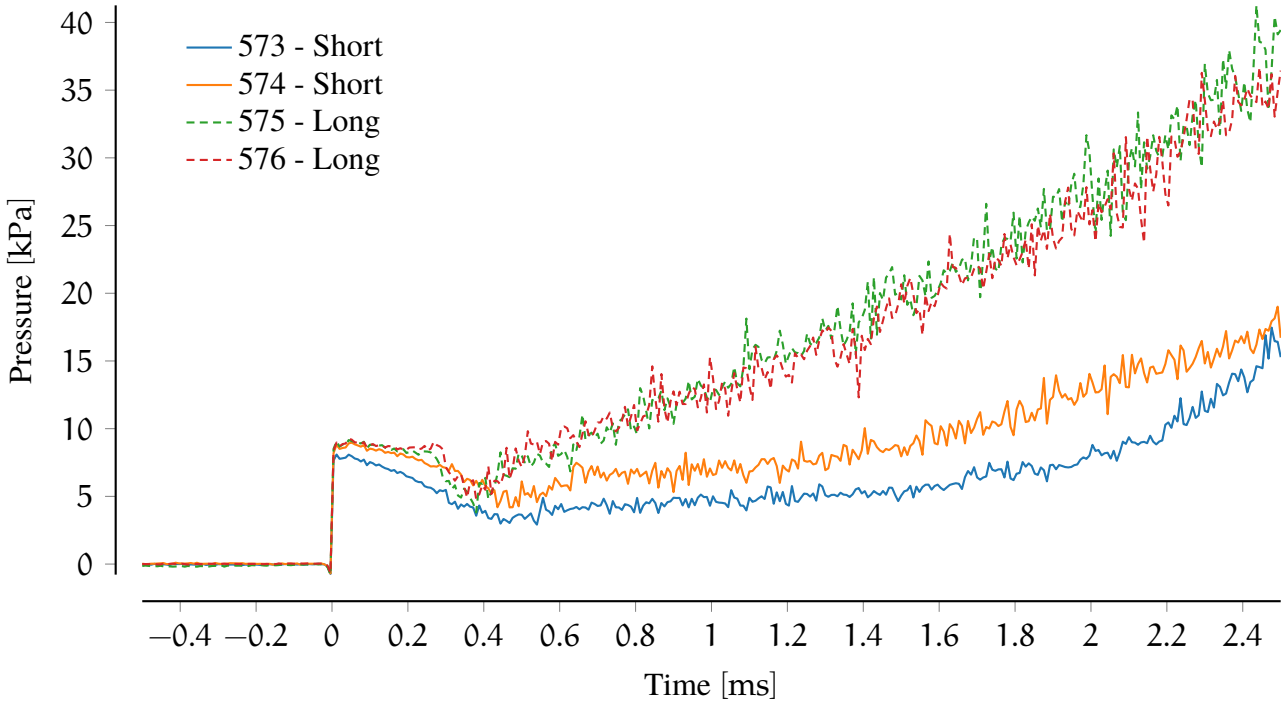

Figure 3.9: AT8 pressure trace for the facility-configuration experiments. AT8 is the last sensor prior to the nozzle inlet. Dashed lines correspond to long shock tube while solid lines correspond to short shock tube

Shortly downstream of AT8, immediately prior to the nozzle intake, the nozzle inlet rake was used to measure the inflow gas into the nozzle. The rake was briefly introduced in Section 3.3.3. The adopted conehead probes are discussed in detail in Sections 5.2.1 and 5.2.2. In Fig. 3.10 the nozzle inlet rake experiments are presented. In the top figure, the cone pressure measurements taken at the nozzle centreline (P4) are shown for all the experiments. In the bottom figure, an aggregated view of all the pressure probes is plotted. Cone pressure measurements from each of the probes were extracted from the interval indicated in the top figure, and median and median absolute deviation were calculated. Finally, the obtained values were plotted against the position of each probe, relative to the tube bottom wall. Short-shock tube experiments (solid lines) are linked to the right axis, while the long tube experiments (dashed lines) refer to the left axis.

The centreline traces are substantially different between the two configurations with behaviours that mirror what is observed for the wall pressure measurements. The short-shock tube experiments present a very steady test gas, with very low oscillation over the mean value, and a totally absent pressure gradient. On the other hand, long shock tube experiments show a constant (on average) pressure

gradient and some disturbances superimposed over it. Qualitatively, short-shock tube experiments appear to have a reduced amount of oscillations around the mean value and a much longer test time.

The aggregated plot of Fig. 3.10 indicates that, for the long shock tube configuration, the boundary layer is fully developed and occupies the whole tube. Indeed, no constant pressure region can be identified around the tube centreline (in the figure P4 or 91.3 mm). In other words, the boundary layer reaches the tube centreline within the 10 m of the short acceleration tube. Contrarily, the short shock tube experiments do not exhibit a clearly identifiable profile. Additionally, the mean cone pressure values across the whole diameter is significantly lower than the long shock tube experiments.

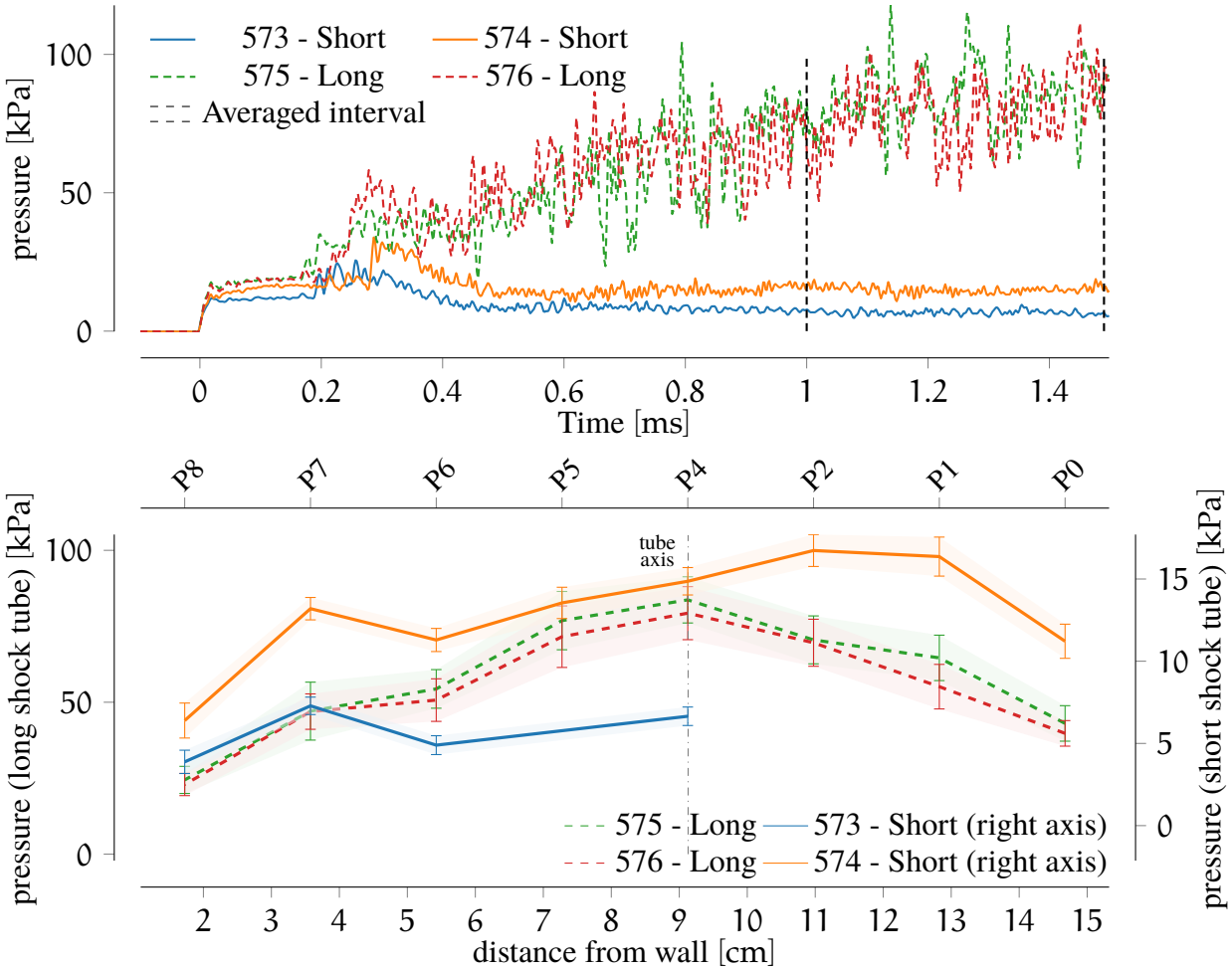

Figure 3.10: Inlet cone-pressure rake comparison for short and long shock tube conditions. In the top plot, the time-varying pressure trace P4 at the nozzle centreline is shown, for both long and short shock tubes experiments. In the bottom plot, aggregated pressure averages and relative uncertainties are presented for all the probes along the rake. Short shock tube experiments have a separate axis on the right. The averaging period is indicated in the top plot between the vertical black lines.

The results of the short shock tube, at first insight, present what looks like a fully expanded, almost ideal expansion tube transient flow. However, the significant drop in the mean-pressure (by a factor of 5) and considering that the long shock tube experiments already presented a boundary layer profile

reaching the nozzle centreline, indicates that the test gas is collapsed and the boundary layer "engulfs" the flow, causing an increase in temperature and a significant drop in Mach number.

Gildfind et al. [129] carried out an analysis for a somewhat different scope that, however, helps in confirming this prediction with a suggested explanation. The proposed mechanism is that, across the acceleration gas/test gas interface, a recirculation zone is created, which pushes test gas into the boundary layer. This recirculation is initially responsible for the dip in pressure that can be observed in the wall pressure measurements when the interfaces arrive. Along the tube, the recirculation is continuously feeding mass from the test gas (in the centreline) into the boundary layer, while re-compressing the flow and mixing with accelerator gas (and thus heating it up). After a certain distance travelled by the shock wave along the acceleration tube, the test gas collapses and the recirculation mechanism fully dissipates. This mechanism takes a significant length to develop, and is only evident in the short shock tube experiments.

Hence, it has been decided to proceed with the long shock tube configuration, against the apparent steadier and quieter short shock tube results. Notwithstanding that, the mechanism for which the boundary layer dissipates all the flow disturbances remains unclear, and it might be of interest in future studies. Finally, it is important to note the aforementioned mechanism has been verified to occur for dense (in expansion tube terms) flows, and it is not guaranteed to exist in high enthalpy flows, so the conclusions for high enthalpy experiments might differ.

3.8 SECONDARY DRIVER AND FLOW DISTURBANCES

In Section 2.10.1 it was briefly illustrated that for scramjet conditions, which require relatively slow speeds (3 $\mathrm{km\,s^{-1}}$ to 4 $\mathrm{km\,s^{-1}}$) and high-density flows (compared to super-orbital flows) the use of a secondary driver does not necessarily increase the performance. Indeed, it has been shown by Gildfind et al. [1] that the secondary driver in this case might act as a relatively passive slug of gas, having negligible effects on the test gas properties. Instead, the test gas approaches the equivalent properties for operation without a secondary driver, but for a shorter test gas slug. Given these observations, it is not clear which ratio might be optimal for low enthalpy conditions, or if a secondary driver is beneficial at all.

On the other hand, in Section 2.10.1 it has been noted that a solution proposed for noise suppression is the use of the secondary driver as an acoustic buffer. When configured in an over-tailored mode, it is expected to prevent the ingress of driver induced flow disturbances. However, as suggested by Gildfind et al. [1], such a use of the secondary driver was proposed for high-enthalpy, super-orbital conditions. For low-enthalpy, scramjet conditions, where a reflected shock would typically be generated at the secondary driver, it is not clear whether the secondary driver remains effective as an acoustic buffer, in accordance with the model developed by Paull and Stalker [149]. In any case, the shock tube could be under-tailored in relation to the shock-processed secondary driver gas. Indeed, whether the secondary diaphragm

rupture introduces a new source of noise to the flow, and how this noise is transmitted to the test gas is a question that remains to be investigated, and could further limit the usefulness of a secondary driver.

At the same time, in another publication, Paull [151] expanded his previous theory by discussing how using a low-speed-of-sound driver gas can actually produce a quieter test gas. Furthermore, he actually predicted that for large diameter expansion tubes, of which X3 is a good example, a low speed of sound is a necessary condition to ensure low levels of disturbances in the test gas. The two chosen conditions in this chapter operate with respectively 100 % and 40 % Argon driver gas and, as such, if the Paull's theory is correct, they might already have low noise levels in the test gas.

No systematic analysis of these behaviours has ever been undertaken for the X3 expansion tube. Thus, it was decided to explore the performance of the aforementioned condition, to assess whether the use of a secondary driver could increase the performance of a low enthalpy condition and reduce flow disturbances and unsteadiness.

A series of experiments were run repeating Condition x3s506 and Condition x3s582 with the addition of a secondary driver as outlined in Table 3.7. It is important to note that the standard, no secondary driver, Condition x3s506 is over-tailored with respect to the driver gas and, as such, should present a reduced amount of noise in the test gas traces, as the theory of Paull and Stalker [149] suggests. Conversely, Condition x3s582 is under-tailored and should demonstrate flow disturbances to the point that no clear test time can be identified. Therefore, this condition was expected to greatly benefit from the adoption of a secondary driver. Two different secondary drivers have been tested for Condition x3s506, for filling pressure ratios of 5 and 10. For Condition x3s582, only a single configuration was tested. With respect to Fig. 3.2, the secondary driver is the 10 m long part of the shock tube between the primary and the secondary diaphragm. The shock tube is the 12 m long second part of the shock tube.

3.8.1 Condition x3s506: over-tailored

Figure 3.11 depicts the usual shock speeds along the facility for the experiments of Table 3.7 for Condition x3s506. Lines are interrupted where there is a diaphragm in between. Overall, it is noted that for the secondary driver experiments there is an increased shot-to-shot variability along the tube, especially significant in the acceleration tube. This is probably due to the added operational complexity in having an additional driver to fill, with increasing filling times, allowing an increased amount of air to leak in the two independent volumes, so that the relative error in fill pressure is higher.

Shock speeds in the shock tube are well aligned with the no-secondary-driver reference experiments, with no distinct difference. Specifically, shot 581 was expected to produce a shock speed increase larger than 400 m s^{-1}. Shock speeds in the acceleration tube are more inconsistent, with a higher shot-to-shot variation, but the measurable speed increase is well within the margin of error. Hence, we can conclude that for this set of experiments, the theoretical performance increase due to the use of a

Table 3.7: Secondary driver experiments: operating conditions. $\frac{a_2}{a_3}$ is the over-tailoring ratio between the shock-processed test gas and either the unsteadily-expanded secondary driver gas or the unsteadily-expanded primary driver gas. $\frac{a_{sd2}}{a_{sd3}}$ is the over-tailoring ratio between the shock-processed secondary driver gas and the unsteadily-expanded primary driver gas.

Nominal cond.	Shot n.	Primary driver	**Sec. driver** He [kPa]	Shock tube Air [kPa]	Acc. tube Air [Pa]	$\frac{a_{sd2}}{a_{sd3}}$	$\frac{a_2}{a_3}$
x3s506	575 576	49 kPa 100 % Ar	—	22.7	58	—	1.5
x3s506	577 578 579 580	49 kPa 100 % Ar	100	22.7	58	3	0.47
x3s506	581	49 kPa 100 % Ar	200	22.7	58	2.69	0.57
x3s582	582 583	49 kPa 60 % He 40 % Ar	—	45.5	118	—	0.93
x3s582	584 585	49 kPa 60 % He 40 % Ar	100	45.5	118	2.35	0.45

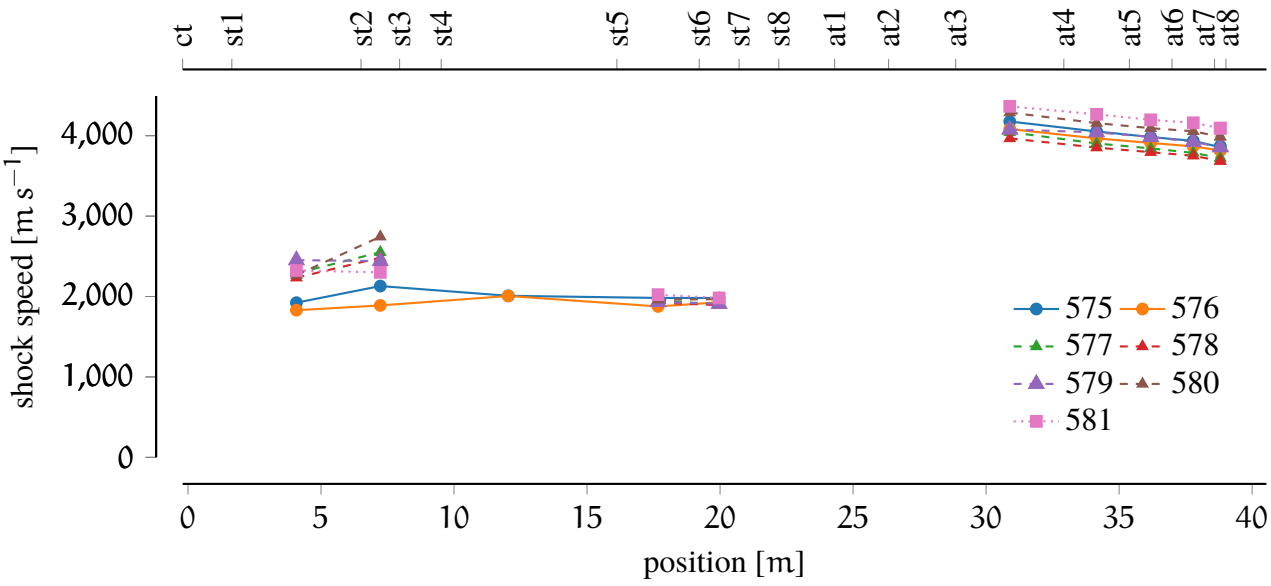

Figure 3.11: Shock speeds variation in the series of secondary driver experiments for CONDITION x3s506. Reference (no secondary driver) shots: solid lines/circle; 100 kPa sec. driver shots: dashed lines/triangles; 200 kPa sec. driver: dotted lines/squares. Refers to Table 3.7 for full details.

secondary driver is not observed. As suggested in another publication [1], the diaphragm rupturing is often neglected and likely responsible for the over-prediction of shock speeds and performance process. A thick secondary diaphragm introduced to hold the high initial pressure difference required for the dense, low enthalpy condition does not behave as an ideal, instantly disintegrating diaphragm. Indeed, it can be shown that these thick diaphragms create a reflected shock travelling upstream, slowing down the secondary driver gas and therefore negating any performance increase [1].

Finally, in Fig. 3.12 a summarised view of the cone-pressure measurements taken at the nozzle inlet rake (see Sections 3.3.3 and 5.2.2) is presented. In the top picture, the tube centreline transient traces are shown. Only three traces are shown for clarity, each representing a different configuration. These traces have been time-referenced to the shock wave arrival. On the bottom picture, an aggregated view of all the rake pressure probes is shown, where each pressure probe has been averaged (across the interval indicated in the top figure). In addition, medians together with median absolute deviations (median is a better estimator for noisy data [173]; for further detail see Section 5.2.5) are presented as a function of the distance from the bottom wall.

Figure 3.12 confirms that the flow at the nozzle inlet presents no difference with or without a secondary driver. Most importantly, it is clear its use does not improve flow quality both at 100 kPa and 200 kPa. In the top picture, the oscillations around the mean value are qualitatively the same, as confirmed by the bottom plot, where the error bands are of the same magnitude around an equally similar median value.

The thick secondary diaphragm is, again, a possible explanation. Paull and Stalker proposed the primary diaphragm rupturing process as the noise source that in the final unsteady expansion is focused into flow disturbances. When a secondary-driver is adopted, according to their theory, the secondary driver slug should isolate the test gas from the noise being generated at the primary diaphragm station [100]. However, in this case, the shock tube test gas is still under-tailored with respect to the secondary driver gas, where the new source of noise could be the rupturing of the secondary diaphragm. This explanation, however, does not clarify why the standard, no secondary-driver condition, which is naturally over-tailored, still shows a significant amount of noise.

3.8.2 Scaled condition: under-tailored

Condition x3s582 is under-tailored with respect to the primary driver gas with a ratio $\frac{a_2}{a_3} = 0.93$. well below the recommended threshold of 1.25 to achieve useful acoustic buffer levels [100]. Experiments have been carried out with and without the secondary driver, and inlet results are described in Fig. 3.12. Indeed, comparing Fig. 3.13 with Fig. 3.12, the overall level of the disturbances is significantly increased, even taking into account the doubling of the baseline pressure. Although not reported here, the shock speeds do not increase in the shock tube, and marginally increase in the acceleration tube (in the order of 150 $\mathrm{m\,s^{-1}}$). Figure 3.13 shows the plots with time-varying cone

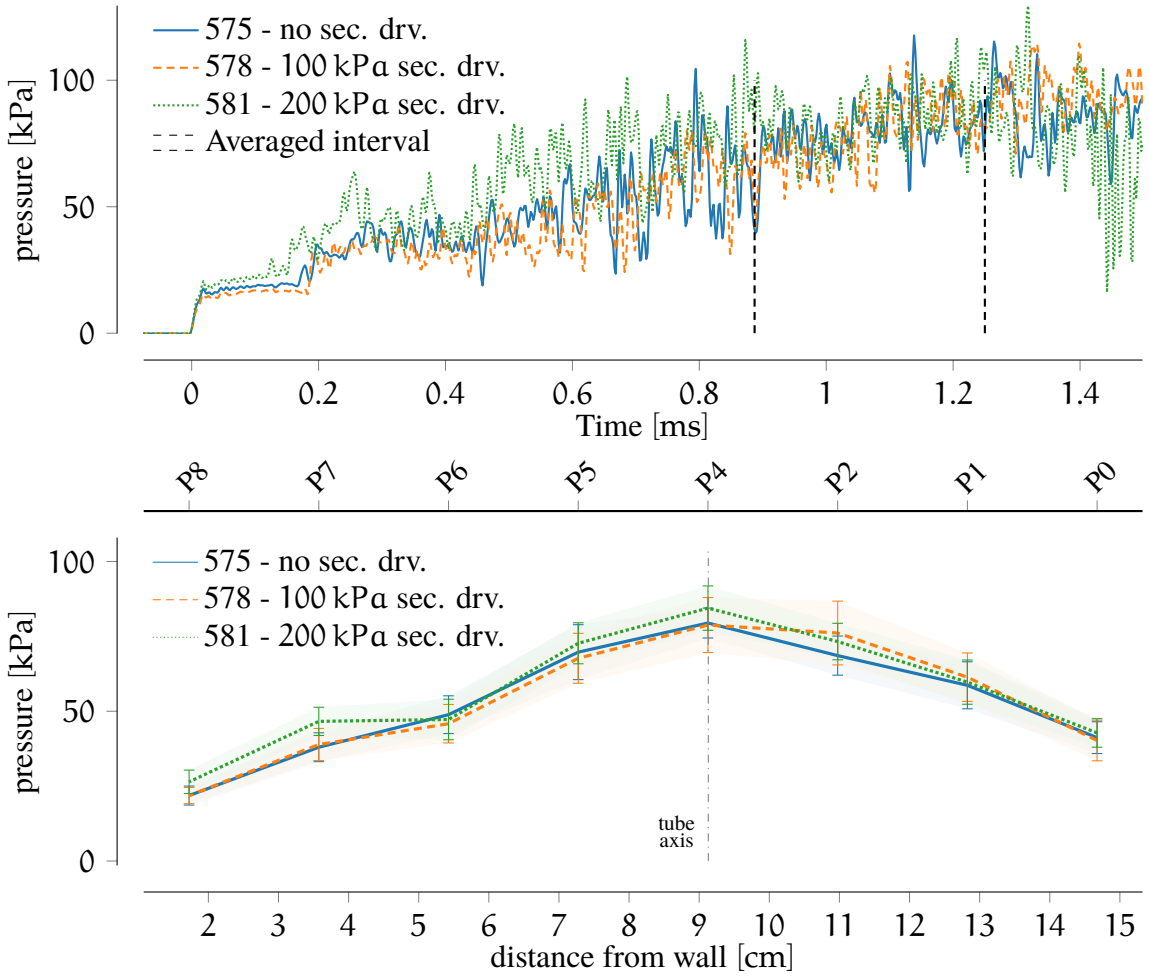

Figure 3.12: Inlet cone-pressure rake comparison for the secondary-driver experiments: CONDITION x3s506. In the top plot, the time-varying pressure trace P4 at the tube centreline is shown. In the bottom plot, aggregated pressure averages and relative uncertainties are plotted for all the probes along the rake. The averaging period is indicated in the top plot between the vertical black lines. Refer to Table 3.7 for full details.

pressure traces and averaged/aggregated rake data. In the figure, it is clear that the secondary driver, even for this under-tailored case, does not significantly improve flow disturbance levels. If anything, the noise amplitude in the experiments with the secondary driver is actually increased.

3.8.3 Summary

To conclude, in this section we have explored the use of a secondary driver for the two Mach 12 conditions. One condition presented an over-tailored speed of sound ratio, while the second did not. However, no performance increase has been observed, and no noise reduction has been identified for all the experiments. For these reasons, a secondary driver was not employed for any conditions in these scramjet experiments.

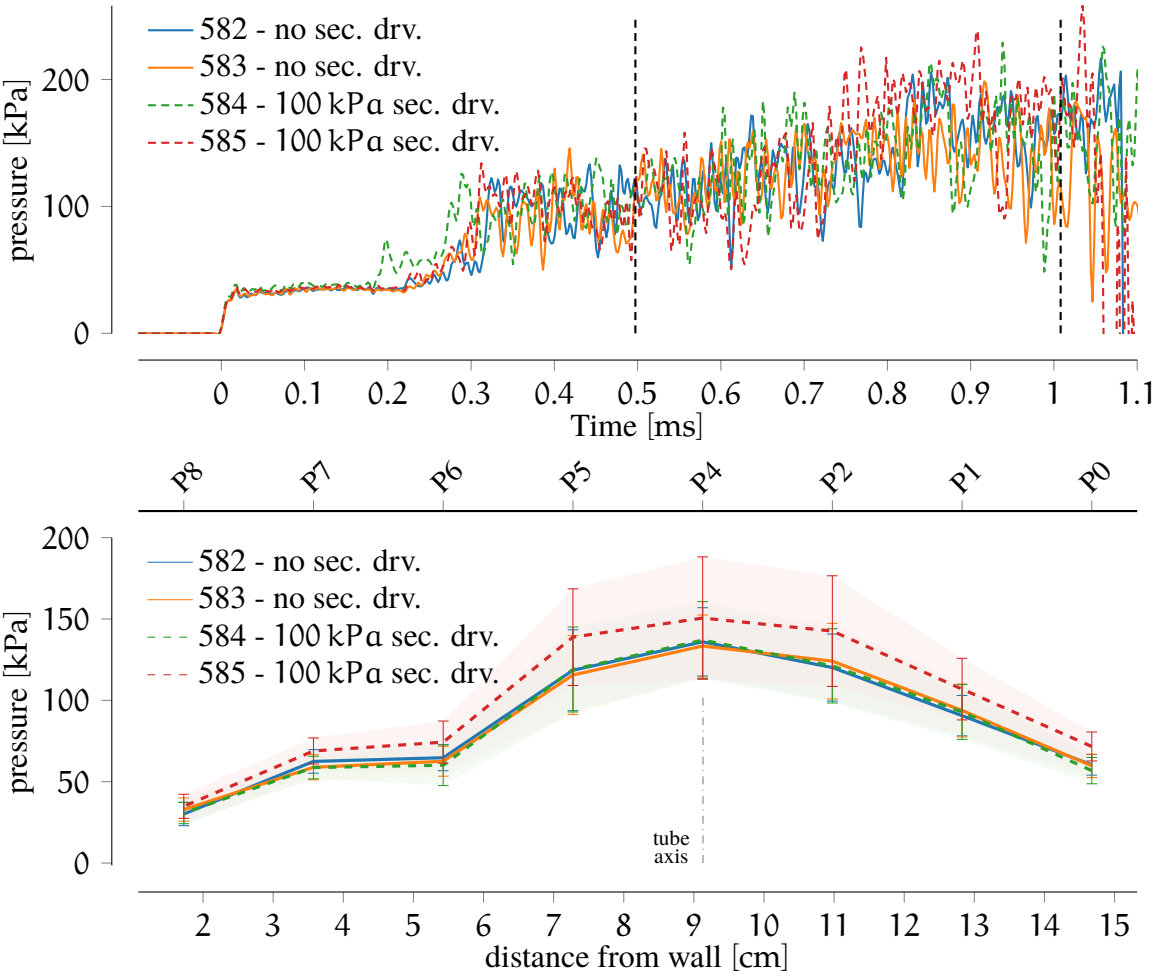

Figure 3.13: Inlet cone-pressure rake comparison for the secondary-driver experiments for scaled pressure Condition x3s582. In the top plot, the time-varying pressure trace P4 at the tube centreline is shown. In the bottom plot, aggregated pressure averages and relative uncertainties are presented for all the probes along the rake. The averaging period is indicated in the top plot between the vertical black lines. Refers to Table 3.7 for full details.

3.9 DIAPHRAGM SCORING

One of the biggest drawbacks of expansion tubes consists of the fact that diaphragm debris of significant sizes can hit the model in the test section. Other facilities, such as RSTs, are also characterised by diaphragm debris impacts where, despite the nozzle throat, small fragments can still hit the models. However, in expansion tubes there are no obstructions between the primary diaphragm station and the nozzle exit, and as such, there is a direct line-of-sight between both primary and secondary diaphragms and the models in the test section. Mylar (secondary diaphragm) and steel (primary diaphragm) debris have shown to impact and significantly damage models. Prior to this study X3 was operated with unscored diaphragms, and significant damage was done to probes, sharp leading edges and blunt bodies. Indeed, the diaphragm bursting process, although consistent in rupture pressure, created some random rupture patterns that sometimes caused large diaphragm chunks to separate and fly into the test section.

With the perspective of testing a M12REST engine, which relies on a sophisticated inlet shape formed by sharp leading edges to successfully operate, and considering that only a single, expensive, aluminium model was available, it was decided to investigate and improve facility operation by adopting scored diaphragms. Indeed, it is well-known from fracture mechanics that cutting a groove of sufficient depth into a diaphragm allows a repeatable and consistent opening pattern. Scoring diaphragm is a well-known and reliable technique to facility the bursting process, as shown in [174]. In Fig. 3.14 a comparison between the previous unscored diaphragm and the final scored diaphragm after rupture is shown.

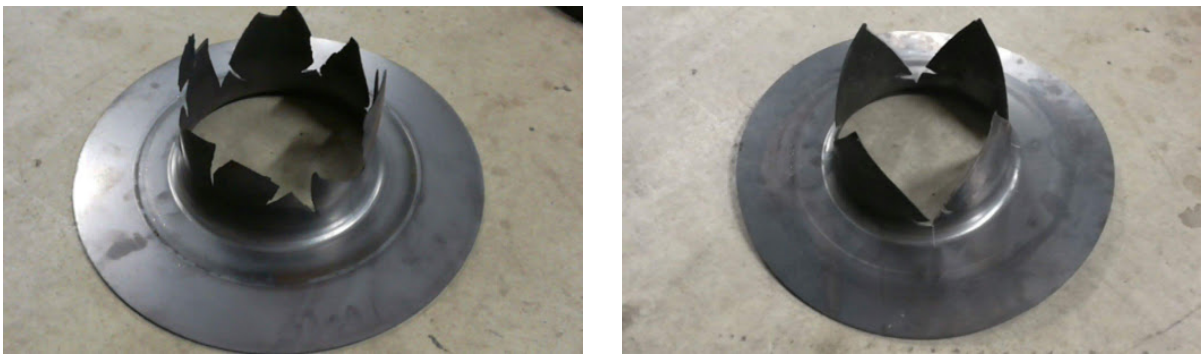

(a) X3 unscored diaphragm after rupture.

(b) X3 scored diaphragm after rupture.

Figure 3.14: Comparison of X3 3 mm steel scored and 2 mm unscored diaphragms after rupture. Note the random fracture pattern that occurs in the unscored diaphragms.

Since the piston operating conditions used in this study were established before any scored diaphragms were tested, the goal was to find a diaphragm thickness and a scoring depth/shape combination that would produce the same driver performance as the unscored diaphragm.

The process, outlined below, can be considered in two parts: the first, identification of a reliable technique to cut a repeatable and consistent groove; and the second, identification of an equivalent scoring depth of a thicker diaphragm to obtain the same rupture pressure.

In X2, the smaller expansion tube, a manual tool that cold-presses a groove in the diaphragm is used. However, this setup was too small, and could not fit the 425 mm diameter X3 diaphragm. Additionally, past experience showed that this manual process was inconsistent. Therefore, this option was discarded, and precision-machining options were examined.

After several iterations, an excellent setup was found, shown in Fig. 3.17, using a double/equal angle cutter wheel (diameter 100 mm, angle 60°). This cutter wheel allows a precise and reliable scoring, with negligible variation between diaphragms. Other tools led to inconsistent scoring depths, required a setup either too complex or too time-intensive to repeat for each diaphragm.

To identify an adequate scoring depth, a direct experimental approach was undertaken. Diaphragms were scored and directly tested in X3 at the target piston and operating condition, by doing a complete experiment. Compression tube (CT) pressure traces were recorded and shock speeds were compared.

It was acknowledged that direct X3 tests could damage the buffer system, but the tested condition was relatively mild for expansion tube standards (100 % Argon) and the buffer system is designed to prevent any permanent damage to the driver for the worst impacts anticipated for these experiments. Moreover, direct testing is the only option for reliable dynamic pressure tests.

Table 3.8: Facility operating parameters for the initial diaphragm scoring tests. CONDITION x3s518 operates with a short shock tube.

Condition	Shot n.	Piston condition	**Diaphragm**	Shock tube Air [kPa]	Acc tube Air [Pa]
x3s518	540 541 542 543	49 kPa 100 % Ar	2 mm unscored 2 mm 0.3 mm score 3 mm 0.5 mm score 3 mm 0.4 mm score	22.7	58.0

Table 3.8 shows a summary of the initial series of tests done to produce an equivalent scored depth that replicates the unscored diaphragm rupture pressure. Starting from an unscored diaphragm, the scoring depth was progressively tuned until the intended CT pressure traces were successfully reproduced as shown in Figs. 3.15 and 3.16. It can be seen that in 4 shots a strong match for both metrics was obtained. As expected, in the process nylon buffers were initially destroyed, and in following shots continued to suffer damage, but no permanent damage to metallic parts was caused. A comparison to the numerical flow reconstruction is carried out in Chapter 5, and more specifically, in Figs. 5.23 and 5.26.

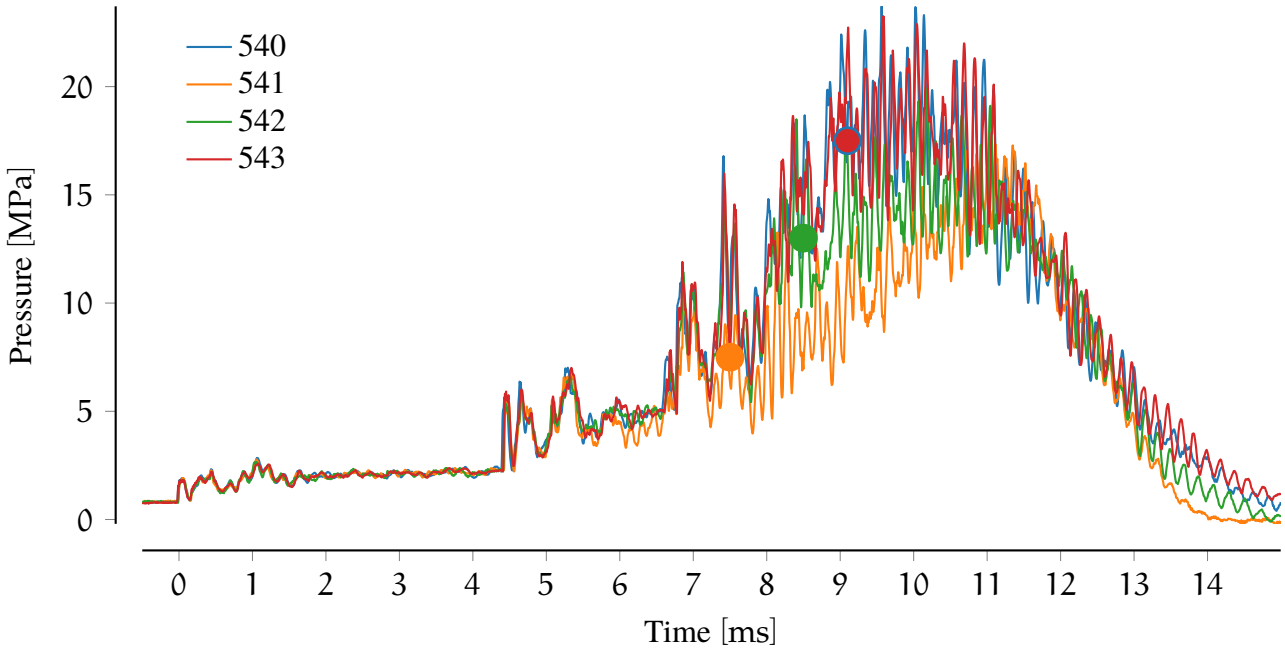

Figure 3.15: CT pressure trace with different diaphragm and scoring thicknesses. CT pressure sensor is located 0.2 m upstream of the primary diaphragm. The round markers indicate the estimated rupture pressure in the corresponding experiment. Final scored experiment (543) overlaps with the original unscored (540) experiment.

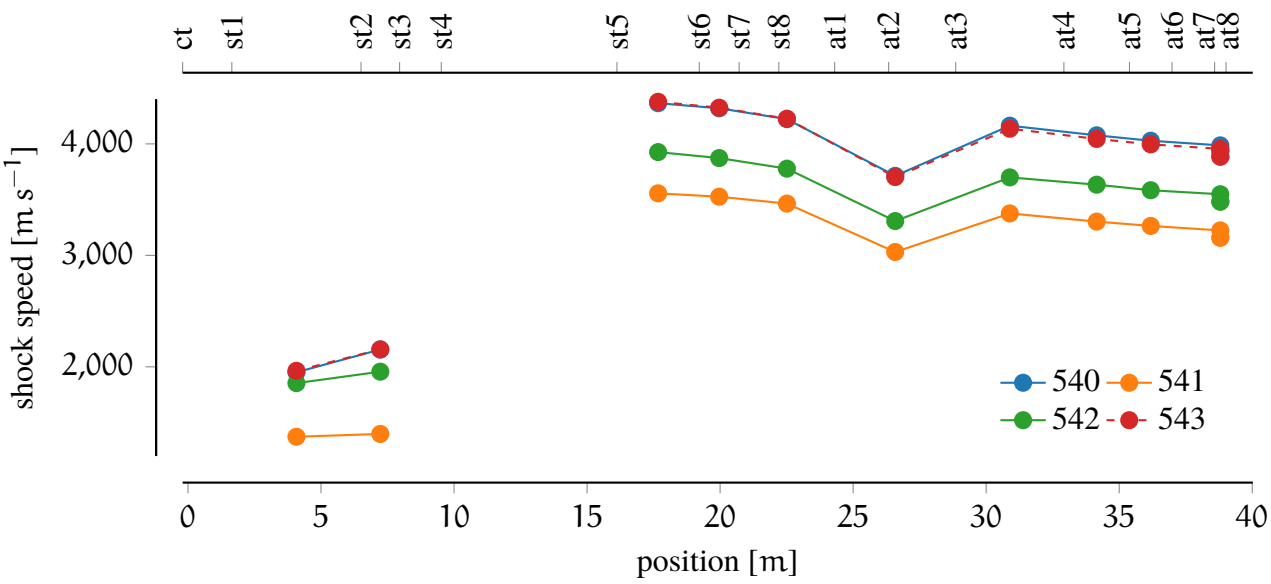

Figure 3.16: Shock speed variation with different diaphragms and scoring thicknesses. Final scored experiment (543) overlaps with the original unscored (540) experiment. Refer to Table 3.8 for complete details.

In the initial run of experiments, it was determined that the equivalent combination to match the 2 mm unscored diaphragm was a 3 mm diaphragm with a scoring depth of 0.4 mm. However, the scoring depth is highly dependent on the steel properties of the diaphragms. It has been observed that the subsequent batches of steel employed during the experimental campaign exhibited variability, and that each batch required a couple of experiments to tune the scoring depth. In Table 3.9, for future reference, a complete specification of the most current batch of steel is shown. If care is taken in sourcing steel with the same specs, the required scoring depth should not change.

Material specification	AS/NZS 1594 - HA350
Thickness	3 mm
Supplier	BlueScope
Heat Certificate	D31265
Yield	385 MPa
Ultimate tensile strength	530 MPa
Sample size	80 mm
Elongation	26 %
Scoring depth	0.3 mm
Cutting tool	Double angle cutter 60°

Table 3.9: Material properties for the steel diaphragm used during the scramjet experiments.

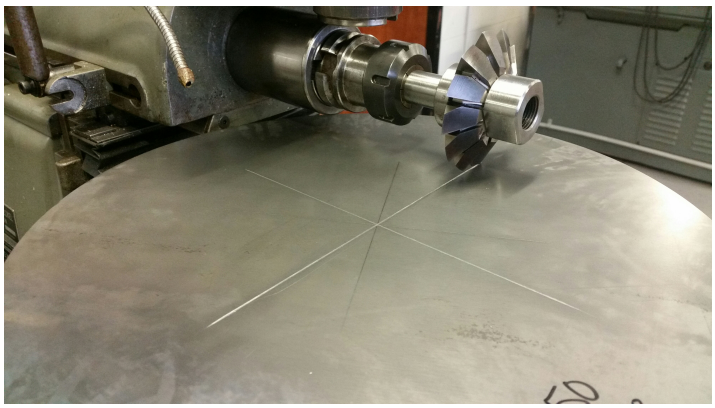

Figure 3.17: Scoring tool and setup

3.10 CONCLUSIONS

In this chapter two new operating conditions for the X3 expansion tube have been obtained, targeting a flow at Mach 7.5 at the nozzle inlet, the same condition that in the next chapter will be used to design the new Mach 12 nozzle. These two new conditions, called CONDITION x3s506 and CONDITION x3s582 were targeted to approximately reproduce nominal flight conditions at 36 km altitude at 50 kPa dynamic pressure, the former without considering any form of pressure-length scaling, while the latter applying a 2:1 scaling.

Shock speeds have been found to closely match analytical calculations, although a shock attenuation in the last part of the acceleration tube is observed. The slow-down is observed in other previously used flow conditions, such as the previous Mach 10 experiments. The author suggests that the slow-down is due its L/D ratio, which is quite high, so that viscous effects and boundary layer interaction reduce the speed of the shock and the flow travelling through the expansion tube.

The new flow conditions have been tested with both a long and short shock tube. It has been observed that, although the short-shock tube experiments have shown a significantly more expanded flow, and potentially much steadier pressure traces, the cone-head pressures are too low during the test time, suggesting that the test gas is collapsed in a mixture of accelerator, test and boundary layer gas at much higher temperature. This would be unsuitable for scramjet combustion testing.

A secondary driver has been tested to verify if it would be able to reduce the flow disturbances measured at the nozzle inlet. For both CONDITION x3s506 and CONDITION x3s582, the first over-tailored and the second under-tailored, no improvements in noise reduction have been noticed. It is suggested that at such low enthalpies, the noise production and focusing mechanisms are other than the ones proposed by Paull and Stalker [149].

Finally, X3 has been upgraded to operate with scored diaphragms. A new scoring methodology has been identified and tested. The new diaphragms have been shown to produce flow conditions with excellent repeatability, compared to the original, unscored diaphragms. It was observed that the material properties affect the required scoring depth, requiring fine-tuning the score depth for each new batch of steel sheet.

This chapter constitutes the ground-work for the following two chapters: in the next one, the design and manufacturing of a new Mach 12 nozzle will be discussed, whose inflow was the target flow condition previously discussed. In Chapter 5, the experimental flow condition obtained with the newly built nozzle will be presented, along with the hybrid numerical simulations carried out to fully characterise the experimental data.

4 A HYPERSONIC MACH 12 NOZZLE

4.1 PREAMBLE

Sections 4.5.5 and 4.6.2 are an extended version of parts of the paper P. Toniato et al. "Optimisation and design of a fully instrumented Mach 12 nozzle for the X3 expansion tube". In: *31th International Symposium on Shock Waves*. Nagoya, Japan: Springer, July 10, 2017

4.2 INTRODUCTION

As widely discussed in the previous chapters, expansion tubes are currently the only ground-test option for recreating the flow conditions required to achieve full freestream scramjet testing, or, to reproduce re-entry speeds. The unsteady expansion mechanism allows reaching hypersonic flows without the need for classical convergent-divergent nozzles, which are affected by driver gas contamination and nozzle throat erosion when used in reflected shock tunnels and arc-heated tunnels. In its basic arrangement, without a diverging nozzle, model sizes are, however, limited by the acceleration tube diameter, which for X3 is 182.6 mm. On the other hand, the total pressure capabilities are generally underused and to reach the full facility potential, a fully divergent nozzle can be added, to increase both test time and core flow diameter. Prior to this study, the X3 expansion tube already had a Mach 10 nozzle that was shown to be successful at producing flow conditions at Mach 10. However, its limited exit diameter and target Mach number made it unsuitable for higher Mach scramjet engines. Therefore, a new nozzle operating at Mach 12 became necessary. This chapter details its design and manufacturing process.

The chapter is divided in three parts: literature review, numerical design and nozzle manufacturing process. The interested reader can find a literature review on hypersonic nozzles and design methods *in the first part* of the chapter. *In the second part* we will introduce and discuss how expansion tube nozzles differ from classical converging-diverging nozzles, examine the methodology that has been adopted for nozzle design, and ultimately present the final profile. Off-design performances are investigated. *In the final part* of the chapter, we will review the manufacturing process and detail the actual outcome.

An experimental validation of this Mach 12 nozzle, along with a full experimental characterisation of the Mach 12 condition presented in Chapter 3 will be provided in the next chapter.

4.3 LITERATURE REVIEW ON EXPANSION TUBE NOZZLES

Supersonic (and later) hypersonic nozzles have comprehensibly been examined through the history of fluid mechanics and aerospace, initially to investigate supersonic flows for rocket engines. The first impulse facility that adopted a hypersonic nozzle was a shock tube used by Hertzberg [175] in 1951, where they produced a steady flow at Mach 4.3. The same author was the first to propose a theoretical addition of a hypersonic nozzle to expansion tubes [103], a concept that at the time was itself just being proposed.

Often in the literature an expansion tube with an additional nozzle is called *expansion tunnel*, as in Callis and Trimpi [176], where the authors carried out the first, perfect gas, analysis of the use of an expansion tunnel. The authors point out that the use of a nozzle downstream of the acceleration tube would lead to a theoretical increase in test time and higher acceleration tube pressure for an equivalent condition (therefore operationally easier to achieve). Callis [177] continued the work on exploring the use of area changes to mitigate boundary layer development and diaphragm opening problems. In this study, nozzles were placed after the primary diaphragm, or after the secondary diaphragm. Ultimately the configurations were rejected, and the author retained the one proposed in [176], where the nozzle is located at the end of acceleration tube. The same author [178] was the first to conduct an analysis for skimmer conical nozzles, where the boundary layer is bled away, theoretically providing uniform flows. He proposed a method that was able to generate nozzle contours that were shock free. In parallel, Norfleet et al. [179] experimentally tested an expansion tube with an abrupt area change at the secondary diaphragm, but they observed some significant flow disturbances that did not permit any form of testing. It is believed that they were simply running an under-tailored driver as described by Paull and Stalker [149].

The NASA Langley tube was the object of several studies for expansion tube nozzles. It was run with and without a nozzle [146]. A conical skimmer nozzle was used for these experiments, but Miller observed that the flow produced with a nozzle was not good enough, as the non-uniformities were significant due to shocks present at the nozzle exit. Therefore, he finally recommended the use without a nozzle. Leyva [180] used one-dimensional numerical codes to investigate area changes in different locations, and observed that area changes, both at the secondary diaphragm location and at the end of the acceleration tube, are a viable way of increasing the maximum model sizes in an expansion tube.

Sudnitsin [181] analytically investigate the use of a generic conical nozzle in the X1 expansion tube located at different locations, and identified the end of the acceleration tube as the most suitable one. Following experiments indicated suitable test times and core flows.

Korte [182, 183], while focusing on standard converging-diverging nozzles, proposed to couple an optimiser with a CFD solver to generate a nozzle profile that minimised certain properties at the nozzle exit, in order to work around the limitation of the MOC (method-of-characteristics) routines available at the time. Specifically, he coupled a non-linear least square optimisation procedure with a parabolised Navier-Stokes solver trying to minimise an objective function derived from certain

properties at the nozzle exit. The same approach was then adopted by other authors (see for example [184]) and it is often referred as "design by analysis" method. Korte's work constitutes the foundation for the method that has been historically adopted at the University of Queensland for the design of most of the supersonic and hypersonic nozzles used in reflected shock tunnels and expansion tubes.

Bakos et al. [185] applied the work of Korte for the design of a full capture nozzle for the HYPULSE facility for an exit diameter of 30 cm. Results showed an exit contour that was far from uniform, as well as discrepancies between expected and measured Pitot pressure profiles.

Craddock [186] was the first to adopt an optimisation process in designing nozzle profiles for the University of Queensland facilities. He used a Nelder-Mead simplex algorithm, coupled with the MB_CNS solver, to design an axisymmetric nozzle for the Drummond Tunnel, a small fixed volume driver RST, to operate at a target Mach number of 7.

In recent times, Chue et al. [134] carried out a thorough analysis and experimental validation of a hypersonic nozzle for the HYPULSE facility. The authors analysed both full capture and skimmer profiles for a target high-enthalpy condition. Importantly, they noticed that the standard method-of-characteristics (MOC) approach, with and without boundary layer (BL) correction, was not sufficient to achieve uniform exit flow for expansion tube flows. They noted that skimmer profiles do not significantly produce a uniform flow at the nozzle exit, as there is a compression wave generated at the nozzle inlet that propagates through the nozzle into the exit profile. In the quest for a better nozzle profile, noting that the main cause of flow non-uniformities are compression waves, they studied full capture profiles that, however, were always diverging. They finally proposed a hyperbolic profile with no inflexion point, allowing a shock free, although quite divergent, flow. The work is in principle very similar to the one that will be presented in Chapter 4, but in practice is subtly different. The focus of their work was to develop a nozzle dedicated to simulating re-entry conditions, and their focus was on Pitot pressure instead of Mach number, pressure and flow exit angle. Thus, the metric that they used — exit Pitot pressure flow uniformity — was very different to the one that will be adopted in this thesis.

The LENS facilities at CUBRC has shown to be working with hypersonic nozzles [187], although little information can be found on the work that has been carried out in those facilities. Nompelis et al. [188] carried out a numerical analysis for the LENS XX facility, where the use of a nozzle is discussed, but no mention on how the nozzle was designed can be found in the literature.

Scott [157] in his PhD thesis designed and developed a hypersonic nozzle for the X2 expansion tube, and it represents the groundwork on which the X3 Mach 12 nozzle developed in this thesis has built upon. He designed a full capture nozzle, 1.4 m long, with an inlet diameter of 85 mm to an exit diameter of 201.8 mm for operating at Mach 10. Although some discrepancies were found between the expected and the experimentally measured outflows, his most important findings were the experimental results showing that the addition of a nozzle approximately doubled the available test time at the nozzle exit for X2. The proposed mechanism increasing test time was an interaction between the boundary layer growth and the flow expansion process, which counteract each other.

Chan et al. [189] over several years followed Craddock's approach, designing three supersonic nozzles, for Mach 4, 7 and 10, for the T4 reflected shock tunnel, coupling a space-marching version of the RANS CFD solver Eilmer3 [190] with a Nelder-Mead optimiser. In subsequent years these nozzles have been validated experimentally and variation in the exit Mach number and flow angularity are less than 2 %.

Finally, Davey [158] designed a scaled-up version of the X2 nozzle for X3 by simply scaling the profile to match the X3 acceleration tube diameter at the nozzle inlet, therefore targeting the same inflow and outflow condition, and validating the scaled geometry in Eilmer3. The Mach 10 nozzle has a final exit profile of 440 mm and a final truncated length of 2.5 m.

4.4 PECULIARITIES OF EXPANSION TUBE NOZZLES

Hypersonic nozzles for expansion tubes, although operating on the same principles of classical convergent-divergent supersonic nozzles, and while often limited by the same factors such as undesired compression waves, are characterised by additional considerations:

- Expansion tube nozzles do not have a throat, but they are purely diverging.
- The nozzle inflow inlet plane is already hypersonic and, for the standard conditions being employed in the UQ X2/X3 facility, the Mach number is 7 to 7.5, as opposed to subsonic or low-subsonic for nozzles with choking throats.
- The flow is highly non-uniform, as shock waves, diaphragm rupture and other flow processes have been interacting with the flow, and each other, upstream of the nozzle inlet.
- The flow has earlier travelled along the expansion tube, promoting the growth of a thick boundary layer, which reaches the nozzle inlet with varying thickness with time.
- The length of test-gas slug is relatively short compared to the nozzle overall length.
- The inflow properties are intrinsically unsteady.

Overall, this kind of nozzle is highly susceptible to shock formation and prone to flow disturbance generation due to expansion/compression waves that originate in the flow "straightening" process. Additionally, the extremely thick boundary layer is such that interaction with wall boundaries is non-trivial, and classical methods for nozzle design cannot be applied.

These specific factors need to be taken into account in the design process whenever possible. If not possible, these have to be accepted as an inherent limitation in expansion tube nozzle design. For example, it is currently not practical to account for a time-varying boundary layer thickness within the optimisation design process, even more so for large-scale facilities like X3. Simulations and optimisation time would be unacceptably high. Given these limitations, many types of nozzles have been proposed over the years, which are now discussed below.

4.4.1 Skimmer nozzles

A skimmer nozzle is a type of nozzle that tries to minimise the boundary layer effect on the impact of flow quality and uniformity, by having an inlet diameter that is smaller that of the acceleration tube. Skimmer nozzles attempt to bleed the boundary layer away, theoretically providing a more uniform flow into the nozzle [157]. Another possible advantage can be found in the delayed boundary layer transition at high Mach number, thus reducing the final boundary layer thickness. The drawback of this nozzle is the shock system that is generated by the skimmer inlet leading edge. It disrupts the flow, with a cascade effect over the quality of the exit flow profile. Even when shocks are weak, formation of compression waves is always observed, as shown by Chue et al. [134]. Finally, because of the reduced inlet diameter, the expansion ratios are necessarily bigger, thus producing either a lower exit pressure or a smaller exit cross-sectional area available for the models.

4.4.2 Full capture: conical and contoured nozzles

The alternatives to skimmer nozzles are full capture nozzles, where the entirety of the acceleration tube flow is ingested in the nozzle. Nozzle contoured profiles are defined such that they are able to cancel and/or significantly reduce compression waves to achieve uniform flows. At off-design conditions, they are more prone to generating non-uniformities, as all the disturbances are focused on the nozzle axis. On the other hand, conical nozzles are much simpler to design and build. They produce a less uniform flow with a marked angularity, although they would not show a significant performance decrease at off-design condition [134, 157].

The analysis carried out by Chue et al. [134] showed that the disadvantages of the skimmer nozzle outweigh the advantages, and full capture nozzles were recommended for future development. Scott [157] developed a contoured nozzle for the smaller-scale X2 expansion tube, which has been shown able to operate at a variety of on-design and, more importantly, off-design conditions. Thus, for this study, a full capture contoured nozzle design has been chosen.

4.4.3 Test time increase

Another fundamental feature of expansion tube nozzles is the experimental observation that, contrary to a common-sense expectation, they are capable of increasing the available test time at the nozzle exit. Scott [157] purposely built and tested a hypersonic nozzle and experimentally verified the test time increase. It is of vital importance for the scramjet test of this thesis, where test times are of the same order of magnitude as the flow establishment times, that the mechanism is effective.

4.5 DESIGN METHODOLOGY

There has previously been extensive work on nozzle design methods, especially focused on supersonic nozzles for use in rockets or missiles, and this history has been discussed in Section 4.3. Traditionally, the majority of nozzles have been designed using the method-of-characteristics, as firstly developed by Prandtl and Busemann [99], a technique that assumes inviscid flows. This profile then would be corrected to account for the boundary layer thickness, which at increasing Mach number is more and more significant. The boundary layer correction implicitly assumes that the core flow and boundary layer are independent of each other. This is not correct when the boundary layer is a significant part of the exit flow, as the acoustic waves (u+a and u-a waves) are not reflected at the nozzle wall (as it would be in the inviscid case) but away from it, due to the shear stresses in the boundary layer, as shown in [191], where the MOC/BL method is not able to generate uniform flow above Mach 8.

The method originally developed by Korte [183] overcomes the limitation by coupling CFD solvers (originally parabolised Navier-Stokes equations) with optimisation methods that would attempt to minimise an objective function derived from relevant performance parameters. This method can be applied to a variety of different designs and is limited only by the accuracy of the CFD solver that has been adopted, along with the capability of the optimiser to find the global solution.

The method used in this thesis is the one mentioned above, coupling the Reynold-Averaged Navier-Stokes CFD solver Eilmer3 [190] with a modified, parallel version of the Nelder-Mead optimisation algorithm [192] to produce a flow that minimises the flow angularity and the difference between actual and target Mach numbers.

4.5.1 Eilmer3

The CFD solver Eilmer3 is an open-source program developed at the University of Queensland over the years, which solves the compressible Navier-Stokes equations for multi-block–structured 2D planar, 2D axisymmetric, and 3D grids. The solver is time-accurate, comprises Baldwin-Lomax and $k-\omega$ turbulence models, includes several thermochemical models, but also finite-rate chemistry for non-equilibrium flows. The code has been validated over the years for a variety of supersonic and hypersonic test cases. The solver is explicit and time accurate, therefore relatively slow compared to implicit codes. To accelerate convergence to steady state simulations in the case where the flow is mainly in one direction and there is little-to-no axial upstream feedback a block-marching mode, Nenzf-R, has been implemented on top of Eilmer3 [193]. Nenzf-R compensates for the lack of an implicit solver, and allows nozzle-simulations to complete relatively quickly.

4.5.2 Optimisation algorithm

Optimisation of computational fluid dynamics is a vast and very active topic. There are a variety of approaches and techniques that are available such as multi-objective, Pareto optimal algorithms, and adjoint shape optimisation methods (for example, see [194] for a review). Although the adjoint method (a technique to efficiently compute gradients) would be very suitable for this purpose, at the time of writing, to the author's best knowledge, there was no readily available CFD software supporting adjoint methods along with the hypersonic, turbulent, chemical reacting flows that are required for the nozzle optimisation. A newer version of Eilmer3 is currently (2018) being developed and it will include an adjoint solver for shape optimisation. It was outside the scope of this project to develop these techniques for the nozzle design.

The CFD nozzle design optimisation is a so-called *black-box optimisation* in which the optimisation algorithm is supposed to minimise an objective function $f(x)$ with no available detail other than the value $f(x)$ at any given point x. No information on the gradient/Jacobian or no assumption over the analytic behaviour or the form of the function are available. Additionally, for the nozzle design for the X3 expansion tube, the computational time for each evaluation is very expensive (in the order of few hours). These two constraints rule out the majority of available optimisation algorithms, as a suitable one needs to be a gradient-free method that is able to find a solution with relatively few evaluations. For these reasons, traditionally, for the nozzle designs that have been carried out for the UQ's facilities, the classical Nelder-Mead algorithm has been adopted [189, 195]. It is a proven method that has been shown to converge quickly to a global solution within a relatively small number of iterations and few CFD calculations [189].

A parallel Nelder-Mead optimisation algorithm

The UQ T4 facility nozzles that have been designed with the Nelder-Mead algorithm had a maximum length of 1 m. Therefore, compared to the desired X3 nozzle they are almost three times shorter and half the exit diameter [189]. Thus, the associated CFD calculations were several times quicker than those required for the X3 nozzle. Initial calculations for the new X3 nozzle showed that to obtain convergence, the optimisation would have required a few months to run. To overcome this limitation, a parallel, improved Nelder-Mead algorithm by Lee and Wiswall has been identified, implemented, tested, and applied to this nozzle optimisation process. The algorithm is explained in detail in Section 12.1.

In summary, in this algorithm the concept of the simplex as a replacement for descent-gradient estimation is retained along with the heuristic steps that allow the simplex to evolve. The key difference is that for any given degree of parallelisation p, the algorithm evaluates and replaces in parallel the worse p points (the reflection, expansion or contraction points), whereas in the classical Nelder-Mead only the worse point is changed at every iteration. As a consequence, the search path of the parallel version can be different from the serial one. For example, the reflection direction is necessarily different,

as only the best $n - p$ points are used for the centroid calculation. Theoretically, this could lead to better or worse convergence rate, but as shown in [192], the algorithm offers an overall wall-clock speed-up over the serial Nelder-Mead algorithm. The amount of speed-up depends on the function, and it varies from about $0.75p$ to $3p$, depending on the smoothness of the function around the solution.

Although no direct benchmark has been carried out for the specific nozzle profile optimisation problem, the following observations were deemed sufficient to adopt the Lee-Wiswall parallel simplex algorithm:

- Empirical observation that the objective function is relatively smooth.
- Ease of implementation.
- The algorithm is very similar to the proven Nelder-Mead algorithm.

4.5.3 Objective function

The optimisation design has as its objective the production of a nozzle profile that at its exit produces the target Mach number — in this case equal to twelve– and a target flow angle (always assumed to be zero) with a minimal variation. The two requirements can be expressed as follows:

$$f_\theta\left(\vec{X}\right) = \frac{1}{N}\sum_{j=1}^{N}\left(\theta_j\left(\vec{X}\right) - \theta_{design}\right)^2 \tag{4.1}$$

$$f_M\left(\vec{X}\right) = \frac{1}{N}\sum_{j=1}^{N}\left(M_j\left(\vec{X}\right) - M_{design}\right)^2 \tag{4.2}$$

Other flow properties, such as pressure or velocity were determined to be of secondary importance, and thus not considered amongst the optimisation objectives. A discussion on the choice of Mach number and exit flow angle is carried out in Section 4.6.5.

In principle, this is a multi-objective optimisation, as the two quantities are mostly unrelated. A multi-objective (Pareto-optimal) solution, on the other hand, would give a set of different solutions that are equally optimal, but with a different trade-off between Mach number uniformity and flow divergence. In this specific case the goal is to manufacture an optimal nozzle profile, and not to find all the possible solutions. As such, to simplify the approach, a classic linear scalarization has been applied to reduce the problem to a single objective optimisation. Opportune weights need to be chosen to reduce the two terms to a single expression. Although the choice of the weights is arbitrary, the experience with the design of previous nozzles at the Centre for Hypersonics has produced some recommended values [186, 189], as outlined below.

The optimisation function is therefore defined as follows:

$$f\left(\vec{X}\right) = \left(f_\theta\left(\vec{X}\right) + f_M\left(\vec{X}\right) + f_P\left(\vec{X}\right)\right)^2 \tag{4.3}$$

With f_θ, f_M, and f_P given by:

$$f_\theta\left(\vec{X}\right) = \frac{\phi_\theta}{N}\sum_{j=1}^{N}\left(\theta_j\left(\vec{X}\right) - \theta_{design}\right)^2$$

$$f_M\left(\vec{X}\right) = \frac{\phi_M}{N}\sum_{j=1}^{N}\left(M_j\left(\vec{X}\right) - M_{design}\right)^2$$

$$f_P\left(\vec{X}\right) = \begin{cases} Z_1 & x_i < 0 \\ 0 & 0 < x_i < x_{max} \end{cases}$$

where $\vec{X} = [x_0, \ldots, x_i]$ is the vector of Bezier points defining the profile (see Section 4.5.7 on page 89), ϕ_θ, ϕ_M weights, Z_1 a very large number, and where N indicates the number of cells in the radial direction that are inside the core flow. Following Chan et al. [189], the core flow is defined as the connected region in which $\frac{\partial M}{\partial r} >= -20$. f_P is a penalty term included to avoid an inwards nozzle contraction. The penalty function has been introduced after noticing that the optimiser tends to bend the last part of the profile inwards to improve flow redressing, which is undesirable as it introduces weak shock waves detrimental to the flow quality. Also, such a profile would make it difficult to make the nozzle by filament winding (see Section 4.7.3).

For this optimisation, we have defined the weighting parameters following the approach indicated by Chan et al. [189]. Specifically, the ideal goal was to generate a nozzle profile able to produce an exit flow Mach number that varies by less than 0.01 from 12 and a flow exit angle that is at most 0.02° in the core flow. These design targets were purposely extremely strict, and set in order to help the optimiser to converge. Therefore, we defined the optimisation parameters as follows:

$$\phi_\theta = \frac{1}{\tan 0.02} = 2.86 \cdot 10^3 \tag{4.4}$$

$$\phi_M = \frac{1}{0.01} = 100 \tag{4.5}$$

It is important to note that the choice is arbitrary, and it is definitely possible to obtain different nozzle profiles with different weighting parameters, as discussed later in Section 4.6.4.

4.5.4 Expansion tube nozzles: simplifying hypotheses

In Section 4.4 on page 80 the peculiarities that differentiate expansion tube nozzles from standard nozzles have been outlined. To simplify the optimisation problem, the following two assumptions are made:

- The inflow at the nozzle inlet, although assumed to be non-uniform (see Section 4.5.5 for details) has been assumed to be steady.
- Although the flow through the nozzle is predominantly unsteady, the optimisation has been carried out for steady state flow fields.

Those two assumptions were necessary, otherwise the computational cost of the optimisation, already very significant, would have become prohibitive. Additionally, optimising for a transient flow would introduce a series of questions such as how and when the quality of the nozzle output could be evaluated. Most importantly, it would require accurate CFD simulations of the full facility to obtain the transient inflow. Answering those questions would not be trivial, and surely out of the scope of this project.

4.5.5 Nozzle inflow

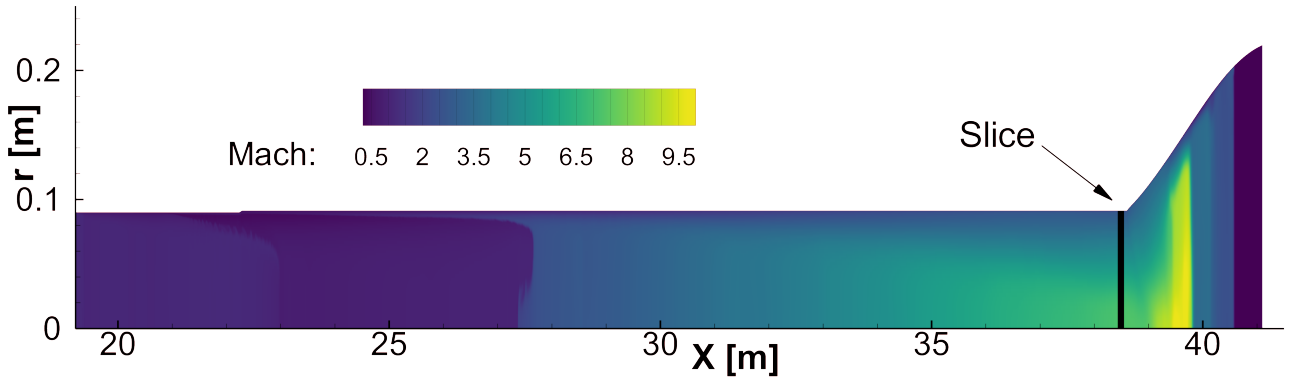

Figure 4.1: EILMER3 simulation of the X3 acceleration tube, used to estimate the boundary layer thickness at the nozzle inlet. Data courtesy of Gildfind et al. [129].

The flow in an expansion tube is time-varying and radially non-uniform, and full facility simulations are necessary to provide detailed insight into the nozzle inflow properties. At the time of this project, work towards full facility simulations of X3 was being carried out in a separate study (later published [129]), where hybrid simulations of a Mach 10 condition were used to estimate the flow through the acceleration tube and nozzle. These simulations, although done for a different condition, are similar to the intended Mach 12 condition. As shown in Fig. 4.1, the boundary layer thickness is significant and varies between 30 mm and 50 mm through the test gas. The relevance of the boundary layer is clear compared to the tube radius, 91.3 mm. In Fig. 4.2, a slice of flow properties at the axial location identified in Fig. 4.1 and at two different instants shows how the flow is varying in space and time.

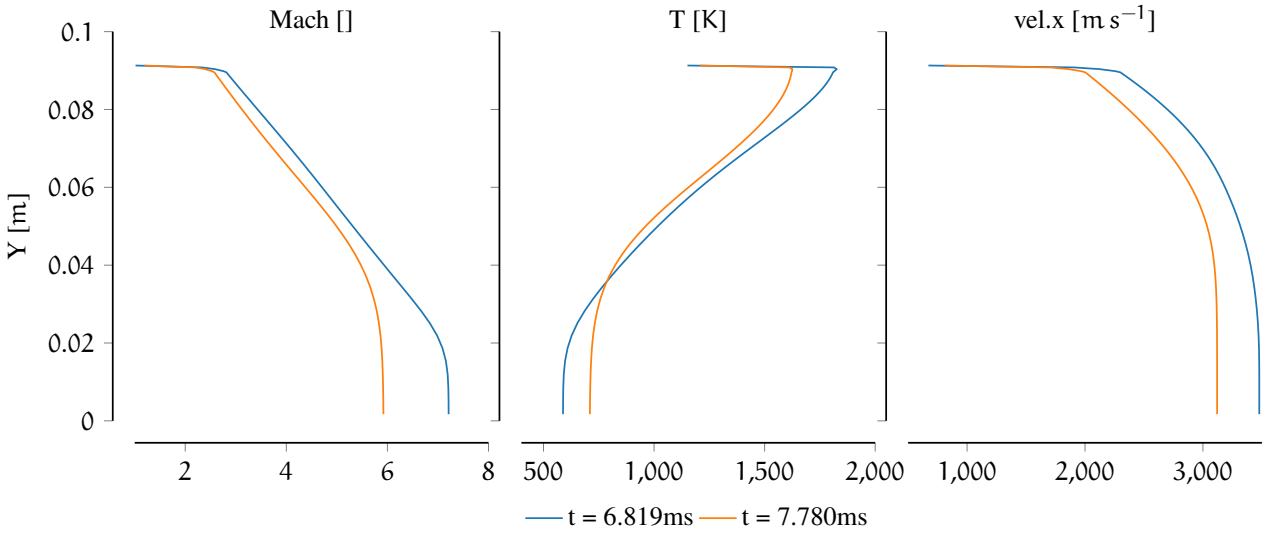

Figure 4.2: Flow properties of the test at two distinct instants on the slice shown in Fig. 4.1.

Table 4.1: Target flow conditions assumed **steady** inflow condition.

	Units	Value
p	Pa	10000
u	m s^{-1}	3650
T	K	600
M	[]	7.48
BL thickness	mm	30

The nozzle inflow has been computed assuming that the axial velocity follows a $\frac{1}{7}$ boundary layer power-law (i.e. fully turbulent) and that the boundary layer thickness is 30 mm radially. The inflow profile has been determined assuming an inflow pressure of 10kPa, constant across the radius. The velocity and temperature follow the boundary layer power law, and a summary of the profile is shown in Table 4.1. These values correspond to the flow properties presented in Section 3.4, originally chosen as the target facility operating condition, selected to closely reproduce the freestream design condition of the M12REST engine (dynamic pressure of 50 kPa at 36 km altitude).

In previous studies, the nature of the tube boundary layer of the expanded test gas has been found to be directly correlated with the test flow quality. It has been noted [88] that laminar boundary layers produce flows of good quality whereas fully turbulent ones produce lower but still reasonable flow quality. However, if the boundary layers are transitional, the quality is unacceptable. Prediction of hypersonic boundary layer transition in expansion tubes has been difficult to establish, with only a few correlations being proposed [74, 88]. The simplest method, often used at the HYPULSE facility, suggests that if the unit Reynolds number is larger than a critical value, $Re_l \geqslant 1.4 \times 10^6$ m^{-1}, the flow will be fully turbulent. Therefore, for the nozzle inflow condition shown above with $Re_l \approx 6.5 \times 10^6$ m^{-1}, the inflow is assumed as fully turbulent.

4.5.6 On the importance of the inflow

The inflow properties are the main drivers for the final nozzle shape. As stated in the sections above, ideally the optimisation routine should use a transient inflow boundary condition. However, at the time of this design it was not available, and for a nozzle of this size, would have in any case made the computation unachievable within an acceptable time-frame.

A boundary layer correction was introduced due to the lack of a transient profile. This correction is of fundamental importance and, if neglected, can lead to an analysis and conclusion that significantly differs from the desired result. The author has found that in the past several nozzle designs for expansion tubes did not include boundary layer corrections, for example in [95, 196].

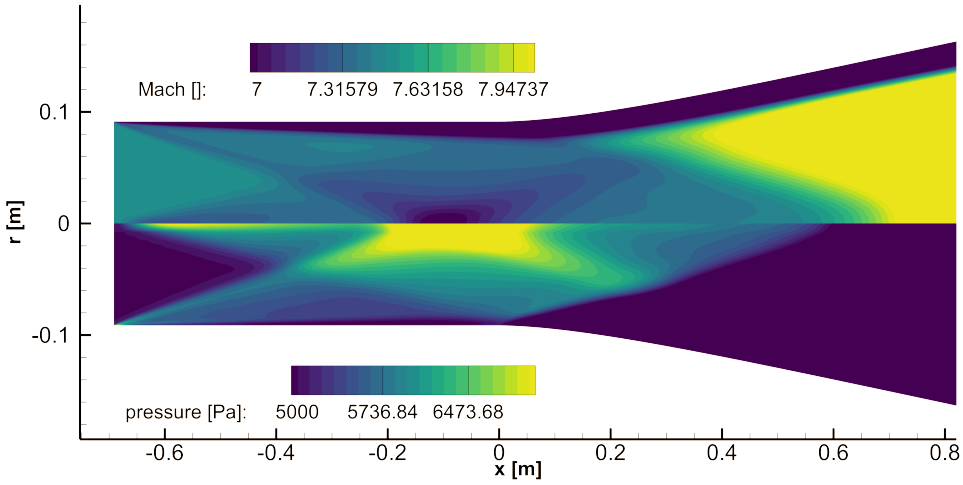

Figure 4.3: Effects of using a radially-uniform inflow with no boundary layer for nozzle designs. An oblique shock is generated at the inlet due to the no-slip condition, creating a strong disturbance at the nozzle inlet.

As it can be observed in Fig. 4.3, if a boundary layer profile for the nozzle inflow is not introduced, an oblique shock would propagate from the "initial" edge of the wall, with a focusing effect on the nozzle centreline. The centreline disturbance then would have a rippling effect downstream, on to the nozzle axis, where significant non-uniformities would be transmitted. The focused disturbance is so important that no nozzle profile would able to remove it, and the optimisation methods would need to be corrected trying to diminish its effect, such as, introducing additional terms in the objective functions penalising nozzle axis disturbances.

Wei et al. [196] introduced a correction term for the objective function. They tried to minimise the disturbances on the nozzle axis, and finally had to truncate the nozzle, as the obtained exit profile was not as uniform as desired. The simulation of that nozzle profile with a boundary layer corrected profile showed an actual over-expanded and non-uniform profile in terms of Mach number, a significantly reduced core flow size and poor flow exit angle.

In summary, the use of a boundary-layer-corrected profile is necessary for the design of a correct nozzle profile, and if neglected this, can lead to misleading results and under-performing nozzles profiles.

4.5.7 Nozzle profile modelling

The nozzle profile is described with a Bezier curve with eleven control points. Using a Bezier curve allows a smooth description of the nozzle contour, while retaining a small number of control variables. Additionally, it can be proven that the derivative of a Bezier curve is itself a continuous Bezier curve, thus ensuring that the changes are locally smooth, which is specifically important to produce shock free nozzles. The axial position of all the points was fixed and mildly clustered towards the initial part of the nozzle. The clustering was selected as it was expected that the bulk of the curvature would be in the initial part of the profile.

The first two control points are fully fixed, with their radial position set to the acceleration tube diameter ($r_{throat} = 182.6\,mm$). This ensures that the curve is also tangent to the acceleration tube profile. A description of the setup is presented in Fig. 4.4. For this study, the optimisation variables were the angles between each consecutive Bezier points $y_2, y_3, \ldots, y_{10}$. This choice was observed to help the convergence of the optimisation procedure [197]. Finally, the length was fixed and chosen at $2.8\,m$. Longer nozzles would enable a smoother flow expansion and smaller flow angle, but there would be a significant growth in boundary layer thickness, thus reducing the overall benefits. A longer nozzle is also heavier, and more complex to build. For these reasons, a compromise was reached to use a relatively short nozzle (with respect to the ideal inviscid nozzle, $4.5\,m$ long, according to the MOC analysis).

4.5.8 Simulation parameters

The boundary condition of the nozzle wall was set to isothermal with a temperature of $300\,K$, a reasonable assumption for expansion tube flows where the test time is around $1\,ms$ (therefore not allowing enough time for a significant change in temperature). The gas model used for the simulations was a thermally-perfect air with 5 species (N2, O2, N, O, NO). The Gupta finite-rate chemistry model was included in the simulation [198], although temperatures in the nozzle were relatively low and little difference was (a-posteriori) observed with or without the chemistry model. Two turbulence models were adopted. Baldwin-Lomax [199] was used in the first optimisation runs, while the $k-\omega$ turbulence model [200] was used for the final run. Turbulence intensity level was assumed to be 5 % and the ratio of turbulent-laminar viscosity of the inflow was set to 100. The simulations were carried out using Nenzf-R. However, given the significant size of this nozzle ($2.8\,m$) the simulation was still slow, as the block-marching code needed to physically "march" through the whole nozzle length.

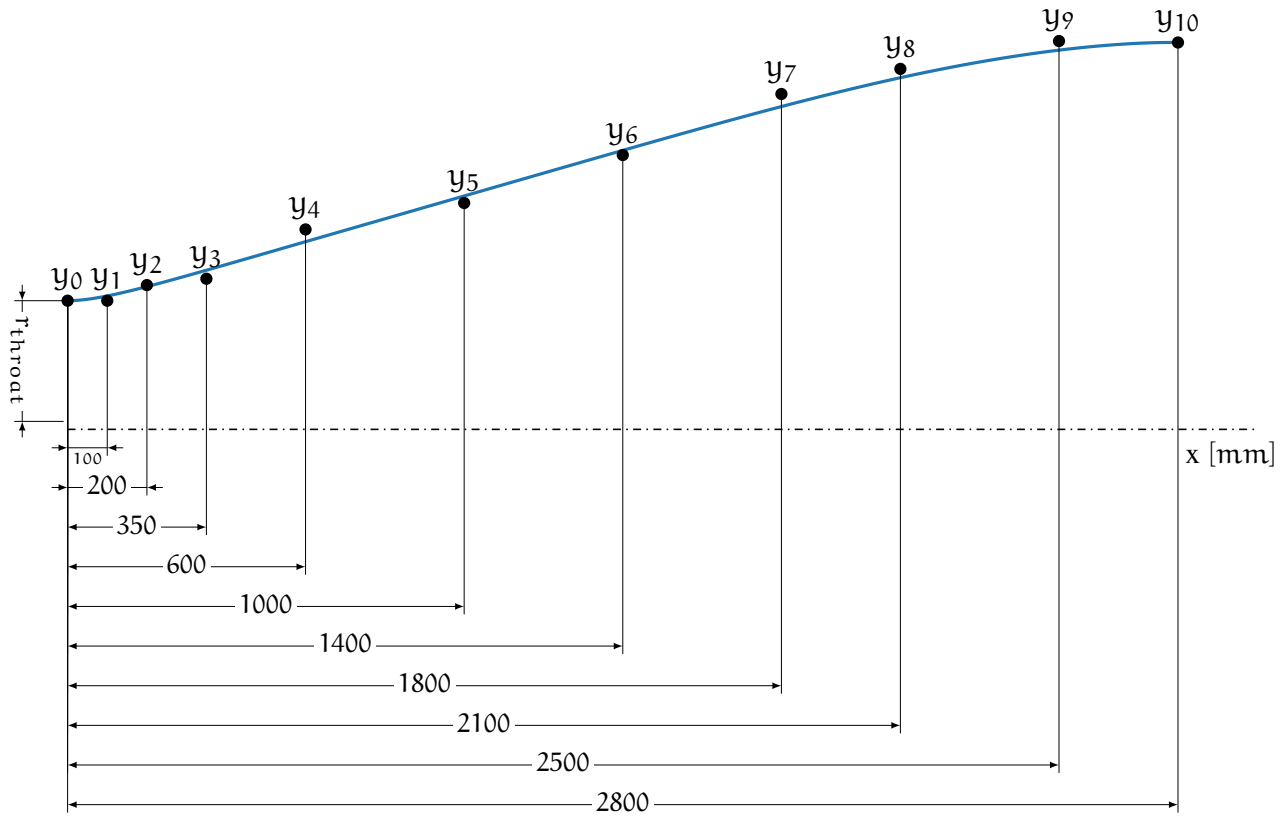

Figure 4.4: Layout of Bezier control points defining the nozzle profile.

As such, the solution time is directly proportional to the nozzle length. Thus, to further accelerate the solver, a modified implementation of the program was used. Normally, the grid is split in axial blocks and NENZF-R simulates two sequential blocks at the same time. The modified version further splits every axial block into 4 sub-blocks, allowing the underlying CFD solver, EILMER3, to operate in MPI mode.

4.5.9 Nozzle optimisation process

The parallel Nelder-Mead algorithm, described in Section 4.5.2, was implemented in Python and tested with several classical optimisation problems. Great care was taken into actually developing a fully deterministic, robust, and restartable implementation, such that every optimisation restart would be consistent. A templating engine was used to automatically generate the required CFD files to be simulated with NENZF-R, and every simulation was independently contained.

Several runs of the optimisation were carried out. Initially, a laminar profile was optimised. The Baldwin-Lomax turbulence model was then activated and another optimised profile was obtained starting from the approximation obtained for the laminar case. These runs showed that the whole set of programs were giving expected and consistent results. Finally, the $k-\omega$ turbulence model was used for the definitive run, along with a couple of restarts to effectively verify that the optimiser converged

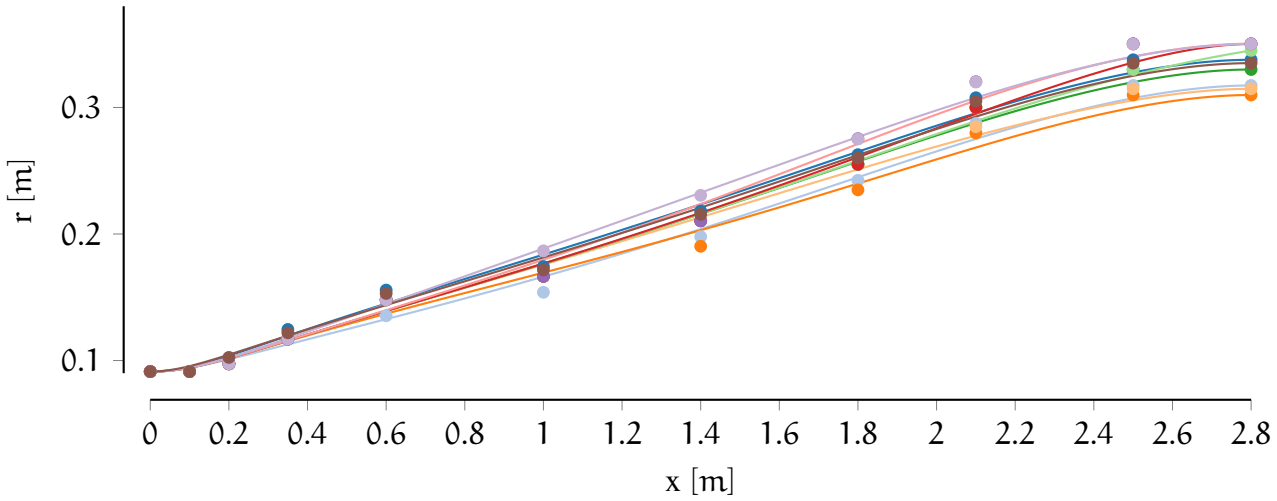

Figure 4.5: An example of the solutions explored by the optimiser at a single iteration.

to a non-local minimum. In Fig. 4.5, an example of an early simplex iteration algorithm is shown. All the different nozzle profiles presented in the figure are evaluated independently and in parallel by the optimiser.

4.6 RESULTS AND DISCUSSION

The final optimisation run evaluated 1897 different nozzle profiles and converged to the profile shown in Fig. 4.6. For a length of 2.8 m, the final exit diameter is 0.573 m wide. In the same figure, a comparison with the previous Mach 10 nozzle is shown. It can be observed that both nozzles are qualitatively similar, presenting an initial rapid flow expansion around the nozzle throat and then a gentle flow-redressing turn in the rest of the nozzle. In Table 4.2 the final Bezier points defining the nozzle profile are indicated for future reference.

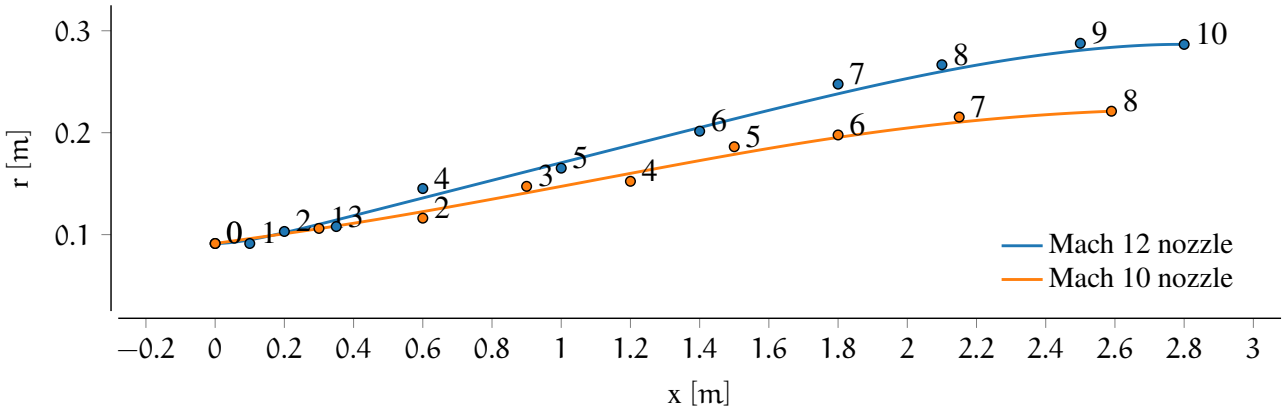

Figure 4.6: Mach 12 nozzle final profile compared to the original Mach 10 nozzle profile.

Table 4.2: Final Mach 12 nozzle profile Bezier points: radial position is indicated with the full precision that the optimisation routine used to define the curve.

x[m]	y[m]
0.0	0.091 300 0
0.1	0.091 300 0
0.2	0.103 102 3
0.35	0.107 916 1
0.6	0.145 204 7
1.0	0.165 220 3
1.4	0.201 490 2
1.8	0.247 666 6
2.1	0.266 650 2
2.5	0.287 716 4
2.8	0.286 618 9

In Fig. 4.7, final Mach number and contour plots are shown. It is important to note the continuous boundary layer growth that takes place at those speeds which inevitably limits the core flow. On the other hand, there are few to no disturbances in the pressure contours, thus indicating that the nozzle is essentially shock and disturbance free for the steady inflow.

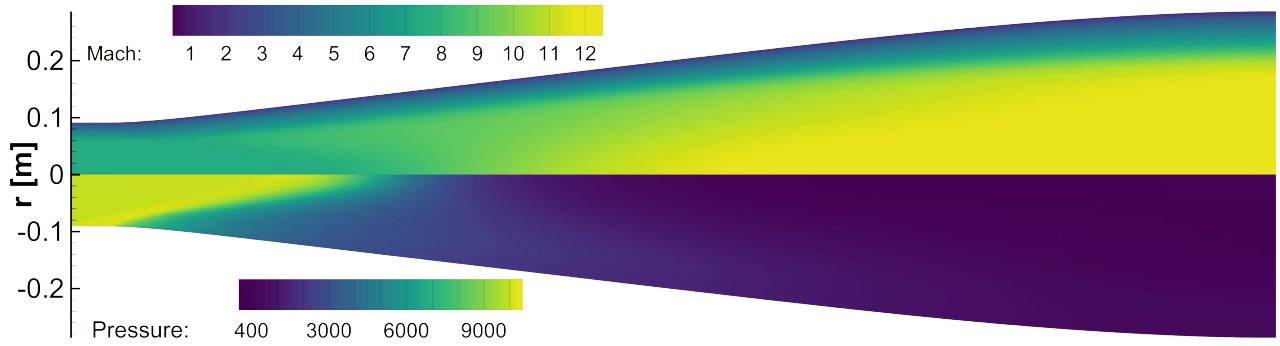

Figure 4.7: Optimised Mach 12 nozzle Mach number and pressure contours.

In Fig. 4.8 the flow exit profiles, in terms of Mach number, flow angle, and pressure, are shown. The figure presents an excellent result in terms of Mach number, with a core flow diameter exceeding 340 mm and an exit flow angle on average less than ~1°. Conversely, pressure presents a less satisfactory profile due to the re-compression effects that take place in the last 0.3 m, as a side effect of the flow redressing process. This is an expected result generated by the weights chosen for the different parts of the objective function, as the flow exit angle has been prioritised over pressure. The use of an additional weight term for the pressure profile homogeneity has been considered. However, as shown in Section 4.6.5, its use would be redundant and unnecessary. Specifically, if one were to optimise the pressure profile, in addition to having a detrimental effect on exit flow angle, it would create stronger waves forming at the nozzle exit edge, thereby reducing the total core flow diamond available for model testing.

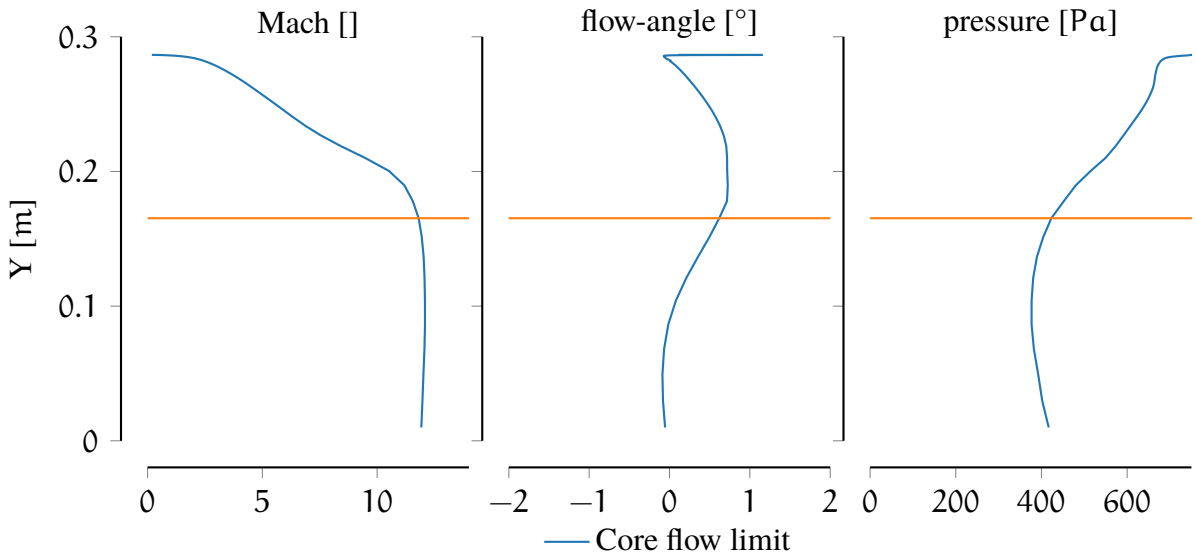

Figure 4.8: Mach 12 nozzle exit flow profile for pressure, Mach and flow angle.

4.6.1 Core flow diamond and eventual nozzle truncation

To validate the optimised profile, a thorough analysis of the final nozzle shape was carried out. In this section we discuss the effectiveness of the nozzle at producing a sizeable core flow diamond in the test section and the possible nozzle truncation.

The calculation of flow properties downstream of the nozzle exit are required to define the core flow diamond, i.e. to define the core flow size not only in the radial but also the axial direction. For these purposes, a generic grid modelling the volume available for expansion in the test section was prepared and connected to the nozzle profile, and CFD simulations were run. Results for Mach number, flow angle, and pressure are shown respectively in the top part of Figs. 4.9 to 4.11.

The core flow diamond in terms of Mach number extends well beyond the end of the simulated test section (which for ease of simulation, was selected as 1.5 m downstream from the nozzle exit). In terms of flow angle, a centred expansion wave develops from the nozzle edge, but is external to the Mach-defined core flow diamond. Similarly, the expansion wave is observed in the pressure contour plots, where the 425 Pa contour line defines an equivalent diamond in terms of pressure.

A possible nozzle truncation was considered. It was observed in previous nozzle designs (see for example [196]) that the boundary layer growth can overshadow the flow redressing capability of the second half of the nozzle. Thus, the last part of the nozzle can have little benefit, especially when the increased manufacturing cost and size is taken into account. Moreover, a nozzle truncation allows removing possible nozzle centreline disturbances that are generated by the re-compressing process in the second half of the nozzle. This was also the case for the nozzle proposed in [196].

A brief analysis was carried out to assess if any of the above motivations for nozzle truncation apply for the nozzle profile obtained in this thesis. The relevant results are shown in the bottom part of

Figs. 4.9 to 4.11. It is observed that, in the truncated case, in terms of Mach number there is little to no difference, whereas in terms of flow angle and especially of pressure, we can observe a significant reduction of the core flow diamond. Additionally, looking at the equivalent 2.8 m exit plane, where a model would be located, formation of strong adverse pressure gradients can be noted. Those pressure gradients are highly undesirable and further limit the usable core flow. Finally, no nozzle centreline disturbances were observed for this nozzle profile in either configuration. In summary, it was deemed that nozzle truncation was not necessary.

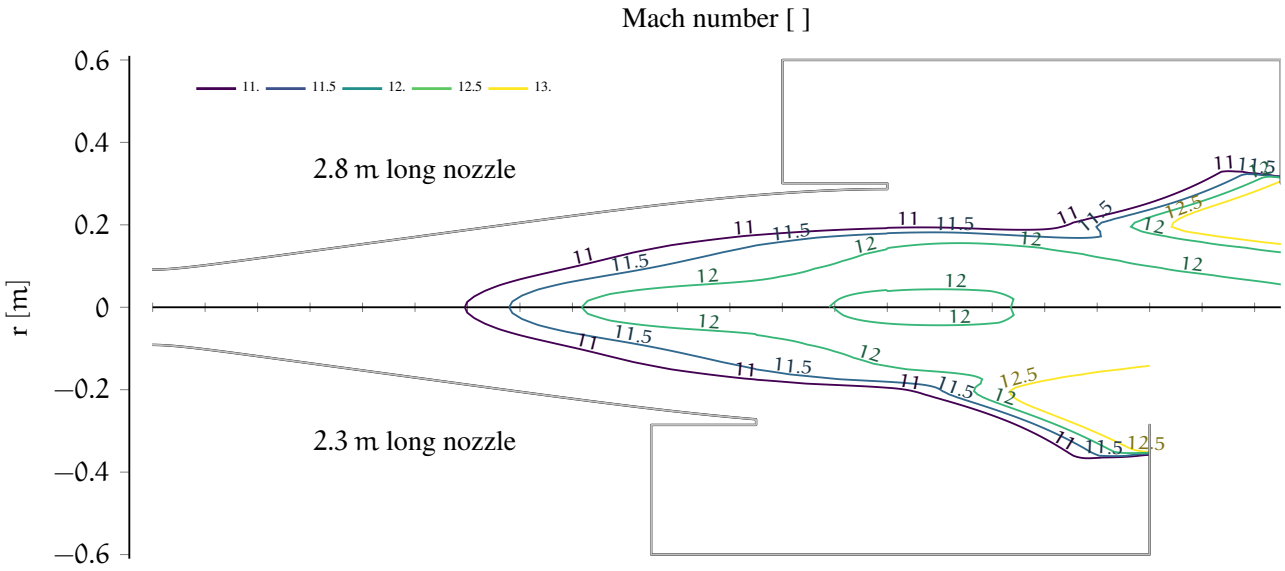

Figure 4.9: Mach 12 nozzle and dump tank Mach number contours at full length and truncated by 0.5 m. Simulated length of test section: 1.5 m.

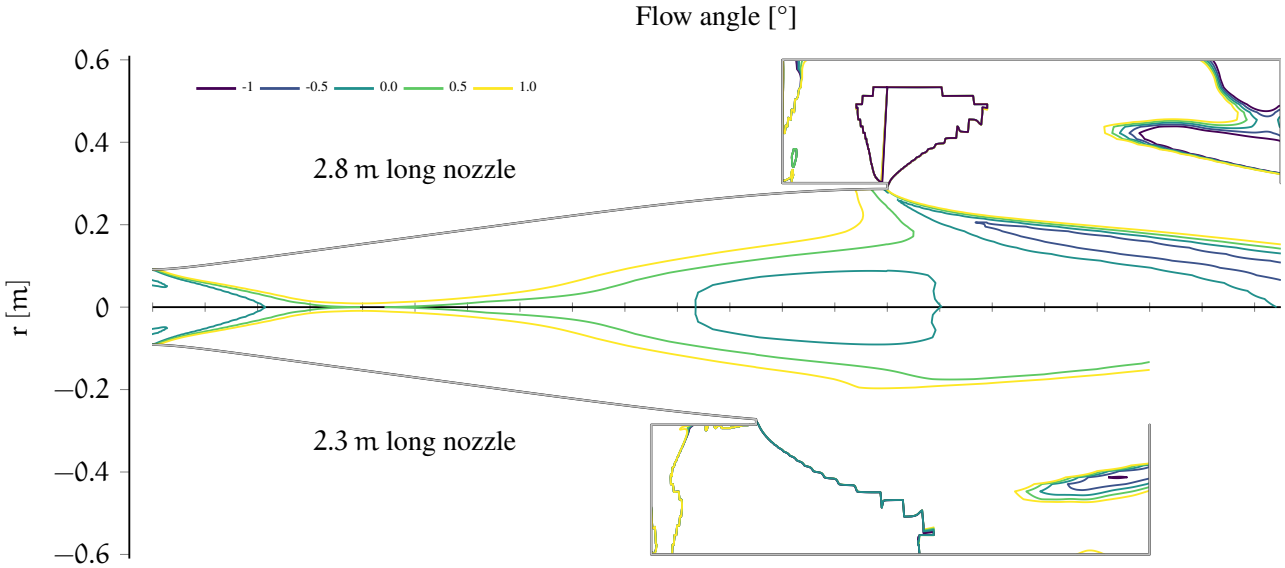

Figure 4.10: Nozzle and dump tank flow angle contours at full length and truncated by 0.5 m. Simulated length of test section: 1.5 m.

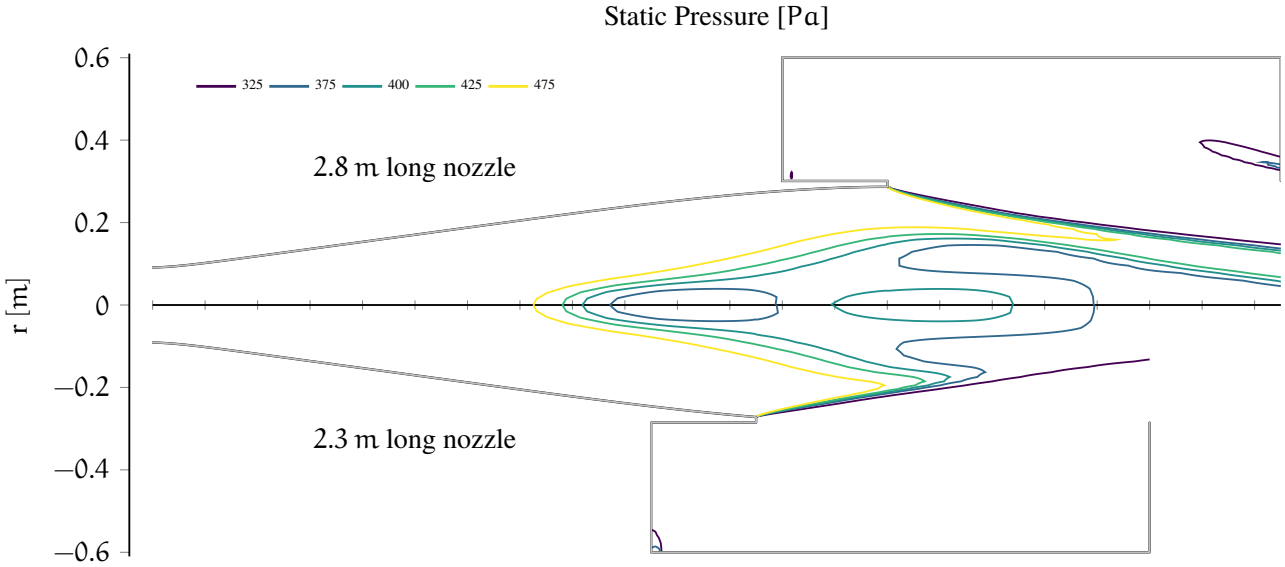

Figure 4.11: Nozzle and dump tank pressure contours at full length and truncated by 0.5 m. Simulated length of test section: 1.5 m.

4.6.2 Off-design performance

The nozzle was designed to target the specific Mach 12 condition (mentioned above), but it will often operate at off-design conditions in terms of Reynolds number and/or boundary layer thickness. A sensitivity study was therefore undertaken, and a detailed summary of the results is shown in Figs. 4.12 to 4.14. Inflow velocity, inflow Mach number, and boundary layer thickness were varied as stated below:

- Inflow velocity: [3000 $\mathrm{m/s}$, **3650 $\mathbf{m/s}$**, 4000 $\mathrm{m/s}$];
- Inflow Mach number: [7.0, **7.48**, 8.0];
- Boundary layer thickness: [0 mm, 10 mm, 20 mm, **30 $\mathbf{mm}$**, 40 mm, 50 mm];

where the original design condition has been highlighted in bold. The parameters were chosen in order to analyse off-design behaviour around the target condition and do not offer a comprehensive analysis for other flow conditions.

All the exit parameters are found to be insensitive to changes in inflow velocity. Exit flow angle is found to be largely invariant to the inflow properties with a maximal variation of $\pm 1°$ across the core flow. Exit pressure and exit Mach number exhibit a certain sensitivity to inflow Mach number.

If inflow Mach number is greater than 7.5 the gas is over expanded in the nozzle centreline, resulting in a less uniform core flow that significantly affects both pressure and exit Mach number. The design boundary layer thickness was 30 mm, but the analysis shows that acceptable Mach number exit profiles are maintained for any boundary layer thicknesses above 20 mm. With lower thickness, exit flow quality is significantly decreased. It is therefore recommended that for any off-design use of this nozzle, great care is taken to avoid any flow condition that would produce a Mach number greater than 7.5 at the nozzle inlet. The analysis, although carried out for steady state simulation, shows that the nozzle is expected to respond well to changes in the inflow condition, although future analysis needs to be carried out for the full unsteady flow conditions.

4.6.3 Transient behaviour and test time extension mechanism

The Mach 12 nozzle transient behaviour has been investigated and the test time extension mechanism is briefly described. The shock wave travelling in the acceleration tube slows down as soon as it enters the nozzle and the duct area increases. The acceleration tube/test gas contact surface also slows down, but by a reduced amount, so that the expanded test gas undergoes a further expansion. A reverse shock is then formed and travels upstream relative to the fluid (but is still going downstream in the laboratory reference frame), processing acceleration tube gas and test gas as it crosses the contact surface. The accelerator and test gas in between are both compressed and near the nozzle wall, ingested in the boundary layer. This compressed gas is responsible for the spike in Pitot pressure that is observed in the numerical and experimental traces.

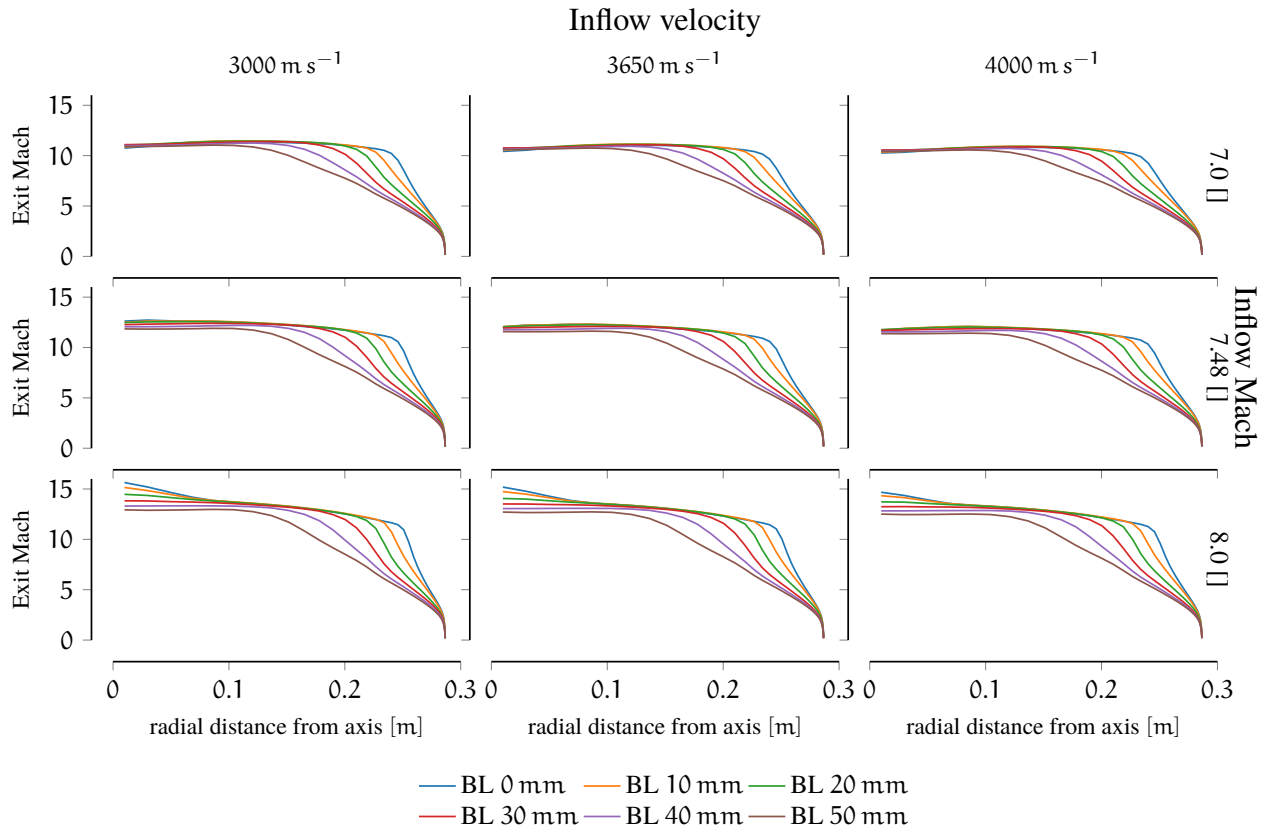

Figure 4.12: Nozzle exit Mach number for varying inflow Mach number, velocity and boundary layer thickness.

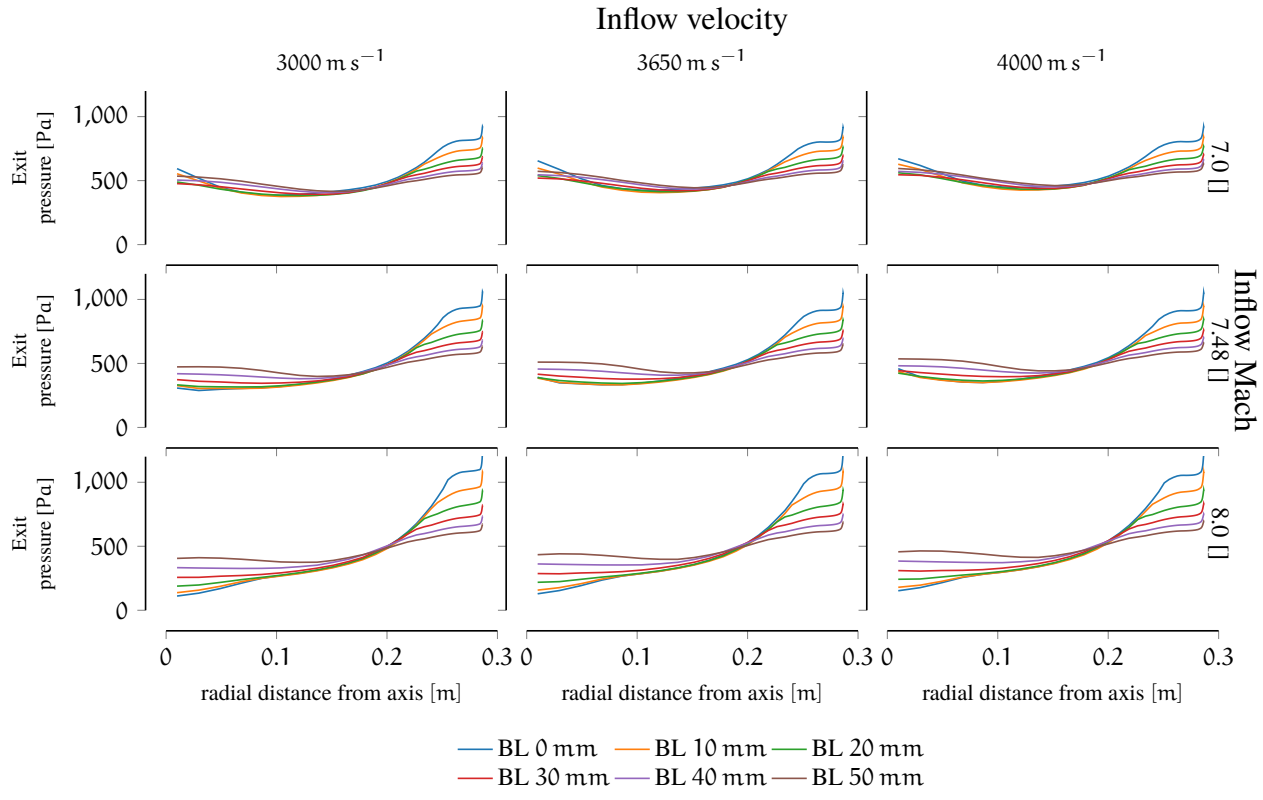

Figure 4.13: Nozzle exit pressure number for varying inflow Mach number, velocity and boundary layer thickness.

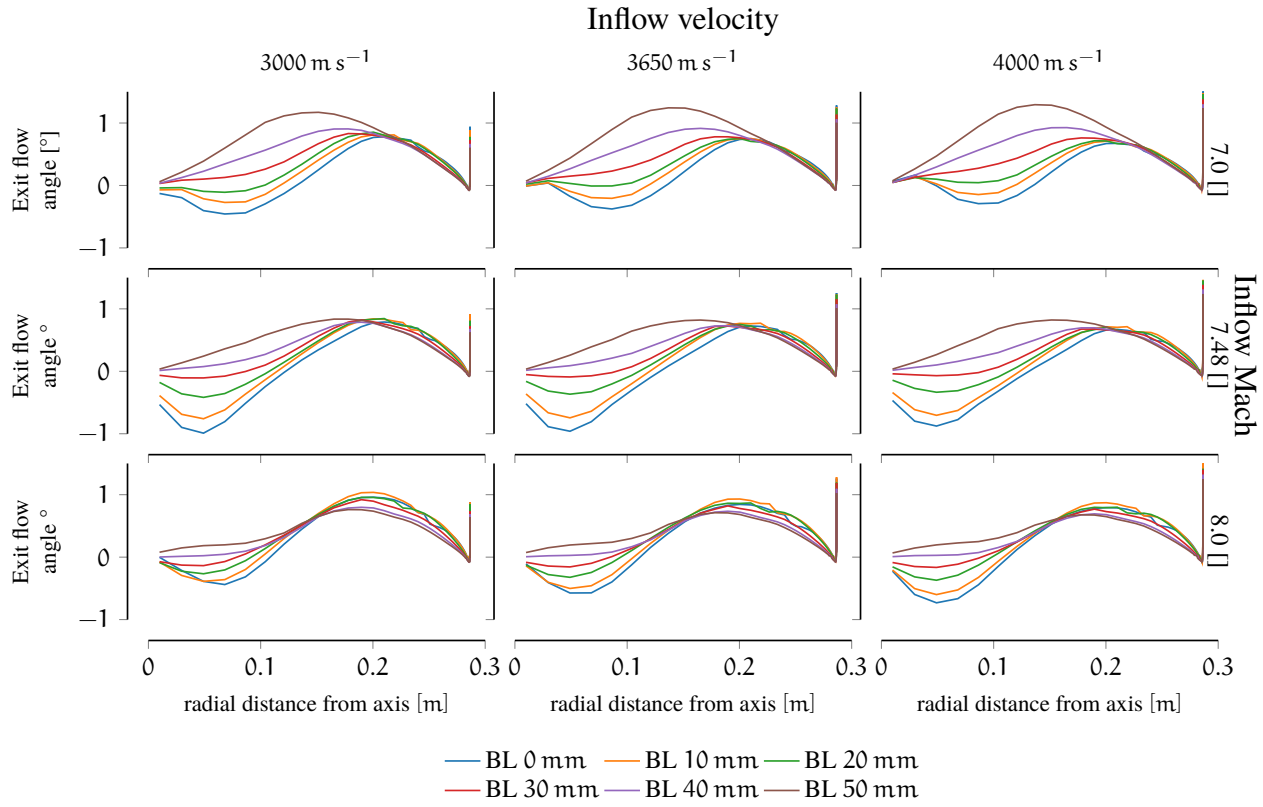

Figure 4.14: Nozzle exit flow angle number for varying inflow Mach number, velocity and boundary layer thickness.

On the other end, the tail of the expansion wave arrives and as the sound speed decreases, it accelerates down the nozzle. The two phenomena should in theory cause a test time reduction, but this has not been observed experimentally in previous nozzle designs [157].

This happens because there are other compensating mechanics that lead to larger than the theoretically allowed test times. The transient flow coming from the acceleration tube has a thick, but varying boundary layer, causing the core flow to see a changing nozzle area as it progresses further along, such that the gas that arrives later (and that in the acceleration tube was the under-expanded test gas) undergoes a bigger expansion. Additionally, as discussed in [129], the increase in the duct area simply facilitates the unsteady expansion process in a boundary layer limited expansion-tube flow.

4.6.4 Weighting parameters choice

The choice of the weights Φ_M, Φ_θ is arbitrary, and different choices can lead to different profiles. Two additional optimisation runs were calculated with slightly different parameters and the obtained nozzle profiles were compared. The results are shown in Fig. 4.15, where *option B* indicates a nozzle where the relative weight of the flow angle term was increased and *option C* where the weight of the Mach number term was increased. It is clear that there is a "competition" between the two terms of the

optimisation function. A nozzle with a higher flow angle weight would increase the curvature in the last part of the profile to redress the flow, at the expense of core flow size. On the other hand, a nozzle with higher Mach number weight would tend to expand more flow to essentially reduce the re-compression waves that disrupt the exit Mach number profile. The final profile lies in between, indicating a reasonable compromise. It is worth pointing out that the initial expansion is relatively unchanged amongst the different profiles, indicating that the defining section of the nozzle profile is its second half.

All the three profiles are equally valid, and could be chosen to be manufactured, according to the design preference in terms of balance between core flow size and exit flow quality.

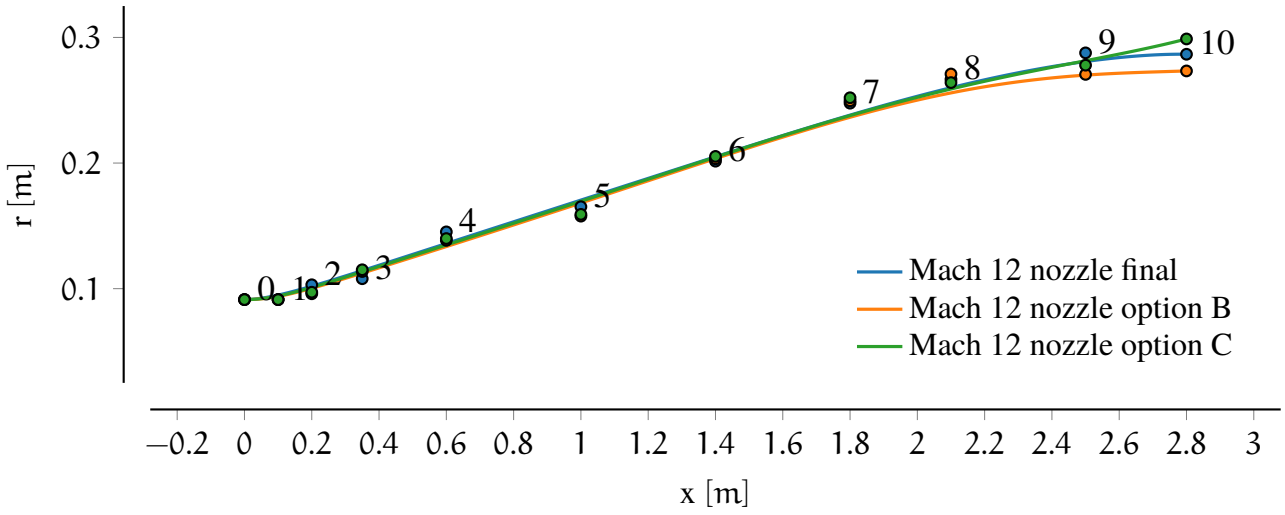

Figure 4.15: Alternative nozzle profiles, if optimisation weights are changed.

4.6.5 Validation of the objective function

The choice of Mach number and flow angle as the two flow properties to optimise relates to the fact that these two are the dominating parameters for scramjet experiments [186]. However, one could decide to optimise for different parameters, such as pressure, density and temperature. Previous nozzle designs never explored whether other terms (relating to different flow properties) need to be added to the objective function, or if totally different terms need to compose the objective function.

An a-posteriori analysis was carried out on results from the Mach 12 optimisation presented in this chapter to verify this assumption. The final run of the optimisation process simulated roughly 1900 distinct nozzle profiles. This constitutes a sizeable dataset that was analysed. Over this dataset, hypothetical terms of the form $f_y = \frac{1}{N}\sum_{j=1}^{N}\left(y_j\left(\vec{X}\right) - \bar{y}\right)^2$ can be calculated, where y is any flow property (for example pressure, temperature), and $\bar{y}$ is the mean value in the core flow of that property. As shown in Fig. 4.16, one then can apply a robust linear regression to verify whether there is any

correlation between the Mach number and flow angle term and the newly calculated hypothetical terms. A robust regression method is required as there are a number of outliers representing unusual nozzle contours that have seldom been generated by the optimiser. A confidence interval on the regression was then calculated via a bootstrapping method, and it is overlaid in the graphs.

Figure 4.16 shows that there is a clear correlation between the Mach number term and the pressure term, with an estimated pseudo-Pearson coefficient very close to one. Similarly, for a temperature term, the correlation with the Mach number term is around 0.9. On the other hand, there is no correlation that can be observed with the exit flow angle term.

The direct interpretation is that the Mach number term f_M, which itself is a metric for the Mach number smoothness in the exit core flow, is well correlated with pressure and temperature smoothness. In other words, it can be reasonably assured that if the Mach number objective function term is low, the Mach number profile is close to the target Mach number, but also that pressure and temperature are relatively uniform around the mean value. Additionally, Mach number, pressure and temperature completely define the flow state, such that all the other properties will present a uniform profile across the exit core flow.

As such we can be confident that, in the first order, the aforementioned objective function, while optimising only for Mach number and flow angle, is sufficient to obtain a flow that not only is close to the desired Mach number and the desired flow angle, but also that is able to minimise the disturbances that might arise in all other flow properties. As a consequence, any other additional term would be redundant and effectively would be equivalent to an increase of the weight term Φ_M. On the other hand, this is a conclusion that can be considered valid for the local solution space that has been explored in this case, as the selected variables were not randomly chosen by the optimiser.

This analysis shows that the objective function $f = (f_M + f_\theta)^2$ is sufficient and capable to produce an optimal, disturbance free nozzle profile.

4.6.6 Grid convergence

The computational grid for the flow simulation had 500 cells in the axial direction and 50 cells in the radial direction. With respect to previous studies, this grid is slightly coarser and it was a compromise between simulation accuracy and simulation time. A grid sensitivity study was carried out and three grids were evaluated: the nominal one (50x500), a medium one (70x710) and a fine one (100x1000), for the nozzle contour named "option C" in Fig. 4.15. All the grids were clustered towards the nozzle walls and the y_+ was $\leqslant 1$. In Table 4.3 the grid convergence study results are shown: the Richardson extrapolation factor (R_c) [201] and the Grid Convergence Index (GCI) [202]. R_c is an indicator of monotonic convergence when $0 \leqslant R_c \leqslant 1$ for every variable of interest, which was satisfied for all the values apart from flow exit angle. This has been deemed to be acceptable as the overall exit flow angle was very

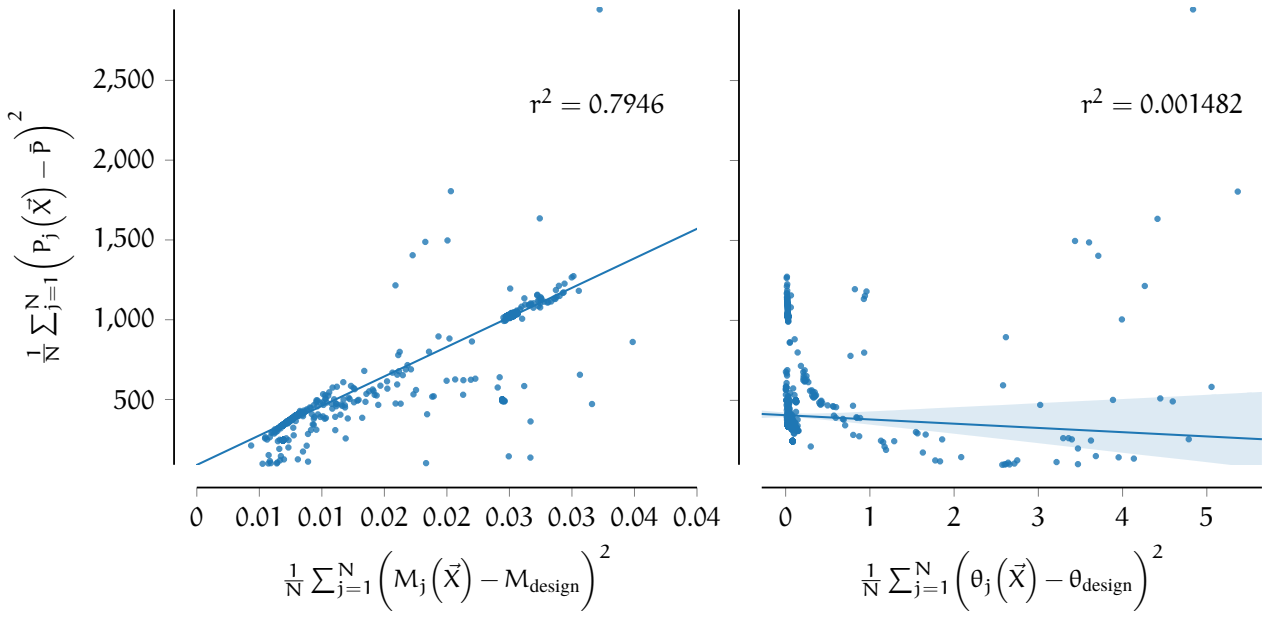

Figure 4.16: Relationship between the two main terms of the objective function and a hypothetical pressure term, defined as indicated in the axis labels. N is the number of CFD cells in the core flow. A robust linear model is fitted and indicated in the figure, and a confidence interval is indicated in lighter blue, estimated with a bootstrapping method. The pseudo-Pearson coefficient is indicated in each plot.

close to zero, especially in the optimised nozzle profile and therefore not significant. The GCI factor, for the coarse grid, was calculated with a safety factor of 1.25 and both errors were less than 5 % The results showed that the original grid was deemed to be sufficiently grid-converged, as a compromise between accuracy and optimisation run length was required. Additionally, it has assumed that the grid was sufficiently converged for all the nozzle profiles that have been simulated in the nozzle optimisation process, although their dimension and shaped varied with respect to the one used for the grid convergence study.

Table 4.3: RE and GCI analysis of the grid used in the nozzle optimisation.

	exit Mach number	exit flow angle	exit pressure
R_c	0.22	-0.17	0.19
f	5.2876		664 Pa
δ_{RE_2}	-8.7×10^{-3}		-7.8×10^{-2}
δ_{RE_3}	-1.9×10^{-1}		-2.3×10^{1}
GCI_2	-0.20 %		-0.15%
GCI_3	-4.55 %		4.31%

In Fig. 4.17 the main exit flow parameters for three different density grids are compared. Differences between profiles are minor for both Mach number and exit flow angles. The only noticeable distinction was with the estimated pressure in the exit boundary layer. The estimated differences in the core flow are overall negligible, thus qualitatively reinforcing the idea that the nominal 50x500 grid is a sufficient choice to model the flow.

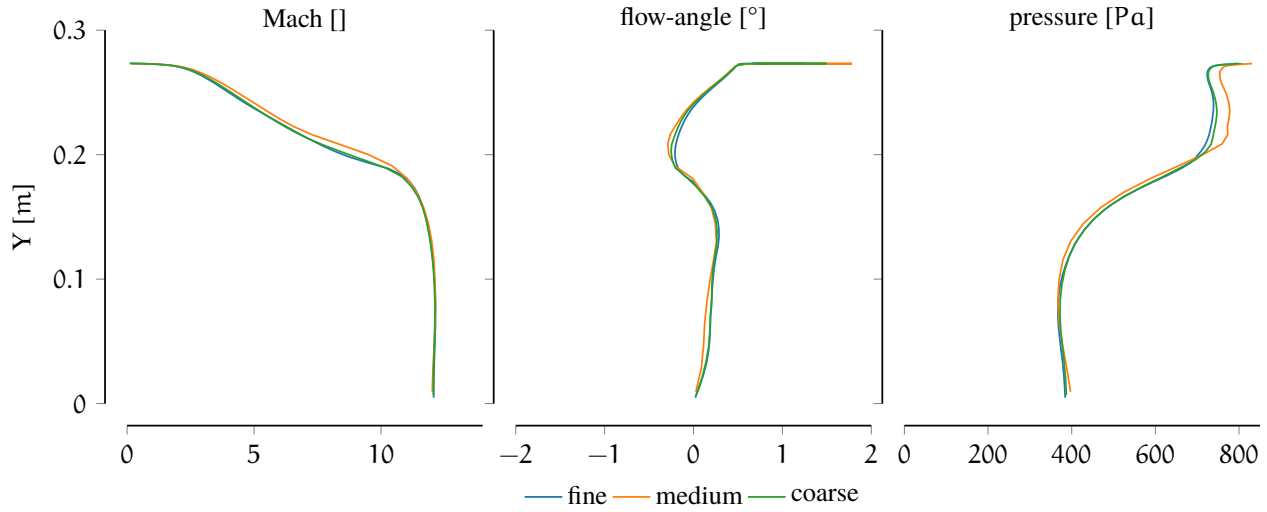

Figure 4.17: Grid convergence study of a generic nozzle profile.

4.6.7 Simulation accuracy validation

As previously discussed, to speed up the simulations, an increased number of radial blocks was adapted. The speed up was close to the theoretical 4x, however, the use of additional blocks slightly decreased the accuracy of the code (it is noted that despite the spatial order of accuracy being 2 within blocks, the theoretical order of accuracy at block interfaces is only 1). To verify that the loss of accuracy was negligible and that the simulations were accurate, a comparison over the same grid has been carried out with US3D (Section 6.5.1), both in axis-symmetric mode and full 3D. Results comparing these two simulations from US3D with the axisymmetric results from Eilmer3 are shown in Fig. 4.18. Additionally, this comparison serves as a validation of Nenzf-R/Eilmer3 as a nozzle flow solver, of the modified MPI-enabled Nenzf-R, and finally of the Wilcox $k-\omega$ turbulence model, as US3D only implement the SST $k-\omega$ turbulence model. Differences in the main exit properties are negligible. The US3D axisymmetric solution slightly differed in Mach number in the boundary-layer and the flow angle, whereas Eilmer3 and the more accurate 3D US3D are overall much closer.

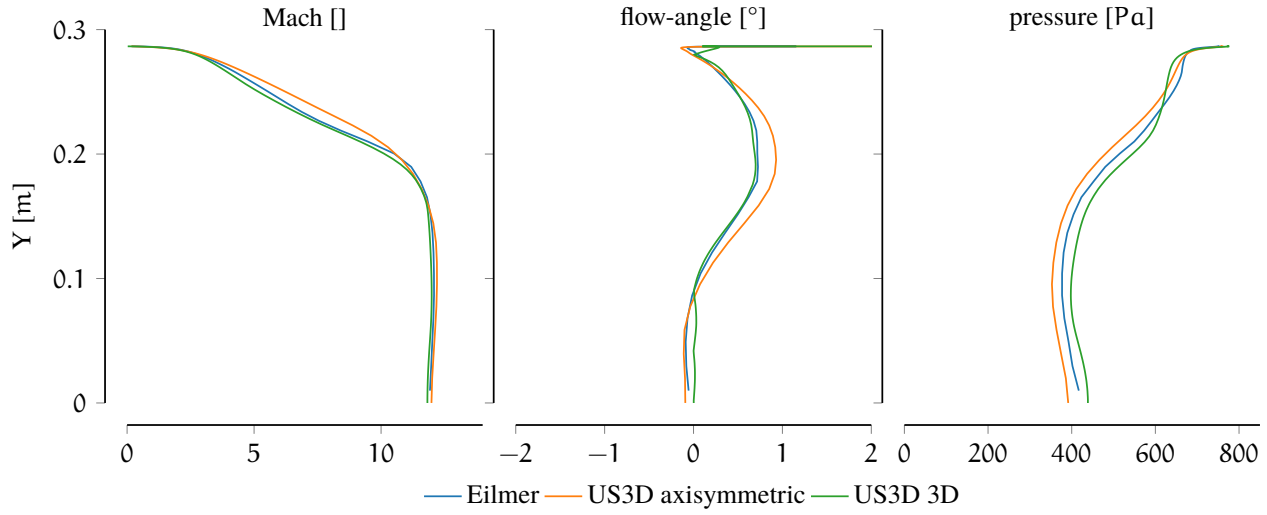

Figure 4.18: Comparison of results given by US3D and Eilmer3 for the final Mach 12 nozzle profile.

4.7 FACILITY INTEGRATION AND NOZZLE MANUFACTURING

In the previous section a nozzle profile has been obtained and analysed. With the nozzle profile in hand we proceeded to design and build the nozzle. In this section we will detail requirements, design, and construction method, and then experimentally evaluate the actual Mach 12 nozzle that has been built.

4.7.1 Scientific requirements

The accuracy of calculating nozzle exit flow conditions can be improved by the use of surface instrumentation along the expanding wall and inlet surveys. As such, it was proposed to include:

NOZZLE WALL MEASUREMENTS Notwithstanding a very detailed analysis for the steady state case, the real unsteady expansion-tube flow remains difficult to describe through numerical methods. A characterisation of the nozzle with pressure measurement and heat gauges is highly desirable and potentially very useful. A series of sensor mounts that can host pressure and heat transfer sensors were to be integrated along the nozzle wall.

INSTRUMENTED RAKE AT THE NOZZLE ENTRY Nozzle inlet flow properties are difficult to correlate with CFD simulations, and for the Mach 10 nozzle, impossible to fully measure. Additionally, Scott [157] observed that the use of a nozzle might increase the test time, reducing the effects of boundary layer growth. However, these effects have not been studied in detail for any hypersonic nozzle. An additional detachable instrumented rake that can be inserted at the nozzle entry was proposed, so that it would be possible to study the effects of the nozzle expansion on the test gas.

4.7.2 Technical requirements

A series of technical requirements have been identified, following the experience gained in building and using the previous Mach 10 nozzle and adapting it to ongoing facility modifications. With the ongoing project to allow a new reflected shock tunnel mode (X3R, [203]), a new dump tank section has been designed and built. The main goal of this new section is to house the new X3R Mach 7 convergent-divergent nozzle, with an estimated diameter of 750 mm sitting inside the new extension, which reduces the pressure load on the wall of the new nozzle when the system is under vacuum. The new Mach 12 nozzle needed to be fully compatible with this new configuration. The mechanical requirements for the nozzle are the following:

SEALING SURFACE AROUND THE THROAT The integration of the new extension to the dump tank allows the Mach 12 nozzle to sit inside the tank, which places the sealing surface on the nozzle "throat" external surface.

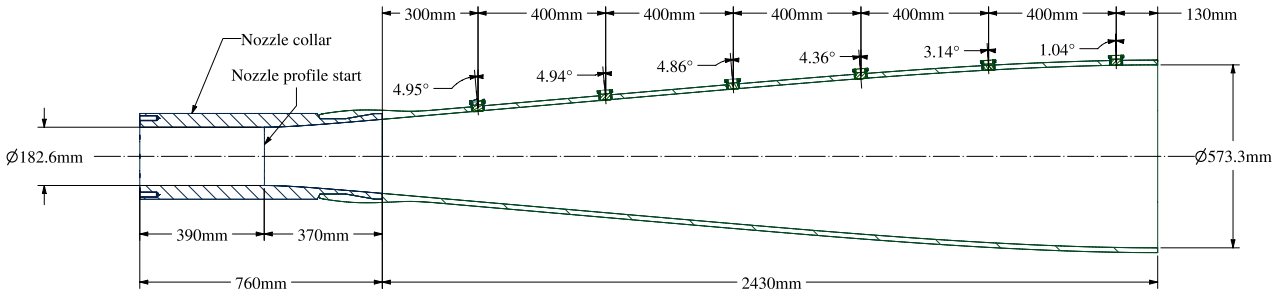

Figure 4.19: Nozzle and steel nozzle collar schematics and main dimensions.

USE OF SLIDING SEAL O-RINGS X3 has a recoil joint that isolates the dump tank from the recoil movement of the rest of the tunnel. However, a sliding seal is considered necessary to avoid overloading and rupturing of the nozzle in case of recoil-joint failure, while ensuring at the same time a good vacuum seal.

EASY ACCELERATION TUBE — NOZZLE CONNECTION The existing Mach 10 nozzle was connected to the acceleration tube through a threaded connector. This installation has proven to be difficult because the nozzle had to be screwed into the acceleration tube, while keeping it aligned to the tube with its weight temporarily suspended. It is clear that the Mach 12 nozzle, being longer, heavier, and bigger, required an easier system to connect to the facility. Additionally, such a system is necessary to facilitate transition from and to X3R.

LIGHTWEIGHT NOZZLE The nozzle, while sitting inside the test section, is cantilevered. The nozzle is required to be lightweight, to allow easy day-to-day operation, and avoiding the need for inner supports.

All these requirements were satisfied as briefly discussed in the following sections, and the nozzle technical drawings are included in this thesis and are presented in Chapter 13.

4.7.3 Nozzle construction

The Mach 12 nozzle has been constructed in two sections: the first part is a mild-steel nozzle collar, in which the first part of the nozzle contour has been machined. The main part of the nozzle was made from fibreglass by filament-winding around a foam mandrel. The nozzle collar was inserted on the mandrel, and fibreglass was wound around the mandrel and the steel part. The concept is illustrated in Fig. 4.19. The mandrel was initially fabricated by *Teakle Composites*, and then was re-machined and re-coated by *ABCO Machining*. The nozzle winding was performed by *Teakle Composites*. In the same figure the wall pressure measurements mounts are indicated.

4.7.4 Nozzle wall sensors

On the nozzle wall six instrumentation holders have been installed. As shown in Fig. 4.19, they start 670 mm downstream of the start of the nozzle profile, and they are equispaced every 400 mm, with the last one located around 130 mm from the nozzle exit. They are shown in Fig. 4.20. Each of the sensor mounts are able to house two PCB pressure sensors *112A22*, in flush-mount configuration. The sensor mount is purposely bigger than necessary, to allow future use of other instrumentation, such as heat transfer gauge or thermocouples. For some experiments, some Kulite XCEL-100 have been mounted in the PCB mount via an adapter. Each sensor mount can be replaced with a plug. Sensor mounts and plugs have been designed to be flushed to the surface, and their inner surfaces have been machined to match the nozzle inner profile.

Figure 4.20: Nozzle wall sensors and optional plugs.

4.7.5 Nozzle interface to the acceleration tube

The interface with the nozzle acceleration tube has been completely revisited. For the previous nozzle a threaded connection was used, but it has shown to be very difficult to install and remove.

A flange-connection system was designed, manufactured and installed. The nozzle assembly is connected to the acceleration tube by means of three flanges, with the middle one able to host an instrumented rake with up to eight PCB pressure sensors. The system significantly simplifies installation and operation of the Mach 12 nozzle and it has been subsequently retrofitted to the existing Mach 10 nozzle. Most importantly, it allows use of a compact, plug-and-play instrumented rake, which can easily be inserted and removed prior to a shot, without the need to remove the nozzle and/or install adapter pieces to measure flow properties at the nozzle inlet. Figure 4.21 illustrates the components of the central flange and of the inlet rake. For a complete discussion of the inlet rake the reader is referred to the next chapter.

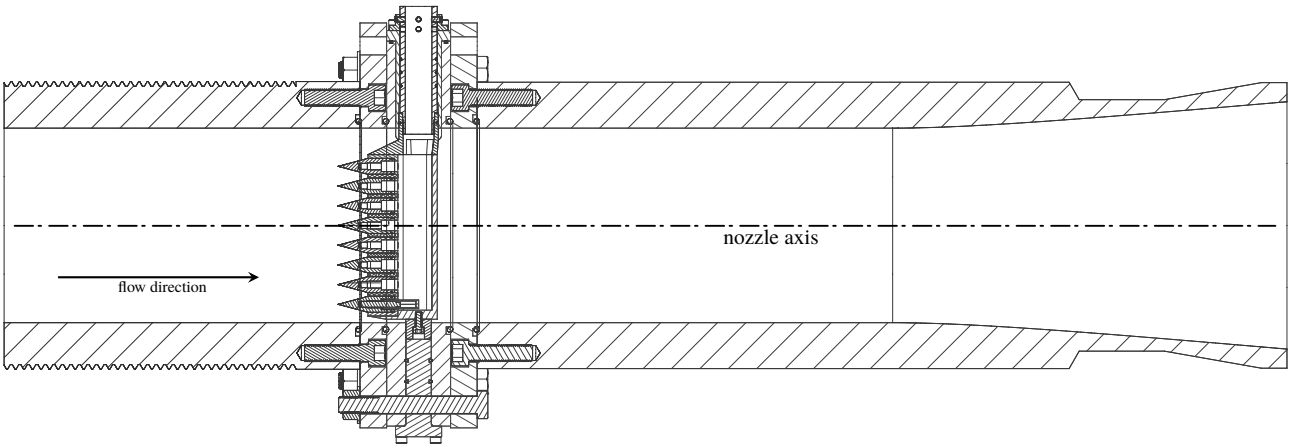

Figure 4.21: Inlet rake connection system. Flow from left to right.

4.7.6 3D measurements of the nozzle

Several issues were encountered during the fabrication and machining process of the mandrel. The existing mandrel, which was originally fabricated several years ago to initially wind another nozzle (that has since then been discarded), showed a lack of adequate rigidity, probably due to the decay of structural properties of the foam over the years and the use of weak shaft and insufficient foam density. The problem was mitigated by adding a layer of fibreglass around the mandrel foam, however, doubts were cast over the actual shape of the mandrel. It was therefore decided to proceed with a 3D scan of the last part of the nozzle and the mandrel to evaluate the error of the final constructed shape from the target theoretical profile. Only the last 75 cm of the nozzle inner surface were scanned due to the limited range of the 3D scan in use.

The scan results are illustrated in Figs. 4.22 and 4.23 and summarised in Table 4.4. The scan results show that there is a small average deviation from the nominal profile, and that there is a localised spot where the measured difference exceed 1 mm. Although a numerical sensitivity analysis has not been carried out, the measured difference is not expected to have any significant impact on the flow properties. Assumptions like steady state simulation and use of a nominal steady inflow condition are expected to have far more impact on to the exit flow properties.

A 3D scan of the mandrel was also carried out. The removal process of the mandrel from the newly wound nozzle damaged the structural integrity of the mandrel itself, eliminating the possibility of re-establishing the complete nozzle shape from the mandrel measurements. Indeed, a tentative comparison of the nozzle scan and the mandrel scan over the last part showed that the mandrel was irremediably deformed.

For future studies it would be of great interest to investigate different 3D scanning techniques and measure the whole inner surface of the nozzle, to enable a complete numerical study of the actual shape of the Mach 12 nozzle.

Table 4.4: 3D scan results.

	Units	
Max Upper Deviation	mm	1.0669
Max Lover Deviation	mm	−0.2478
Average Deviation	mm	0.311 14
Standard Deviation		0.2047

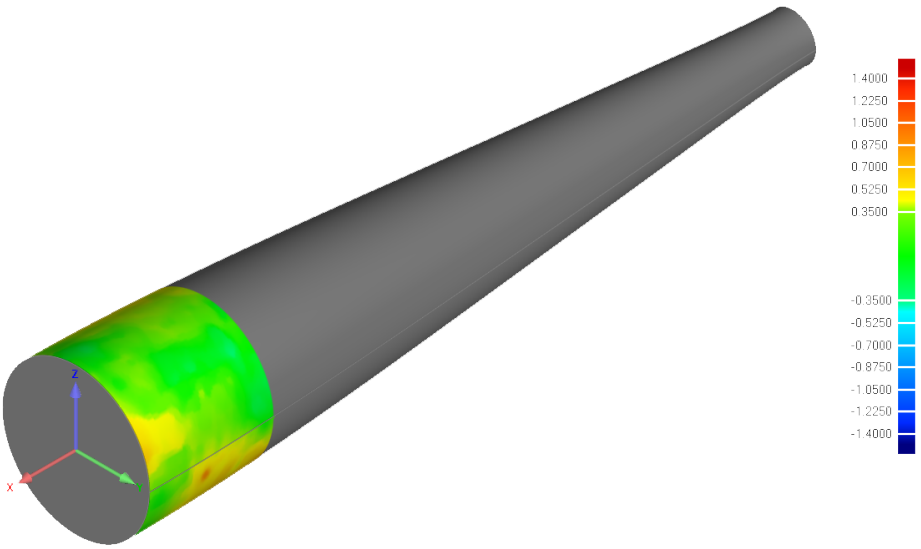

Figure 4.22: Isometric view of the results of the 3D nozzle scan.

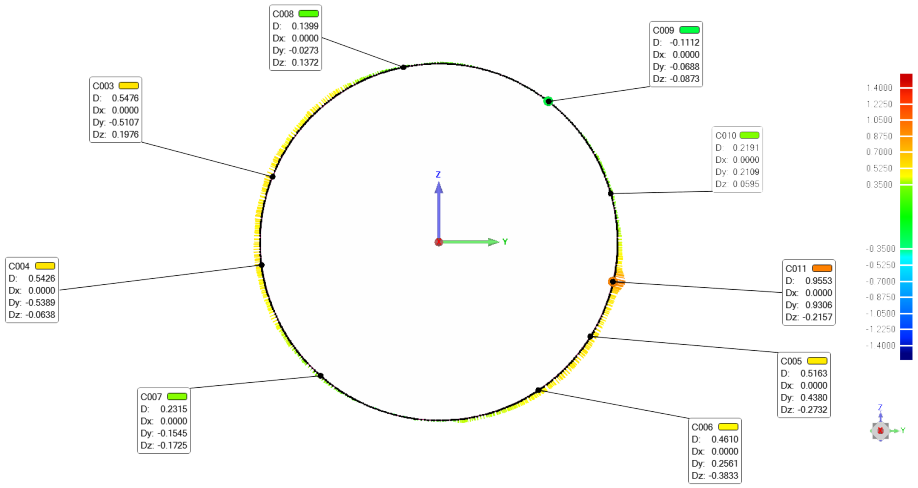

Figure 4.23: Cross section of the 3D nozzle scan results at the worse plane. Deformation is not to scale.

4.8 A FINAL OVERVIEW

A new hypersonic Mach 12 nozzle has been designed for the X3 expansion tube. An improved approach based on a coupled CFD/optimisation process has been used. The methodology has built upon previous work, but was improved to allow for a nozzle of this size to be designed. A newly parallel version of the Nelder-Mead algorithm has been developed and used, allowing for the optimisation of a nozzle that is almost 3 m long and has 600 mm, exit diameter of the biggest ever built for an expansion tube. The nozzle simulation took place with EILMER3, a RANS CFD explicit solver, including non-equilibrium chemistry and a turbulent model. Several flaws in previous nozzle design methodologies have been identified and corrected for this study.

On the other hand, a certain range of simplifying assumptions were required, amongst which the most important one was the assumption of a steady inflow, as a transient inflow for the X3 expansion tube was not available and, in any case, would have significantly increased computational time.

A parametric study in off-design conditions has been carried out, and it has indicated that the performance of the nozzle is substantially degraded if the inflow Mach number is greater than 7.5. Future conditions designs should avoid higher inflow Mach numbers.

Transient behaviour has been discussed and a mechanism for test time extension has been proposed. The theoretical test gas is partially processed by a reverse shock generated by the interaction between shock and contact surface. The actual test time is actually generated by a differential expansion that the gas undergoes due to a varying boundary layer thickness.

The manufacturing and mechanical design of the nozzle has been outlined. Several new measurement capabilities were integrated in the nozzle, which will be discussed and utilised in the next chapter where experimental performance of the nozzle will be reviewed. The manufacturing process has indicated evidence of some shortcomings, which have reduced the precision of the manufactured nozzle with respect to the nominal nozzle profile, and these shortcomings have been addressed in other nozzle construction process, such as the Mach 7 nozzle for the X3R reflected shock tunnel.

New additional measurements capabilities have been included into the design. The new flange connection system allows an inlet rake to be inserted at the nozzle inlet, and new wall-mount along the nozzle have been installed. They will be discussed in the following chapter.

Further studies could investigate:

- the use of a quasi-transient or fully transient inflow to effectively improve the realism of the nozzle optimisation and derivation of corresponding objective functions which accounts for transient exit test flow;
- the use of more coupled methods for gradient estimation, such as adjoint methods;
- improve manufacturing accuracy, and use of carbon-fibre;

- a complete 3D scan of the manufactured nozzle, and a numerical study of the effects of measured shape on the flow properties;
- investigate non-axisymmetric nozzles. A great deal of the effort went into ensuring that the nozzle was not generating flow disturbances at the centreline. Rectangular nozzles, for example, would remove the focusing effect on the axis.

In the previous chapter a Mach 12 operating capability was presented. A new nozzle has been designed and built. In the next chapter, experimental validation of the flow condition and commissioning of the nozzle will be presented.

In the following pages, Figs. 4.24 to 4.26 show the complete CAD overview and the manufactured and the assembled Mach 12 nozzle dump tank interface currently operated in the Expansion Tube laboratory at the University of Queensland.

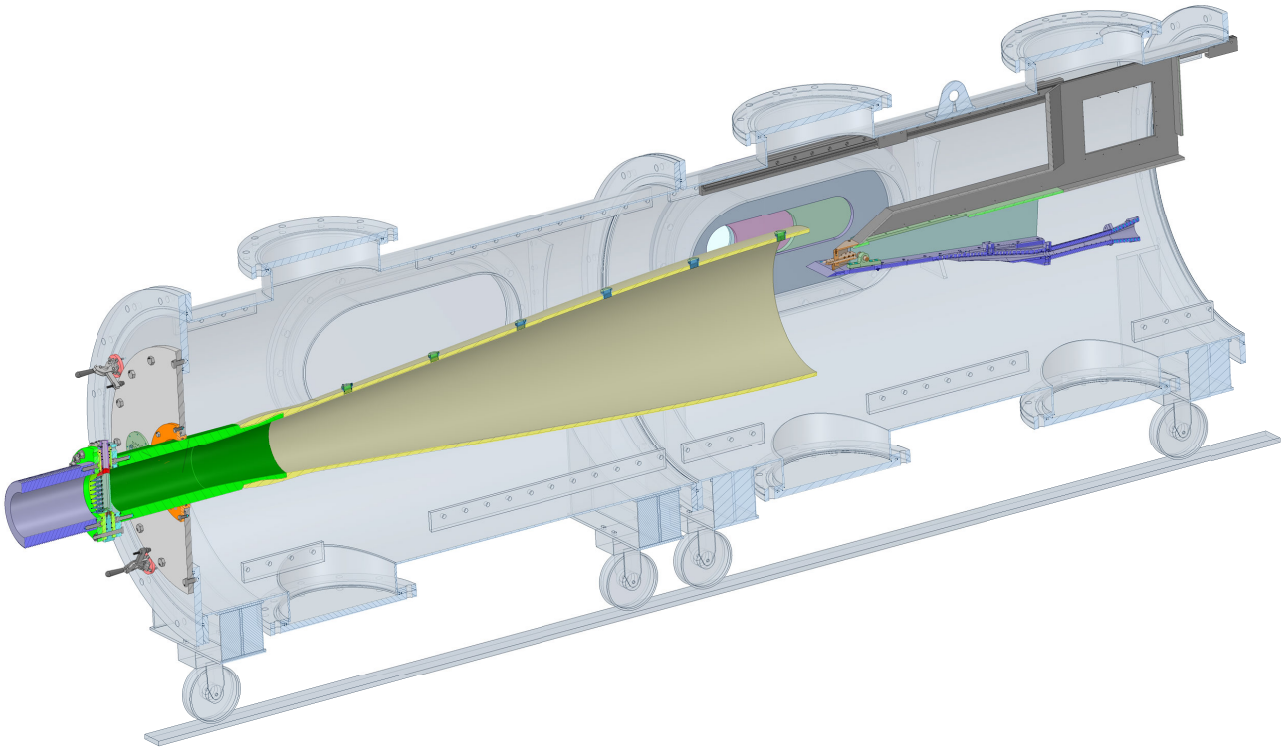

Figure 4.24: Cross-sectional view of the Mach 12 nozzle inside the X3 test section. The inlet Pitot rake is present as well.

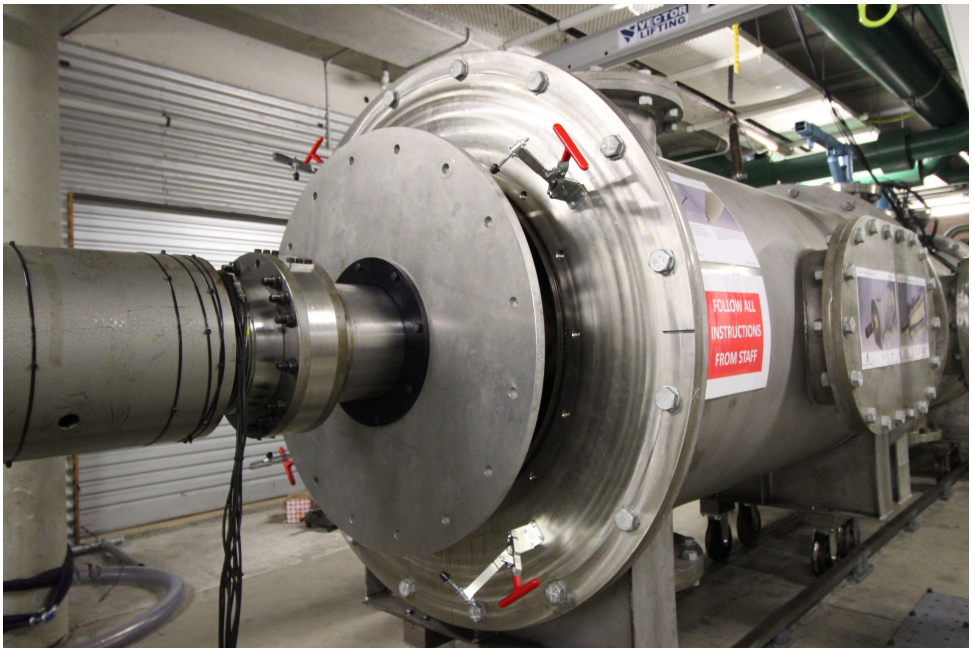

Figure 4.25: New nozzle and dump tank interface. The nozzle is housed inside the test section. An aluminium plate seals around the nozzle collar and on the front of the test section with o-rings. A fast-release system to facilitate operation has been installed. On the left side, the three-flange system connecting nozzle and acceleration tube is visible.

Figure 4.26: The new Mach 12 nozzle installed and cantilevered off the acceleration tube. On the aluminium plate the nozzle instrumentation plate can be noted. On the bottom surface of the nozzle the nozzle sensors mounts are visible.

5 FLOW CONDITION CHARACTERISATION

5.1 INTRODUCTION

Armed with a newly operational Mach 12 condition and a newly manufactured nozzle, in this chapter the experiments commissioning the nozzle and the flow condition will be detailed. The goal of this set of tests, and hence of this chapter, is to quantify the test flow properties at the nozzle exit, to verify that the new nozzle is able to produce the high Mach number flow, and to estimate core flow size, test time and test flow quality.

Characterising freestream flow conditions in expansion tubes is extremely challenging; high total enthalpies and total pressures, as well as short test times, together make intrusive measurements complex and subjected to high uncertainties. Diaphragm fragments and the effects of acoustic noise focusing add to the complexity. For this reason, the approach is twofold, both experimental and numerical, with the latter used to augment experimental data and to provide estimates of the flow properties which cannot be measured directly. At the same time, numerical simulations of expansion tubes are equally challenging, as it requires modelling a variety of flow regimes and include mechanical processes such as piston motion and diaphragm rupturing. Therefore, various simplifying assumptions become necessary.

In the first part of the chapter we will discuss the experimental techniques and results. Pitot pressure probes located on instrumentation rakes, both upstream and downstream of the nozzle, have been used to characterise core flow sizes and test times. However, by themselves, they are not sufficient to fully describe the flow properties. As such, an independent Mach number measurement has been carried out at the nozzle exit, based on the measurements of oblique shocks angles generated by a 30° wedge with a schlieren-based technique.

The second part of the chapter focuses on the numerical work done to simulate the flow condition. As expansion tubes are intrinsically transient, full facility simulation is required to accurately describe the flow. Due to the significant size of the X3 expansion tube, a hybrid approach has been adopted, in which the first part of X3 has been simulated using a Lagrangian one-dimensional code, L1D (see Section 3.3.2). Tuning of some empirical parameters was required to replicate the experimental shock speeds. This was achieved using an optimisation routine. The second part of the facility — the acceleration tube, nozzle, and test section — was then modelled with a RANS axisymmetric simulation carried out with Eilmer3 (see Section 4.5.1), with the inflow extracted from the results of the optimised L1D simulations. Finally, the results obtained are presented and reconciled with the experimental estimates.

5.2 PITOT PRESSURE MEASUREMENTS

In this section, the different probes used to measure Pitot pressure, along with a description of the nozzle inlet and nozzle exit rake are presented.

5.2.1 Pitot pressure probe caps

Pitot pressure measurements were primarily used to evaluate the test time, core flow size and flow unsteadiness. As an intrusive measurement, they are extremely challenging to carry out in hypersonic flows, due to significantly high pressures and temperatures that occur at the probe surface. The short test times require extremely high frequency responses. Additionally, Mylar secondary/tertiary diaphragms and steel primary diaphragm fragments can cause significant damage to expensive pressure transducers. A shielding mechanism is required to avoid permanent damage to the probes. Over the years several design concepts have been explored and tested. Amongst these, two different designs were employed for these experiments: classical flat Pitot probes, and conical glancing impact pressure probes (otherwise referred to as 'conehead' probes), as shown in Fig. 5.1. Both probes have been designed to host PCB sensors.

Flat Pitot probes incorporate a 4-hole swirl system in an attempt to dampen the Helmholtz resonance that is observed in a simpler cavity [204]. The probes are useful to obtain Pitot pressure measurements; however, the swirling system is not fully effective in reducing the Helmholtz resonance phenomenon, and these measurements present a notoriously high level of noise. Conehead probes, described in detail by Gildfind [30], were designed to reduce the pressure and temperature load on the probe by allowing the flow to be processed by an oblique shock, rather than a normal shock. They are designed with a cone half-angle of 15°, and 8 holes, 2 mm in diameter, normal to the surface feeding the probe cavity.

The measured pressure on the conehead probes can be correlated back to Pitot pressure, but the knowledge of the flow Mach number is required. However, at high Mach number, its influence is significantly reduced. In a similar way, if Mach number is known, static pressure levels can be re-established using CFD simulations, or with classical Taylor-Maccoll equations, including real-gas effects. Conehead probes have been shown to exhibit a significantly reduced noise level, with increased survivability rates compared to flat pressure probes [30].

Gildfind [30] thoroughly investigated correlation factors for the conehead probes and estimated a sensitivity between $3.6\,\%\,\mathrm{Mach}^{-1}$ at Mach 6.9; to $1.0\,\%\,\mathrm{Mach}^{-1}$ at Mach 15. The correlation factors $\frac{p_{cone}}{p_{Pitot}}$, proposed by the same author were estimated at 0.0956, 0.0859, 0.0823 and 0.0803 at Mach numbers 6.9, 10.0, 12.5 and 15.0.

It is understood that the use of conehead probes introduces significant complexities in flow measurements, and makes necessary the introduction of correlation factors that neglect second-order

dependencies, such as, Reynolds number, but its adoption has shown to be useful for expansion tube flows. In the case of nozzle inlet measurements, where the flow is not yet expanded to lower pressures, this is even more important and notable.

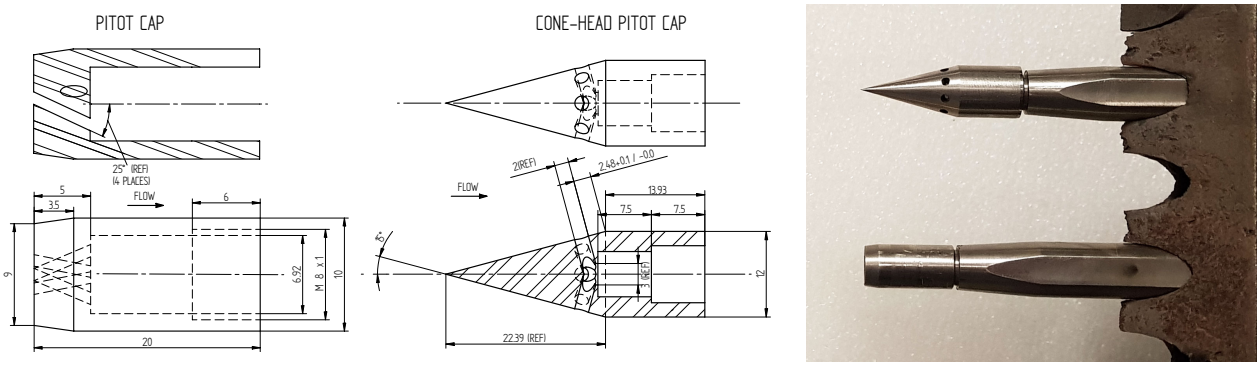

(a) Probes schematics [205, 206]

(b) Installed probes

Figure 5.1: Classical Pitot pressure probes and conical glancing impact pressure probes (conehead probes).

5.2.2 Inlet rake

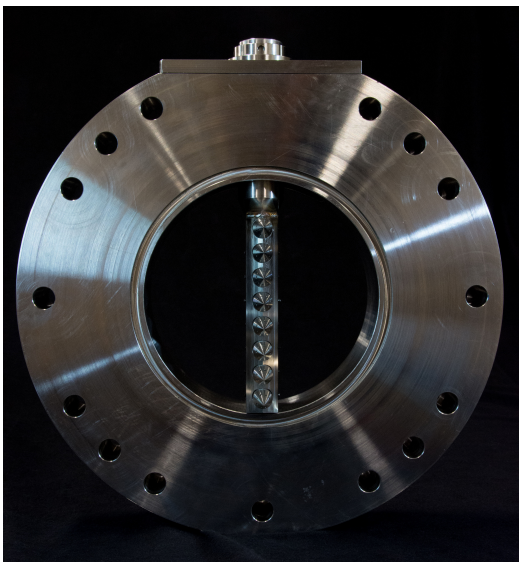

(a) Inlet rake inside the rake holding flange. View looking downstream

(b) Conehead pressure sensors used in the inlet Pitot rake

Figure 5.2: Nozzle inlet instrumented rake and probes used within the rake.

Inlet measurements were made possible with the redesign of the nozzle attachment system, as discussed in Section 4.7.5. A new inlet rake has been designed and built together with the nozzle hardware, and is depicted in Fig. 5.2. The rake enables inlet pressure measurement without the removal of the nozzle. The rake can host up to 8 probes with a spacing of 18.5 mm between any two consecutive probes. Table 5.1 indicates the whole setup for both configurations. The rake can be located in two

alternate positions, where the distance between the two settings is 9 mm, i.e. half of the distance between two consecutive pressure probes. The rake is positioned such that the pressure sensor face is located 500 mm upstream of the nozzle inlet and 366 mm downstream of the last acceleration tube wall pressure sensor AT8. The two configurations allow increased spatial resolution of the rake.

Table 5.1: Inlet rake probes vertical location with respect to tube centreline. The inner radius of the tube is 91.3 mm.

	Config A [mm]	Config B [mm]
P1	55.5	64.75
P2	37	46.25
P3	18.5	27.75
P4	0 (centreline)	9.25
P5	-18.5	-9.25
P6	-37	-27.75
P7	-55.5	-46.25
P8	-74	-64.75

The inlet rake currently hosts cone head pressure sensors to reduce the pressure load and ensure survivability of the sensors. The flow properties at the nozzle inlet are denser since gas is not yet fully expanded, and taxing due to the diaphragm debris that are likely to impact the probes. These probes, which can be seen in detail in Fig. 5.2a are equipped with 50 psi PCB 112A22 pressure sensors, housed in the central part of the assembly. The conehead cap, shown in Fig. 5.2b, is a modified version of the one previously presented in Fig. 5.1a, allowing for a vibrationally isolated PCB mount.

5.2.3 Ducted flow choking at nozzle inlet rake

The starting process of the rake, or a generic model, in a supersonic system is very complex and usually cannot be captured by simple normal shock relationships. In the past, it has been observed that a model of significant size can block a supersonic duct flow and generate a normal shock in front of it, reducing the flow to subsonic Mach and thus corrupting the experiment and significantly increasing the structural load in front of a model. This was a significant concern for the design and use of the current nozzle inlet rake, as it represents a substantial obstacle for the incoming flow, which can be observed in Fig. 5.2a.

In the literature it has been noted that a correlation between flow choking and frontal area ratio can be established, along with flow Mach number and drag coefficient. The work of Czysz [207] has established such correlations for a variety of models and shapes at different angles of attack, and the work is summarised in Fig. 5.3. The figure, however, needs to be used with precaution as the author noted that there is a large experimental scatter around the indicated maximum allowable area. Most importantly, the data were extracted from a continuous supersonic wind tunnel, and significant differences are expected for the flow in an expansion tube, where the flow is intrinsically continuously varying in speed, temperature, pressure and composition.

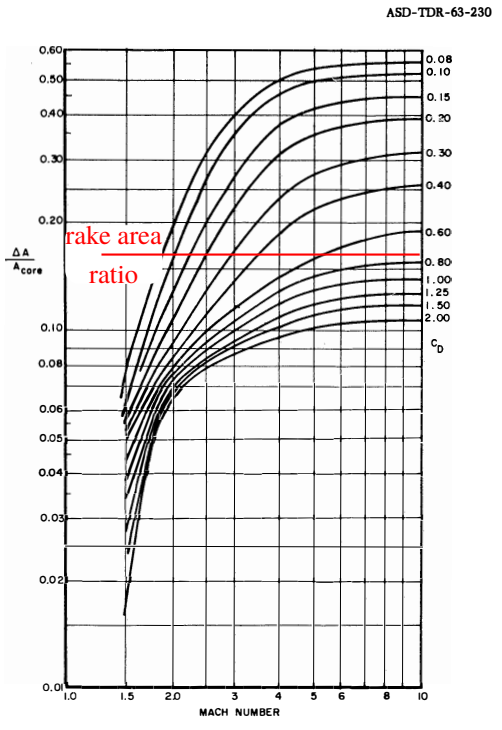

Figure 5.3: Permissible model frontal area as a function of Mach number and the drag coefficient to avoid blockage.

The rake has been designed to be as compact as practically possible but at the same time able to withstand a significant pressure load. The rake frontal area was limited by the conehead pressure probe sizes, which in turn were limited by the need to host a PCB sensor internally. The depth of the rake (i.e. its length in the axial direction) was restricted by the available space to insert the rake in the rake flange. The space to feed through the cable was also a limiting factor. To withstand an eventual choked flow load, the rake is supported on both the top and bottom sides of the inlet flange (Fig. 4.21).

The final area ratio between the frontal area of the model and the duct area was 0.175. It can be observed from Fig. 5.3 that, for a predicted Mach flow of 7.5, the flow choking was definitely possible, assuming a certain drag coefficient. As a result, the final design included stronger material and thicker rake walls, to ensure survivability of the whole rake in case choking occurred.

Computational simulations of some rake elements were carried out to investigate if the formation of a normal shock was likely. These simulations were done assuming a steady state inflow, which was the same flow as that assumed for the nozzle contour computational design. The much hotter accelerator gas, theoretically more likely to choke the flow, was not simulated, as it was considered that its estimated slug length (less than 0.5 m) was too short to fully start a normal shock and maintain it. On the other hand, the test gas slug length was expected to be sufficiently long to be able to sustain a steady shock. Finally, given all the considerations above, it was expected that later in the experiment, when under-expanded test gas and driver gas arrived, the rake would choke the flow. However, the pressure and velocity condition of those lower Mach slugs would be significantly milder and did not represent a design concern.

Results are presented in Fig. 5.4, where the shock surface around the probe is depicted. A noticeable oblique shock is propagated from the rake towards the outer walls (not shown in the figure). However, the thick boundary layer of the flow is such that the shock dissipates before reaching the walls and does not reflect on it. Although not presented here, it has been experimentally verified that the lower probe, the one fully included in the boundary layer, does not form any normal shock in from of it. Additionally, as expected, it has been observed that there are no interactions between each part of adjacent cone probes.

A full transient simulation of the flow on the model was not carried out, as it was outside the scope of this study. *However, it is strongly recommended further analysis to be performed before the use of this inlet rake for operating conditions other than the one indicated in this work.*

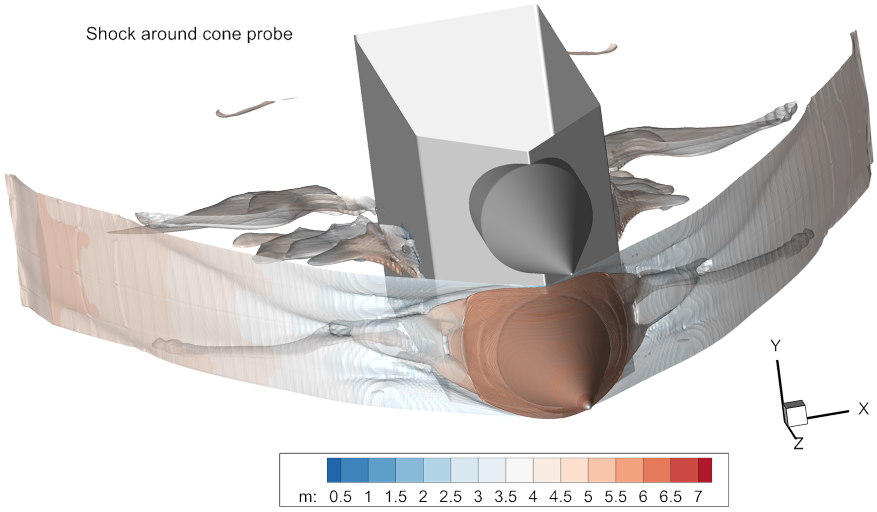

Figure 5.4: Shock wave surfaces over a conehead pressure probe, for a Mach 7 inflow.

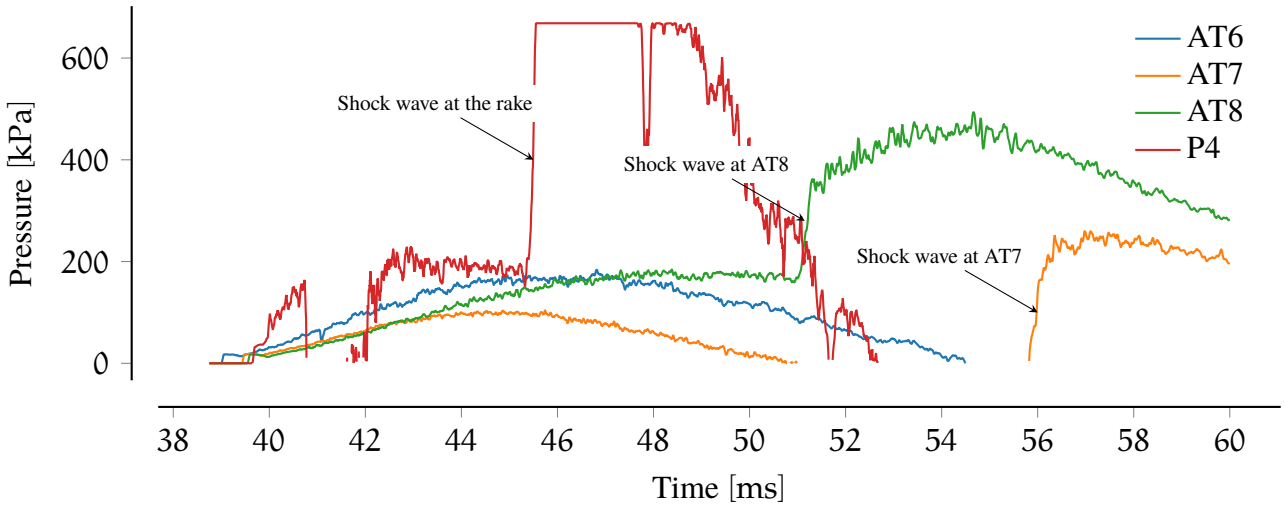

Figure 5.5: Normal shock wave forming at the inlet rake and travelling upstream. P4 is the rake centreline conehead pressure probe. AT8, AT7, AT6 are the upstream acceleration tube pressure sensors, located 1.05 m, 1.48 m and 3.08 m upstream of the inlet rake. Shot number: 582, scaled-pressure condition.

The rake was successfully operated in 20 distinct experiments, at the design and pressure-scaled conditions indicated in Chapter 3. The experiments did not indicate the formation of normal shocks-loading to choking of the flow during the test time or immediately after it. However, as expected, a normal shock has been detected in the final parts of the under-expanded test which has been observed travelling upstream. In Fig. 5.5 a sharp sudden pressure rise is observed at the rake (probe P4 in the nozzle centreline) about 5 ms after the initial flow arrival. A similar pressure rise, although decreasing in strength, is observed in AT8 and AT7 a few ms later, but does not reach AT6 further upstream. The test time for this condition starts shortly after the flow arrival, and ends well before the shock arrival.

5.2.4 Nozzle exit rake

Pitot pressure and conehead pressure measurements at the nozzle exit have been carried out with the use of an instrumented rake, as shown in Fig. 5.6. This rake can host up to 15 probes, with probe to probe spacing of 20 mm. All the probes hosted PCB 112-A22 pressure sensors with nominal 50 psi range, and both Pitot pressure and conehead pressure measurements have been made with the caps presented in Section 5.2.1. The rake was oriented vertically, occupying one radius of the nozzle, with PT1 the first probe aligned with the nozzle axis. Schematics of the rake location are shown in Fig. 5.7.

Figure 5.6: X3 expansion tube test section, enclosing Mach 12 nozzle and instrumented rake with conehead sensors.

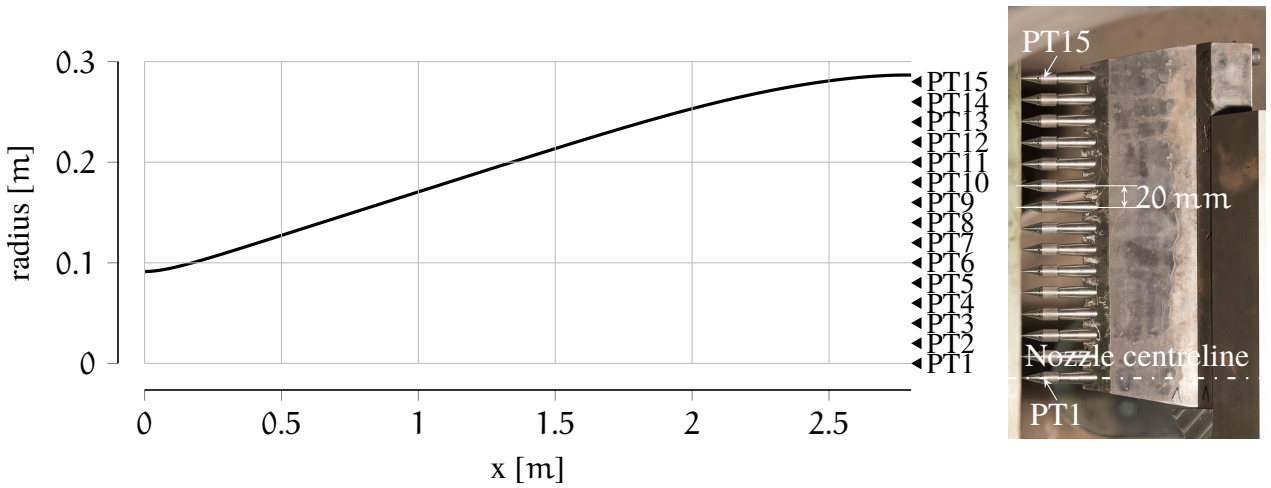

(a) X3 Mach 12 Nozzle profile and Pitot probe locations.

(b) X3 instrumented Pitot rake with conehead probes installed.

Figure 5.7: Nozzle exit plane pressure measurements: (a) nozzle profile and nominal probes location, (b) picture of the installed rake. Flow from left to right.

5.2.5 Median vs mean pitot pressure

Experimental Pitot pressure measurements in expansion tubes present high levels of noise and oscillation around the central value, to the extent that the mean might be skewed by the presence of outliers. In other words, mean is not a robust estimator for noisy data. On the same line of reasoning, the use of standard deviation, especially when the underlying distribution of the data is not normal, is heavily influenced by outliers [208]. Filtering in the post-processing phase is partially effective in removing outliers, but the presence of low frequency noise arguably cannot be removed.

The median is a robust estimator for central tendency, like the mean, but it is insensitive to the presence of outliers in the pressure measurements. Accompanying the median, the median absolute deviation (MAD) [209] can be used as a robust estimator of scale, defined as:

$$\mathrm{MAD} = \mathrm{median}\Big(\big|X_i - \mathrm{median}(X)\big| \Big) \tag{5.1}$$

where $X = X_1, X_2, \cdots, X_n$ is a univariate data set. Several authors recommend the use of median and MAD in presence of noisy data and outliers, such as [173, 208–210] and the reader is referred to those works for further discussion.

In practical terms, the "aggregated" pressure measurements presented here have been initially filtered using a constrained equiripple FIR low-pass filter, with a cut-off frequency of 150 kHz — the resonant frequency of PCB pressure sensors — and an order of 100 [170] and then the median of the pressure measurements has been taken, along with the median absolute deviation.

A comparison of average and uncertainty, estimated by using mean and standard deviation versus median and median absolute deviation is presented in Fig. 5.8, where the radial pressure profile is plotted. It can be noted that the calculated mean values along the nozzle centreline (r=0) are slightly, but not significantly, smaller than the median values. Further away from the centreline, the difference is negligible.

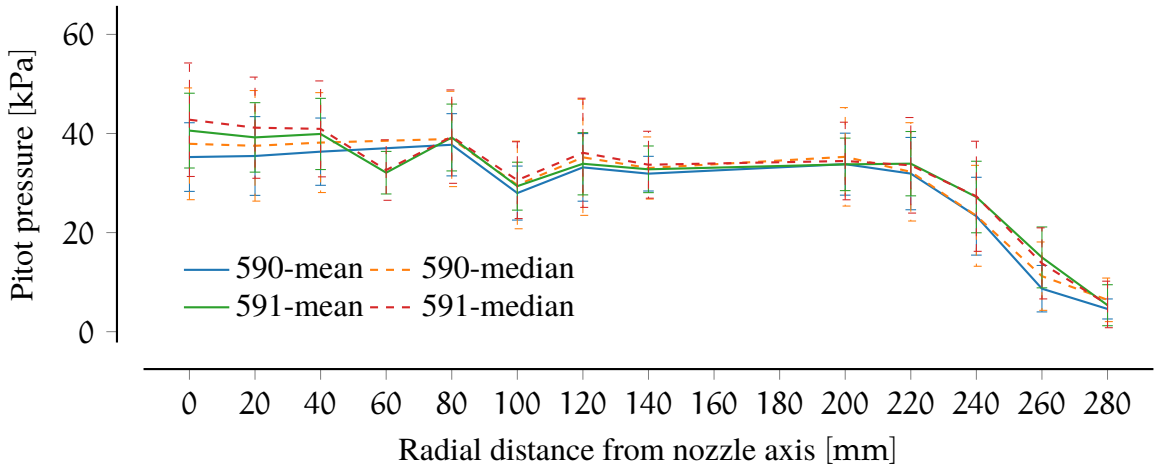

Figure 5.8: Comparison of mean and median as a central tendency estimator for the nozzle exit profile.

5.3 NOZZLE INLET RESULTS

In this section the experimental data obtained at the nozzle inlet is briefly discussed for both CONDITION x3s506 and CONDITION x3s582. For the design of the Mach 12 nozzle, initially, a boundary profile was selected with a thickness of 30 mm from the acceleration tube wall. This estimate was derived from simulations of previous flow conditions. In Fig. 5.9 the conehead pressure profile across the nozzle centreline is presented for both the nominal CONDITION x3s506 (dashed lines, pressure scale in right axis) and the pressure-scaled CONDITION x3s582 (solid line, left axis). It is apparent that a core flow region is not clearly identifiable, and the boundary layer occupies the entirety of the tube, reaching the nozzle centreline. The same profile shape is obtained for both conditions.

In Fig. 5.10 the evolution of the flow after shock arrival, in 200 µs intervals is shown. The first graph, in the top left corner, corresponds to the acceleration tube gas slug, where the profile is uniform as expected. Progressing through the test time from 600 µs onwards, it is immediate to note that there is a steady gradient pressure rise, and that the profile rapidly assumes a V-like shape, with the boundary layer occupying the entirety of the tube.

These observations show that this flow condition does not operate very closely to the one used to estimate the inflow for the nozzle design. Additionally, it was previously noted in Fig. 3.7 that there is a ~15 % shock speed attenuation in the acceleration tube and therefore the test gas is under-expanded. The acceleration tube ratio length/diameter is likely to be too high, in accordance with the Mirels' theory (discussed in Section 2.9.3). In these off-design conditions, where the inflow in the nozzle is slower and at higher pressure, with a thicker boundary layer, the nozzle is expected to under-perform and produce a lower exit Mach number flow.

For future studies, to fully restore the nozzle capabilities and to solve this problem, it is proposed to shorten the acceleration tube, removing one or more of its 4 m long sections. As it stands, the flow is too slow and boundary layer too thick. Additionally, the last section of the tube is where most of the shock speed attenuation occurs, so that both phenomena could be greatly reduced if the acceleration tube was shortened.

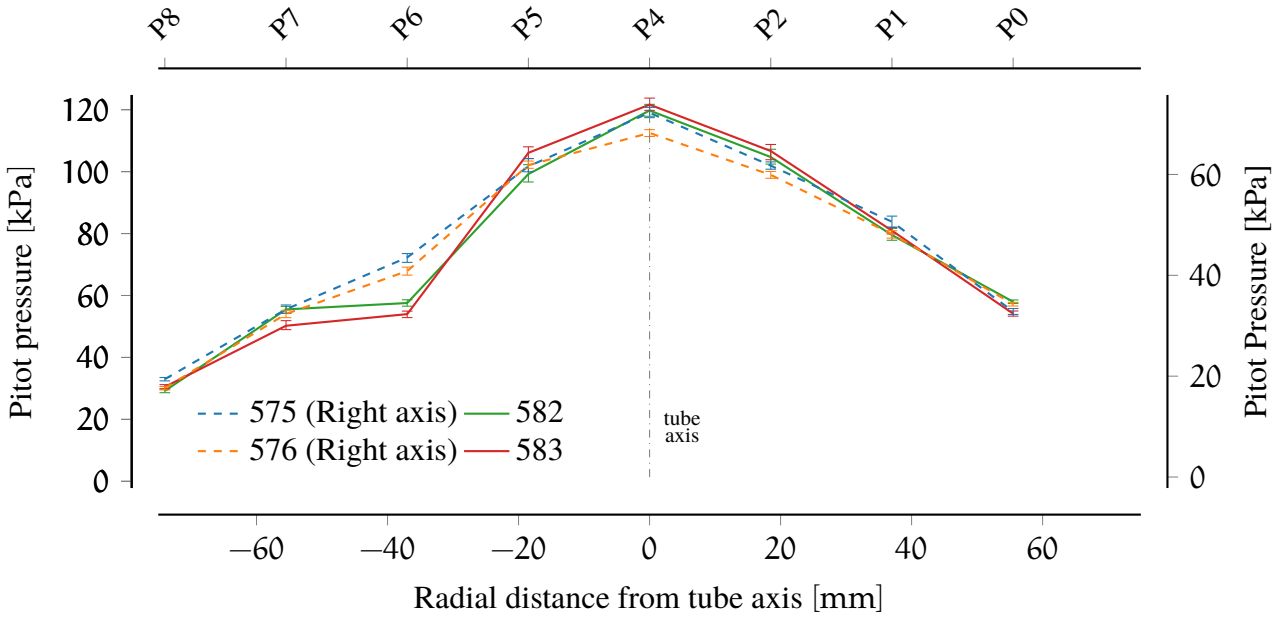

Figure 5.9: Nozzle inlet aggregated conehead pressure profiles for the nominal Condition x3s506 (dashed lines, right axis) and the pressure-scaled Condition x3s582 (solid lines). Selected test time length 1 ms. The error bar corresponds to the 0.95 confidence interval for the median.

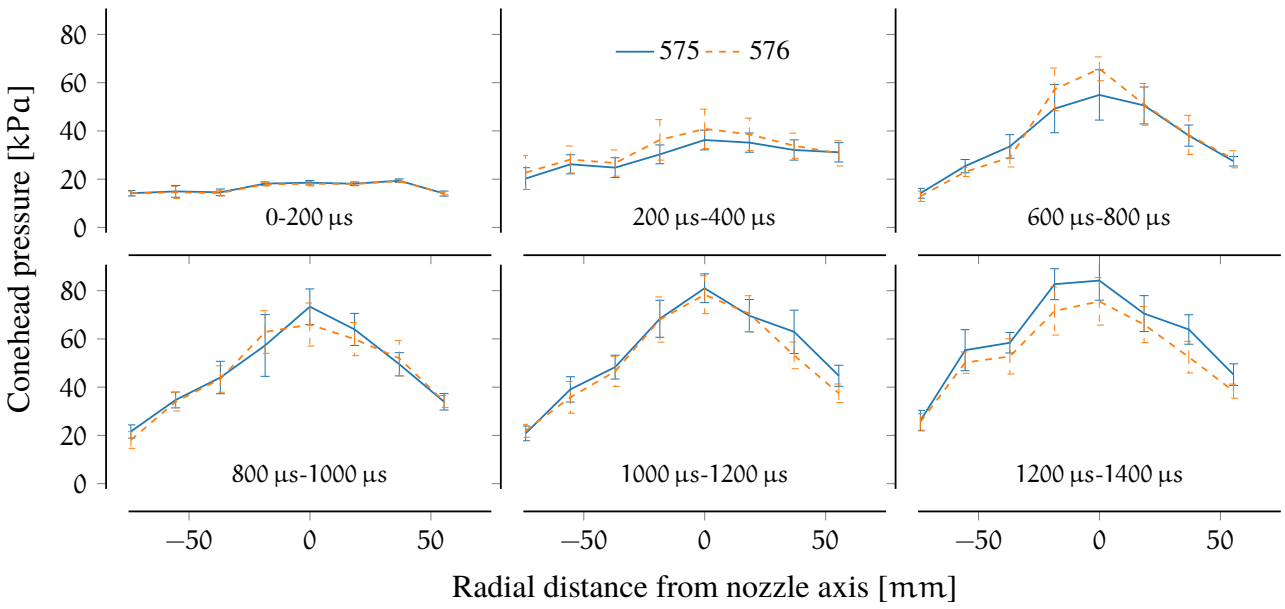

Figure 5.10: Nozzle inlet conehead pressure profiles across time for Condition x3s506. Shock arrival corresponds to t=0 s.

5.4 CORE FLOW AND TEST TIMES

Expansion tubes are, in theory, limited by the arrival of the unsteady expansion — either its downstream end or the reflected upstream head — but in practice, as shown in [129], the arrival of the unsteady expansion cannot clearly be identified, so there are no clear limits apart from a measurable departure from certain "mean properties".

High enthalpy expansion tube experiments may be limited by other flow processes, such as radiation or contamination from diaphragm debris, but in the case of low enthalpy scramjet conditions, the test time is generally limited by acceptable levels of noise in the Pitot traces and acceptable levels of departure from nominal condition. Figure 5.11 and Fig. 5.12 illustrate a typical set of Pitot traces at the nozzle exit. Prior to the test time, there is an initial pressure rise for about 200 μs, due to the nozzle startup process. Immediately following, the test time starts, continuing until some high frequency noise makes any measurements impossible. This noise may be associated with diaphragm particulate impacts, as shown by Miller et al. [211]. The test time duration for Condition x3s506 is 1.3 ms, and for Condition x3s582 is slightly less at 0.95 ms.

A decomposition of the transient behaviour of the flow at the nozzle exit is shown in Fig. 5.13.

Core flow estimates can be obtained by plotting the averaged pressure data across the test time as shown in Figs. 5.14 and 5.15 for Condition x3s506, and Fig. 5.16 for the pressure-scaled Condition x3s582. A core flow of 400 mm is clearly identifiable, exceeding the numerical prediction of 360 mm. The pressure-scaled condition shows an increased variability across the nozzle radius, for a reduced core flow size of 320 mm.

The results have exceeded the numerical prediction carried out for a steady inflow. It is noted, however, that this hypersonic nozzle has the largest area ratio ever tested at the University of Queensland and, more generally, for this application, the largest in world (according to the literature).

In the core flow the Pitot pressure measured over 11 experiments is 42.2 ± 12.1 kPa and the conehead pressure is 3.2 ± 0.7 kPa. These measurements do not directly translate to a flow condition estimate, and their consistency with flow shock speeds, numerical and analytical estimate needs to be assessed. This discussion will take place in the last part of the chapter, in Section 5.8.2.

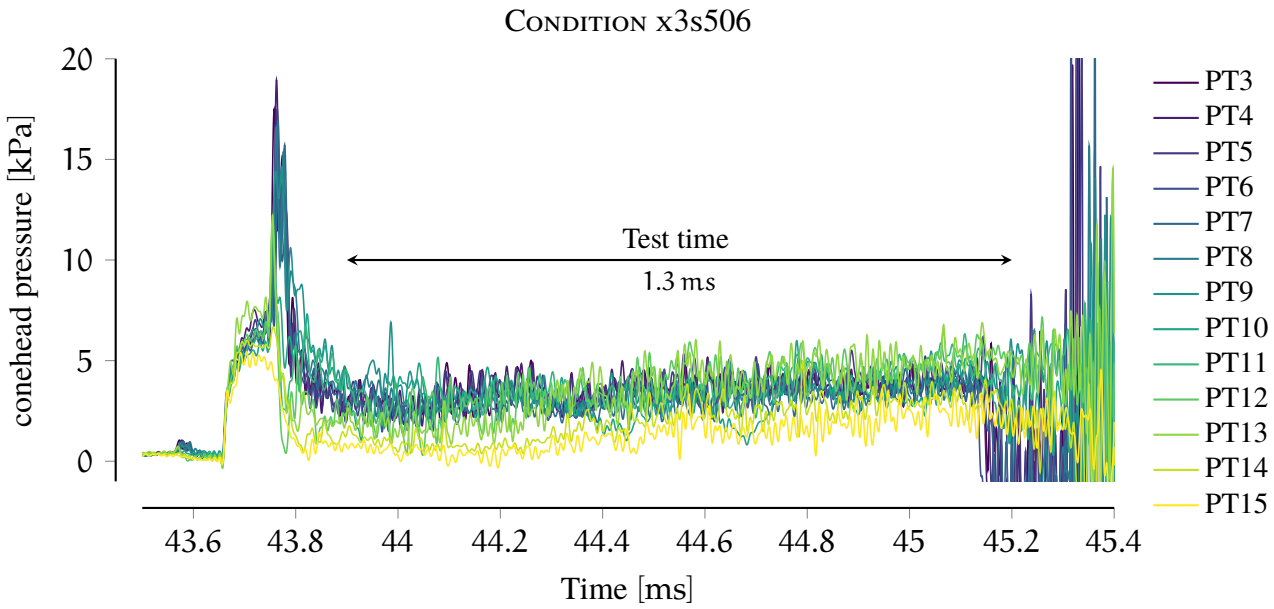

Figure 5.11: Experimental conehead pressure traces for shot x3s586, nominal flow Condition x3s506.

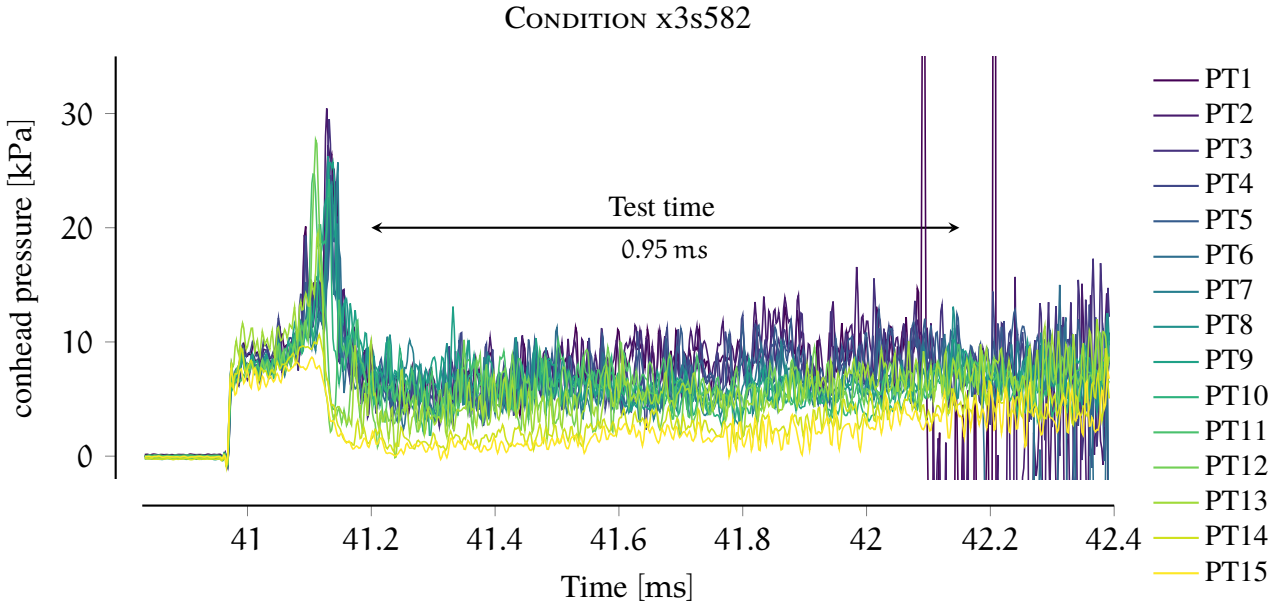

Figure 5.12: Experimental conehead pressure traces for shot x3s588, pressure-scaled flow Condition x3s582.

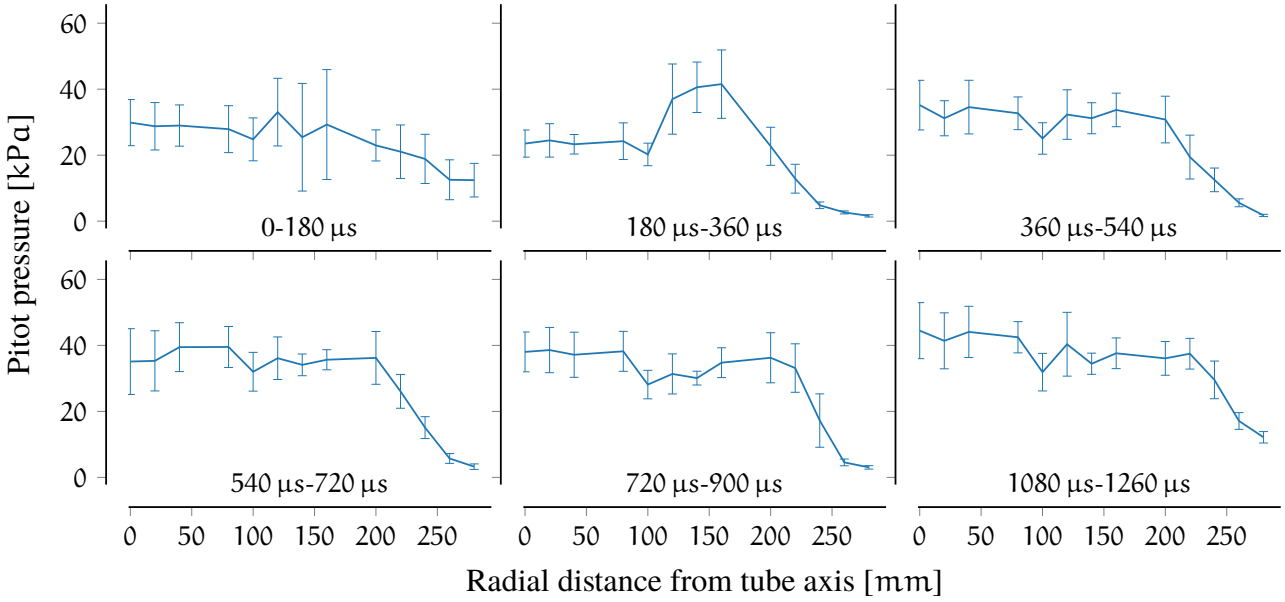

Figure 5.13: Nozzle exit Pitot pressure profiles across time for CONDITION x3s506. Shock arrival corresponds to t=0 s.

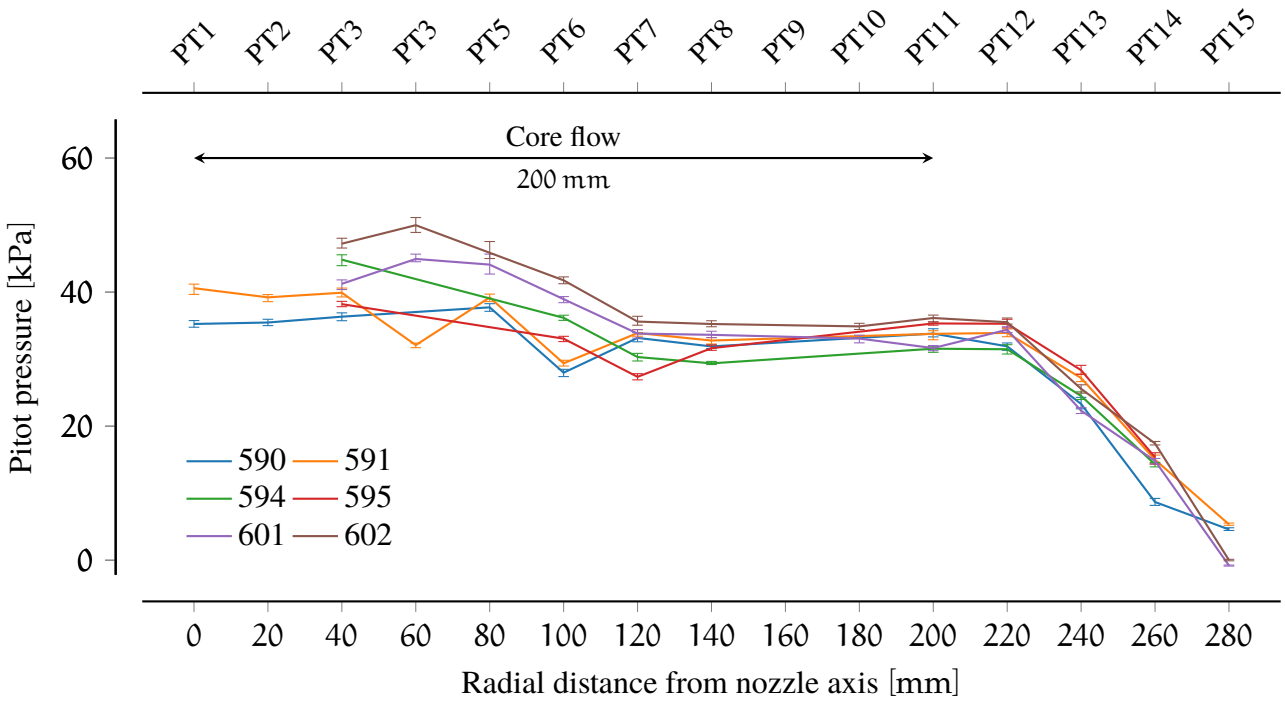

Figure 5.14: Averaged *Pitot pressure* across the nozzle for CONDITION x3s506. The nozzle centreline corresponds to x=0. A core flow of 400 mm in diameter can be noted. The error bars correspond to the 0.95 confidence interval for the median.

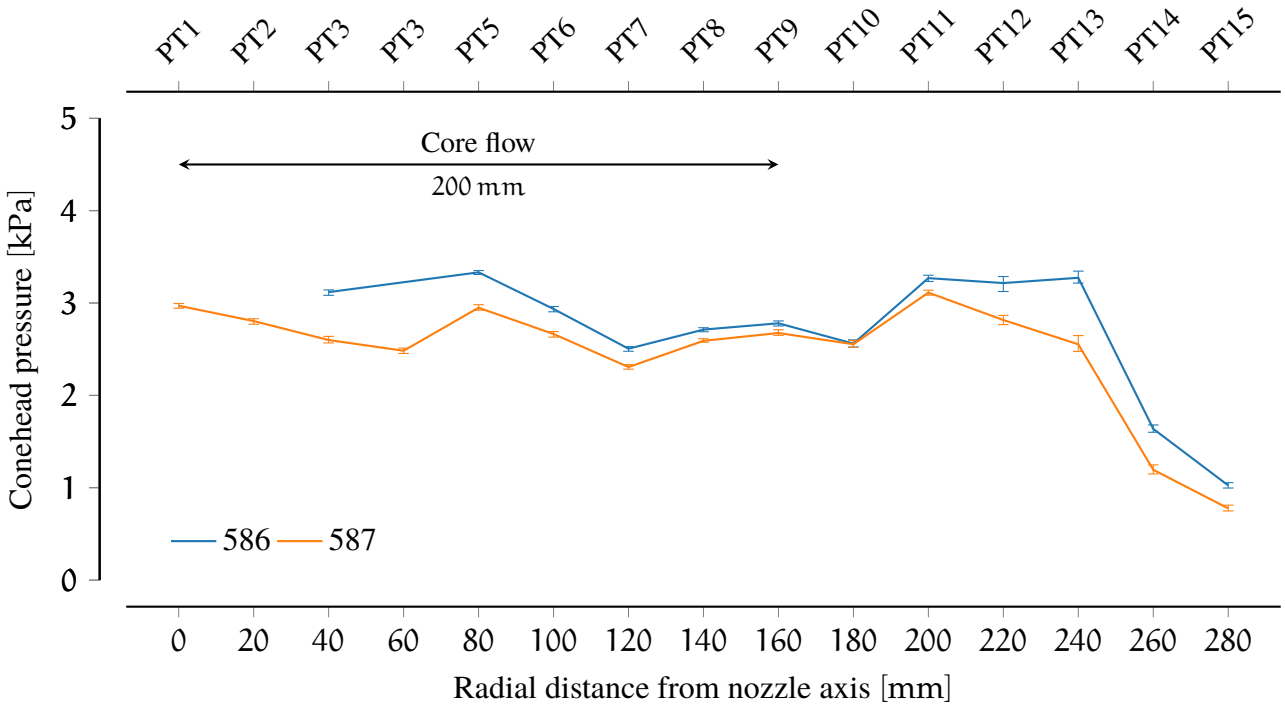

Figure 5.15: Averaged *conehead pressure* across the nozzle for Condition x3s506. The nozzle centreline corresponds to x=0. A core flow of 400 mm in diameter can be noted. The error bars correspond to the 0.95 confidence interval for the median.

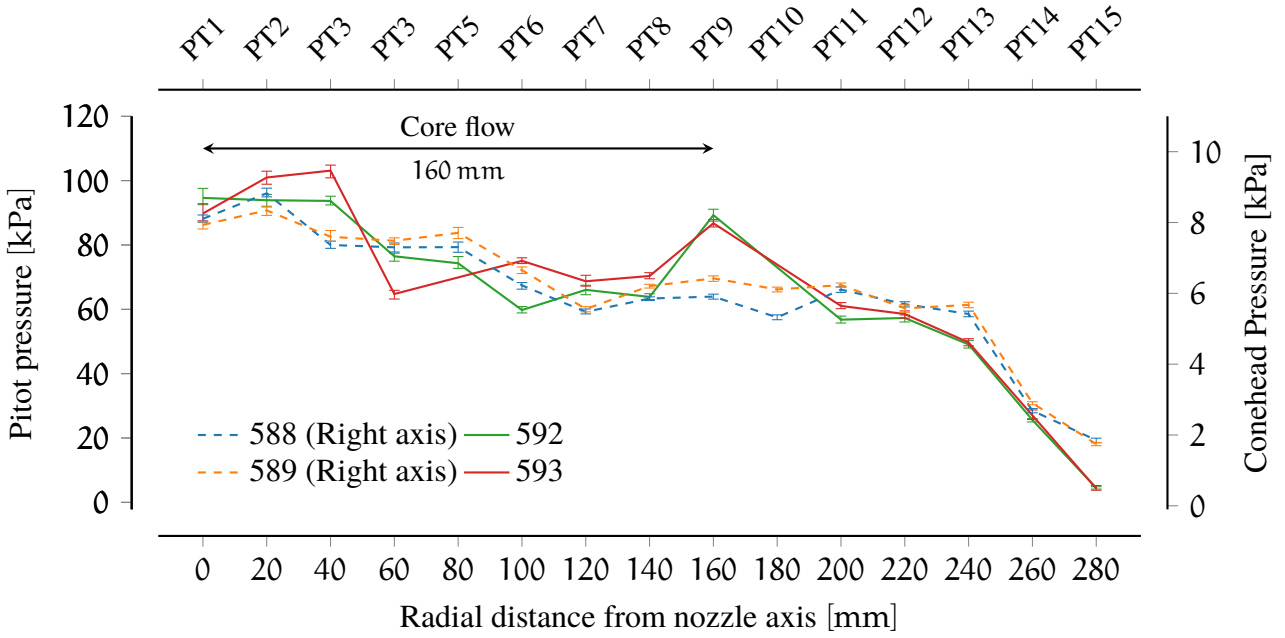

Figure 5.16: Averaged *conehead and Pitot pressure* across the nozzle for Condition x3s582. The nozzle centreline corresponds to x=0. A core flow of 360 mm in diameter can be noted. The error bars correspond to the 0.95 confidence interval for the median.

5.5 MACH NUMBER EXPERIMENTAL ESTIMATION

The experimental results in the previous sections do not allow easy and direct estimation of the flow Mach number. An additional series of experiments took place where a 30° wedge was located on the nozzle axis, and a schlieren imaging system was used to measure the shock-wave angle. Measured shock-wave angle then allows an estimate of the Mach number, independently of the noisy pressure measurements previously discussed. If successful, these tests would experimentally confirm that the facility is able to produce the desired flow condition at high Mach number, the underlying requirement for effective and useful high Mach number scramjet experiments.

Schlieren imaging relies upon the change in the refractive index of the gas that is proportional to the gradient of density. A collimated light beam traversing the gas, within which density gradients are present (generated for example by shock waves), is deflected proportionally to the density gradient. The beam is then focused on a knife-edge, where the proportion of deflected rays are "cut" leading to local darkening, whereas other deflected ways are superimposed, leading to local brightening. The remaining light is subsequently focused on a camera, where recorded images show an intensity dependent on the density gradient. This technique allows clear visualisation of compressible flow features, such as shock waves, produced in supersonic and hypersonic flows. The reader is referred to the detailed dissertation of Settles [212] for more details.

5.5.1 Experimental setup

The experimental setup is shown in Fig. 5.17. For these tests the instrumented rake was lifted 26 mm to allow sufficient space for the 30° wedge to be installed 5 mm below the nozzle axis. BK7 optical quartz windows were installed to maximise transmissivity in the visible region. Three experiments were carried out in this configuration, but for sake of brevity, only the set of experimental data from a single test is discussed. The experiments were a repeat of Condition x3s506.

5.5.2 Schlieren setup

The schlieren setup adopted for these experiments is shown in Fig. 5.18. A custom-made high-power LED was used as a light source, and combined with a small diaphragm to create an adequate point source. A planar mirror, and a spherical mirror with 1 m focal length, were used to redirect and align the light with the wedge located at the nozzle centreline. The LED light source was over-driven to maximise the light intensity. The LED output is also characterised by a narrow green band high-power light so that it can be isolated from the luminosity of the hypersonic flow with a corresponding green filter.

On the opposite side, with respect to the test section, the image recording system consisted of a Phantom v611 high speed camera, with a Nikkor 100–300 mm lens. A green light filter (bandpass 532 nm) was installed in front of the lens to filter all the light not produced by the LED source. A combination of planar mirrors and a spherical mirror with 1 m focal length redirected the light onto the knife-edge and then onto the camera for recording. The camera frame-rate was set at 22 kHz with an exposure time of 40 µs, for an image resolution of 512x504. An example of the acquired raw schlieren image is shown in Fig. 5.19.

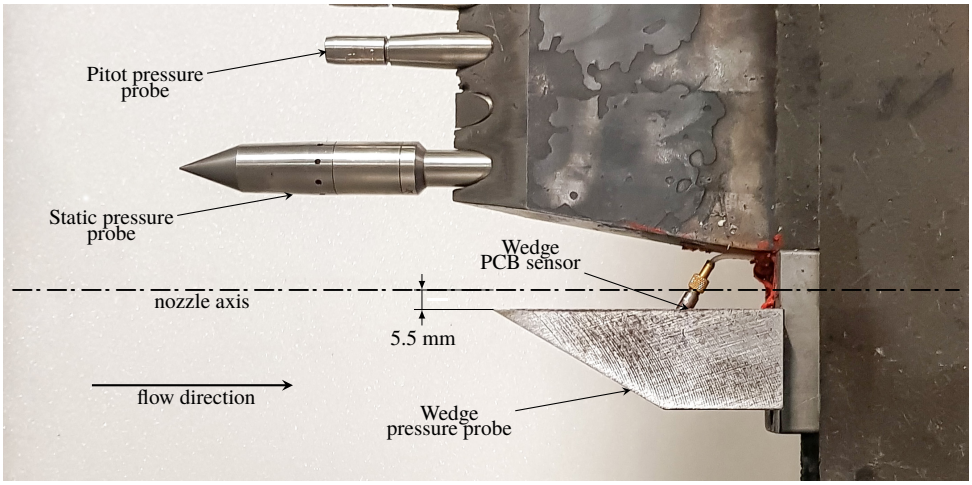

Figure 5.17: Details of the rake experimental setup including a 2D 30° wedge, static pressure probe and flat Pitot probes.

5.5.3 Shock angle detection methods

A time-accurate image tracking routine, capable of sub-pixel resolution, developed by Laurence and Karl [213] and based on the Canny edge detection algorithm [214], was adopted to detect and measure the shock angle in the recorded schlieren images. The Canny algorithm is a classic multi-stage algorithm that has shown to be easy to implement and very effective at detecting edges in images. The time-accurate algorithm identifies the initial edges and follows them across time and space. The routine is able to achieve a sub-pixel resolution, which is required to obtain improved angle measurements. It is based on the use of quadratic polynomial interpolation of the local edge gradient intensity magnitude field. This technique has been used for a variety of time-accurate force-measurements in hypersonic facilities. For further details the reader is referred to references [213, 214].

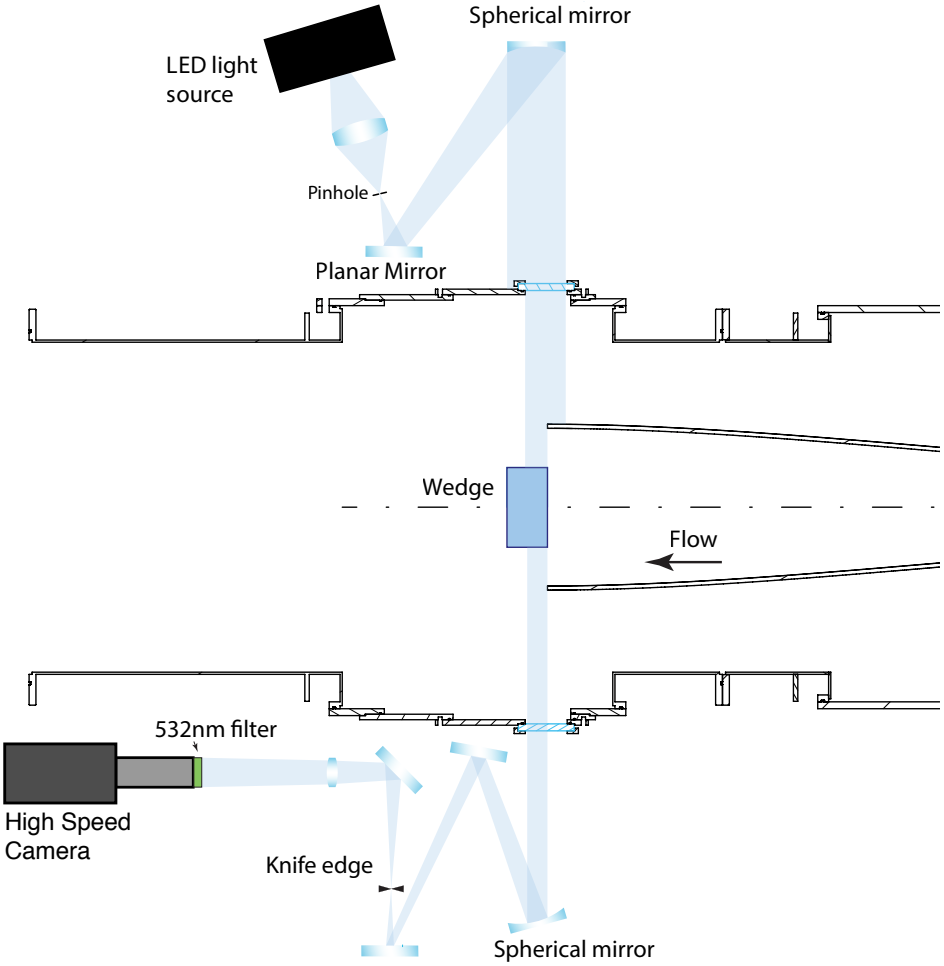

Figure 5.18: Schlieren setup around the test section. Flow from right to left. A periscope was used to bring the light path at the correct height for the camera, not represented in figure.

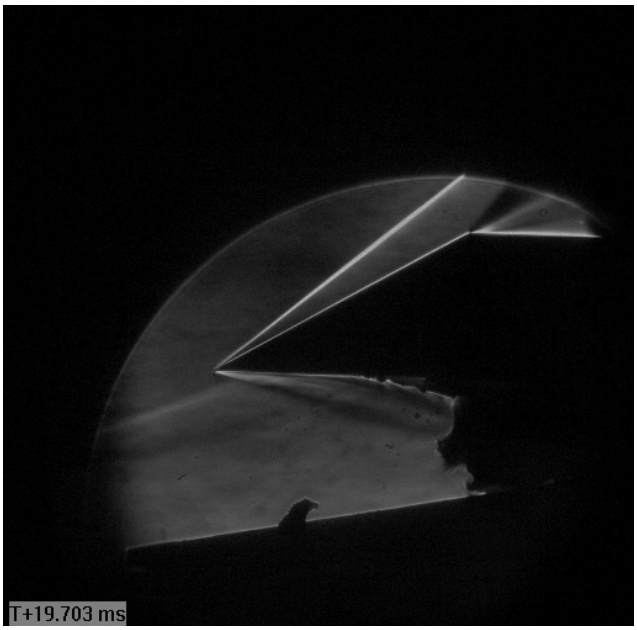

Figure 5.19: Raw schlieren image around the wedge. Flow from left to right.

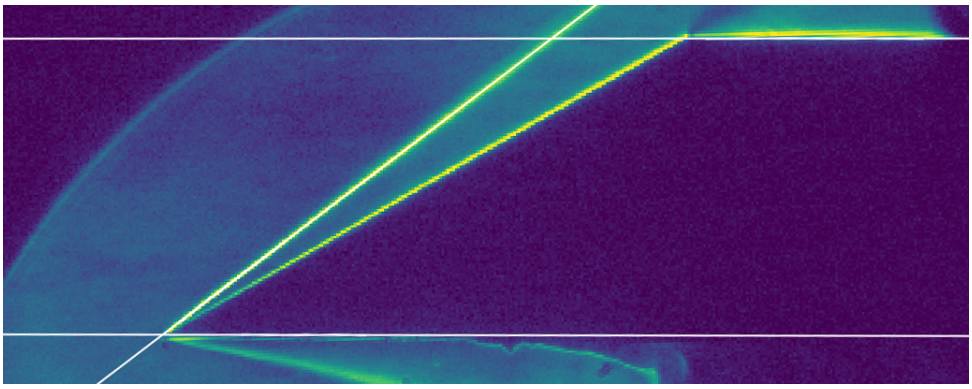

Figure 5.20: Example of a post-processed frame from schlieren video, enhanced colours and edges detected. Flow from left to right.

5.5.4 Results and discussion

The results are presented in Fig. 5.21, where the angle versus time is plotted. An angle increase with time is noted, compatible with the steady pressure gradient experimentally observed for the Pitot pressure traces, as the gas going over the wedge has undergone a reduced amount of the theoretical unsteady expansion and is getting hotter, thus reducing the Mach number. The average measured angle of the wedge was 30.1°, both through the edge detection system and manually. Error bars indicate the standard deviation obtained by adopting different ways to estimate the angle (depending on the selected edges for the angle calculation).

Conversion to Mach number needs to consider the real-gas effects that can have a significant influence over the shock angle, exacerbated by the high Mach number. Taking these into account, an average Mach number was calculated with a value of 11.0 ± 0.9 during the test time, relatively close to the target Mach number of 12.

It is important to note that the measurements assumed that the flow is aligned with the wedge and that it is not angled with respect to the nozzle centreline.

A parametric CFD analysis, where the freestream temperature, pressure and Mach number were varied, was carried out to incorporate the real gas effects and the temperature dependency, as an independent check of the estimate calculated in the previous section. A simple 2D wedge was simulated with the US3D flow solver. Shock angles are detected and estimated using the same routines adopted for the experimental images. Results are indicated in Fig. 5.22. In the range of temperatures between 250 K to 300 K the Mach number at the mean measured angle of 37.3° is in the range 10.5 to 11. A slight pressure dependency is noted. The lower-than-expected Mach number is consistent with the shock speed attenuation already observed for Condition x3s506 experiments, but also with the thick boundary layer measurements with the inlet rake. The nozzle is operating at off-design conditions, explaining why the target Mach 12 is as not precisely met for this flow condition.

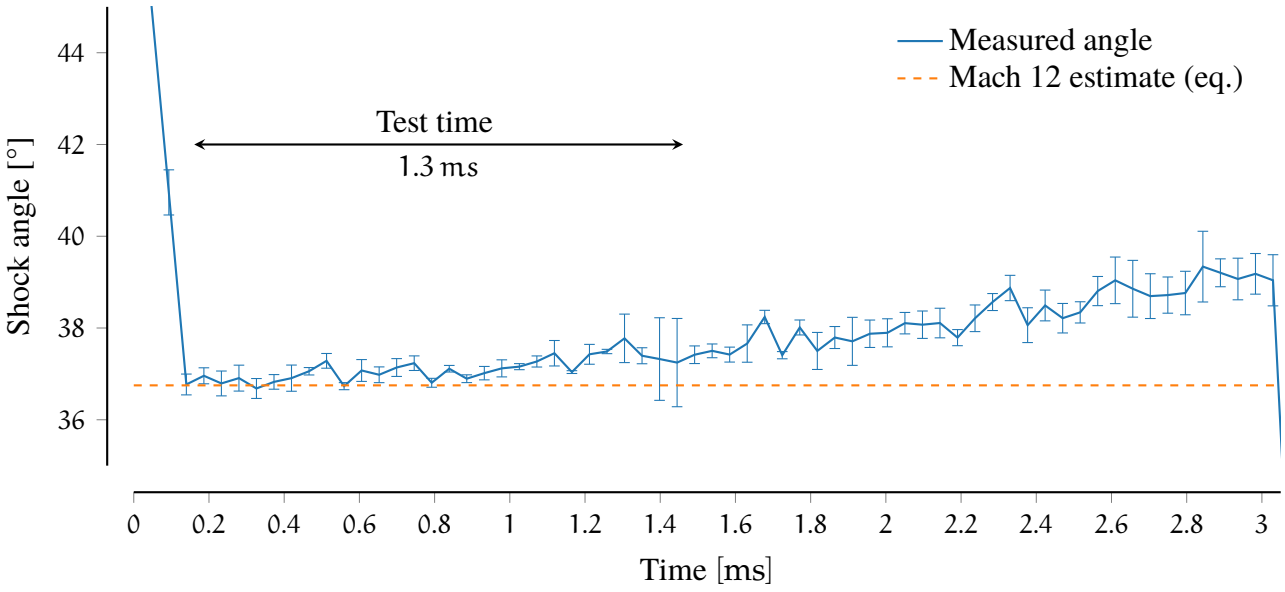

Figure 5.21: Measured oblique shock wave angle generated by a 30° wedge during experiment xs605. Average shock angle during test time= 37.3°.

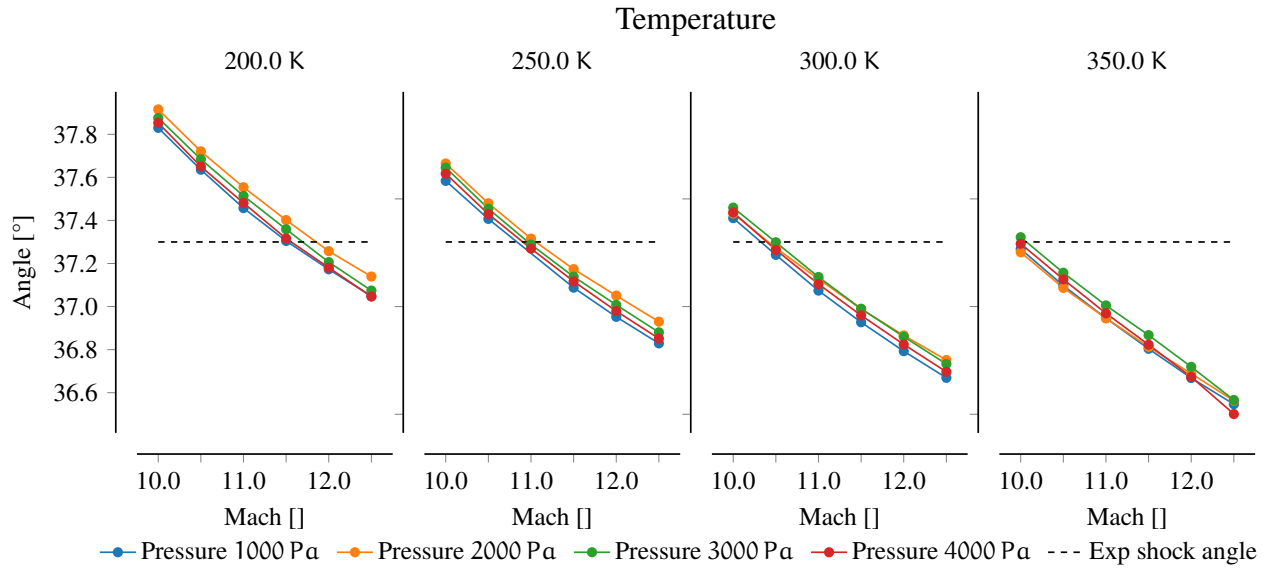

Figure 5.22: Parametric CFD study of oblique shock generated by a 30° wedge. Inflow temperature, pressure and Mach number have been varied and oblique shock detected with the same technique used for the experimental measurements.

In conclusion, these experiments have shown that is possible to have time accurate measurements of flow angle at high Mach number, showing that the estimated Mach number is close to the ideal, target Mach number albeit a bit lower than the targeted due to viscous effects in every long acceleration tube. However, the uncertainty in the calculation of the Mach number is significant, therefore it can only be claimed that the experimental number Mach during the test time is, on average, 11 ± 0.9. As previously stated, a time-accurate facility CFD analysis is required to fully quantify the freestream properties. As will be seen in Section 5.8.2, significant discrepancy between computed and measured Pitot pressure was observed; this Mach measurement, although having moderate uncertainty has proven crucial to consolidating contradictory aspects of the final data.

From a condition development perspective, the result is very good, as it remains extremely challenging to design an expansion tube condition that is able to exactly match the desired target trajectory point. Also, in the context of this work, where the goal was to show that high Mach number scramjet experiment can be carried out in expansion tube, the exact match of the target flow condition has a reduced importance. In any case, the author is well aware that more work needs to be done to simplify the flow condition development and improve its accuracy.

5.6 NUMERICAL MODELLING OF THE FLOW CONDITIONS

The previous section discussed the experimental results that have been obtained using the new Mach 12 nozzle and the Mach 12 operating condition designed for the X3 expansion tube. Core flow sizes exceeded the earlier numerical prediction, and average Mach number was measured to be approximately 11. However, extrapolations of flow properties from measured Pitot pressure and conehead pressures are more difficult. Flow uncertainties, the steady pressure gradient in the test time and noise disturbances, make achieving correlation amongst the different measurements extremely challenging. To complement experimental results and to obtain an estimate of the freestream properties, the analysis was augmented with numerical simulation tools.

In this second part of the chapter, we will discuss the approach and results of the numerical work carried out to fully characterise the flow condition. It is important to note that this analysis has only been conducted for one of the two conditions developed in this thesis, the reference Condition x3s506. The pressure-scaled Condition x3s582 has not been numerically simulated and is scaled instead.

5.6.1 On the difficulties of simulating expansion tube flows

Simulating expansion tube flows is without doubt complex topic due to the very elaborate interactions and the intrinsically dynamic and transient nature of expansion tubes. The expansion mechanism, while producing significantly high enthalpy conditions, essentially couples all the different gas slugs

of the facility. Thus, any simplifying hypothesis assumed for each gas slug has a direct effect on the final flow properties.

Diaphragm rupturing pressures and rupturing processes have a measurable effect on the gas, and they cannot be neglected. Free-piston driven expansion tubes have the increased complexity of a high-speed moving piston compressing the gas which needs to be integrated into the numerical simulations. Finally, the flow encounters a variety of different conditions, from a low speed subsonic compression prior to diaphragm rupture, then high-density supersonic flows in the shock tube, to low-density extremely fast hypersonic flows in the acceleration tube. The unsteady expansion mechanism is such that the flow exiting the hypersonic nozzle is time-varying, and viscous effects in the hypersonic flow are responsible for radially non-uniform flows, but the levels of spatial compared to temporal property gradients are such that a quasi-steady analysis is valid.

To put things in perspective, reflected shock tunnels are somewhat more straight forward to simulate numerically. Although the initial shock production mechanism is the same — with a free-piston driver rupturing a diaphragm and generating a shock travelling downstream — once the shock is reflected the flow is then stagnated. Albeit complex transient phenomena are still present, such as driver gas contamination and shock bifurcation, however numerical models simulating a nozzle expansion from steady stagnation properties have shown to closely reproduce experimental measurements. Indeed, 2D axisymmetric simulations, taking no more than a day to complete, are able to compute the experimental condition with good agreement with the measurements, and be re-run to capture shot-to-shot variations [193].

Expansion tube numerical calculations require higher computational power and cannot reach the same level of accuracy because of the reasons listed above. Notwithstanding these difficulties, it is of fundamental importance to progress and advance towards better numerical models, in order to improve the use of the expansion tube capabilities at high enthalpies and Mach numbers.

5.6.2 On the limits of analytical models

Analytical models, such the one presented in Section 3.3.1 and Pitot, [121] although useful in the design phase, fail to capture all the phenomena that occur in real expansion tube flows. The simple expansion tube abstraction on which they are based is the one discussed in Section 2.9.1: in each tube section a shock wave processes the standing gas, and the gas coming from the previous section undergoes a full unsteady expansion to match flow properties of the shock-processed gas. The most important assumptions are that the shock speeds are constant in each section of the tube, and that the shock-processed test gas and unsteadily expanded test gas maintain the same pressure and velocity across the contact surface. Additionally, no viscous effects, such as partial unsteady expansion or shock speed attenuation, are considered. These phenomena, as previously discussed, have a significant impact on expansion tube flows.

A common solution is the introduction of empirical factors tuned to match experimental data, coming in the form of Pitot pressure. It is unclear, however, how other freestream properties are affected by em-

pirical factors. The experimentally observed behaviour of X3 test flows deviates significantly from the ideal expansion tube flow, and any data obtained from analytical models (including tuning loss factors) is unlikely provide an adequate representation of the flow properties in the expansion tube. The analytical estimates are still useful as a "sanity check" for experimental measurements and CFD results, but high fidelity CFD simulation is required to fully capture the flow dynamics of expansion tube experiments.

5.6.3 Methodology overview

As stated in previous chapters, full facility CFD simulations, including piston dynamics and rupturing diaphragms, for a facility of the scale of X3, is well beyond our current capabilities. For this analysis, therefore, a hybrid approach was adopted.

The first part of the facility has been simulated using L1D, the 1D lagrangian code previously introduced in Section 3.3.2 and employed to design the lightweight piston operating conditions. The shock tube has been included in the L1D simulations. This code is able to adequately capture the piston motion and the axial wave processes: adopting appropriate loss factors, the piston motion and the driver wall pressure measurements can be "tuned" to closely match the experiments. However, the code fails to reproduce viscous and heat transfer effects, along with radial waves. These effects are much more significant in the high-speed low-density flows that develop in the acceleration tube. For this reason, the second part of the facility has been simulated with the CFD RANS code Eilmer3, previously presented in Section 4.5.1 This hybrid approach has the advantage of notably reducing the required computational time, along with exploiting the excellent piston modelling capabilities of L1D, which, by using Lagrangian description of the gas flows, is naturally well suited for the modelling of moving sections

This approach is derived from the work of Gildfind et al. [166], who successfully reproduced the experimental results of a X3 Mach 10 condition with a similar hybrid technique. Gildfind proposed the use of a "driver equivalent temperature", estimated from shock speed calculations, to be used in the simulations. The technique for the Mach 10 condition was effective, and numerical flows were close to the experimental data.

In the first iteration of this analysis, a wide range of driver equivalent temperatures were simulated and compared to the experimental data; however, they failed to reproduce the experimental shock speeds and pressure traces in the shock tube. It is supposed that such failure is linked to the fact that Condition x3s506 used a 100 % Argon driver. This gas driver generates much stronger waves in the flow compared to a helium driver (used in the Mach 10 condition). It is postulated that the acoustic waves are sufficiently strong to partially open the diaphragm, so that the shock tube flow becomes "wave-dominated" and leads its modelling to require a modified approach.

Considering the above, a different approach was attempted, disregarding the "driver equivalent temperature" approach. A facility L1D model was developed, including the use of several loss-factors and other constants (that will be described later) that effectively can be varied to reproduce

the experimental conditions. An optimisation routine was then applied, to select the most adequate combination of tuning parameter, and a model that was able to most adequately reproduce the required shock speeds was chosen. The flow hence obtained was then fed to the 2D axisymmetric simulations that completed the numerical analysis. The following section will examine the first part of the analysis.

5.7 DRIVER AND SHOCK TUBE 1D MODELLING

A model has been developed to include reservoir, piston, and compression and shock tube. This is an extension of the model used to develop and tune the lightweight piston operating condition in Section 3.5. In Fig. 5.23 a comparison of the numerical model against the experimental pressure trace near the primary diaphragm is shown, where excellent agreement can be observed.

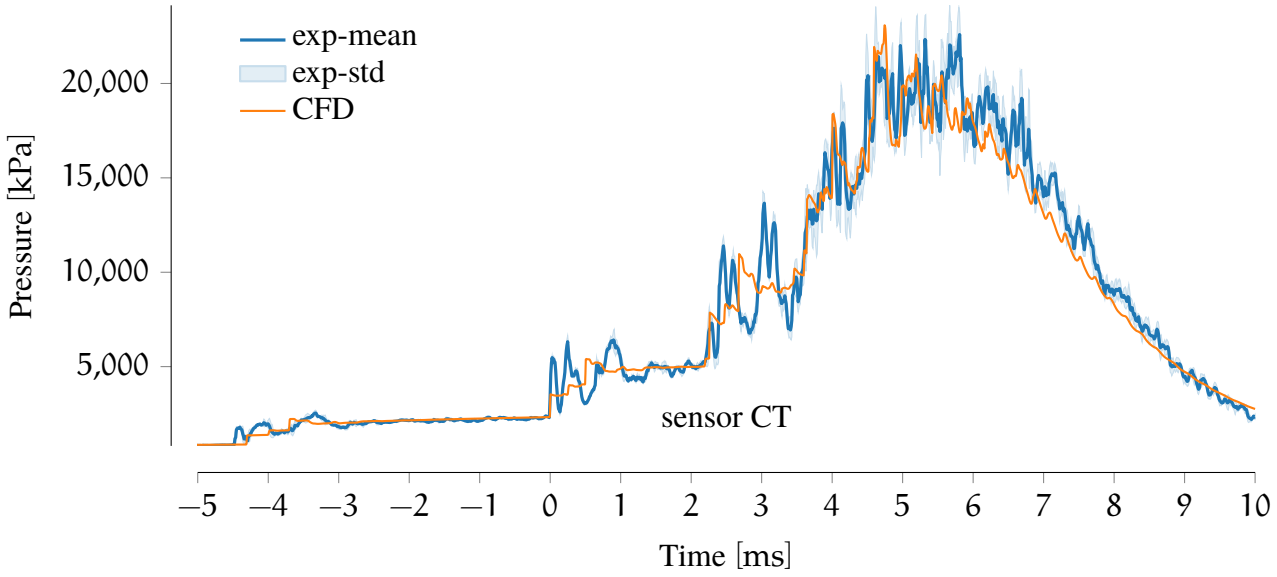

Figure 5.23: Experimental and L1D comparison of the wall pressure traces at the CT location (0.2 m prior to the diaphragm). Experimental data is an 11-shots average.

The final L1D model geometry that has been prepared is shown in Fig. 5.24. The shock tube includes the area change that is present at the secondary diaphragm station. Initial iterations indicated that the primary diaphragm rupturing process was the most significant phenomenon affecting shock speeds and shock tube pressure traces, which is, from both the experimental and numerical perspective, the region where the physics is most complex. The flow is inherently three-dimensional in this area, and the steel diaphragm fracture mechanics is not trivial. It is not surprising that this region is difficult to model effectively with the 1D code, where the diaphragm model is treated as a simple boundary that is automatically removed once a target rupture pressure is reached in a region immediately upstream of the diaphragm.

Loss factors, as presented below, are usually applied to make up for the discrepancies. Additionally, to improve the simulation capabilities, the diaphragm opening model was improved, introducing a time-varying geometry capability for the code. Together, loss factors and the new gradually opening

diaphragm model introduced a series of parameters that effectively could be optimised to produce a flow that closely matched the experimental traces. Rather than employing a time-consuming manual iterative approach, an optimisation routine was setup.

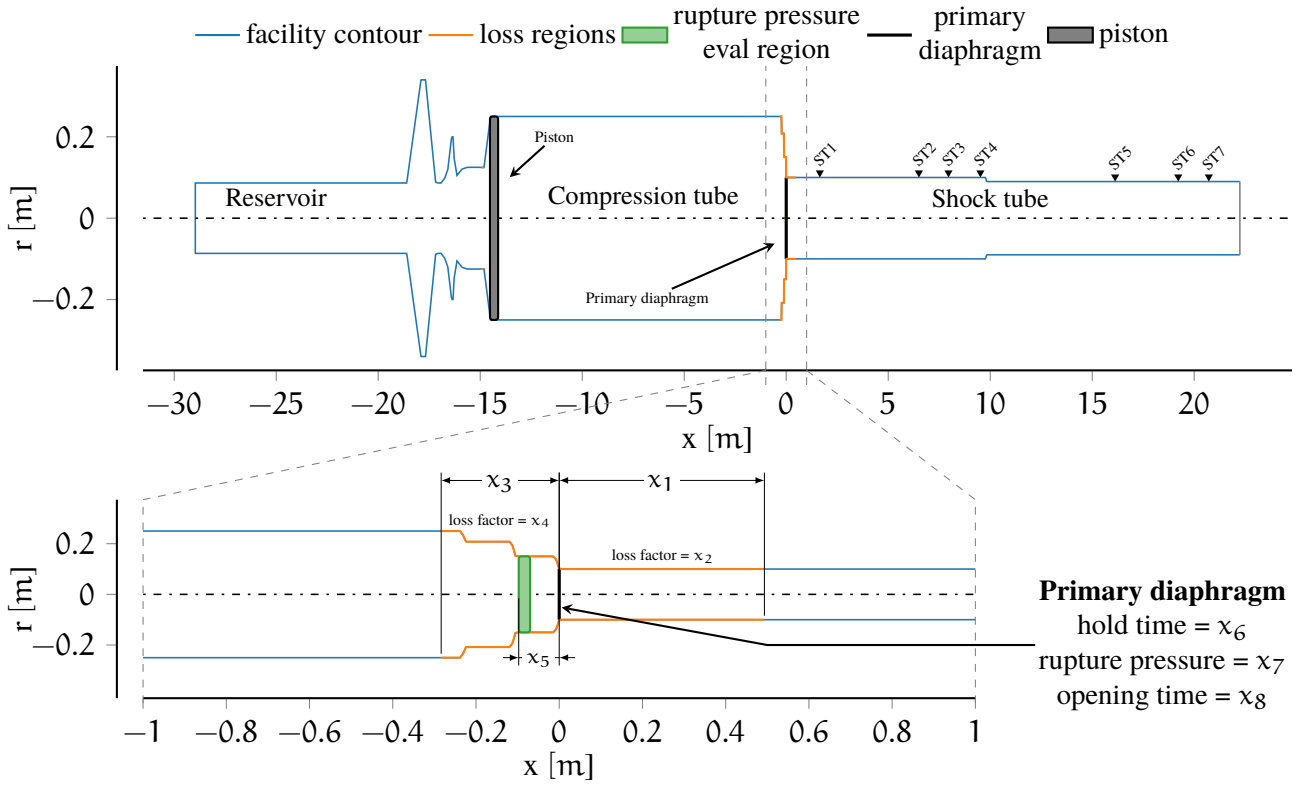

Figure 5.24: L1D model used for the numerical analysis of CONDITION x3s506. The top part is a complete overview. The bottom part shows at detail the diaphragm station, where all the modifiable tuning parameters and loss factors are presented and indicated as x_i.

5.7.1 Loss factor and loss region

The losses, due to three-dimensional effects and sudden changes in the cross section of the facility, are modelled in L1D with the introduction of "effective forces" that affect the discretised momentum equation [150]:

$$F_{loss} = \frac{\Delta P_{loss}}{L_{loss}} \bar{A} \left(x_{j+\frac{1}{2}} - x_{j+\frac{1}{2}} \right) \tag{5.2}$$

where:

$$\Delta P_{loss} = -K_L \frac{1}{2} u|u| \tag{5.3}$$

with L_{loss} the length of the section of the tube where the ΔP_{loss} is applied, $\bar{A}$ is the area of a single cell, ρ density, and u the local flow velocity. The values of K_L and the regions on which each K_L factor is applied are customizable in the L1D model. The regions that have a loss factor applied upon are highlighted in orange in Fig. 5.24.

5.7.2 A new gradually opening diaphragm model

A new diaphragm model was developed to include the following modifications in order to more closely replicate the effect of the diaphragm opening process on the tunnel flow.

- Gradually opening diaphragm: rather than fully opening instantly, the diaphragm gradually opens in a specifiable time.
- Initial hold time: once the rupture target pressure is reached, the diaphragm does not immediately start the rupture process, but waits for a custom holding time.
- Rupture pressure averaging area: the rupture pressure is not measured in the region immediately preceding the diaphragm. Indeed, numerical routines were responsible for the generation of localised, non-physical, extremely high pressure waves able to trigger rupture while the flow had not yet reached the realistic target pressure. Two parameters, exposed as simulation variables, allowed specification of the start and the end of the averaging region.

The augmented model introduced a new group of parameters, some of which were kept fixed, and the rest exposed as variables of the optimisation routine, as discussed below.

5.7.3 Tuning parameters

With the newly improved model of the first part of the X3 expansion tube (compression tube, primary diaphragm and shock tube), the parameters to which the flow was most sensitive were selected as the input variables for the optimisation process. They are identified in Fig. 5.24 and can be listed as follows:

- x_1: L_{loss}, extent of the shock tube loss region, starting at the diaphragm location ($x = 0$)
- x_2: K_L, loss factor of the shock tube loss region
- x_3: L_{loss}, extent of the primary driver loss region, starting at the diaphragm location ($x = 0$)
- x_4: K_L, loss factor of the primary driver loss region
- x_5: Upstream end of the pressure-averaging region used to calculate the rupture pressure. The downstream end of the pressure averaging region was set at $x = -0.07\text{m}$
- x_6: primary diaphragm hold time
- x_7: primary diaphragm rupture pressure
- x_8: primary diaphragm opening time

5.7.4 Grid convergence

The model includes 1000 cells in the reservoir gas slug, 1000 cells in the primary driver gas slug, and 2000 in the shock tube. No grid convergence has been carried out, as the model is derived from the one presented in [166], where it is shown that the 4000 cells model is a good compromise between simulation accuracy and simulation times.

5.7.5 Objective function

The objective function translates the goal of closely reproducing the shock speeds in the shock tube, along with the last pressure measurement ST7 as accurately as possible. Similarly to what was developed for the nozzle design objective function, the two objectives were scalarized using some arbitrary weight functions. The objective function is therefore defined as follows:

$$f\left(\vec{X}\right) = \left(f_{ss}\left(\vec{X}\right) + f_{P_{ST7}}\left(\vec{X}\right)\right)^2 \tag{5.4}$$

With f_{ss}, the shock speed term, $f_{P_{ST7}}$, the pressure term, given by:

$$f_{ss}\left(\vec{X}\right) = \phi_{ss} \sum_{j=1}^{4} \left(V_{L1d3,j}\left(\vec{X}\right) - V_{exp,j}\left(\vec{X}\right)\right)^2$$

$$f_{P_{ST7}}\left(\vec{X}\right) = \phi_{P_{ST7}} \sum_{0<t<8\,ms} \left(P_{L1d3}\left(\vec{X},t\right) - P_{exp}\left(\vec{X},t\right)\right)^2$$

The suffix L1d3 indicates the numerically calculated properties, whereas the suffix *exp* specifies 11-experiments-averaged properties. $P_{L1d3/exp}$ are the wall pressure measurements at the ST7 location. $V_{L1d3/exp,j}$ indicates the measured shock speeds between ST1-ST2, ST2-ST3, ST5-ST6, and ST6-ST7. $\phi_{ss}, \phi_{P_{ST7}}$ are the weights of the two terms of the objective function respectively set at $0.8, 0.2$. t indicates time from shock arrival at ST7.

5.7.6 Optimisation algorithm

Several optimisation techniques can be used for the parameter tuning task. For this task, each function evaluation requires running a L1D simulation, so that the objective function is expensive to evaluate. Additionally, the function is implicit in nature (i.e. "black box") as no information on the function itself or the gradients is available. A class of algorithm that has proven to work well with expensive black box objective functions is that based on response surface methods, where the objective function is reconstructed by a response surface that has been fitted to the few function evaluations previously calculated [215].

The optimisation algorithm adopted for the parameter tuning is a modified CORS (Constrained Optimisation using Response Surfaces), originally developed by Regis and Shoemaker [216]. This algorithm is specifically design for the evaluation of expensive black-box functions. It was chosen as it is easily scalable on computing clusters, and an initial implementation was originally available [217], although it was then modified to work in multi-node cluster jobs. In Section 12.2 the optimisation algorithm is described. The most significant advantage is that the algorithm is easily parallelisable up to hundreds of processors, and its accuracy and rate of convergence are proportional to the number of parallel function evaluations.

5.7.7 Optimisation results and discussion

Two final optimisations were evaluated, one using the standard "instant-opening" diaphragm model, and one using the previously described "gradual-opening" diaphragm, in order to assess whether, effectively, the moving diaphragm model is able to reproduce much more closely the physical behaviour. Each of the final optimisations evaluated around 3500 simulations. The results are shown in Figs. 5.25 to 5.28, where a handful of the best configurations are compared in terms of both shock speed and ST7 wall pressure history. The moving diaphragm model is able to closely reproduce the experimental shock speeds, down to within $\pm 10\,\mathrm{m\,s^{-1}}$ (~0.5 %) for the ST6-ST7 shock speeds measurement, as shown in Fig. 5.26. On the other hand, the standard diaphragm model could get only to within $90\,\mathrm{m\,s^{-1}}$ (~5 %) from the target shock speeds (Fig. 5.25).

Wall pressure measurements, shown in Figs. 5.27 and 5.28, exhibit a lower level of agreement between experimental and numerical data. The instantaneous diaphragm model exhibits a significant pressure rise in the first millisecond after the shock arrival. The gradually opening diaphragm model shows a much closer behaviour, although a discrepancy is still present immediately following the shock arrival. Further analysis have shown that upstream experimental pressure traces demonstrate the arrival of two shock waves one after the other, which coalesce into one between ST6 and ST7, a behaviour that is not observed in the L1D simulation. The cause of the double pressure rise is unclear but likely due to the strong waves generated in the argon driver, possibly opening the diaphragm in a multi-stage process, or a wave reflected off the piston face, travelling downstream at similar speeds as the primary shock wave.

The parameters generated for the final selected simulation, to be used as an inflow for the 2D CFD simulation of the acceleration tube, are shown in Table 5.2.

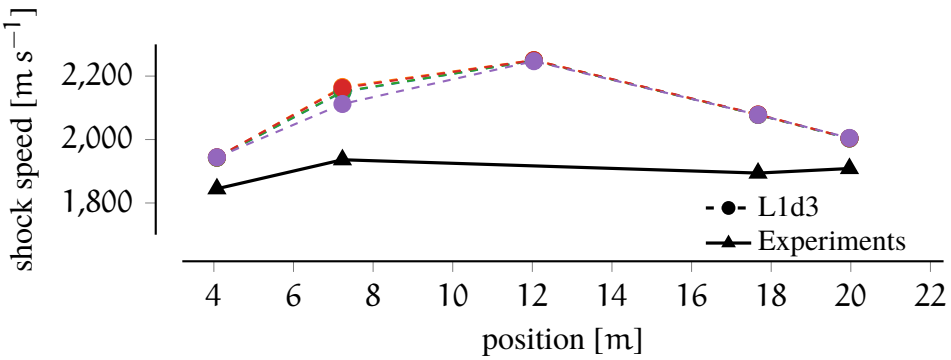

Figure 5.25: Shock tube shock speeds of the best four L1D experiments compared to an 11-shot experimental average, using the *instant-opening* primary diaphragm model.

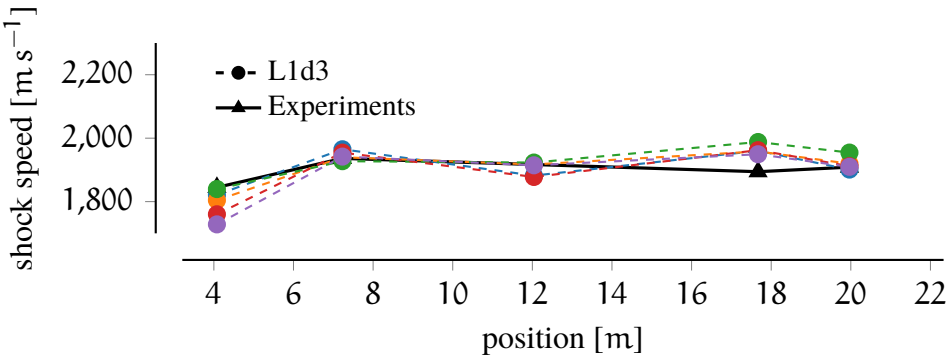

Figure 5.26: Shock tube shock speeds of the best four L1D experiments compared to an 11-shot experimental average, using the newly implemented *gradual-opening* diaphragm model for the primary diaphragm.

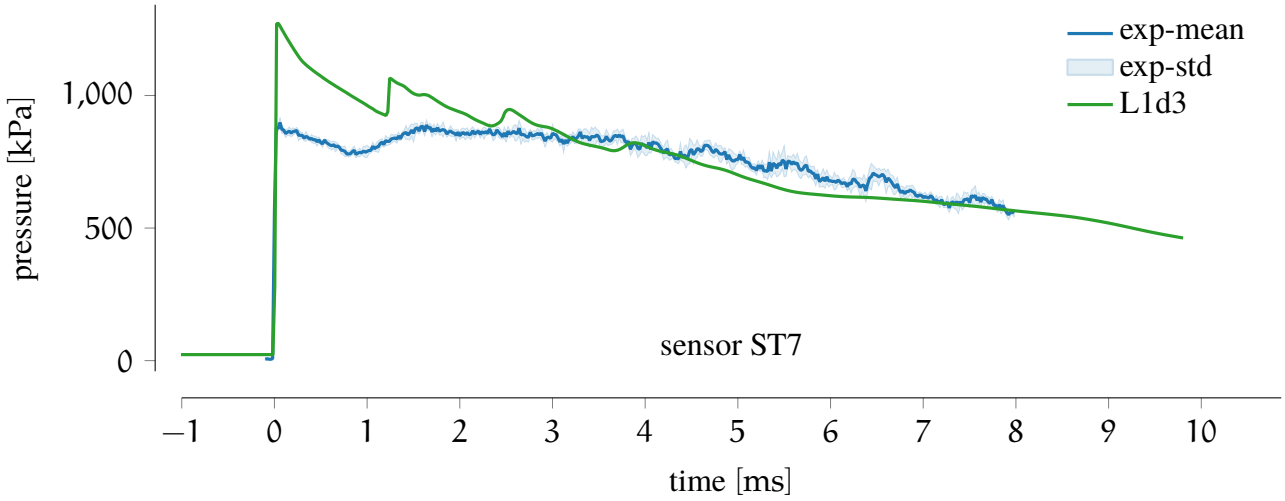

Figure 5.27: Experimental and numerical comparison of the wall pressure traces at the ST7 location: numerical data obtained with the *instant-opening* wall model for the primary diaphragm. Experimental data is an 11-shots average.

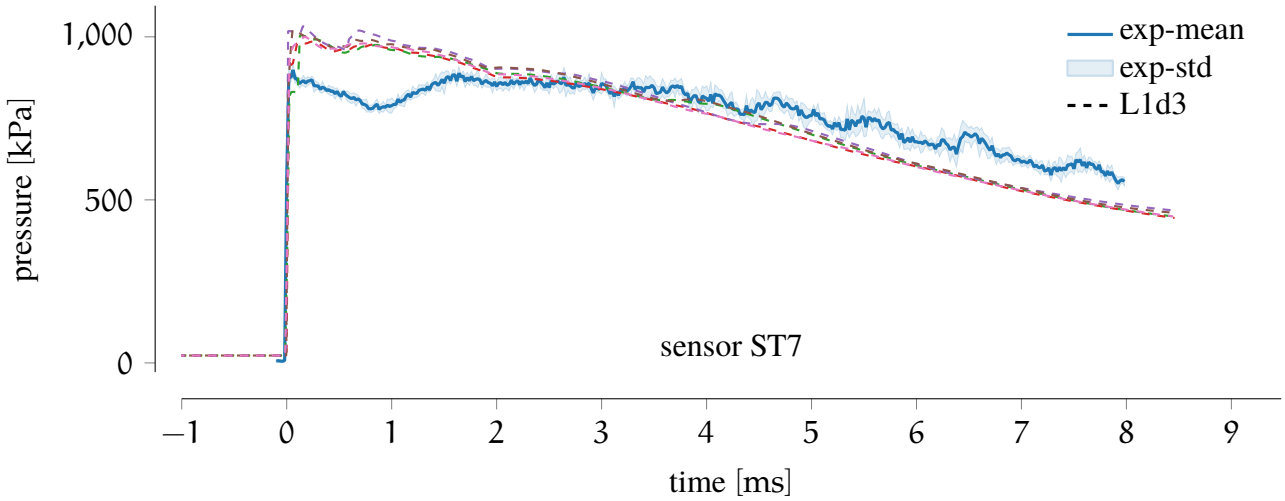

Figure 5.28: Experimental and numerical comparison of the wall pressure traces at the ST7 location: numerical data obtained with the *gradual-opening* model for the primary diaphragm. Experimental data is an 11-shots average.

Table 5.2: Optimised parameters of the selected L1D simulation.

variable	description	value	unit
x1	L_{loss} shock tube	0.284	[m]
x2	K_L shock tube	4.890	[]
x3	L_{loss} primary driver	0.495	[m]
x4	K_L primary driver	4.356	[]
x5	L pressure averaging region	0.0973	[m]
x6	PD hold time	0.221	[ms]
x7	PD rupture pressure	12.546	[MPa]
x8	PD opening time	1.126	[ms]

5.8 CFD AXISYMMETRIC SIMULATION

The selected L1D optimisation run has generated numerical simulations able to reproduce a flow condition closely matching shock speeds and a reference wall static pressure. The use of a gradually opening diaphragm in L1D has significantly increased the accuracy of the model. As previously discussed, the next part of the analysis is now done with CFD axisymmetric simulation, capturing the phenomena, such as radial waves and viscosity, that L1D is not able to reproduce, but which have a significant importance in the acceleration tube flow processes. In this section the CFD model is presented, and the results of the numerical analysis are discussed.

5.8.1 The model

The EILMER3 axisymmetric model used for this simulation is the one employed by Gildfind et al. [129], with minor modifications to include the new Mach 12 nozzle, and its schematic is presented in Fig. 5.29.

The model includes the last part of the shock tube, the whole acceleration tube and nozzle, and a reduced-size dump tank, simulating 25 m of the overall facility. A hold diaphragm model at the shock/acceleration tube is included, which instantaneously opens a finite time after a set ΔP is reached. In the same figure, the position of experimental wall pressure and Pitot pressure probes, used to compare the numerical and experimental data, are indicated.

The simulation was fully transient, with a transient inflow specified at ST6, extracted from the final optimised L1D solution (per Table 5.2) at the same location. This simulation used a time-accurate, explicit, third order Runge-Kutta scheme. The Baldwin-Lomax [199] turbulence model was used. The model is a structured grid with ~500 000 elements. This grid is unable to fully resolve the boundary layer for all the different flow regimes that develop in the simulation, as the required cell density to always satisfy the $y^+ < 1$ requirement would make these simulations unfeasible to carry out. It is

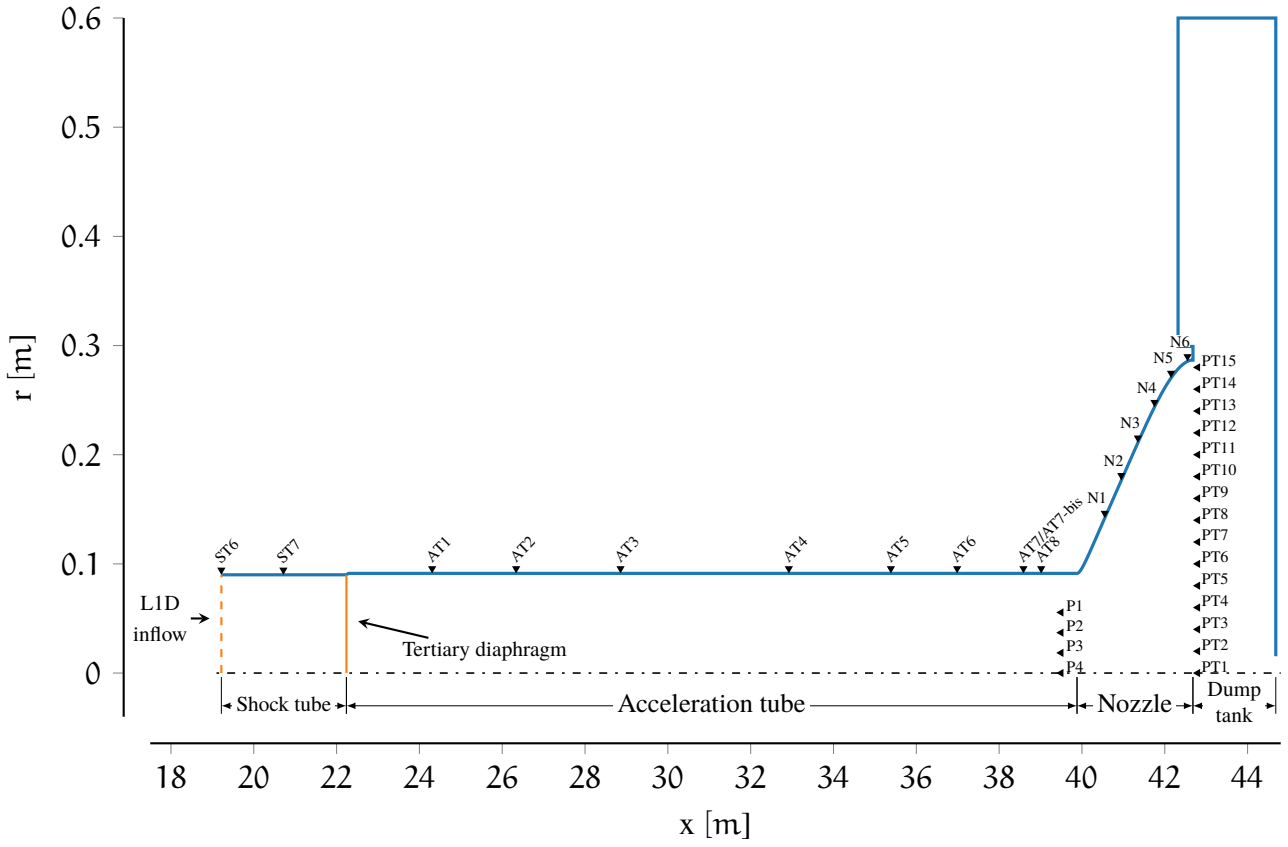

Figure 5.29: CFD model of the acceleration tube, nozzle and dump tank of the X3 expansion tube used for the second part of the hybrid simulation of CONDITION x3s506. Probe locations are indicated in figure. Note: maximum pressure and temperature clipped by axis scale.

noted that a single simulation requires about 1 month on 264 processors. Gildfind et al. [129] carried out a detailed grid analysis and has shown that this grid is sufficient to capture the main features of the flow in the case of the Mach 10 condition.

5.8.2 Results and discussion

Centreline results at the nozzle exit are shown in Fig. 5.30, where pressure, temperature, Mach number and velocity are shown. The data are referenced to shock arrival at the nozzle exit plane. Test time, in accordance with the experimental measurements, is indicated in the figure.

The initial 200 µs, where pressure and temperature are significantly higher, correspond to the hot acceleration tube gas starting the nozzle. After that, there is a notable drop in both pressure and temperature, and the test time starts shortly thereafter. A steady gradient is noted in all the properties, similarly to what is experimentally observed. It is important to point out that the test time was experimentally ended by a high level of noise measured by the sensors, which is likely due to the vibration caused by the arrival of fragments of the secondary diaphragm. Indeed, in the numerical

simulation, this noise is absent. If the change in properties can be tolerated and if the measured noise could be filtered away, test time could be potentially extended substantially.

Calculated mean CFD flow properties are shown in Table 5.3, along with the variation across the defined test time.

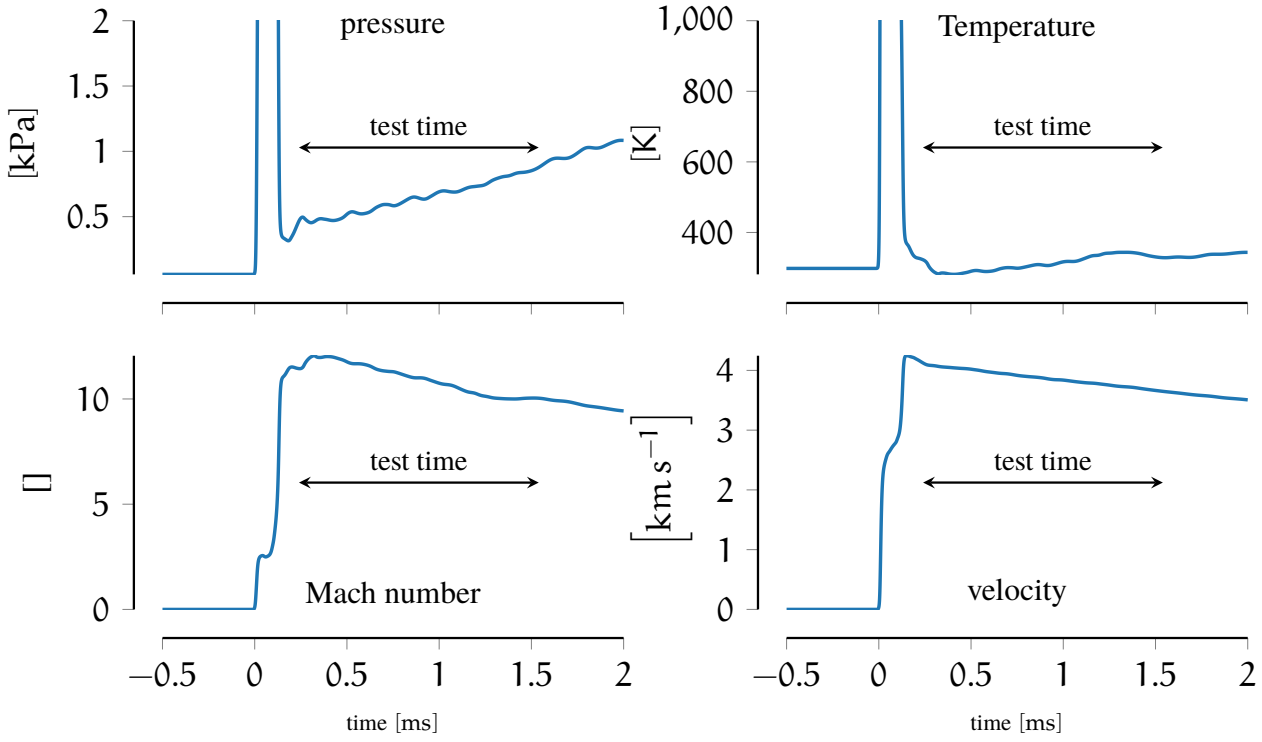

Figure 5.30: Computed nozzle exit centreline flow properties. The peak in temperature and pressure in the first 200 µs corresponds to the nozzle startup process.

Table 5.3: CFD estimate of the flow properties: CONDITION x3s506. Selected test time:0.24 ms to 1.54 ms.

property	value	std-dev	unit
T	308	21	K
p	607	123	Pa
v	3911	129	$m\,s^{-1}$
M	11.1	0.7	
Pitot pressure	95 610.0	7020	Pa
nominal total enthalpy	6.0		$MJ\,kg^{-1}$
nominal total pressure	223.3		MPa
nominal dynamic pressure	52.7		kPa
equivalent altitude	34.6		km

Shock speeds

Shock speed are by far the most accurate and reliable measurements that can be taken during an experiment in an expansion tube. PCB sensors guarantee almost instantaneous responses (in the order of 1 µs, and the detection of the arrival of the shock wave is independent of the sensor sensitivity. As such, shock speed comparison is the primary metric to compare expansion tube flows and simulations. In Fig. 5.31 experimental and numerical shock speeds are presented. Nozzle wall shock speeds measurements are also included. The hybrid model is able to closely match the shock speeds along the whole acceleration tube and the nozzle. The relative difference is, on average, 0.63 % in the acceleration tube and 0.1 % in the nozzle.

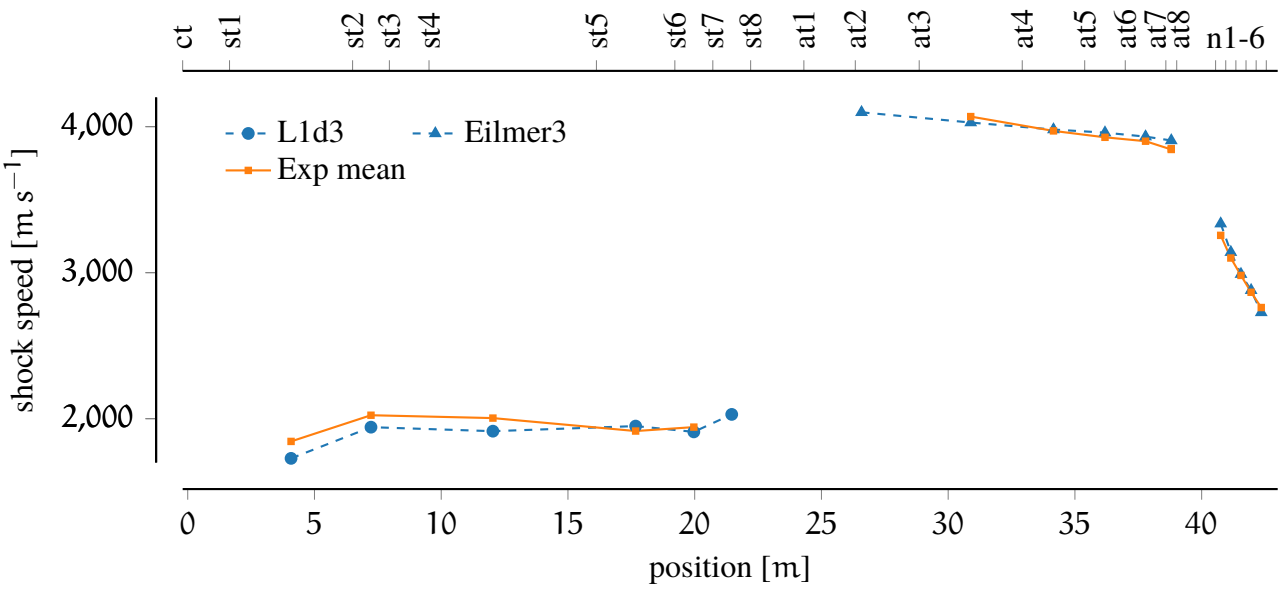

Figure 5.31: Experimental and numerical shock speeds comparison. Shock tube shock speed are calculated with L1D (see Fig. 5.26). Experimental trace is an 11-shot average.

Static wall pressure

Wall pressure measurements in both the acceleration tube and along the nozzle wall, presented in Figs. 5.32 and 5.33, show an excellent agreement, when examining the accelerator gas slug (the initial steady section of the trace). With the arrival of the contact surface, represented by the pressure dip following the initial steady accelerator gas, a discrepancy ~10 % arises between numerical and experimental pressure levels in the test gas. This indicates that the CFD test gas is under-expanded compared to the experimental data.

This dip in pressure has been thoroughly discussed in [129]. Called “test gas necking”, it is a region of maximum boundary layer thickness that is a localised manifestation of the Mirels’ effects (discussed in Section 2.9.3). This area constricts the core flow limiting the unsteady expansion of the test gas and is responsible for the steady gradient in the pressure traces.

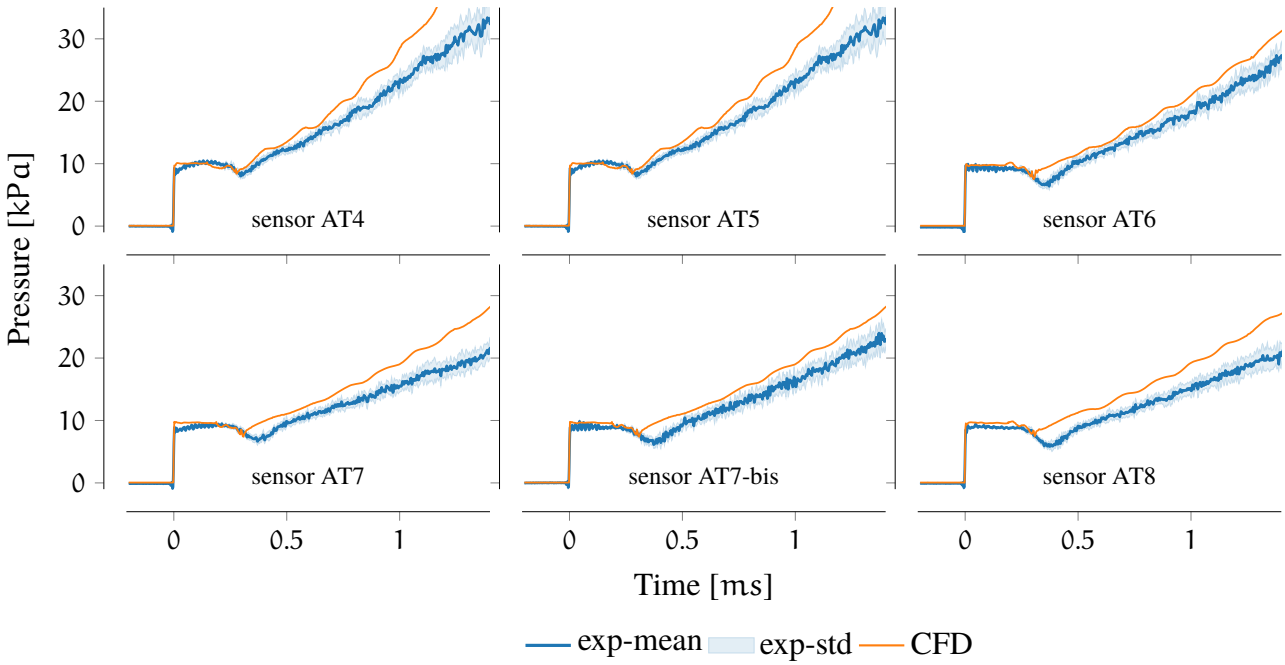

Figure 5.32: Experimental and numerical comparison of **wall pressure** measurements in the **acceleration tube** at different locations. Experimental trace is an 9-shot average.

It is important to note that, in first approximation, the difference between numerical and experimental wall static pressure levels past the "necking" could be interpreted as a "time delay" in the arrival of an equivalent slug of gas with similar properties. In other words, the simulation requires the test gas slug to travel an increased length, and therefore a longer time, to achieve the experimental expansion levels noted in the experiments. This is an indication that the simulation is not reproducing the high level of shear stresses developed in the thick boundary layers in the acceleration tube.

Nozzle wall static pressure measurements, shown in Fig. 5.33, indicate a similar behaviour, where the accelerator gas is well-matched, with a discrepancy arising with the arrival of the test gas interface. It is interesting to note the behaviour of the accelerator gas, which gets compressed between the shock front slowed down, with the test gas expanding and accelerating behind it. At the last nozzle sensor N6, the test flow is expanded, with no visible pressure gradient, and numerical-to-experimental discrepancy is significantly reduced.

Mach number comparison

The experimental Mach number was calculated to be 11.0 ± 1.0, with the numerical one 11.14 ± 0.7, indicating the reliability of the numerical data. Moreover, it is noted that the transient behaviour is also qualitatively similar, as across the test time, the Mach number is decreasing with a comparable gradient.

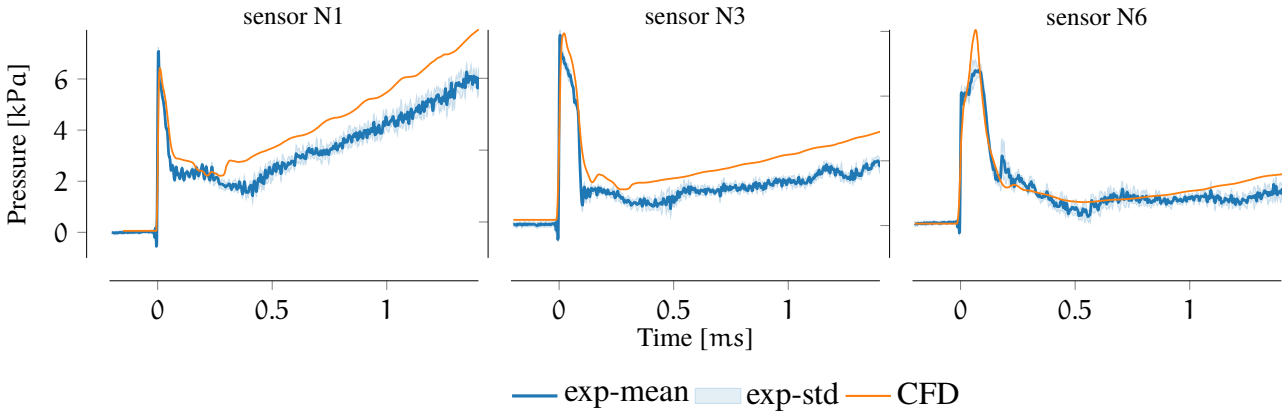

Figure 5.33: Experimental and numerical comparison of **nozzle wall pressure** measurements. The sensors are respectively located 670 mm, 1470 mm and 2270 mm downstream of the nozzle inlet, with the last one 130 mm from the nozzle exit plane (see Figs. 4.20 and 5.29 for details). Experimental data is a 9-shot average.

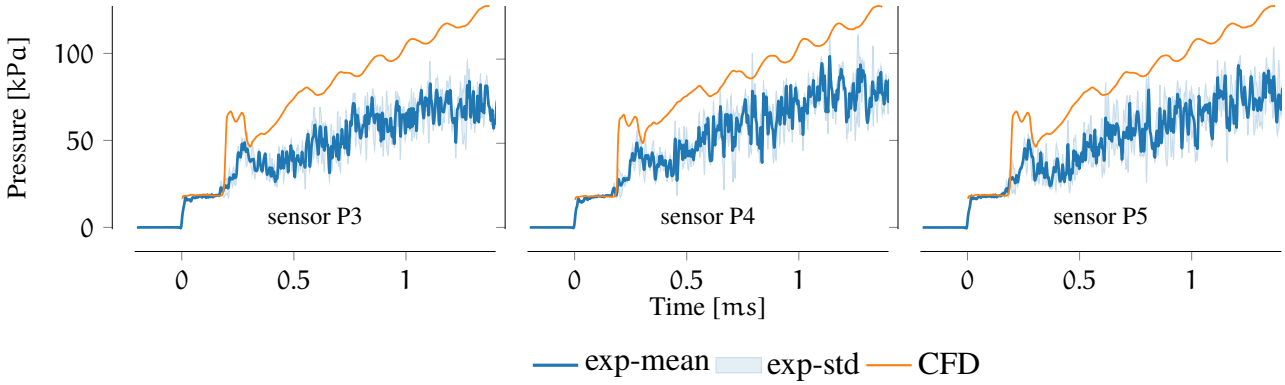

Figure 5.34: Experimental and numerical comparison of **conehead pressure** at the **nozzle inlet**. P4 is located on the tube centreline, P3 and P4 20 mm above and below the centreline (see Fig. 5.29 for details). Experimental data is a 9-shot average

Pitot pressure measurements and comparison

Conehead pressure comparisons at the nozzle inlet inside the core flow, shown in Fig. 5.34, show an increased discrepancy between numerical and experimental results, with the numerical predictions indicating pressure levels twice as high as the experimentally observed traces.

Finally, nozzle exit plane measurements for both Pitot pressure and conehead pressure are shown in Figs. 5.35 and 5.36. On the centreline (sensor P1) significant difference is noted, which is progressively reduced to a good agreement near the nozzle wall (sensor P14).

In summary, shock speeds and wall pressure measurements have shown excellent and good agreement, whereas on the centreline significant discrepancies in Pitot and conehead pressures are noted. Higher pressure levels indicate that the gas is under-expanded, i.e. the CFD is unable to reproduce the unsteady expansion process that is observed in the experiments, or that the experimental measurements are not accurately measuring the correct Pitot pressure. However, estimated Mach number is in good agreement with the experimental one.

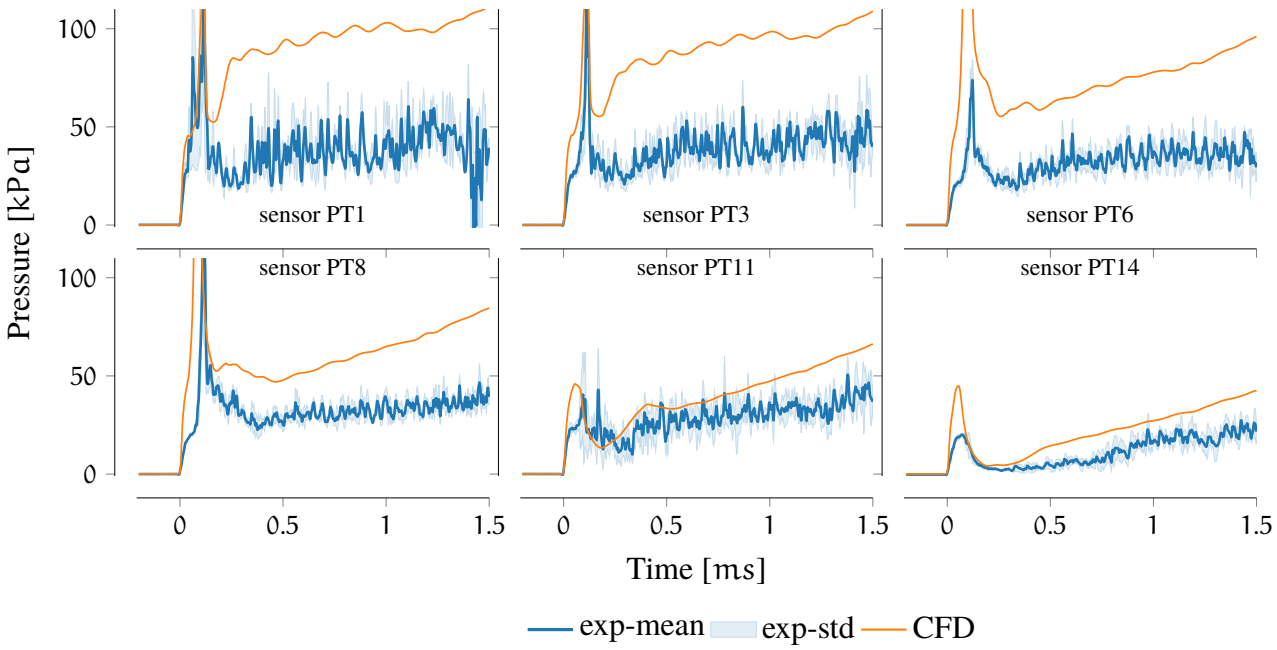

Figure 5.35: Experimental and numerical comparison of **Pitot pressure** measurements at the **nozzle exit** (see Fig. 5.29 for details). Experimental data is a 9-shot average.

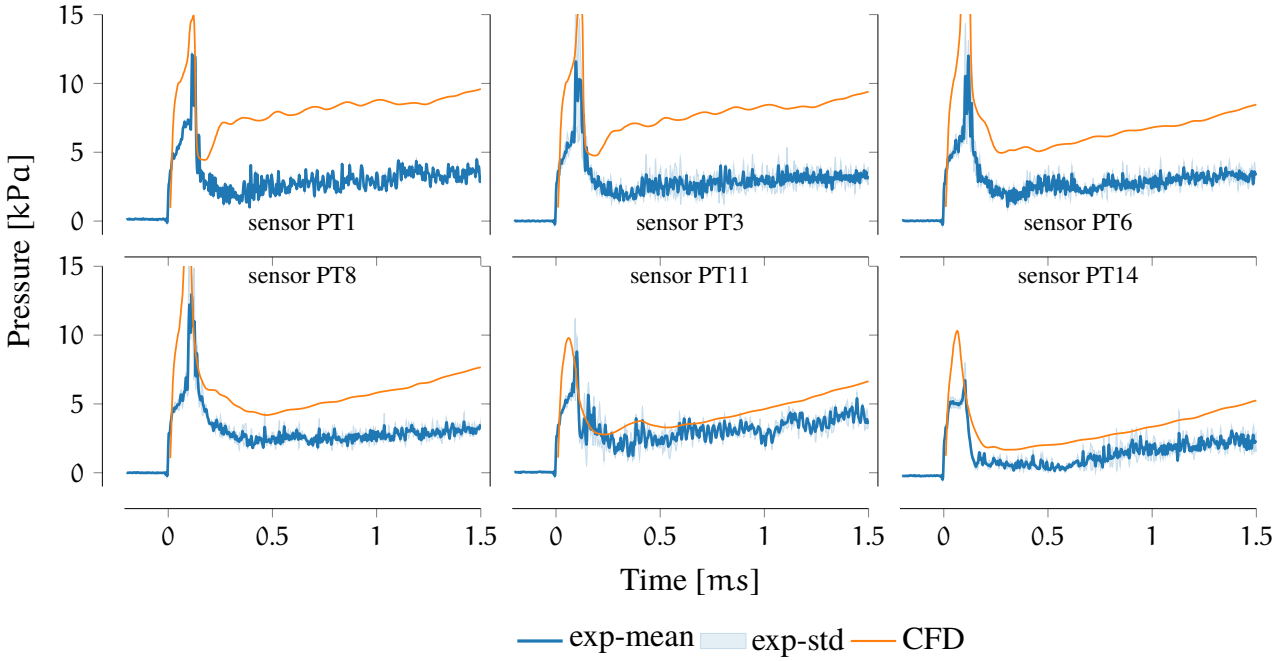

Figure 5.36: Experimental and numerical comparison of **conehead pressure** measurements at the **nozzle exit** (see Fig. 5.29 for details). Experimental data is a 2-shot average.

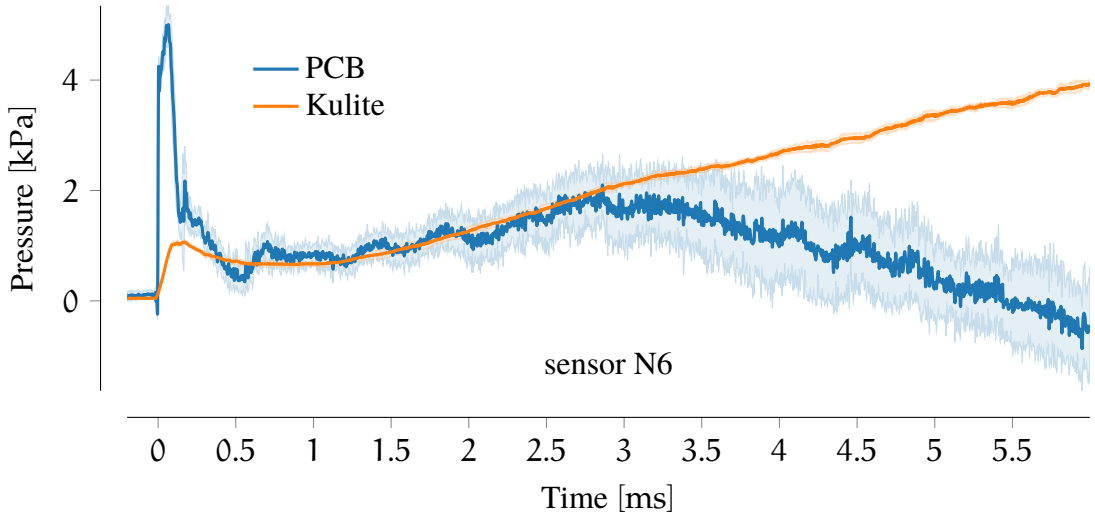

Figure 5.37: Nozzle wall pressure measurement, taken with a PCB and a Kulite pressure sensor at the same location, in the same experiment. A PCB allows faster response time, but is more sensitive to high heat transfer rates.

A couple of explanations can be proposed. Firstly, assuming that the experimental results are correct, the grid used is too coarse for this flow condition, leading to poorly resolved boundary layer. Indeed, the grid represents a compromise between simulation time and accuracy. This grid roughly requires a month of computational time on 264 processors. Any more refined grid is currently out of the computational capabilities at the author's disposal. The CFD solver also limits the number of parallel processors that can be used, as an excessive number of blocks (i.e. subdivision of the grid which are processed in parallel) significantly reduces the accuracy of simulation.

A second possible explanation is that measured Pitot pressure levels are affected by vibrations, high heat transfer rates on the probes, and cavity effects, in which the filling process of the probe cavity can affect the measured process. Indeed, the raw measured Pitot signals are extremely noisy. It is also known that PCB pressure sensors are affected by significant heat transfer rates that can affect the response of the piezoelectric components. A comparison of a Kulite and a PCB sensor on the nozzle wall is shown in Fig. 5.37, where the heat loads are significantly lower. It is noted that after 2.5 ms the PCB pressure trace diverges from the Kulite pressure trace.

Previous studies with the University of Queensland expansion tubes have shown that Pitot pressure measurements often give inconsistent results and have poor reliability (see, for example, experimental and numerical comparisons in [30]).

Additionally, other considerations indicate that the Pitot pressure measurements are inconsistent with the rest of the dataset. These are discussed in the following paragraphs.

Pitot pressure measurements and analytical estimates

It is possible to derive an analytical estimate of the freestream properties, by using the analytical model of Section 2.9.1. In this case, to closely reproduce the experimental measurements, the shock speeds are set to the experimentally measured levels of Fig. 5.31. An isentropic expansion, defined by an "equivalent nozzle area ratio", allows estimation of the freestream nozzle exit properties. As in this case experimental Mach number estimates are available, the flow is expanded to the measured Mach number of 11.0, and the nozzle area ratio is varied to obtain this desired exit Mach number.

The area ratio required to achieve this expansion is 7.1, which is below the nominal geometric area ratio of 9.85, and consistent with the consideration that the test gas sees a reduced area through the nozzle due to the very thick boundary layer. Additionally, the calculated area ratio is in line with the performance of other nozzles, such as the Mach 10 nozzle of the X2 expansion tube.

With this model, in which experimental shock speeds and measured Mach number were an input, the calculated Pitot pressure and conehead pressure estimates are 100.2 kPa and 8.5 kPa, twice as much as the measured levels noted in Section 5.4 (42.2 ± 12.1 kPa and 3.2 ± 0.7 kPa). Conversely, the estimated Pitot and conehead pressures, along with pressure, velocity and temperature are within the uncertainties of the CFD results.

The same model, in order to match the averaged experimental Pitot pressure and conehead pressure, would require an effective area ratio for the nozzle of 17, producing a flow that is at Mach 13.9 Albeit it might be possible that the effective area ratio the flow sees is higher than geometrical one, the Mach number fells well out of the experimental error bars.

Scramjet forebody pressure measurements

Experimental measurements carried out on the scramjet forebody plate (inclined at 5° angle of attack and described in detail in the following chapter) shows a pressure level of 1.5 ± 0.3 kPa, averaged across the same test time and several shots. The CFD equivalent pressure level is 2.0 ± 0.2 kPa. A hypothetical freestream condition satisfying the measured Pitot pressure levels would produce a forebody pressure level of 0.8 ± 0.3 kPa. The former value is compatible with the measured pressure behind the forebody shock, but the latter is not, supporting the argument that the measured Pitot pressure is inconsistent with the rest of the data and therefore unreliable.

Conclusion

The discussion has shown that numerical simulations, experimental Mach number and shock speeds, analytical models and scramjet forebody experimental measurements produce a dataset that is consistent and in good agreement with each other. Experimental Pitot pressure and conehead measurements

Table 5.4: CONDITION x3s506 Freestream flow properties: CFD and uncertainties. δ_{time} is the absolute standard deviation across the test time, δ_{shot} the relative shot-to-shot uncertainty calculated in Section 10.2, and $\delta_{total} = \sqrt{\delta_{time}^2 + (value \cdot \delta_{shot}/100)^2}$. T is temperature, p pressure, v velocity, M Mach number, P_p Pitot pressure,H_0 nominal total enthalpy, P_0 nominal total pressure, q nominal dynamic pressure, and h equivalent flight altitude. *Target value* column indicate the original target flow condition.

	value	δ_{time}	δ_{shot}[%]	δ_{total}	Target value	unit
T	307.6	21	3.9	24.0	239	K
p	607.0	124	9.9	137.6	496	Pa
v	3911.1	129	1.5	142.8	3722	$m\,s^{-1}$
M	11.1	0.7	2.1	0.7	12	
P_p	95.6	7.0	6.4	9.3	101.9	kPa
H_0	6.0				7.2	$MJ\,kg^{-1}$
P_0	223.3				310	MPa
q	52.7				50	kPa
h	34.6				36	km

cannot be reconciled with the rest of the data, and therefore have been disregarded. Further studies are strongly recommended to fully resolve this discrepancy. The CFD freestream flow properties estimate is selected for the analysis required in the following chapters.

5.9 SUMMARY: FREESTREAM PROPERTIES

To conclude, an overview of the estimated flow condition and uncertainties is presented. As a reminder, only CONDITION x3s506 has been thoroughly analysed. The pressure-scaled CONDITION x3s582 is assumed to have the same flow properties, with a freestream pressure twice the pressure calculated for CONDITION x3s506.

Table 5.4 includes mean freestream properties and standard deviation across the test time for the two estimates. The calculated uncertainties derived from the variability of the facility filling parameters are also included, and total uncertainties are calculated. Details on the calculations are presented in Section 10.2.

Figure 5.38 presents some classic scramjet constant dynamic pressure ascent trajectories for access to space, and the location of this flow condition is shown.

This and the previous two chapters have covered the work carried out from the definition of a target flow condition, through the design and manufacturing of a Mach 12 nozzle, to the experimental and numerical validation of the flow condition. The goal was a Mach 12, 50 kPa flow condition. The final result provided a slightly lower Mach number condition: Mach 11.14, 52.66 kPa dynamic pressure. Despite this discrepancy, the condition was deemed adequate for the intended study. Indeed, the

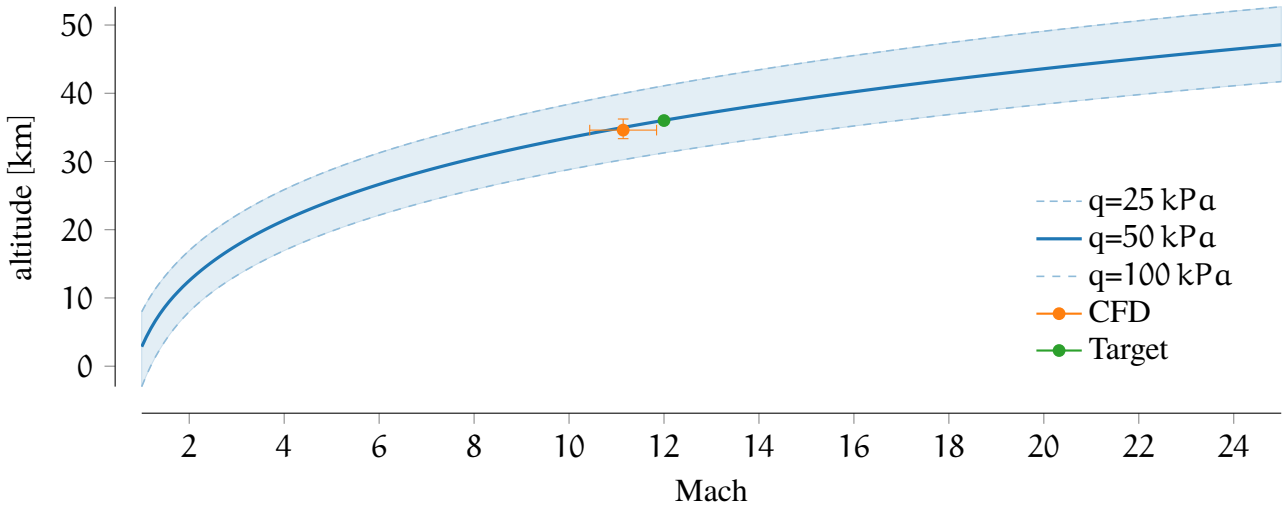

Figure 5.38: Scramjet flight corridor and flow condition estimate.

costs associated with additional iterations of the flow condition was deemed too high, considering the computational cost of the analysis.

Most importantly, the discrepancy can be attributed to the length/diameter ratio of the acceleration tube, which produces very thick boundary layers in the tube. This has as a consequence a lower nozzle inlet Mach number, and off-design operation of the nozzle. To solve these issues, a solution was identified in the shortening of the acceleration tube. Additional iterations on the flow condition were subordinate to this hardware modification, and were not feasible in the time-frame of this thesis.

5.10 CONCLUSION

This chapter has successfully shown that the X3 facility is able to produce a Mach 12 flow condition, for a test time of 1.3 ms with a core-flow diameter of 400 mm. Quantification of the actual freestream properties have shown to be extremely difficult, due to the inherent flow unsteadiness and the high level of noise in the measured Pitot pressures. An independent centreline Mach number measurement has been carried out using a 30° wedge and an optical schlieren system, allowing measurement of the shock angle. These results have indicated that Mach numbers in the range 10.0 to 12.0 are within the uncertainty, with a mean value of 10.95.

The new Mach 12 nozzle has produced a core flow exceeding the numerical prediction for a steady inflow. The properties of the steady inflow originally used for the CFD assumed a 30 mm boundary layer thickness. The experimental measurements have shown that no core flow could be identified in the inflow, and the boundary layer reached the tube centreline. As such, the nozzle is operating at slightly off-design conditions, but still able to generate a core flow of significant size.

A hybrid numerical approach has been adopted in order to establish the flow condition at the nozzle exit. Piston dynamics, compression tube and shock tube have been simulated with a lagrangian one-dimensional code, which, with opportune parameter tuning, has been able to closely reproduce shock tube shock speeds and wall pressure traces at the end of the tube. The acceleration tube and nozzle have been simulated with the Eilmer3 CFD solver, which has shown excellent agreement in terms of shock speeds, good agreement for the wall static pressure measurements, but poor agreement with Pitot and conehead pressures. Mach number numerical predictions are within the uncertainties of the experimentally estimated Mach number.

Estimates have shown that the nominal Mach 12 condition is actually Mach 11, due to incomplete expansion of the test gas, with a total enthalpy of $7\,\mathrm{MJ\,kg^{-1}}$ and total pressure of $224\,\mathrm{MPa}$, for an equivalent dynamic pressure of $53\,\mathrm{kPa}$ and flight altitude of $34.60\,\mathrm{km}$. The pressure-scaled Condition x3s582, although not thoroughly analysed, has shown comparable shock speeds and test time. It is assumed that it produces the same speed and enthalpy, with doubled pressure for a total pressure of $450\,\mathrm{MPa}$.

It is important to highlight that this is the first successful attempt at producing high Mach number flow conditions in the X3 expansion tube above Mach 10, and significant work is required in order to improve flow accuracy estimates and fine-tune the operating condition. Indeed, as previously discussed, freestream estimation is probably the most challenging problem for expansion tube flows.

From an experimental perspective, the author recommends the development and use of non-intrusive optical techniques such as, for example, TDLAS (Tunable Diode Laser Absorption) to measure freestream velocity and temperature, developing upon the work of Wheatley [218]. Improved Pitot pressure measurements, with reduced noise level, would also allow for more accurate flow property estimation. Currently, reliance on the Pitot pressure (and conehead pressure measurements) for freestream estimation significantly affects the accuracy of such estimates. On the numerical side, the current computational capabilities limit grid sizes, which can be used to simulate the facilities. Advances in the solver, to allow faster full facility simulations are necessary to improve the flow conditions.

The next two chapters will present the experimental test of the Mach 12 REST engine. Chapter 6 will discuss the adopted methodology, while Chapter 7 the successful experiments will be detailed.

6 SCRAMJET EXPERIMENTS: METHODS

Figure 6.1: Mach 12 Rest engine fully assembled inside the X3 test section. For this picture, swept ramp trip has been used.

6.1 INTRODUCTION

In this chapter, the test engine (Fig. 6.1) is described, along with the instrumentation, details of the fuel delivery system, and relevant calibrations. A final section is dedicated to the computational grid and the flow solver adopted to simulate the engine.

6.2 EXPERIMENTAL MODEL

The engine adopted for the experiments was the one used by Wise [82], Barth [83], and Landsberg [87]. The configuration chosen was the one proposed by Barth [83], with the tailored injection scheme proposed by the same author, and the long combustor. The work of Landsberg [87] showed that the use of a shorter combustor, including the removal of the backward facing step, improved combustion efficiencies and reduced the viscous drag compared to the engine in Barth's configuration. However,

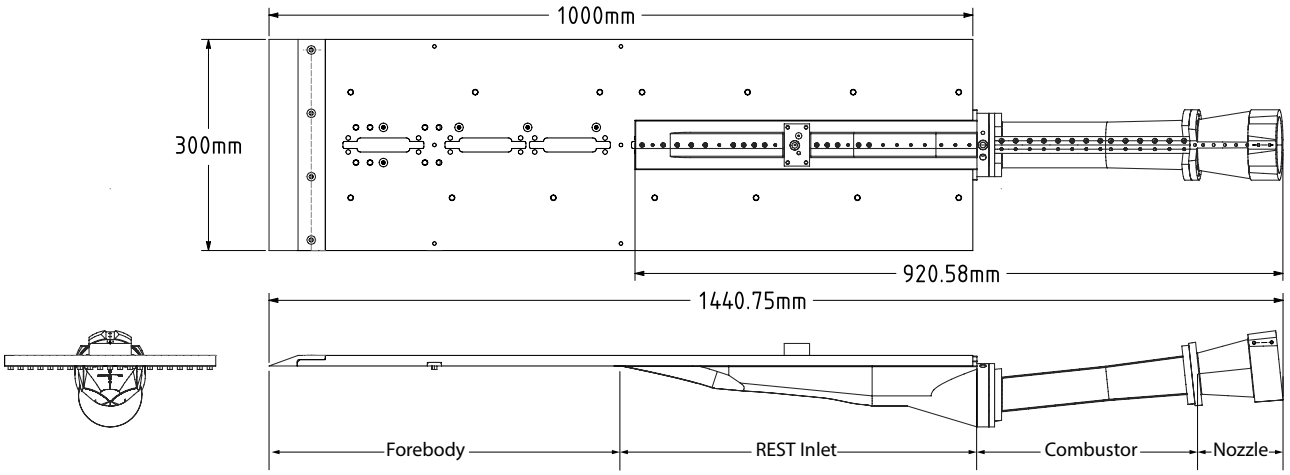

Figure 6.2: Mach 12 REST engine attached to a forebody plate, shown with a long combustor. Engine designed by Wise [82]

the two projects timelines were such that the configuration choice was made before the experimental data from Landsberg was available. In this section, we will briefly discuss the experimental model. For technical drawings and any other additional details, we refer the reader to the work of Wise [82].

The experimental test model is composed of an inlet and isolator assembly, an annular plenum, a combustor, and a nozzle. The shape-transitioning inlet was machined in two halves from aluminium (AL-6061-T6) using a CNC 5-axis machine, then assembled with locating pins and bolts. Combustor and nozzle were machined from the same material, and the internal surfaces machined with a 3D wire cutter. The parts were connected and aligned together with locating pins and connecting bolts. Sealing on the connections was ensured by o-rings.

6.2.1 Forebody and boundary layer trip

The forebody is a 1 m long by 300 mm wide plate. A slotted hole was cut in the centre for the insertion of the inlet, so that the forebody effective length — i.e. prior to the inlet — was 500 mm. The width was determined by the size of the Mach 10 nozzle used for these experiments in T4, while trying to minimise side-wall effects. The leading edge has been kept as sharp as possible, with a blade angle of 20°, because a blunted leading edge has been shown to increase boundary layer transition lengths [219]. A removable boundary layer trip insert can be located 235 mm from the leading edge of the forebody. Wise and Smart [24] experimentally tested different kinds of boundary layer trips to achieve a fully turbulent flow where the engine inlet starts. The main two trip geometries — diamond and swept ramps — are presented in Fig. 6.3. A single swept ramp, 5 mm high, was tested by Wise and Smart [24] along with boundary layer diamond trips 2.5 mm, 5 mm and 7 mm high. For the present X3 set of experiments, the 7 mm diamond trips and the swept ramp trip were employed.

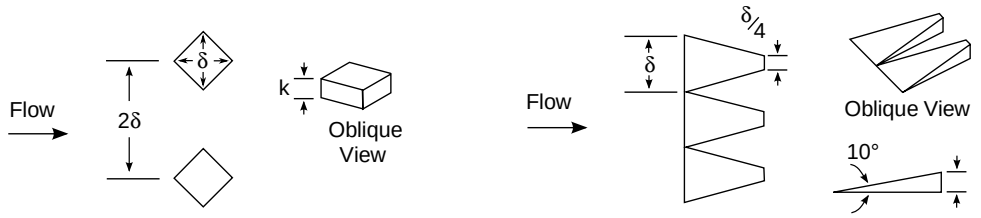

Figure 6.3: Boundary layer trips schematics. Reproduced from [24].

6.2.2 Nozzle core flow and model

The engine, sized and developed to fit the T4 test section, was previously tested in T4 such that only the inlet capture area and relative stream-tube were included within the core flow diamond of that facility [82]. Figure 6.4 illustrates Mach number contour lines and the engine cross section overlaid on top of it for the X3 Mach 12 nozzle. For these experiments, not only the capture area of the engine is within the core flow diamond, but actually, the entire inlet of the engine is inside. On the other orthogonal dimension, the whole forebody plate is also inside the core flow. With the Mach 12 nozzle it is unlikely that there will be any interaction of the engine with nozzle and test section walls.

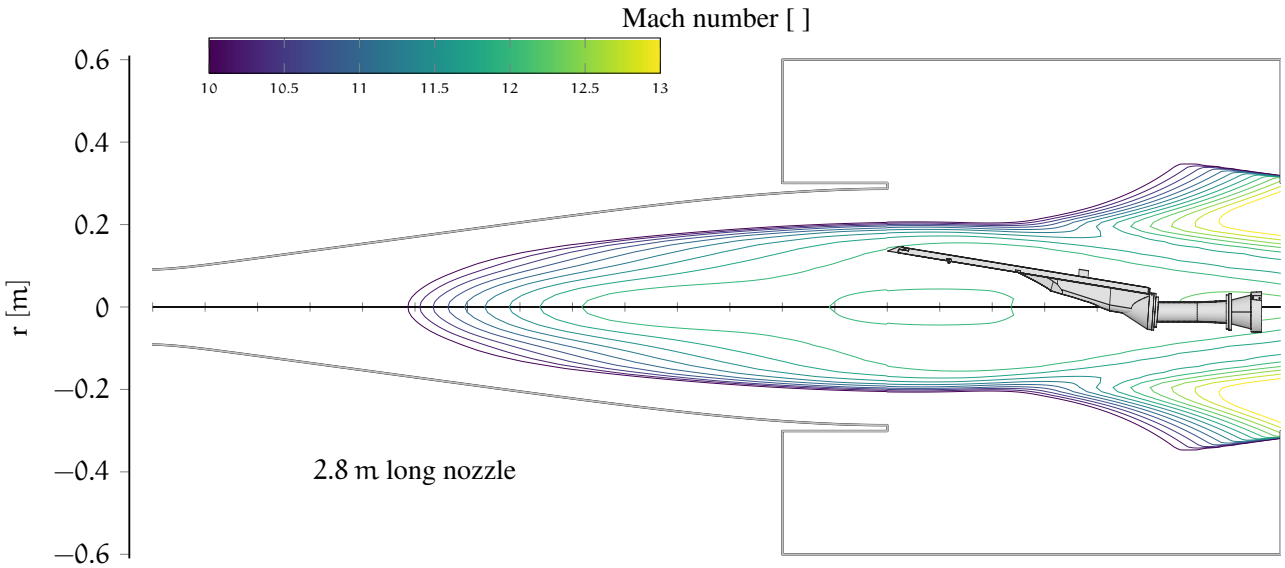

Figure 6.4: Mach 12 nozzle core flow, expressed in terms of Mach number, with the M12REST engine superimposed.

6.2.3 Internal flow-path

Figure 6.5 shows the internal flow path of the Mach 12 REST engine in the selected configuration extracted from Barth [83], along with cross-sectional views at various location. In this section we briefly introduce the main geometric internal characteristics of the engine.

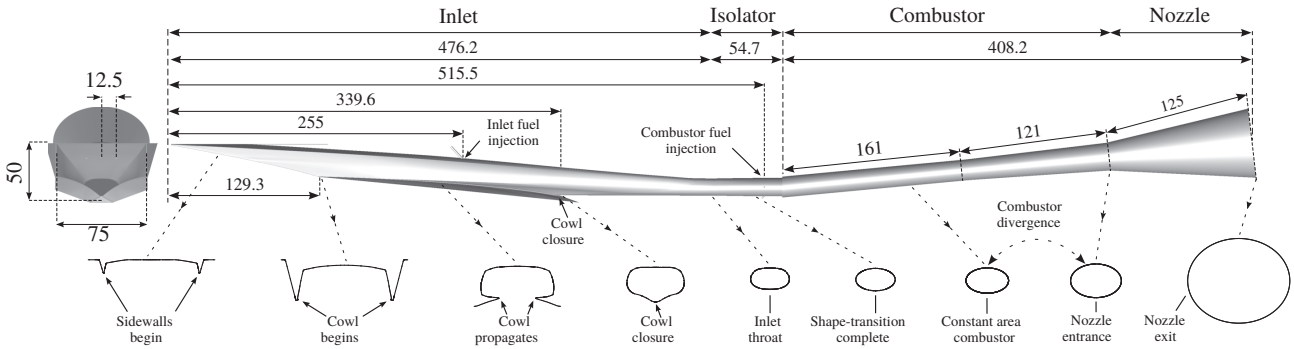

Figure 6.5: Mach 12 REST engine internal flow path and cross-sectional profile. All dimensions are mm. Adapted from [87].

The engine is a 50 % scaled version of the one by Suraweera and Smart [23], with an internal flow path total length of 940 mm. Both the engine and the inlet were designed to be mounted below a flight vehicle flying at 6° angle of attack; the effect of the vehicle on the flow is emulated by a 500 mm forebody plate (not represented in the figure). This engine size was the maximum allowable for the T4 RST used for the earlier experiments, given the flow-establishment and test section constraints of that facility. Referring to Fig. 6.5, the engine inlet transitions from an initial rectangular capture area 75 mm × 50 mm to a final ellipse with aspect ratio of 1.76 along a length of 505.8 mm. The cowlside is fully closed 339 mm from the inlet start. The inlet overall compression ratio is 2.25.

A short isolator, 25 mm long, is included between the end of the inlet and the combustor. An annular injection plenum is interposed between the combustor and the isolator. The injection plenum creates a backward-facing step, which was previously designed to work with the boundary-layer combustion injection system of Wise [82]. The combustor is 282 mm long and is inclined at 6° with respect to the inlet, to realign the flow with the theoretical vehicle flight attitude. The combustor contains an initial constant area section, 161 mm long, followed by a slightly diverging section at 1.6° until the end of the combustor, for a final-to-initial combustor area ratio of 2. A 125 mm conical nozzle then expands the flow by a ratio of 10.

6.2.4 Fuel injection system

The hydrogen fuel injection system in the M12REST engine is composed of two plena, the first located middle-way through the inlet, and the second, is an annular plenum located between the isolator and the combustor, as shown in Fig. 6.6 The first plenum position (denoted “inlet fuel injection” in Fig. 6.5) is 255 mm downstream from the inlet leading engine, and feeds three port-hole injectors. These are inclined at 45° with respect to the surface normal, have an axis-to-axis spacing of 12.5 mm, and a diameter of 2 mm. This location and configuration were originally selected to maximise the mixing length in the experiments in order to accelerate and enhance the combustion of the fuel injected downstream.

The second injection system is composed of the annular plenum system (denoted "combustor fuel injection" in Fig. 6.5) and 5 porthole injectors as shown in Fig. 6.6. The injectors are 0.8 mm in diameter, inclined at 45° with respect to the engine axis (or streamwise direction). One injector was located on the engine symmetry plane. Two injectors were placed 6.75 mm away from the symmetry plane and the two side-wall injectors are aligned with the combustor ellipse main axis.

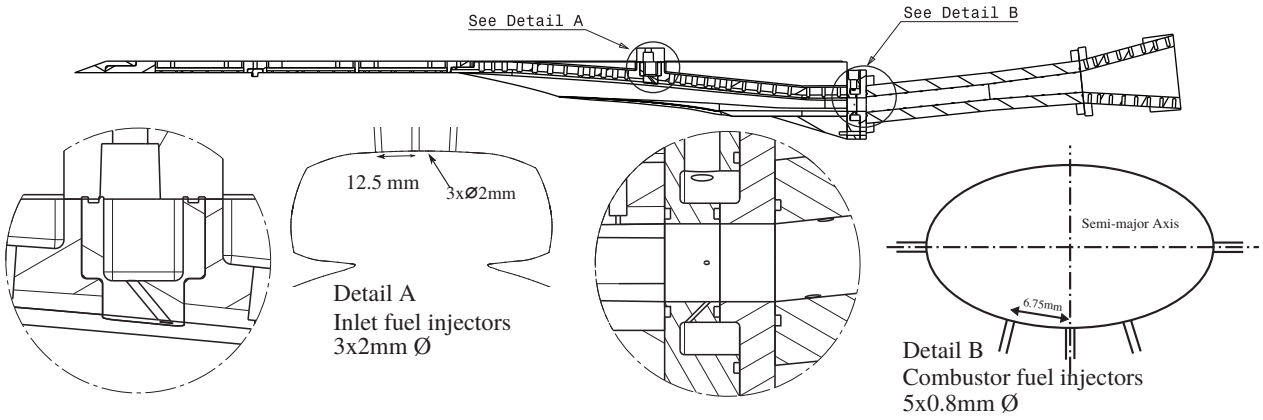

Figure 6.6: Mach 12 REST engine in the configuration of Barth [83].

6.2.5 Engine attachment system

An attachment system was developed to interface the M12REST engine with the existing scramjet mount available in X3. The whole system is depicted in Fig. 6.7. The existing scramjet mount sits on rails allowing for axial position adjustment with respect to the test section. The mount-engine interface was designed to allow easy access to the model fuel system, cabling, and bodyside instrumentation. Most importantly, it was designed with the capability to regulate the angle of attack of the scramjet with respect to the ground. It is recalled that the engine in flight condition is designed to fly at 6° angle of attack. The interface system connects the engine to the mount by means of a frontal freely-rotating pin and a custom variable-length turnbuckle attached to the engine nozzle, allowing the engine to be configured in the range $-6°$ to $10°$ with respect to the ground. A complete view of the test section including the engine model is included in Fig. 6.8.

6.2.6 Model instrumentation

The Mach 12 REST engine was instrumented with heat transfer and pressure sensors. Heat transfer gauges were only located in the forebody, and used to verify the effectiveness in using the trip to transition the boundary layer. Although the engine itself had the capability to host heat transfer sensors, it was chosen not to use them, as heat transfer measurements inside the engine were outside the scope of the project, along with the fact that an expanded data acquisition system would have been necessary.

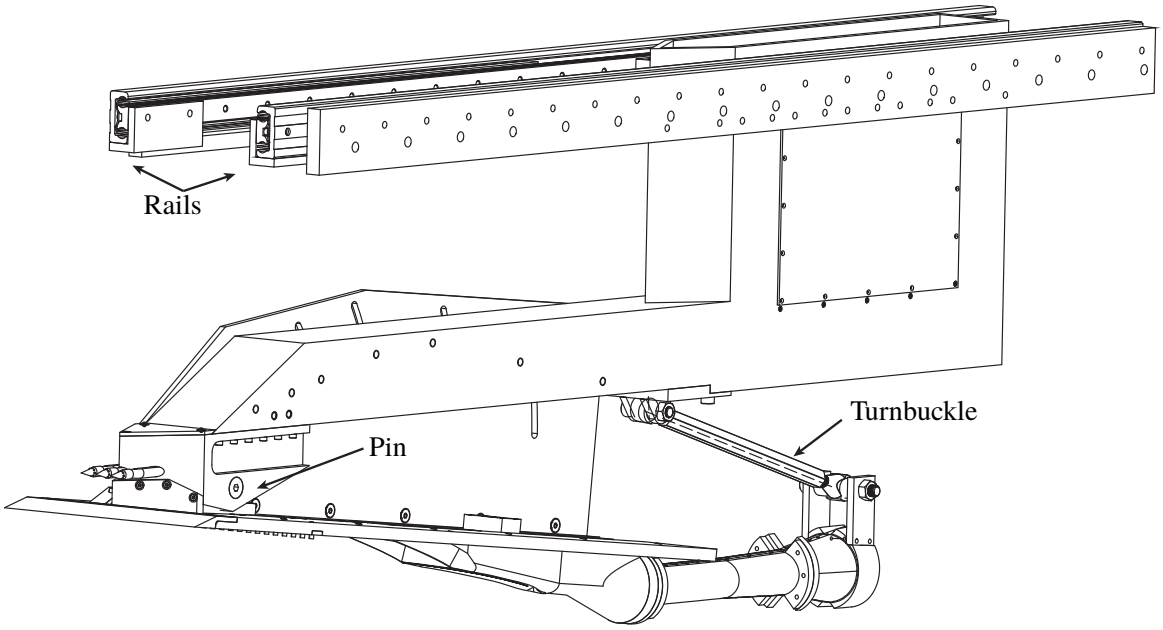

Figure 6.7: Scramjet engine variable-angle-of-attack mount. The nearest side-plate and the back-shielding have been removed from the picture to facilitate inspection of the assembly.

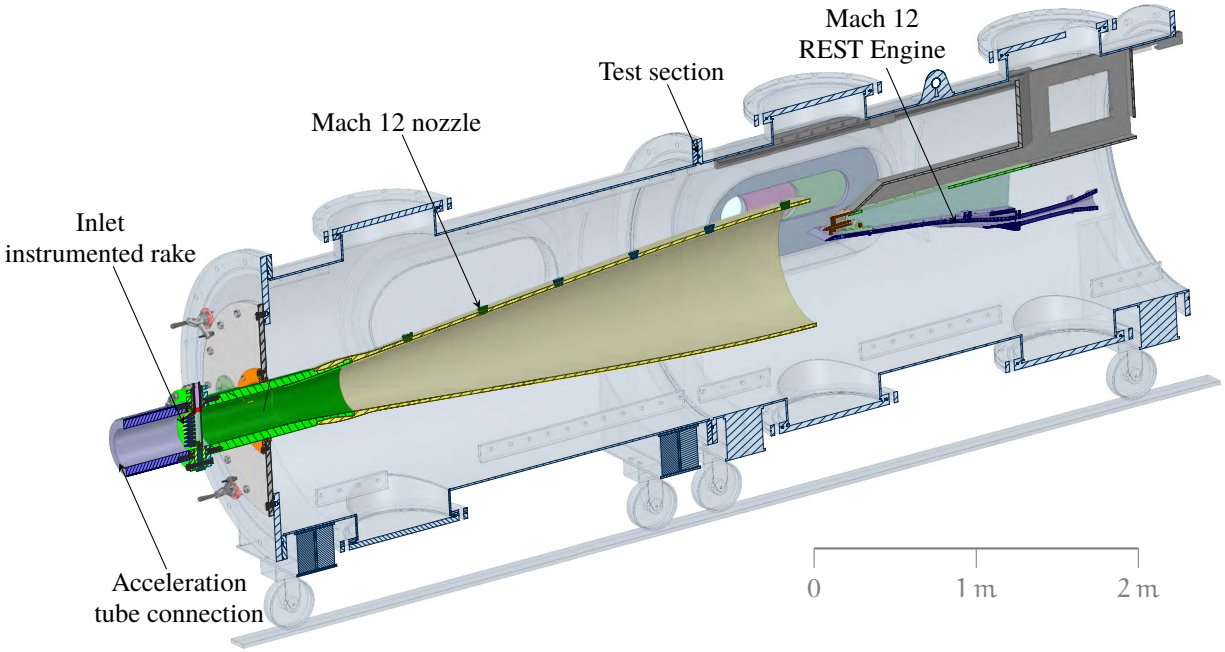

Figure 6.8: Test section of the X3 expansion tube.

The forebody hosted two pressure sensors, 25 mm off the centreline, and 18 thin-film heat transfer gauges. The inlet/isolator component was instrumented with 11 Kulite pressure sensors on the centreline. Two high range Kulite pressure sensors were fitted to the two fuel plena. The combustor section can host 14 sensors each on its top and bottom walls (referred to as bodyside and cowlside, with the first corresponding to the topmost part of the engine, and the second corresponding to the bottom part, where the cowl closure is located). Similarly, the nozzle can host 8 sensors on each of bodyside and cowlside. These sensors were offset 4 mm from the engine main symmetry plane. Heat transfer measurements can also be taken on this engine, with sensors holes located opposite to the pressure sensors with respect to the main symmetry plane. For these experiments, no heat transfer measurements within the engine were taken. In Table 6.1 all sensors labels and positions relative to the forebody leading edge are presented.

Table 6.1: Label and distance from forebody leading edge of scramjet sensors.

Label	Pos.[mm]
Forebody	
F1	162.5
F2	367.5
Inlet	
I1	545.0
I2	638.7
I3	718.3
I4	821.3
I5	871.0
I6	890.8
I7	910.6
I8	930.4
I9	955.3
I10	975.3
I11	995.3
plena	
PLI1	755.0
PLC1	1051.1
⋮	⋮

Label	Pos.[mm]
⋮	⋮
Combustor body side	
CB1	1042.4
CB2	1062.3
CB3	1082.3
CB4	1102.4
CB5	1122.4
CB6	1142.5
CB7	1162.5
CB8	1182.5
CB9	1198.0
CB10	1218.8
CB11	1239.6
CB12	1260.4
CB13	1281.2
CB14	1302.0
Nozzle body side	
NB1	1319.3
NB2	1330.8
NB3	1345.8
NB4	1361.7
NB5	1377.7
NB6	1393.6
NB7	1409.5
NB8	1425.4
⋮	⋮

Label	Pos.[mm]
⋮	⋮
Combustor cowl side	
CC1	1038.5
CC2	1059.3
CC3	1080.2
CC4	1101.0
CC5	1121.9
CC6	1142.8
CC7	1163.7
CC8	1184.6
CC9	1200.1
CC10	1221.0
CC11	1241.9
CC12	1262.9
CC13	1283.8
CC14	1304.8
Nozzle cowl side	
NC1	1322.4
NC2	1334.4
NC3	1349.9
NC4	1366.4
NC5	1382.8
NC6	1399.3
NC7	1415.7
NC8	1432.0
⋮	⋮

Label	Pos.[mm]
⋮	⋮
Forebody: heat transfer	
HTFB1	112.5
HTFB2	132.5
HTFB3	152.5
HTFB4	172.5
HTFB5	192.5
HTFB6	212.5
HTFB7	257.5
HTFB8	277.5
HTFB9	297.5
HTFB10	317.5
HTFB11	337.5
HTFB12	357.5
HTFB14	397.5
HTFB15	417.5
HTFB16	437.5
HTFB17	457.5
HTFB18	477.5

Pressure sensors

The pressure sensors adopted for the measurements inside the engine flow path where Kulite XTEL-190 (M) and XCEL-100 sensors. Kulite pressure sensors are fast response piezoresistive sensors that use a silicon membrane to measure absolute static pressure. They use a recessed mount, with a 1 mm

hole to connect to the engine flow path. XCEL-100 sensors were used with a special adapting piece to fit the XTEL-190 mount. The pressure ranges of the sensors were between 10 psi to 100 psi along the engine, with two 500 psi sensors for the fuel plena.

The signals were amplified and filtered with a custom hardware processing unit, using a 400 kHz low-pass filter. Another filtering pass was carried out in the post-processing phase, using a constrained equiripple FIR low-pass filter, with a cut-off frequency of 150 kHz and an order of 100 [170].

The custom hardware processing unit is also responsible for supplying power to the Kulite sensors, which are individually supplied. The hardware units have built-in supply-voltage stabilisers, that ensure a steady supply voltage. For these experiments, new units were sourced, which were tested prior to the experiment to conform to the specification.

The Kulite sensors used are absolute pressure sensors and are calibrated in-situ, with reference to absolute, known atmospheric and vacuum pressures. Intermediate pressures have been recorded and the excellent linearity of the sensor across the range has been confirmed. The atmospheric pressure was measured by a nearby weather station (which was assumed to be sufficiently accurate), and the vacuum pressure by a Varian Gauge CDG500-1 torr. Ultimate vacuum pressure in the X3 test section was in the range 2 Pa to 4 Pa. The Kulites were checked for sensitivity drift every two days. For detail on the calibration process the reader is referred to Section 10.4.

The data presented in Chapter 7 has been normalised using the first forebody pressure sensor and employing the slug-tracking technique as discussed by McGilvray et al. [152]: a "quasi-steady" slug of test gas is tracked throughout the engine so that an appropriate time shift is applied in the normalisation process (see Eq. (6.1)). In other words, in the test gas reference-frame, all the sensors see the same slug of gas at the same time. We refer the reader to [152] for further details.

$$p_N(t) = \frac{p(t + t_d)}{p_{F1}(t)} \tag{6.1}$$

where p, p_N are raw and normalised pressure at a given measurement point, p_{F1} is the pressure measured at the first forebody pressure tap. Data were averaged across the test times, and the mean and the standard deviation were taken. This data reduction process allows data comparison across different experiments and accounts for the variability due to the presence of noise disturbance.

Forebody heat transfer gauges

Fully turbulent boundary layer convective heat transfer is significantly higher than heating produced by a laminar boundary layer such that the measurement of heat transfer can be used to evaluate the state of the boundary layer. Heat transfer gauges were employed along the forebody to verify that the boundary layer trips, as previously discussed, were able to transition the boundary layer to fully turbulent.

Heat transfer measurements on the forebody flat plate were obtained by using thin-film heat transfer gauges (TFHTG) that are manufactured at the University of Queensland [220, 221] and are capable of very fast response times (on the order of 1 MHz [82]).

The operating principle is based on sputtering a metallic *thin-film* (μm) on top of a sufficient depth of quartz substrate (quartz is very stable with respect to temperature). The thin-film — made out of Nickel — acts as a resistance-thermometer, and with it the temperature is recorded and the transient heat transfer measurements derived. The nickel film is kept as thin as possible to minimise its heat capacity, and the quartz substrate is sized such that it can be modelled with a semi-infinite assumption [222]. For a complete development of the theory see the work of Schultz and Jones [223].

The gauges are mounted flush to the plate. When the flow passes over the sensors, heat transfer increases the metallic film temperature, affecting the resistance of the sensor. A fast response variable current source power source is used to supply the heat transfer gauges. The output voltage is controlled (in this case at 1.7 V) by a slow response voltage regulator, which itself drives a fixed-ohm (70 Ω) resistance. The voltage in the short test times is constant, due to the response time of the slow circuit, which is in the order of ~10 s. The other end is connected to the gauge circuit. This circuit inherently accommodates low values to high values of gauge resistance and allows excited gauge resistance to be determined with just a single output signal. This circuit can also drive a short circuit without excessive current, simply because of the 70 Ω resistance, which also allows gauge circuit cable resistance to be determined. The voltage is recorded at the resistance and gauge circuit junction point.

The calibration process is well described in [82, 87] and summarised here. After an initial annealing process is performed, to relieve internal stress, the gauge is place in a temperature-controlled oven where the temperature is changed in step intervals over several hours. During this process, the voltage data is recorded through the aforementioned amplifier units, and the temperature-variant gauge resistance can be extracted, after having measured the lead resistance, which is temperature invariant and measured via a short circuit. The resistance changes with temperature, and a linear regression is fitted to the measured data, to obtain a nominal sensitivity ($\alpha_R = \frac{\alpha_g}{R_f}$, with $\alpha_g[\Omega\,K^{-1}]$ the curve fit gradient and R_f the nominal resistance at 300 K). The actual gauge resistance has a certain shot-to-shot variation, which is accounted for by measuring the gauge resistance prior to shot arrival (R_0), so that $\alpha_{g,shot} = \alpha_R \cdot R_0$.

The heat flux at the wall can be derived from the voltage reading via a numerical integration process outlined in Eq. (6.2) [223].

$$\dot{q}_n(t) = \frac{\sqrt{\rho c k_T}}{\sqrt{\pi}\alpha_R V_0} \sum_{i=1}^{n} \frac{V(t_0) - V(t_{i-1})}{(t_n - t_i)^{1/2} + (t_n - t_{i-1})^{1/2}} \tag{6.2}$$

where $\sqrt{\rho c k_T}$ is the thermal product of the quartz substrate, taken to be 1540 $Jm^{-2}Ks^{1/2}$ [221], α_R the sensitivity of the individual gauge, V_0 the initial voltage, and $V(t)$ the recorded voltage at time t. The thermal product was not measured, but rather assumed, and it was taken to be constant with temperature, as the overall change in temperature during the experiment was negligible.

The gauges were installed in the forebody using 3 Macor inserts, each housing 6 gauges with their centres 20 mm apart. Macor is a machinable ceramic material initially chosen by Wise in his flat plate experiments due to its electrically isolating capabilities. Details of the setup are shown in Fig. 6.9. Locations relative to the forebody leading edge are presented in Table 6.1.

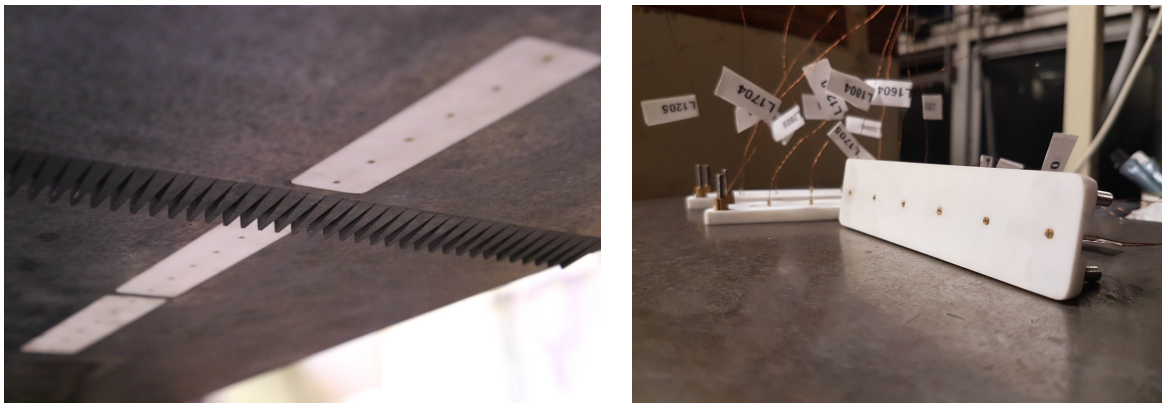

(a) TFHTG installed in the engine forebody (b) Heat transfer gauge Macor inserts

Figure 6.9: Details of the forebody thin-film heat transfer gauges setup. Reproduced from Landsberg [87].

6.3 FUEL DELIVERY SYSTEM

As discussed in Section 6.2.4, hydrogen was injected by two separate sets of injectors. A steady flow of hydrogen was achieved with two plena fuelling the injectors. If hydrogen flow is fed to the plena at sufficiently high pressures, the flow stagnates and the mass flow rates become constant during the test time through the choked injectors.

An overview of the fuel schematic is presented in Fig. 6.10. Referring to the figure, the two plena are connected to a 16 m long Ludwieg tube acting as a fuel reservoir, sufficiently long to delay the reflected expansion wave from interfering with the injection process during the experiments. In this configuration, a single Ludwieg tube was used to fill both hydrogen plena. Different inlet-to-combustor injection ratios were controlled by an interposed needle valve, adjusted prior to the experiments.

6.3.1 Equivalence ratios

Kulite sensors were used to measure initial and final pressures in the Ludwieg tube and plenum pressures. The technique to estimate the flow rate of fuel injected into the engine is briefly explained

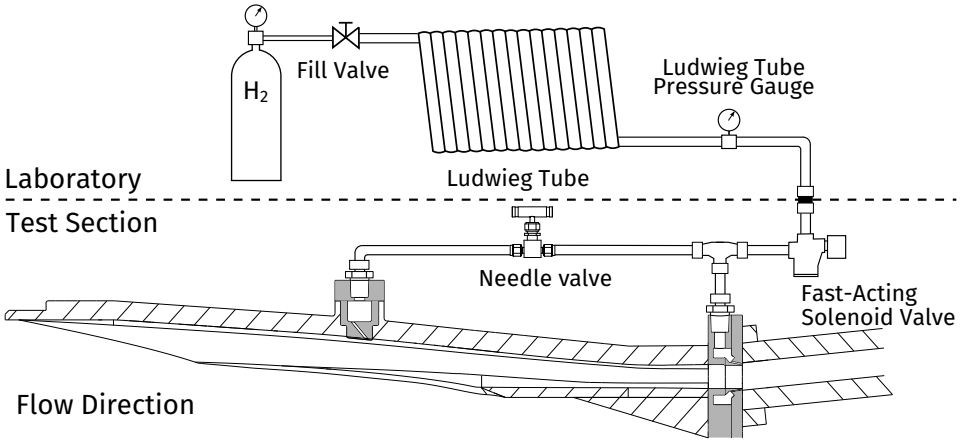

Figure 6.10: Hydrogen fuel system schematic. Needle valve in the system is for testing different injection ratios. Figure adapted from [82].

as follows. If a discharge coefficient C_d is known (see Section 6.3.2) the mass flow rate of fuel through each injector can be estimated as:

$$\dot{m}_{H_2} = \rho_{H_2} a_{H_2} C_d A \tag{6.3}$$

with $\dot{m}_{H_2}$ the mass flow rate of the injector, p_{H_2}, a_{H_2} the fuel sound speed and density at injection and A area of the injector. The sonic condition values ρ_{H_2}, a_{H_2} are calculated with iterative methods that consider the fuel in thermal equilibrium. Assuming an ideal gas model for the hydrogen fuel, as shown by [224], Eq. (6.3) can be expressed as a function of total pressure and temperature p_t, T_t, of the hydrogen in the fuel plenum:

$$\dot{m}_{H_2} = \sqrt{\frac{\gamma}{R}\left(\frac{2}{\gamma+1}\right)^{\frac{\gamma+1}{\gamma-1}}} \frac{p_t}{\sqrt{T_t}} C_d A \tag{6.4}$$

where γ, R are the ratio of specific heats for hydrogen and the universal gas constant.

Referring to Fig. 6.11, the mass flow rate of air to the engine is simply:

$$\dot{m}_{air} = \rho_\infty U_\infty A_{ref} \tag{6.5}$$

where ρ_∞, U_∞ are freestream air density and velocity, and A_{ref} the capture area of the engine. As discussed by Doherty [14], different geometric capture area definitions are available. To include the effect of the forebody, sitting at an angle of attack, where an oblique shock is generated by the leading edge, the capture area needs to be defined as in Fig. 6.11. The inlet capture area is projected over the shock wave generated by the forebody, and then onto a vertical plane. This capture area allow comparison with experiments carried out in semi-freejet mode, where the capture area is simply a projection onto the vertical plane. Note the capture area, in this case, is dependent on the freestream

Mach number as the oblique shock angle depends on it, so that the projected inlet area varies, although little change is observed in the range of Mach 10 to 13.

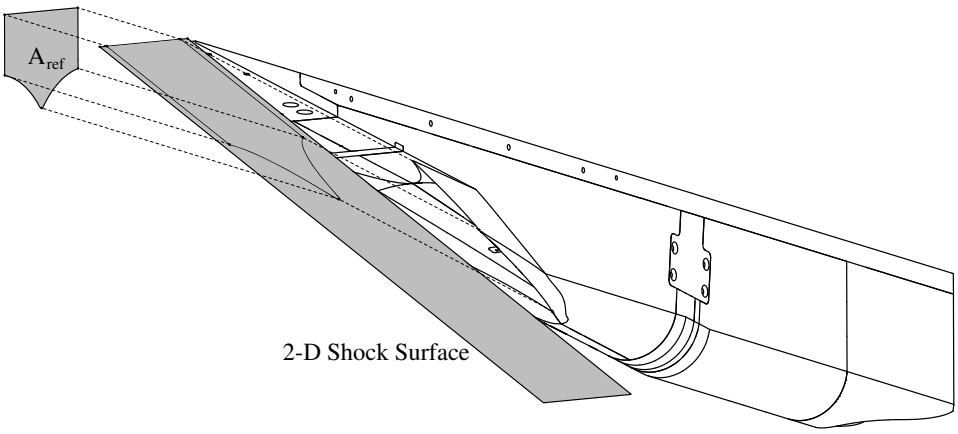

Figure 6.11: Capture area definition. Adapted from [14]. The engine depicted is a 0.32-scaled Mach 12 REST, used by Doherty in his thesis.

If the mass flow rate of both air and fuel are known, then the fuel equivalence ratio can be calculated as:

$$\Phi = \frac{1}{f_{st}} \frac{\dot{m}_{H_2}}{\dot{m}_{air}} \tag{6.6}$$

where f_{st} is the stoichiometric ratio of the fuel being injected.

6.3.2 Discharge coefficients

The discharge coefficient of a set of injectors is defined as the actual discharge rate over the theoretical maximum discharge:

$$C_d = \frac{\rho a A^*}{\rho a A} = \frac{A^*}{A} \tag{6.7}$$

where A^* is the equivalent sonic area of a set of injectors. It is possible to estimate the total amount of mass that has been injected by integrating Eq. (6.3):

$$\Delta m_{H_2} = C_d A \int_{t_i}^{t_f} \rho a \, dt \tag{6.8}$$

with t_i and t_f defining the time interval in which the solenoid valve is open. At the same time, it is possible to calculate the change in mass of fuel in the Ludwieg tube:

$$\Delta m_{LT} = m_{LT,i} - m_{LT,f} \tag{6.9}$$

It is necessary that $\Delta m_{LT} = \Delta m_{H_2}$ so that it is possible to calculate C_d as:

$$C_d = \frac{m_{LT,i} - m_{LT,f}}{A \int_{t_i}^{t_f} \rho a \, dt} \tag{6.10}$$

In the case of hydrogen, and assuming ideal gas behaviour, it is possible to rewrite Eq. (6.10) taking into account Eq. (6.4):

$$C_d = \frac{\frac{V_{LT}}{R}\left(\frac{p_{LT,i}}{T_{LT,i}} - \frac{p_{LT,f}}{T_{LT,f}}\right)}{\sqrt{\frac{\gamma}{R}\left(\frac{2}{\gamma+1}\right)^{\frac{\gamma+1}{\gamma-1}}} A \int_{t_i}^{t_f} \frac{p_t}{\sqrt{T_t}} \, dt} \tag{6.11}$$

where V_{LT} is the volume of the Ludwieg tube and $P_{LT,i/f}, T_{LT,i/f}$ pressure and temperature in the Ludwieg tube at t_i, T_f.

From an operational point of view, following [224], it is assumed that across the solenoid valve opening time, the change in temperature in the hydrogen is negligible and assumed equal to its initial value. The temperature in the Ludwieg tube was then assumed equal to the ambient temperature. In practice, a calibration procedure needs to be carried out for each set of injectors, with the other set of injectors plugged off.

Calibration results are shown in Fig. 6.12, where a slight P_{LT} pressure dependency for the discharge coefficient is noted. Finally, an uncertainty analysis on the obtained discharge coefficient is carried out in Section 10.6.

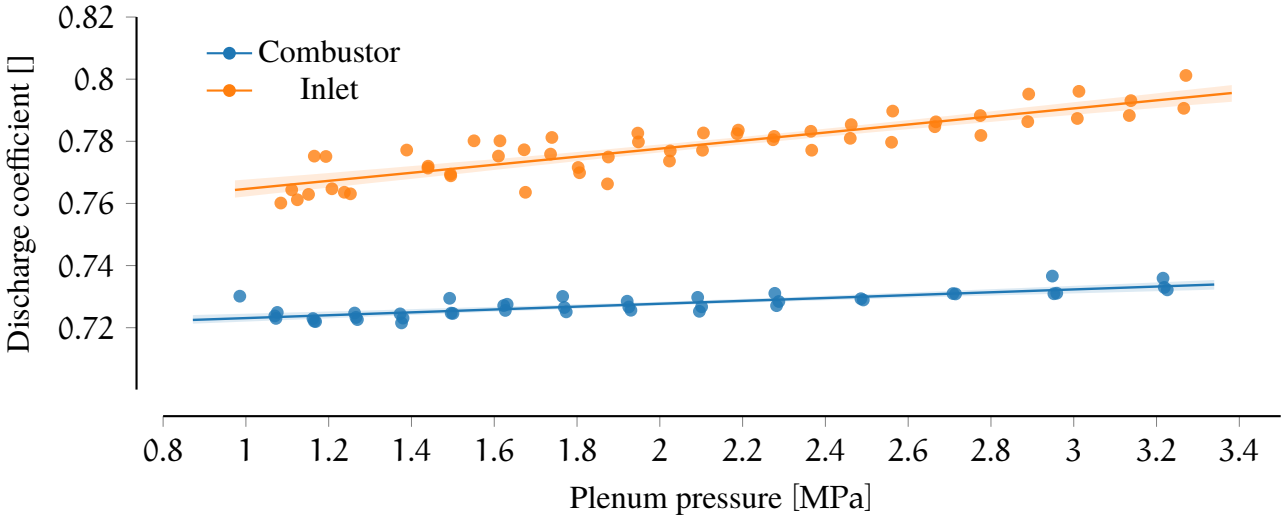

Figure 6.12: Inlet and combustor discharge coefficients as a function of plena pressure. The shaded region indicated the 95 % confidence interval of the linear regression.

6.3.3 Fuel system timescale and triggering

The timescale of the fuel system is significantly longer than the timescale of the experiments, as the reaction time of the solenoid valve is of the order of tens of ms. Additionally, the plena volumes take a finite amount of time to fill and to reach a steady state in terms of hydrogen injection into the engine. A delay system was set up to control the opening of the solenoid valve with respect to the arrival of the test gas. If the fuel was injected too early, it could have caused combustion false-positives or engine unstarts. From an operational point of view, in order to minimise the amount of fuel injected prior to test gas arrival it is important to:

- Minimise the length of the connection between the solenoid valve and the plena, as there is a direct correlation between the length of the piping and the required time for the plenum pressure to reach steady pressure.
- Tune the triggering system so that the test-gas arrives immediately after the fuel system reaches steady state.

An example is illustrated in Fig. 6.13, where the two plena pressure traces are shown along with F1, the first forebody sensor. The combustor plena traces reach steady state in 7 ms and the delay was such that the experimental window arrived shortly thereafter. On the other hand, it is noticed that the inlet pressure does not reach a steady state. This is due to the interposed needle valve, which is significantly slowed the plenum filling time. This feature, although highly undesirable, was unavoidable due to the use of a single Ludwieg tube to supply both injection systems. The previous experiments of Barth [83] and Wise [82] adopted a similar setup and noticed a similar inlet plenum rise in their experiments. They did not observe any experimental consequence, apart from an increased uncertainty in the estimated equivalence ratio. For this reason, the same setup was used in their experiments.

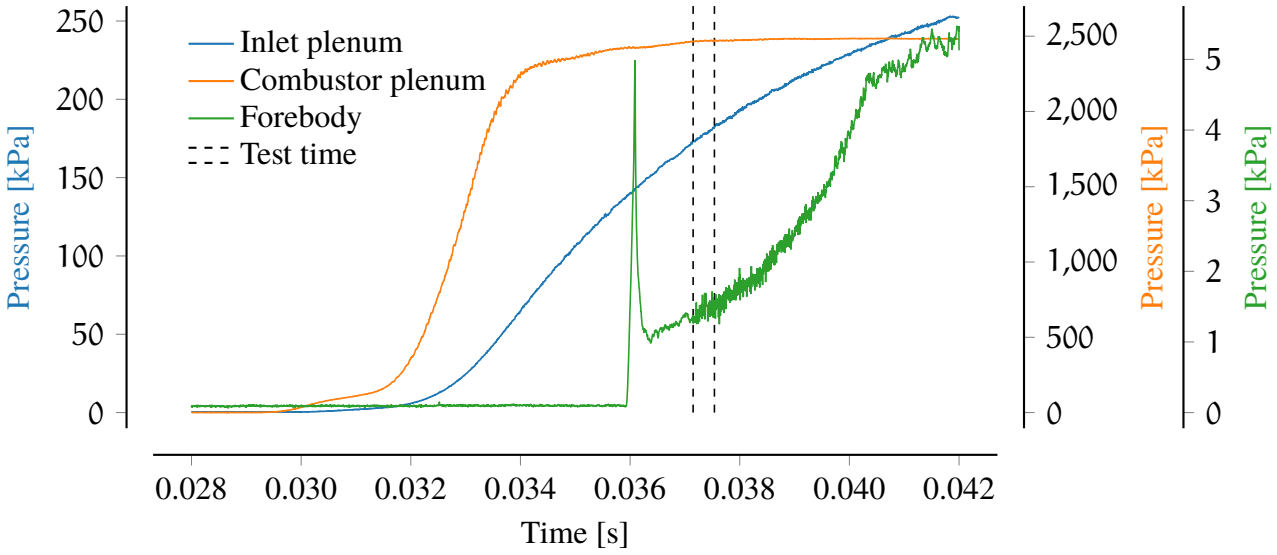

Figure 6.13: Fuel system timing for experiment x3s628. Inlet plenum on left axis, combustor plenum pressure on the right axis.

6.4 DATA ACQUISITION SYSTEM

Data was acquired via two National Instruments (NI) PXI-8110/PXI-8105 controllers, using $8+5$ NI PXI-6133 data acquisition cards, allowing measurement of up to 104 channels. These were mounted on two NI PXI-1042Q chassis. Two timebases were used for these experiments, one at 2.5 MHz and the second one — the fuel timebase — recording at 50 kHz. The whole system was triggered by ST1, the first shock tube sensor. The two DAQs were time-synced with a step pulse. The facility and model instrumentation were connected with BNC-coaxial cables, with interposed signal-conditioning units to filter and amplify all the sensors signals.

6.5 NUMERICAL METHODOLOGY

In this section, the numerical methodology is briefly discussed, introducing firstly the CFD solver, and secondly the computational grid adopted for the simulation of the Mach 12 REST engine. The EILMER3 CFD flow solver was employed in the previous chapters for the development of the Mach 12 operating condition; this solver was specifically developed at the Centre for Hypersonics and focused in the solving of time-accurate hypersonic flows for both model and facility problems. However, it is based on an explicit time-stepping scheme, which makes it is unsuitable for use in large-scale simulations of steady state flows, such as the internal flow path of the REST engine. For this purpose, the US3D flow solver was therefore adopted [225].

6.5.1 US3D

US3D is a compressible Navier-Stokes solver developed by the group of Candler at the University of Minnesota that is "highly scalable and parallel"[226] for simulating hypersonic and re-entry flows. The code is based on a cell-centred finite volume scheme, and can simulate laminar, fully turbulent, or tripped turbulent flows, and can include finite-rate chemical kinetics [226].

The flow solver is able to solve both the Reynolds-averaged Navier-Stokes (RANS) and Large-Eddy Simulation (LES) equation, but LES is too expensive for the Mach 12 REST engine flow field. Indeed, it is not possible to apply symmetry reduction to the grid, as unsteady effects are not necessarily symmetrical. Additionally, LES requires a significantly increased cell density to capture all the turbulent features. Computational capabilities at our disposal did not allow a full domain LES simulation of a Mach 12 REST engine.

The flow solver is based on finite volume formulation, with inviscid fluxes calculated with a modified Steger-Warming method [227]. The viscous fluxes were computed with the central difference MUSCL method. The code uses a modified Data-Parallel Line-Relaxation (DPLR) method to compute fluxes in strong gradients areas (for example, the near-wall flow fields) [228] and a Full-Matrix Point Relaxation for weak gradients areas (far from wall boundaries or shock waves) [229].

The available turbulence models are the Spalart-Almaras (SA), with the Catris compressibility correction [230, 231], and the Menter Shear-Stress-Transport method (SST-V) [232].

The US3D code has been previously used to simulate several high Mach number scramjet flow fields. Barth [83] and Landsberg [87] simulated the Mach 12 REST engine with good agreement with the experimental data, but much other work has been carried out (see for example [57, 233]), with good agreement found also for mixing and combustion studies [234].

For the simulation of this thesis, initial turbulence values were set to 3 % of the laminar dynamic viscosity. Turbulent Schmidt number and Prandtl number were respectively set at $Sc_t = 0.7$ and $Pr_t = 0.9$. The thermochemical model was based on the NASA Lewis polynomial fits [163] and, for the reacting simulations, uses the 13 species, 33-reactions Jachimowski scheme [235].

6.5.2 Computational grid

The computational grid adopted for this study has been kindly provided by Landsberg [87], itself an evolution of the grid developed by Barth [83]. In this section, a broad overview is provided. The reader is recommended to refer to the two cited works for a more detailed discussion. The grid, a fully structured mesh, contains 45 millions cells and was generated using the GridPro Software [236]. Only half of the engine has been simulated, taking advantage of the symmetry plane. With a wall cell height in the range 0.7 µm to 0.9 µm a $y^+ < 1$ was achieved everywhere, with exclusion of the cowl closure area and some shock reflection locations, where the flow fully stagnates and it was computationally too expensive to resolve.

A grid convergence study was carried out by Barth for the inlet part of the grid, using a series of grids with 5, 12, 20, 40 million cells. The modified Grid Convergence Index (GCI) [201] indicated an oscillatory convergence in the sense of Roy [237]. However, none of the variables considered for the grid convergence study showed a variation greater than 2.5 %, and as such it was deemed converged. The same author attempted a grid convergence study for the whole inlet and combustor grid, but due to its calculation size was unable to complete. However, experimental measurements and numerical results have shown very good agreement [83]. An overview of a coarsened grid is presented in Fig. 6.14.

Wall boundary conditions were selected to be isothermal at 300 K, to closely match the behaviour observed during the experimental test, where the extremely short test times do not allow for a significant

amount of heat to transfer to the model wall. A sonic mass flow boundary condition was chosen for the inlet injectors, as it closely mimics the actual experimental behaviour, where the injectors are choked at the injection point. The rest of the boundary condition were classical symmetry, inflow and outflow boundary conditions.

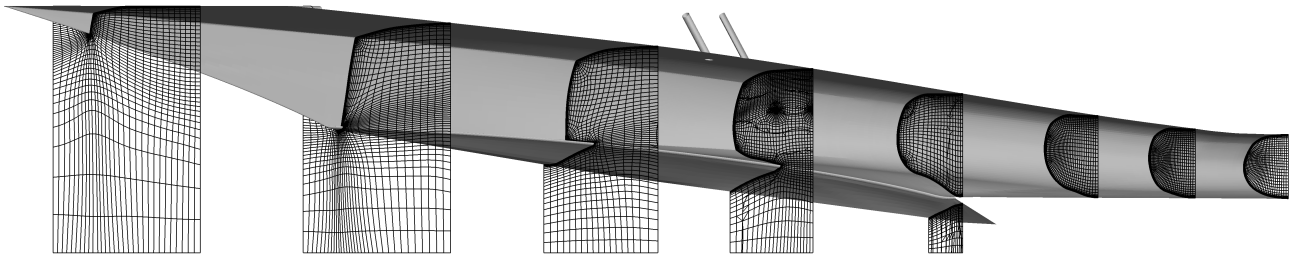

(a) Forebody/Inlet

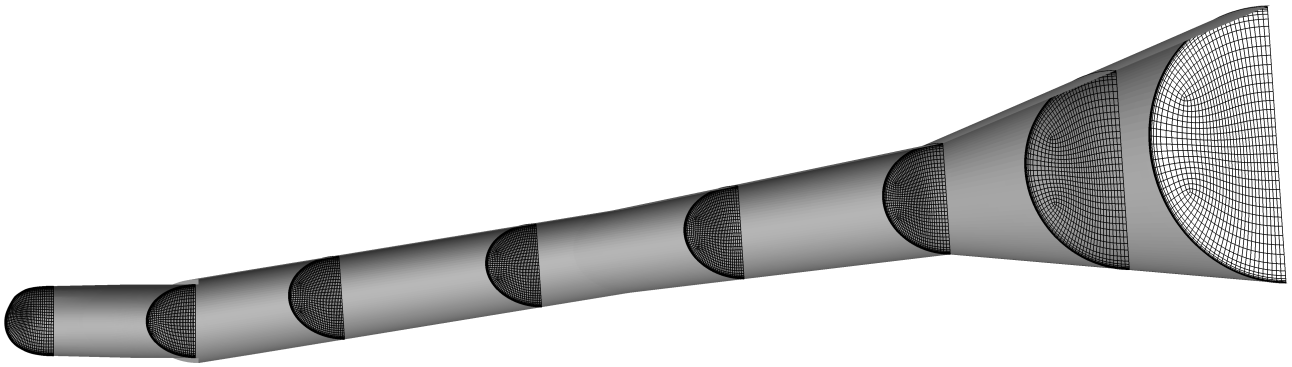

(b) Isolator/Combustor/Nozzle

Figure 6.14: Cross planes view of a 4x coarsened mesh of the M12REST engine [87].

6.6 SUMMARY

This chapter has introduced the experimental model and has given an overview of experimental and numerical tools that are employed to understand its behaviour. The engine is equipped with pressure sensors, and the forebody has heat transfer measurement capabilities that allow evaluation of the effectiveness of the different trips to transition the hypersonic boundary layer. A new fuel delivery system has been built and tested and an overview of the calibration techniques was given. Finally, a brief overview of the CFD flow solver and the computational grid adopted for the numerical part were presented.

In the next chapter, the experimental results of the Mach 12 REST engine tested in the X3 expansion tube are finally introduced and discussed.

7 SCRAMJET EXPERIMENTS: RESULTS

7.1 PREAMBLE

Parts of Section 7.4 are taken from the corresponding section of the paper P. Toniato et al. "Full Freestream Mach 12 Scramjet Testing in Expansion Tubes". In: *2018 Applied Aerodynamics Conference*. American Institute of Aeronautics and Astronautics, June 2018. DOI: 10.2514/6.2018-3818.

7.2 INTRODUCTION

This chapter details the results obtained from the experiments carried out using the half-scale Mach 12 REST engine, the new Mach 12 nozzle, and the new operating condition for the X3 expansion tube. These tests aim to answer the primary objective of this thesis, which is, to determine if a high Mach number scramjet can successfully be operated at fully replicated flight conditions in X3.

The first part of this chapter discusses introductory experimental results. Heat transfer measurements of the forebody to evaluate forced boundary layer transition are presented. Then, the main body of experimental data is presented. Scramjet testing has been performed at two different flow conditions: Condition x3s506 at Mach 11.14 and 52 kPa dynamic pressure, and the second, Condition x3s582, doubling the freestream static/dynamic pressure. Two injection schemes were tested: injection initially only at the combustor, and then using the combined, inlet and combustor fuelling scheme. In this part of the chapter, a facility flow-condition modification employed in the experiments to facilitate the engine starting process is also discussed.

Finally, in the last part of this chapter, the experimental results are firstly compared against numerical data, and then against the data generated in the previous experiments of Barth [83] and Landsberg [87]. A discussion of the pressure-scaling effects on the pressure and combustion level is also included.

7.3 STATE OF FOREBODY BOUNDARY LAYER AND TRANSITION

The state of the forebody boundary layer is of fundamental importance for the successful operation of the Mach 12 REST engine. Initial experiments by Suraweera et al. [238], carried out on a full-scale REST model with a 150 mm forebody, noted a significant pressure rise in the engine inlet. They postulated the presence of a large separation formed in the inlet and caused by the ingestion of a laminar boundary layer. The experiments done by Wise [82] investigated the forced boundary layer transition on a 1000 mm long flat plate with the use of several boundary layer trips. It was found that a swept ramp trip was not able to force a complete transition to turbulence. Diamonds trips were more effective, and 7 mm boundary layer trips were able to shift the transition forward. The transition location however, in these experiments, was still more than 500 mm behind the leading edge of the forebody. The same author installed the Mach REST engine — the same adopted for in this thesis — on the second half of that forebody plate, and carried out experiments with the swept-ramp trip. He noted an increased level of heat transfer and corresponding inlet pressure measurements compatible with a fully turbulent boundary layer. He postulated that the compression shocks of the inlet facilitated the transition to a turbulent boundary layer.

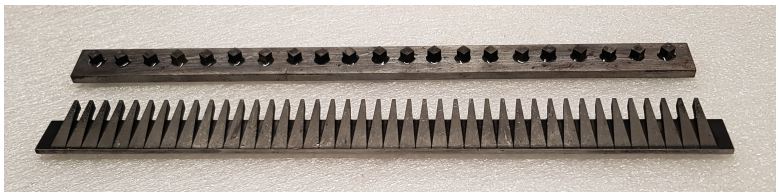

Figure 7.1: Boundary layer trips adopted for the X3 experiments: swept ramp trip in the foreground, and the diamond trip behind.

A similar set of experiments was carried out in the present study to evaluate the state of the boundary layer in the forebody in the X3 expansion tube, to ensure successful operation of the engine. Both a swept ramp trip and the 7 mm diamond trip were employed, and the trips are shown in Fig. 7.1. Heat transfer gauges were located only in the forebody (as noted previously, no heat transfer measurements were taken in the engine). These experiments proved to be extremely challenging, as thin-film heat transfer gauges are delicate and sensitive to impacts of diaphragm fragments. Indeed, any impact occurring during the test time would change the gauge resistance and make the rest of the measurement unusable. Differences in the thin film condition were clearly identifiable before and after an experiment. While shot-to-shot variation can be accounted for, if a change in resistance occurs during a single experiment, this cannot be compensated with current techniques. Additionally, It was not feasible in this campaign to replace the heat transfer gauges one-by-one, as they failed, and the results in this thesis are therefore based on heat transfer measurements gradually degrading during the campaign (although the use of score diaphragms significantly improved these issues from previous X3 experimental campaigns with

unscored diaphragms). For more details on the thin-film heat transfer gauges and the data-reduction process used to process the heat transfer measurements the reader is referred to Section 6.2.6.

Results are shown in Fig. 7.2. The measured heat flux is compared to laminar and turbulent CFD heat transfer levels extracted from the engine simulations that will be discussed in Section 7.5.1. In the figure, the reported measurements are an aggregate view of 11 experiments, 7 with the swept-ramp trip and 5 with the diamond trip, both of which were located at 235 mm downstream of the leading edge. No experiments without the boundary layer trips were carried out. It is important to note that the data is not normalised for shot to shot variation, because it would require a precise estimation of the flow properties for each experiment, which, as thoroughly discussed in Chapter 5, is presently beyond the current modelling capabilities.

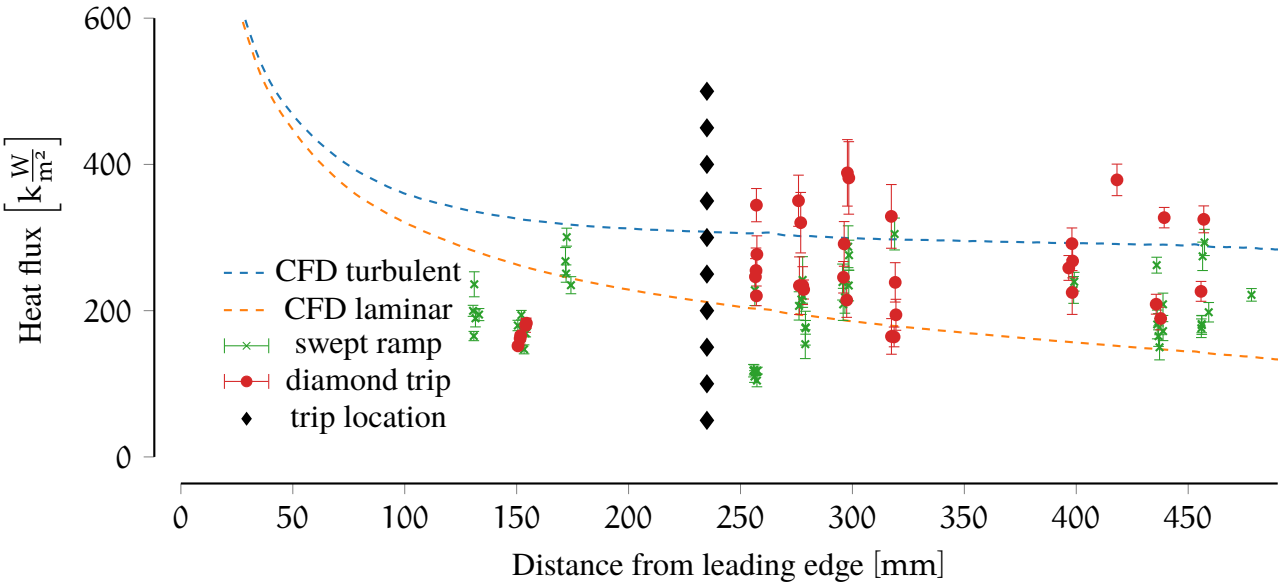

Figure 7.2: Experimental average heat flux distribution on the forebody, compared against numerical and laminar CFD estimates. The trip is located 235 mm downstream of the leading edge. REST engine inlet starts at 500 mm from leading edge. A small jitter is introduced at each location to facilitate visualisation of the aligned measurements.

A significant variability is noted, due to the uncertainty associated with the flow properties during the test time of the expansion tube, as discussed in the previous chapters. However, the data suggests that both the trips are, on average, able to cause transition, with the 7 mm diamonds trip able to achieve heat transfer levels higher than the numerical prediction. Therefore, the diamond trip was selected for the rest of the experiments. Although it is not representative of a flight boundary layer trip, it was a conservative choice to ensure a fully turbulent boundary layer.

Finally, it is noted that the forebody length was limited by the original design of the model, which was required to fit the T4 test section. Therefore, in the future it would be relatively easy to include a longer forebody to facilitate transition. Improved heat transfer measurements capabilities are, in any case, recommended, as the survivability rate of the thin-film probes is currently very low and a

significant number of experiments is required to obtain a sufficient number of measurements, especially since there is also a certain shot-to-shot variability. This shot-to-shot variability, due to both the variation in the flow condition but also the high level of noise that the heat transfer gauges demonstrate, needs to be addressed to provide higher quality and more accurate heat transfer data in the future.

On the numerical side, it has also been observed that RANS simulations can over-predict the heat transfer levels with respect to the more accurate LES [239]. Turbulent Prandtl and Schmidt number adopted for this simulation — respectively set to 0.7 and 0.9 — were calibrated by Barth [83] to match the experimental pressure measurements. The calibration of these parameters, and specifically the Schmidt turbulent number, to match experimental pressure, can lead to increased mixing rates on the near wall flows of the engine, thus producing an overestimated heat transfer. Thus, in this case, the CFD data provides an upper bound for the theoretical turbulent heat transfer levels to the forebody.

7.4 EXPERIMENTAL RESULTS

For the scramjet tests, the main parameters that were varied were the fuel equivalence ratio, the mass flow ratio of the fuel being injected between inlet and combustor, and the use of scaled (CONDITION x3s582: $q = 104\,\mathrm{kPa}$) and unscaled (CONDITION x3s506: $q = 52\,\mathrm{kPa}$) test flows. "Combustion-suppressed" tests, in which the air test gas is replaced with nitrogen, were carried out to decouple the effect of the fuel mass addition from the pressure increase due to hydrogen combustion. It is reiterated that the engine has been tested in the configuration of Barth [83], with a tailored combustor injection scheme.

Scramjet internal flow processes are inherently unsteady due to the turbulent boundary layer, mixing phenomena, and the combustion processes over the short time scales, representative of the convection of turbulent disturbances, but they should have steady time averaged values. Experimental data presented in the following figures is in the form of time averaged measurements at various engine locations. The lines between points are plotted to help distinguish different experimental runs and do not imply a linear behaviour between data-points. Each of these values has an uncertainty associated with the unsteady signals, digital sampling, and the instrumentation sensors, which are discussed in Chapter 10. Slug tracking normalisation, previously presented in Section 6.2.6, has been adopted, referenced to the first forebody pressure transducer F1, located approximately 100 mm downstream of the leading edge, so that the reported pressures are those that are experienced by the same slug of gas as it propagates through the model.

Data is averaged across ~400 µs. The test time has conservatively been defined to start ~1 ms after the initial shock arrival, corresponding to 3 to 4 flow lengths at Mach 12, following the criteria established in [240, 241]. This locates the test time between the end of the low noise steady test gas and the beginning of the under-expanded, noisier test gas. However, with adequate filtering, valid data could be extracted from the noisier part of the test gas. For example, with respect to Fig. 7.6 and considering the air shots (orange lines), the averaged test time is located between 1 ms to 1.4 ms from the arrival of the shock.

7.4.1 Combustor-only injection experiments

The first set of experiments were carried out with hydrogen being injected only in the combustor, with the plenum interposed between the inlet and combustor, 1015 mm from the forebody leading edge (see Figs. 2.6 and 6.5). A comparison between fuel-off and fuel-on, was the main goal of this experimental study. The results are summarised in Fig. 7.3 for two experiments at each case. Additionally, combustion-suppressed shots (i.e. nitrogen as the test gas) have been carried out, and are reported and discussed in Chapter 9. The nitrogen flow condition has shown some discrepancies to the corresponding air condition. Indeed, these combustion-suppressed shots show a slightly different behaviour for these and the subsequent sets of experiments. Whilst great care was taken to match the flow properties at the nozzle inlet when replacing air in the shock tube with nitrogen, it is believed that small differences in gamma and speed of sound were amplified in the unsteady expansion process and viscous effects in the acceleration tube have produced a slightly different flow at the nozzle inlet and this difference have been further amplified at the nozzle outlet.

As expected, data is consistent in the inlet part of the engine where there is no hydrogen, and where any pre-injected H2 is not expected to combust under the nominal flow condition due to low pressure and temperature. The pressure increases in the combustor, whose first section is at constant area, and second section is slightly diverging, shows clearly that there is a significant amount of combustion (orange curves) with respect to the combustion-suppressed case (green lines in Fig. 7.3). The combustion-induced pressure rise for this case shows a peak pressure $\frac{p}{p_{F1}} = 35$ with respect to the fuel-off case.

Figure 7.4 shows the normalised pressure difference between fuelled and unfuelled experiments, for air and nitrogen test gases. The figure allows differentiation of the pressure increase generated by the additional mass injection into the flow from the pressure rise generated by the combustion in the engine. It is noted that there is a certain level of combustion in the combustor section of the engine.

For this engine, the thrust generating surfaces —i.e. the diverging part of the engine— start at around 1190 mm downstream of the forebody leading edge, midway through the combustor. The pressure rise in this part of the engine is of significance for the engine performance, where it can be observed that the average pressure magnitude is 2 to 3 times higher compared to unfuelled air experiments. As noted in the previous experiments [82], the flow field is particularly smooth and uniform in this area as the long combustor regularizes non-uniformities in the flow.

7.4.2 Combined injection experiments

The combined injection mode consists of injecting fuel through both the inlet and the combustor injectors. The inlet injection station is located 840 mm downstream of the forebody leading edge, as

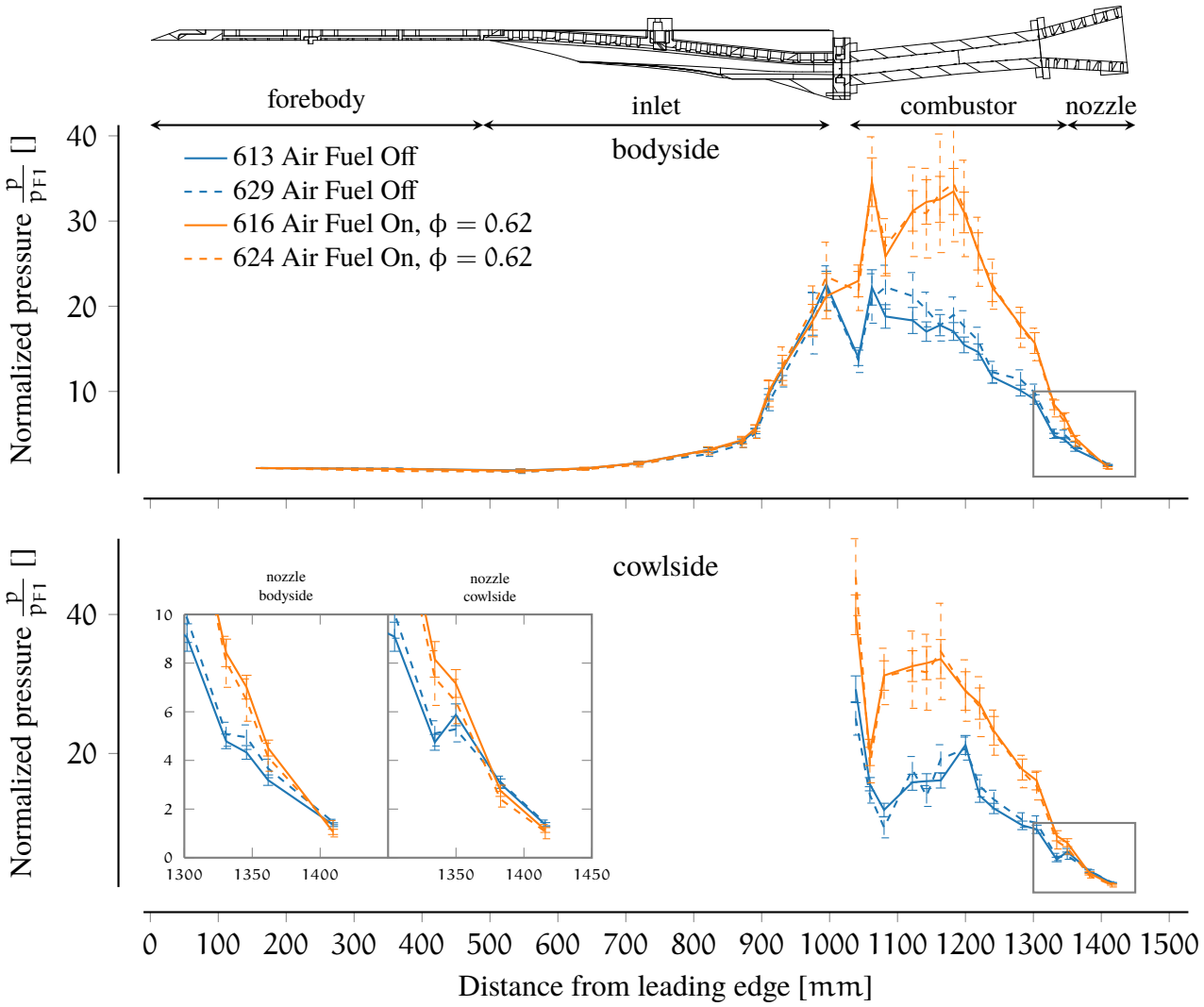

Figure 7.3: Experimental pressure distributions for combustor-only injection. Data averaged over a test duration of 400 µs. Error bars represent standard deviation from mean.

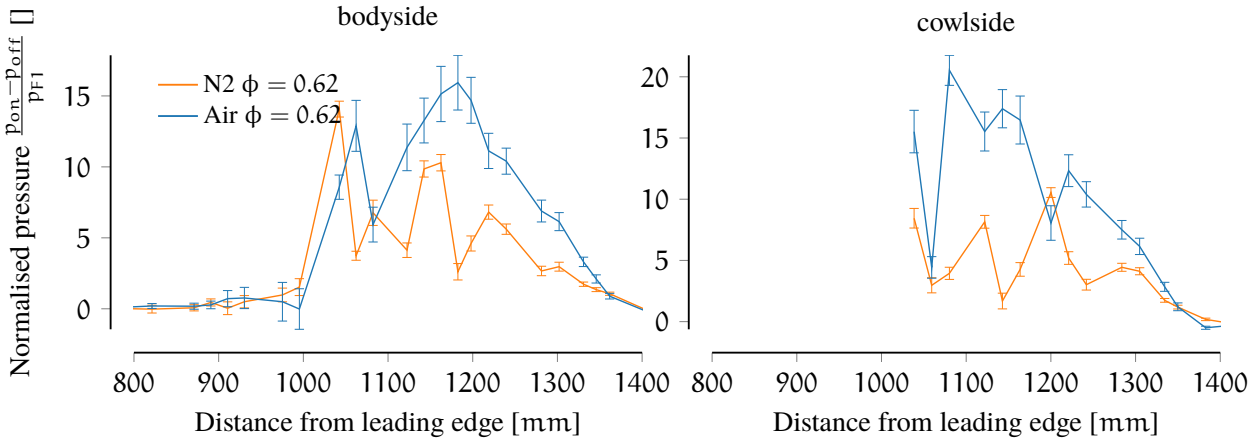

Figure 7.4: Normalised pressure difference between fuelled and unfuelled experiments during standard and combustion suppressed experiments (respectively air and nitrogen test gas), using the combustor-only injection scheme. Error bars represent standard deviation from mean.

shown in Fig. 6.5. This mode aims to increase the mixing length of the fuel/air mixture, enhancing the chance of combustion once the flow is fully compressed in the combustor [82]. For these experiments, two inlet/combustor injection ratios were used: 1:4 and 3:7 (calculated in terms of equivalence ratios). In the initial combined injection mode experiments, consistent unstarts were observed from $\phi = 0.7$ and $\phi = 1.05$, as seen in Fig. 7.5. The unstart is characterised by high pressure at inlet, and low pressure through the combustor, with no evidence of combustion. This was unexpected since it was a fuelling setup that in the previous experiments in T4 showed sustained and successful combustion [242]. Moreover, in the same figure, it can be noted that in the fuel-on cases there is a consistent pressure rise in the inlet that cannot be attributed only to injection of hydrogen in the inlet. Pressure levels in the combustor are considerably lower, as the unstart process spills the incoming flow away from the engine, reducing the oxygen available for combustion. In other experiments [82, 87], it has been determined that the noise in the pressure traces changes significantly in terms of both increasing amplitude and variance as soon as the engine unstarts. The same behaviour was present in this X3 set of experiments, and manifested by a lack of repeatability in the pressure traces and a significant variability across the mean.

Two main theories are proposed to explain the engine unstarts: first, that the inlet-injected hydrogen is being ignited by the shock-processed acceleration tube gas. For these flow conditions, the accelerator gas has a temperature upwards of 3000 K. The relatively short length of the compressed accelerator gas (in this case an inviscid estimate gives a slug length of 0.6 m) is not enough to sweep away all the pre-fuelled hydrogen, after which it would sustain the combustion through the rest of the test time. The pressure increase due to the combustion would potentially be sufficient to cause the engine to unstart. A second explanation is that the inlet pressure rise is due to a large flow separation occurring in the engine inlet, but this seems unlikely since it is not present in the fuel off cases.

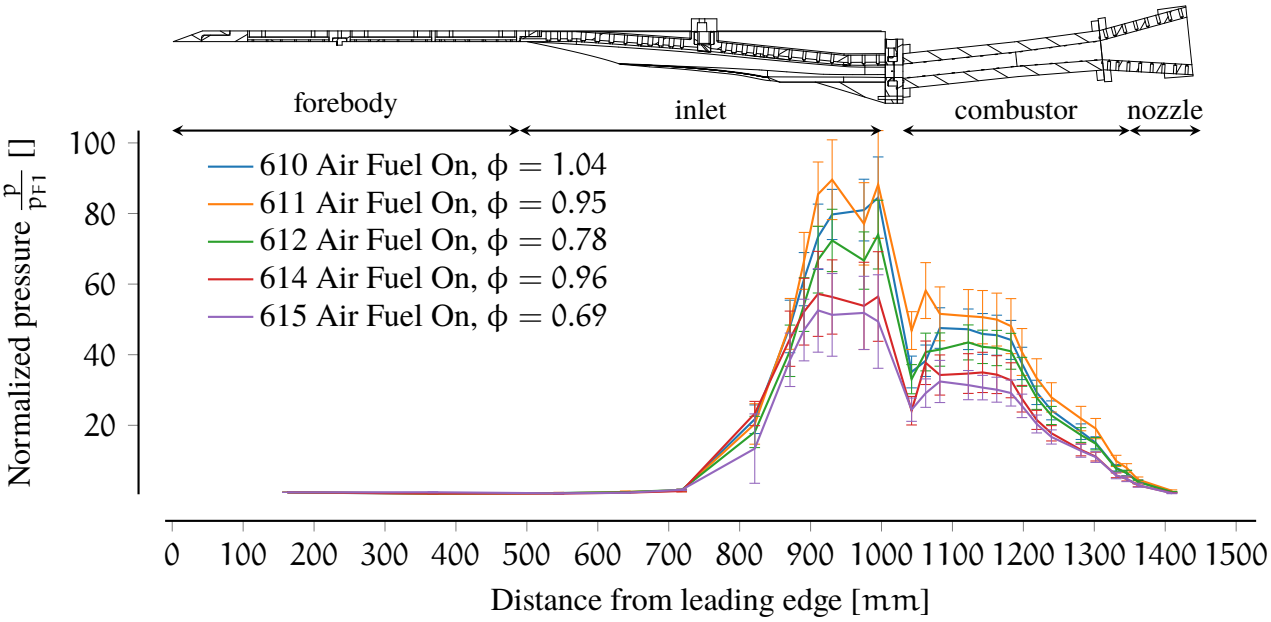

Figure 7.5: Experimental pressure distributions for combined injection: *unstart experiments*. Data averaged over a test duration of 500 µs. Error bars represent standard deviation from mean.

7.4.3 A helium accelerator gas substitution

An equivalent flow condition, initially replacing air with helium in the acceleration tube, was developed and adopted for a part of the experiments, to the aforementioned theory causing the engine unstarts. Traditionally, the adopted gas in the acceleration tube is simply air. Indeed, air is operationally easier to use, as unavoidable leaks of air from the lab do not affect the tube gas composition and therefore, performance. Other gases, such as helium, have been used in the past, especially in the first exploratory studies to understand the behaviour of expansion tubes [243]. Helium gas behaves as a perfect gas up to very high temperature, and allows ionisation-free flows at scramjet enthalpies. On the other hand, it requires high vacuum capabilities and low leaks rates, because low volume fractions of contaminant air correspond to non-negligible mass fractions compared to the much lighter helium. In the case of scramjet experiments, the purpose of using helium as the acceleration tube gas is to avoid the air/hydrogen reaction that was postulated to have occurred in the preceding experiments.

Due to the differences in specific mass and speed of sound, it is not possible to change the accelerator gas while maintaining the same filling pressure. An equivalent flow condition requires finding the helium filling pressure such that the expanded test gas properties are the same for both air and helium. The chosen approach was the one outlined in Section 3.3.1, initially adopted to find the target Mach 12 flow condition. Results are shown in Table 7.1, where the amount of contaminant air leaking into the test section is taken into consideration.

From an operational point of view, the target filling pressure was selected based on the ultimate pressure level achieved in the tube (usually in the range between 0.4 Pa to 1.0 Pa) and helium was filled immediately prior to the experiment.

Scramjet forebody pressure traces are compared in Fig. 7.6. It is clear that the startup process of the initial slug of accelerator gas for the helium case significantly differs from the one for standard air. However, the gas behind it, the expanded test gas, has similar pressure levels and pressure gradient, producing a test flow condition with the same properties. Finally, fuel-off experiments have shown near identical behaviour, as shown in Fig. 7.12, where experimental run no. 633 is done with helium, and run 629-613 done with air in the acceleration tube.

Table 7.1: Helium acceleration tube filling pressures required to match the flow properties of CONDITION x3s506 (100 % acc. tube = 58 Pa). Shock tube and piston conditions are the same.

Air in acc. tube [Pa]	Total acc. tube (air + He) [Pa]
10.0	271.5
5.0	298.7
4.0	304.1
3.0	309.6
2.0	315.1
1.0	320.6
0.0	326.1

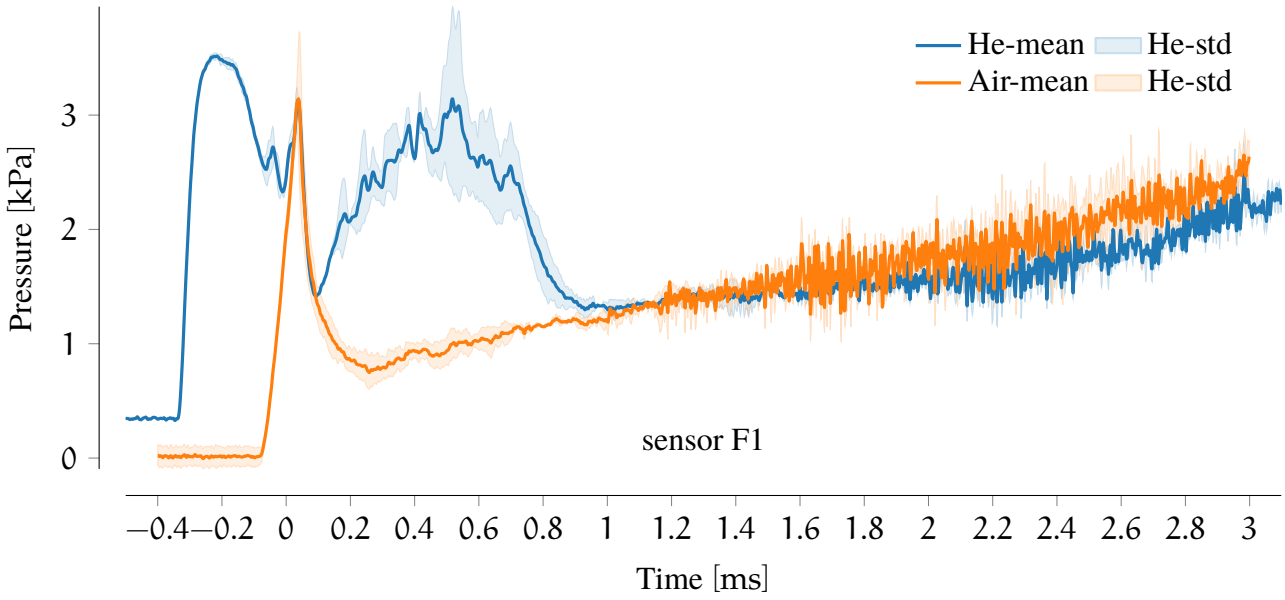

Figure 7.6: Comparison of forebody pressure trace with helium and air acceleration tube. Each set of data is a 3-shots average.

7.4.4 Combined injection mode: helium substitution

The flow condition with helium used as the accelerator gas, discussed in Section 7.4.3, was adopted for a second set of combined fuel injection experiments, to verify the proposed theory. The helium acceleration tube condition showed successful combustion for combined injection, and the test gas was found to have less unsteadiness than for the reference air acceleration tube condition. Results from the scramjet experiments with helium as accelerator gas are shown in Fig. 7.7. The combined injection with the helium acceleration gas was tested at both equivalence ratios of $\phi = 0.75$ and $\phi = 1.05$, with $\frac{\phi_{inlet}}{\phi_{comb}} = \frac{1}{4}$.

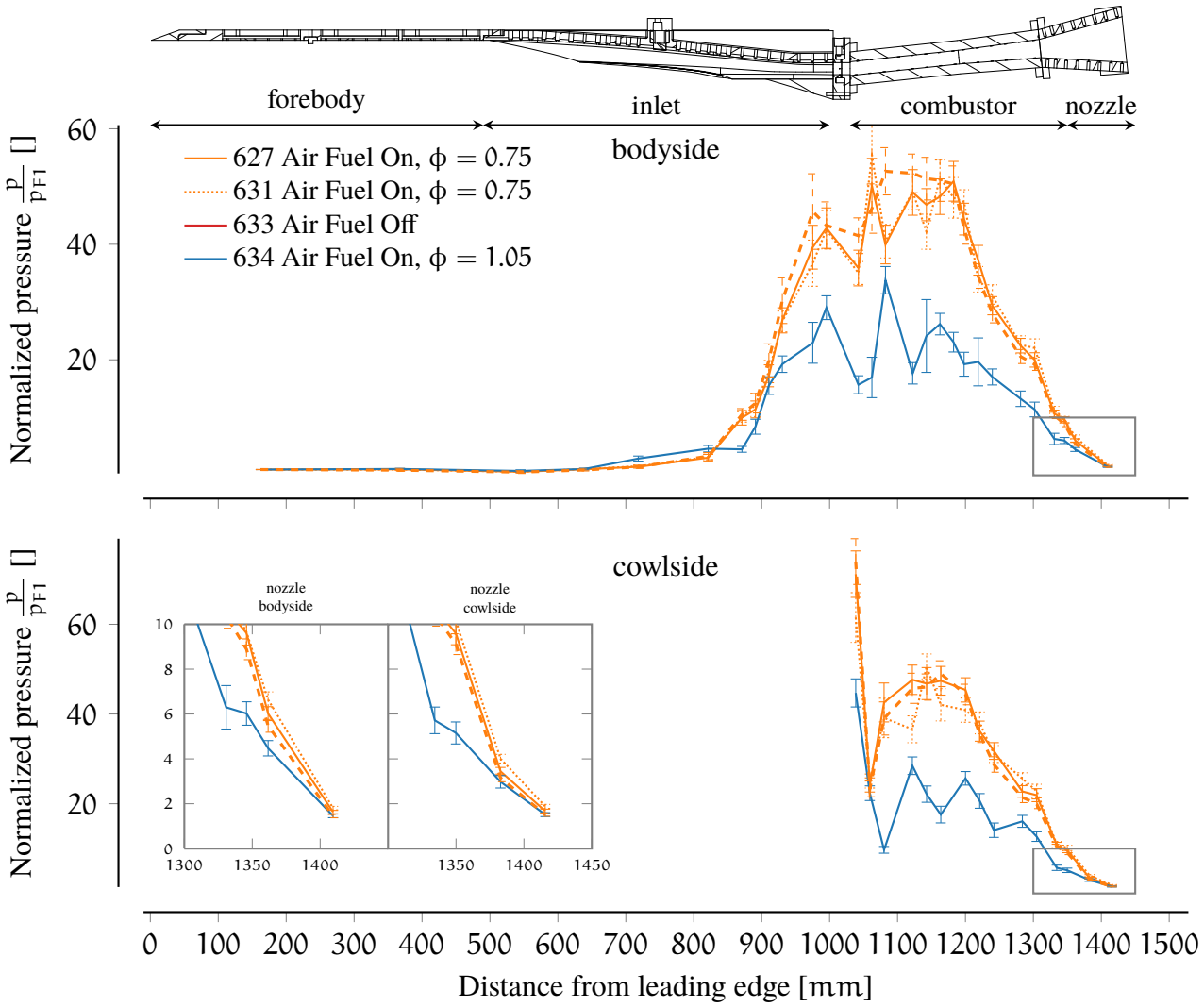

Figure 7.7: Experimental pressure distributions for combined injection with a helium acceleration tube. Data averaged over a test time of 500 µs. Error bars represent standard deviation from mean.

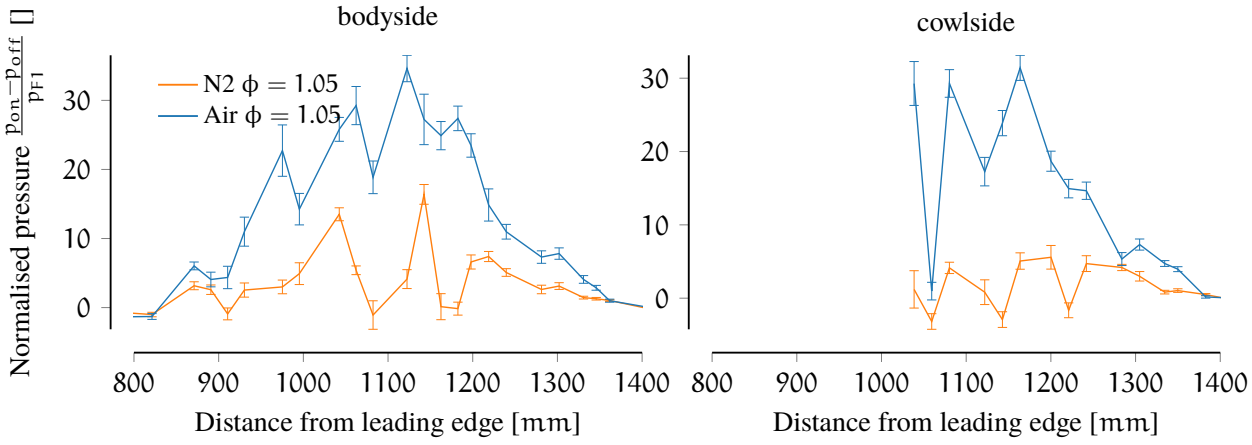

Figure 7.8: Normalised pressure difference between fuelled and unfuelled experiments during standard and combustion suppressed experiments (respectively air and nitrogen test gas), using combined injection scheme. Error bars represent standard deviation from mean.

The normalised pressure traces show a significantly greater pressure rise compared to combustor-only experiments. As observed in previous experiments and simulations [242], the inlet injection can provide a stream of radicals relatively well mixed that enhance combustion of the fuel downstream. A second and important observation in Fig. 7.7 is that there is little improvement when increasing to a higher equivalence ratio (dashed lines). Indeed, there is a slight pressure increase in the first part of the combustor, but further downstream the normalised pressure traces converge on top of each other. The injection scheme is not able to distribute the increased amount of fuel efficiently enough to fully combust the available air. Finally, there is a visible and significant pressure increase in the second part of the inlet, compatible with partial combustion prior to the combustor injection point. This observation reinforces the likelihood of the hydrogen igniting in the inlet when using air as the accelerator gas, which produces an earlier high temperature mixture of oxygen and fuel.

Figure 7.8 clearly illustrates the significant and robust combustion that occurs in the engine by comparison to the pressure rise in combustion-suppressed experiments. Additionally, comparing this figure with Fig. 7.4, the idea that this injection scheme is more effective than the combustor-only one is reinforced.

7.4.5 Scaled condition, combustor-only experiments

The final set of experiments involved the application of a pressure-length scaling to the test condition, which enabled the engine to be tested at its original designed flight condition. For this set of experiments, a configuration with combustor-only injection was tested, as the fuel system was limited by the maximum pressure rating of the Ludwieg tube; as higher fuel pressures are required for higher dynamic pressure flows. The pressure-scaling applied to this condition essentially doubled the test flow static pressure exiting the nozzle (with respect to the original Condition x3s506, indicated in Table 5.3), while maintaining a similar gas slug length and an almost identical test time.

The results are presented in Fig. 7.9, where it can be noted that the overall trends are very similar the unscaled cases of Fig. 7.3. Moreover, both nitrogen shots and air experiments present features that are almost equivalent both in shape and location to the ones previously observed. However, in this case it appears that the combustion efficiency, evaluated simply in terms of overall normalised pressure rise, as shown in Fig. 7.10, is lower at the scaled condition.

In summary, all of the presented experiments have shown successful and significant combustion at correctly scaled, freestream flight conditions, with both combustor-only injection and combined injection schemes.

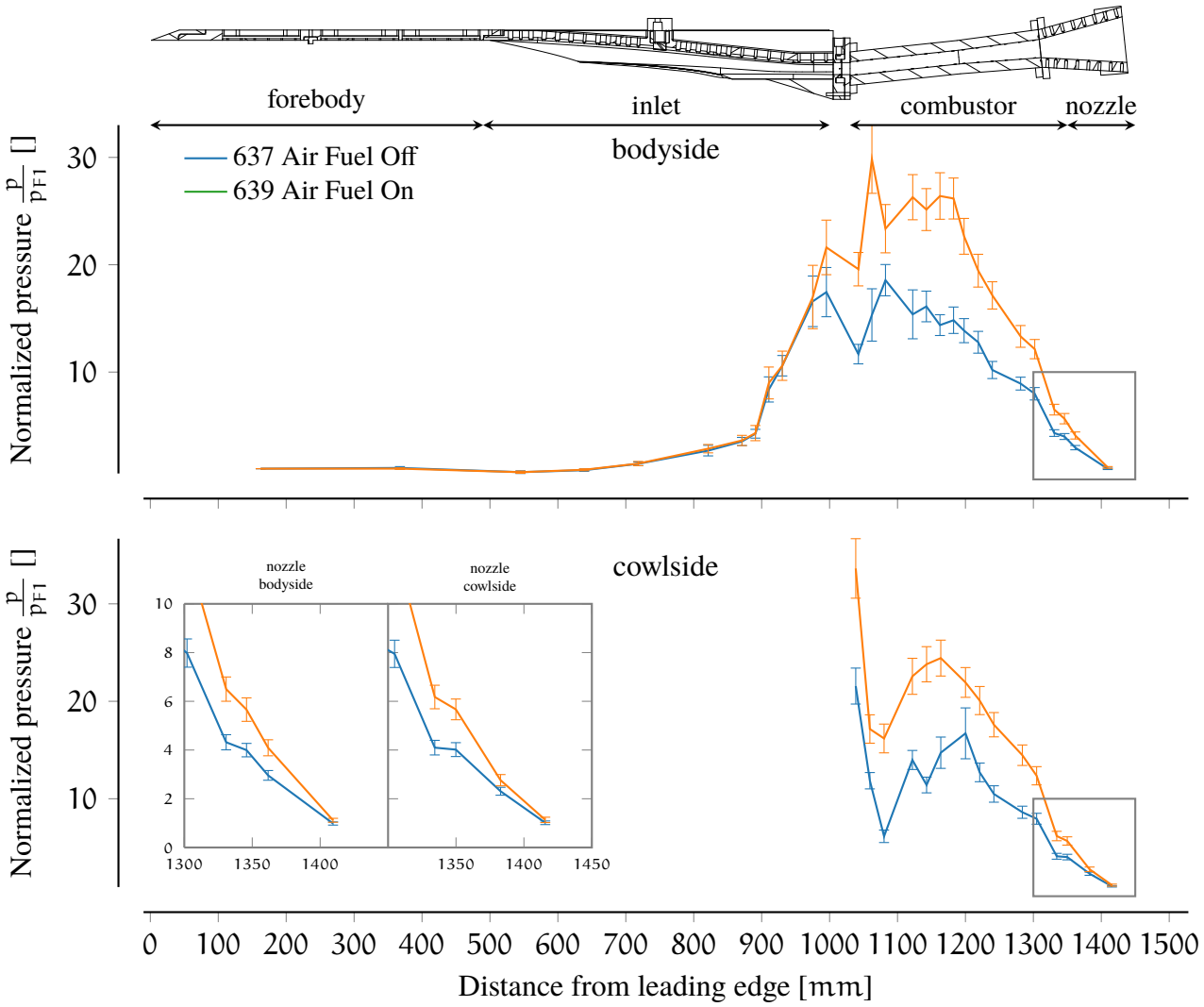

Figure 7.9: Experimental pressure distributions for combustor-only injection at scaled condition, $\phi = 0.56$. Data averaged over a test time of 450 µs. Error bars represent standard deviation from mean.

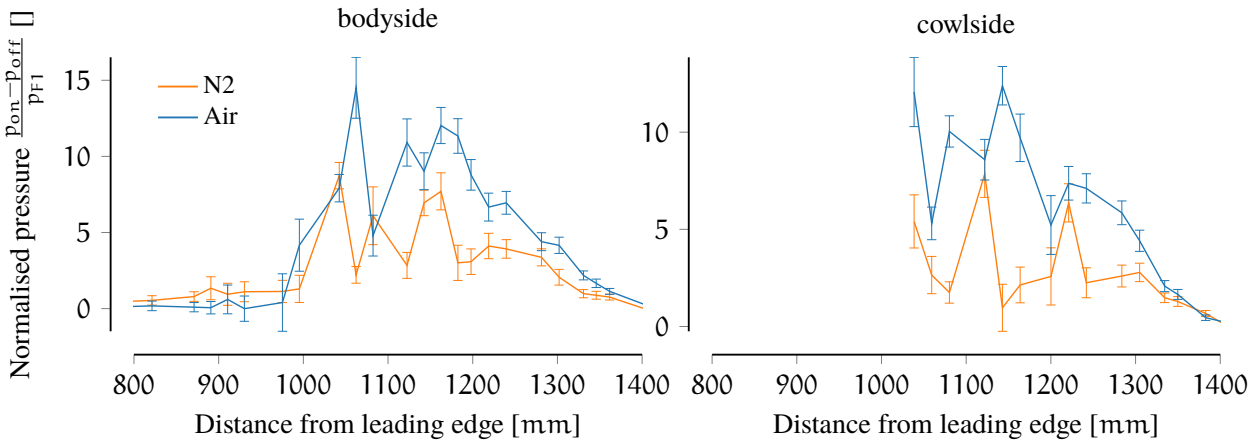

Figure 7.10: Normalised pressure difference between fuelled and unfuelled experiments during standard and combustion suppressed experiments (respectively air and N2 test gas), using the combustor-only injection scheme and pressure-scaled condition. Error bars represent standard deviation from mean.

7.5 DISCUSSION

In the previous sections we have answered and satisfied the main objective of this thesis, by testing the engine in freejet condition, with pressure-length scaling, and showing successful combustion. In this section the data is compared with numerical simulations to provide further insight in the flow processes inside the engine. The different fuelling schemes utilized are discussed with reference to the previous experimental campaigns of Barth [83] and Landsberg [87].

7.5.1 CFD comparison

While expansion tube flows intrinsically produce unsteady freestream properties, steady state simulations at the nominal conditions of Table 5.3 were carried out to allow a comparison to the experimental data. Whilst it is recognised that these steady state simulations cannot fully capture the transient experimental behaviour, they can potentially still give useful insight into the engine operations, serve as a tool to evaluate the accuracy of the experiments, and highlight differences from the theoretical behaviour. Considering the unsteady experimental freestream properties, time-accurate full engine simulations would be ideal. However, the enormous computational cost required makes them infeasible. On the other hand, previous comparisons of experimental data for this engine — in RST tests at semi-freejet mode — and numerical data showed very good agreement [83]. On the other hand, the levels of spatial compared to temporal property gradients that occurs are such that a quasi-steady analysis still holds, as discussed by McGilvray et al. [152].

The inflow condition for the engine simulations comes from Table 5.3, which corresponds to the inflow for a scramjet at angle of attack of 5°. Simulations were performed for the unfuelled case only, from which pressure traces were extracted and compared to the experimental results.

Figure 7.11 shows the centreline contour plots for Mach number, pressure and temperature. To be noted is the shock train structure that is formed in the last part of the inlet and then inside the combustor, which is responsible for the multiple pressure rises that can be observed in the pressure centreline traces.

The comparison of numerical and experimental pressure measurements on the bodyside of the engine is shown in Fig. 7.12. The comparison is carried out with normalised pressure traces. Indeed, as discussed by Barth [83], the slug-tracking normalisation process incorporates the transient effects inherent to the test condition. The comparison shows good agreement, both in the inlet and nozzle parts of the engine, with overlapping pressure traces. On the other hand, it is noted that the main combustor pressure rise — due to a shock impinging onto the wall — is shifted forward by ~20 mm. Similarly, the second pressure rise from the combustor presents a similar forward-shift at x=1250 mm.

To investigate the root cause of this shift in location of the shock impingement, simulations have been carried out with modified inflow conditions. Mach number and angle of attack have been varied,

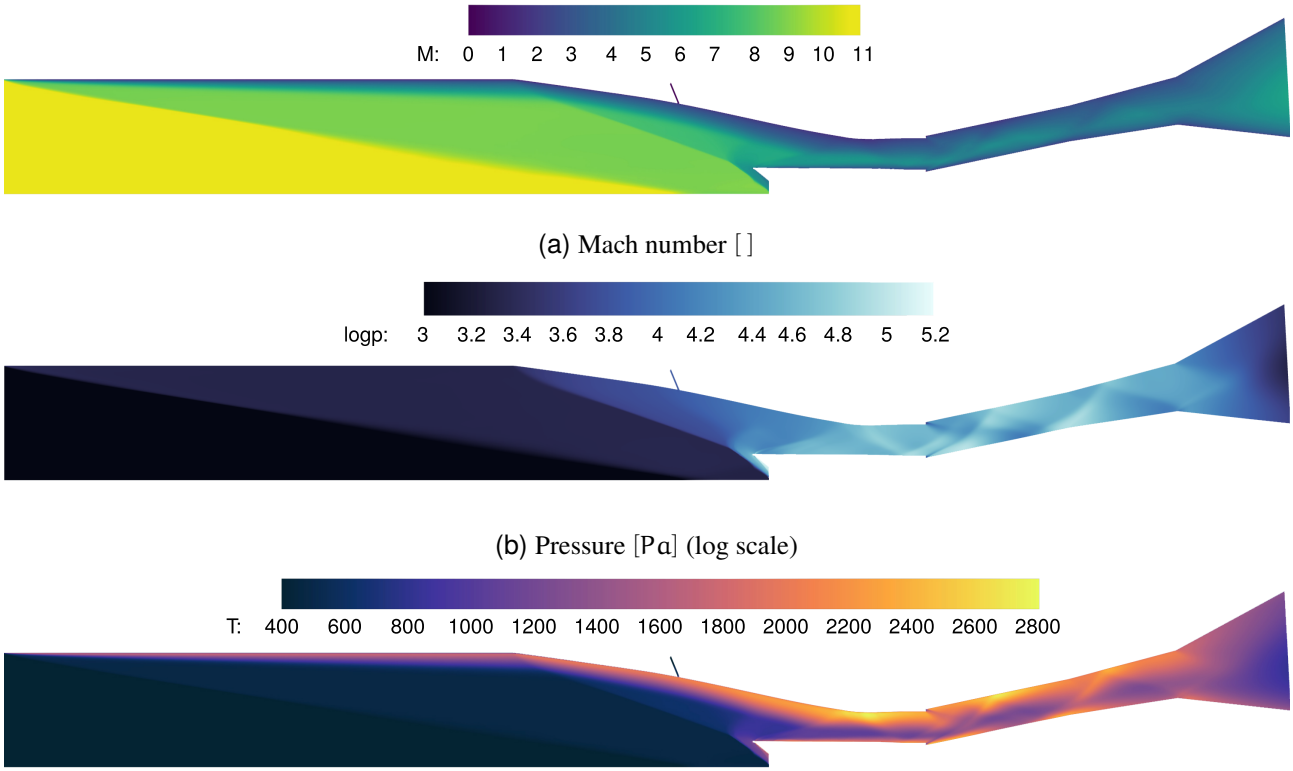

(a) Mach number [ ]

(b) Pressure [Pa] (log scale)

(c) Temperature [K]

Figure 7.11: CFD contours of *a)* Mach number, *b)* static pressure and *c)* temperature in the Mach 12 REST engine: symmetry plane, unfuelled case.

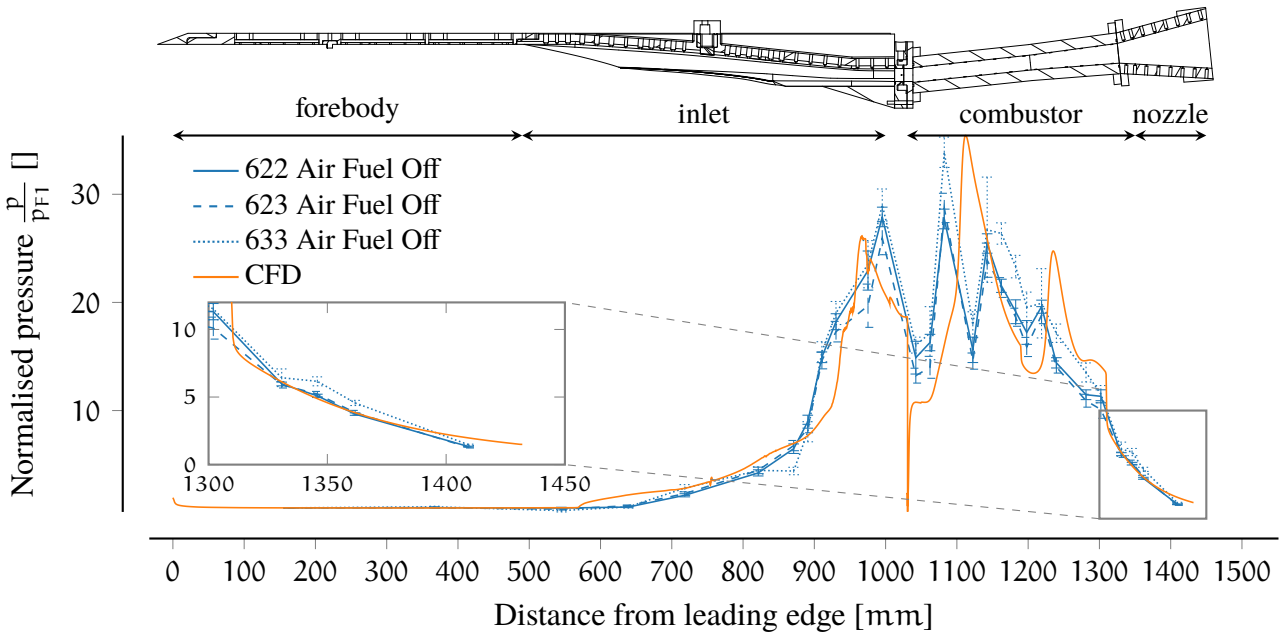

Figure 7.12: Comparison of experimental and numerical pressure traces along the engine, CONDITION x3s506, unfuelled case. Data averaged over a test duration of 450 µs. Error bars represent standard deviation from mean.

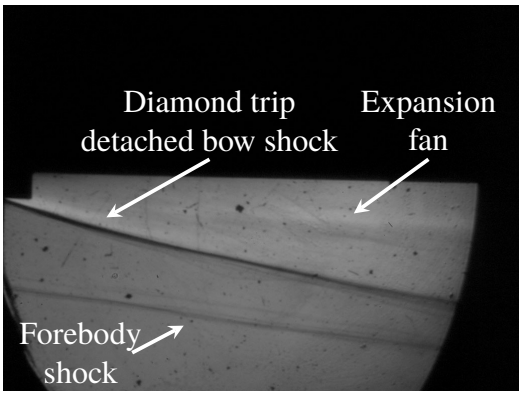

Figure 7.13: Schlieren images of flow structure around the diamond trip. T4 shot 12000, 5 mm diamonds. Image from [87].

and a fully laminar simulation has been done. Results are shown in Figs. 7.14 to 7.16, where the blue line always indicates the reference CFD solution of Fig. 7.12. It is noted how the position of the main combustor pressure rise is not affected by the change in these properties. The most notable difference can be identified in the laminar flow case, in which it appears that the pressure rise location is sensibly shifted further downstream in the engine.

It is also noted that the nominal turbulent simulations have been assumed fully turbulent, and did not model the boundary layer trip accurately. Indeed, the shock structures induced by the boundary layer are relevant. Specific to the diamond trips employed in this thesis, in [87] a stagnation region was observed in schlieren images, which ensured that the flow created a separation area behind the trip. A notably strong bow shock is formed and an expansion fan follows. Further studies are required for more accurate modelling of forced transition.

In summary, although some discrepancies can be observed with respect to steady state numerical simulations, an overall good agreement in the general trend is shown. The discrepancies cannot be explained with a simple change in the inflow conditions or simulation parameters. Most importantly, this analysis shows that despite the uncertainties in the flow condition due to test flow increasing static pressure during the test time, experiments are able to capture the main features of the steady state numerical data, supporting the proposition that expansion tubes can be effective facilities for scramjet testing.

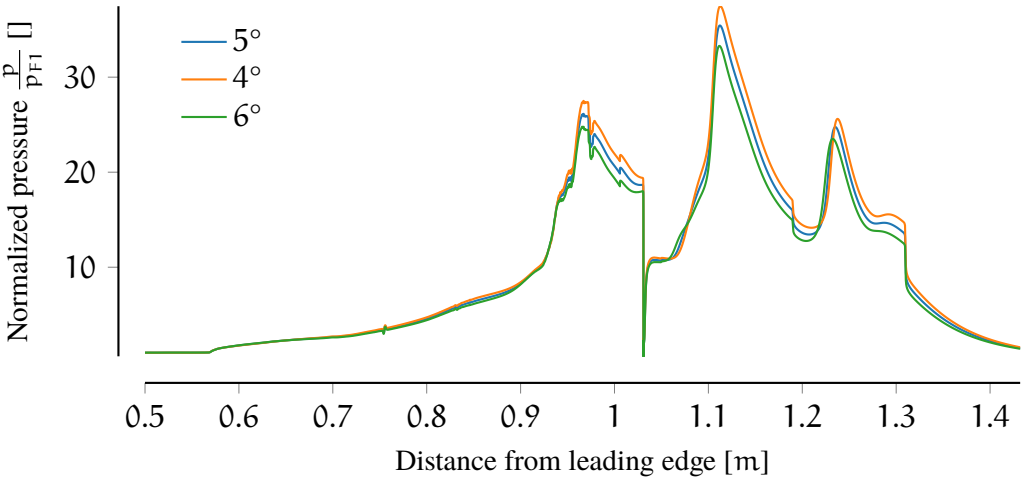

Figure 7.14: CFD comparison of centreline pressure traces at varying angle of attack.

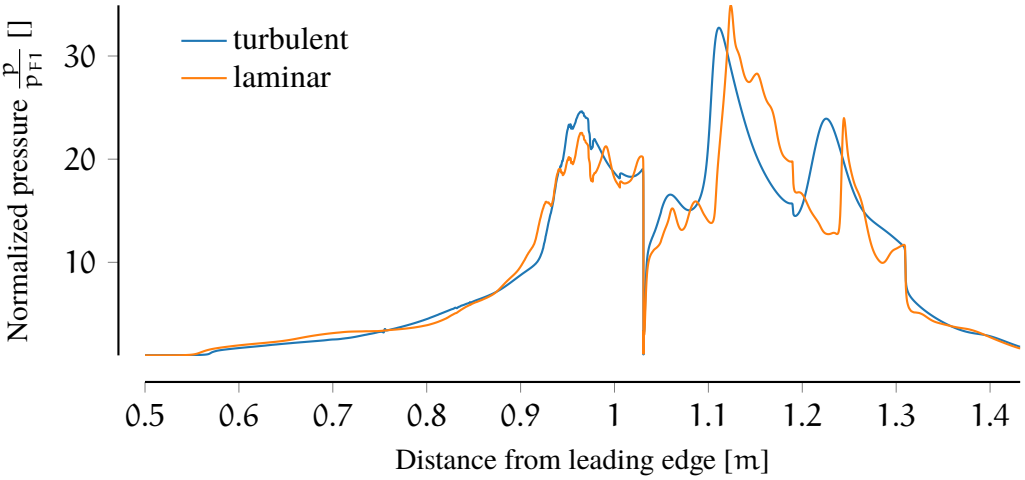

Figure 7.15: CFD comparison of turbulent and laminar simulation data: centreline pressure traces.

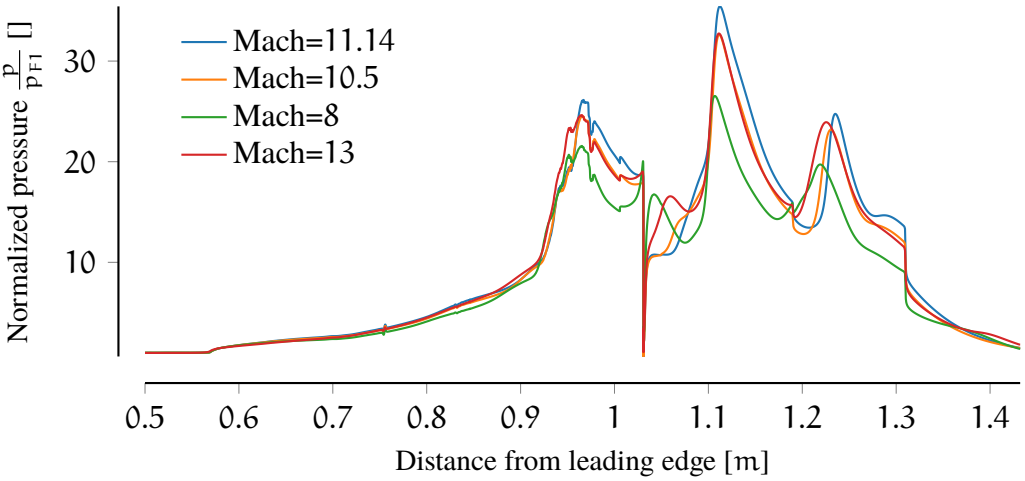

Figure 7.16: CFD comparison of centreline pressure traces at varying inflow Mach number.

7.5.2 Comparison with prior experiments: unfuelled shots

Two previous experimental campaigns were carried out with the engine in the same configuration, by Barth [83] in 2014 and Landsberg [87] in 2018, just prior to the experiments presented here. The experiments were done in semi-freejet mode in the T4 reflected shock tunnel. Averaged equivalent flight conditions were respectively Mach=11.7 and dynamic pressure $q = 36.0\,\mathrm{kPa}$ in the first campaign, and Mach=11.6 and dynamic pressure $q = 31.0\,\mathrm{kPa}$ for the second one. In this and the following section, a comparison of the present X3 data with selected tests from the two T4 experimental campaign is presented.

Figure 7.17 shows a comparison of normalised bodyside pressure traces for present X3 experiments, the previous T4 experiments, and numerical simulation. It is noted that Barth's experiment closely matches the numerical data. Landsberg's experiments, on the other hand, present some discrepancies similar to those noted in the X3 dataset.

Referring to Fig. 7.17, inlet measurements are closely matched between the three experimental campaigns, but the main pressure rise in the combustor exhibits a forward shift for the X3 and the Landsberg experiments, which closely reproduces to the shift discussed in the previous section. Additionally, this feature can be noted in all of Landsberg's experiments.

The analysis of the previous section indicates that differences in the Mach number of the inflow, effective angle of attack of the engine and differences in the boundary layer condition (turbulent or laminar) are not responsible for this forward shift. Other changes in the flow parameters have not been explored, but these are unlikely to be responsible, as the same difference is noted in the Landsberg experiments, which nominally are at the same flow condition of Barth.

Therefore, it can be inferred that this feature is specific to the experimental engine, and probably due to some discrepancies in the internal flow-path, as follows. It is noted, indeed, that the engine has undergone several experimental campaigns and some damage to the internal flow path due to usage and abrasion is likely. For example, the curvature radius of the inlet leading edge is increased due to wear, itself caused by the high number of experiments that the model has undergone. On the other hand, if the shock shifting is excluded, the comparison of X3 and Barth's experimental data indicates an overall good agreement, and the general normalised pressure levels across the combustor are well-matched.

It is also noted that overall there is an excellent agreement in the trends of the different experiments, if the shock forward shift is excluded. The inlet measurements, which are the most sensitive ones to the inflow conditions, match each other within the experimental uncertainty. Considering the facility differences, and how the engine was tested in different modes, (freejet and semi-freejet) there is a strong evidence that the results are meaningful and correct. Moreover, the movement of a shock is relatively unimportant, as the sensors are closely spaced (in this case 20 mm) so that even small changes in the shock angles can exacerbate the difference that is seen in the discrete pressure plots.

In summary, this comparison, together with the numerical discussion of the previous section, validates unfuelled experiments of the REST engine. The discrepancy with respect to the numerical data is noted to be present in the prior experimental campaign in T4, and its origin is likely related to wear and tear of the experimental model employed. The consistency between X3 and Landsberg's results indicated that it is not a facility-based issue.

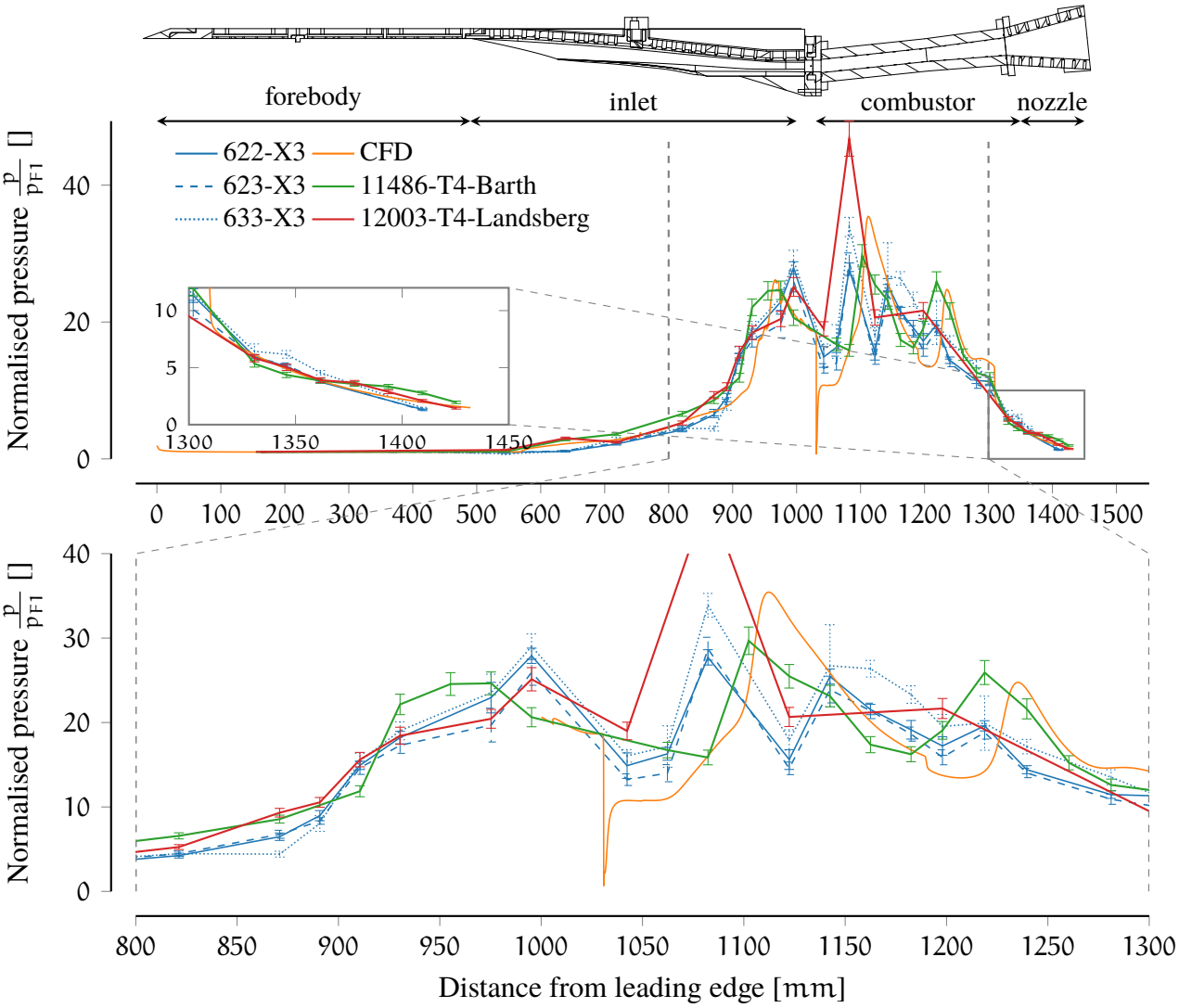

Figure 7.17: X3 and T4 comparison of unfuelled shots. Uncertainty for T4 experiments calculated as 5.5 % [87].

7.5.3 Comparison with prior experiments: combustor-only injection scheme

Comparison of fuelled experiments has the additional variable of the amount of fuel injected in each experiment. Uncertainties associated with freestream flow condition estimation have led to differences in the fuel equivalence ratios. Despite that, in this and the following section, a simple comparison is presented.

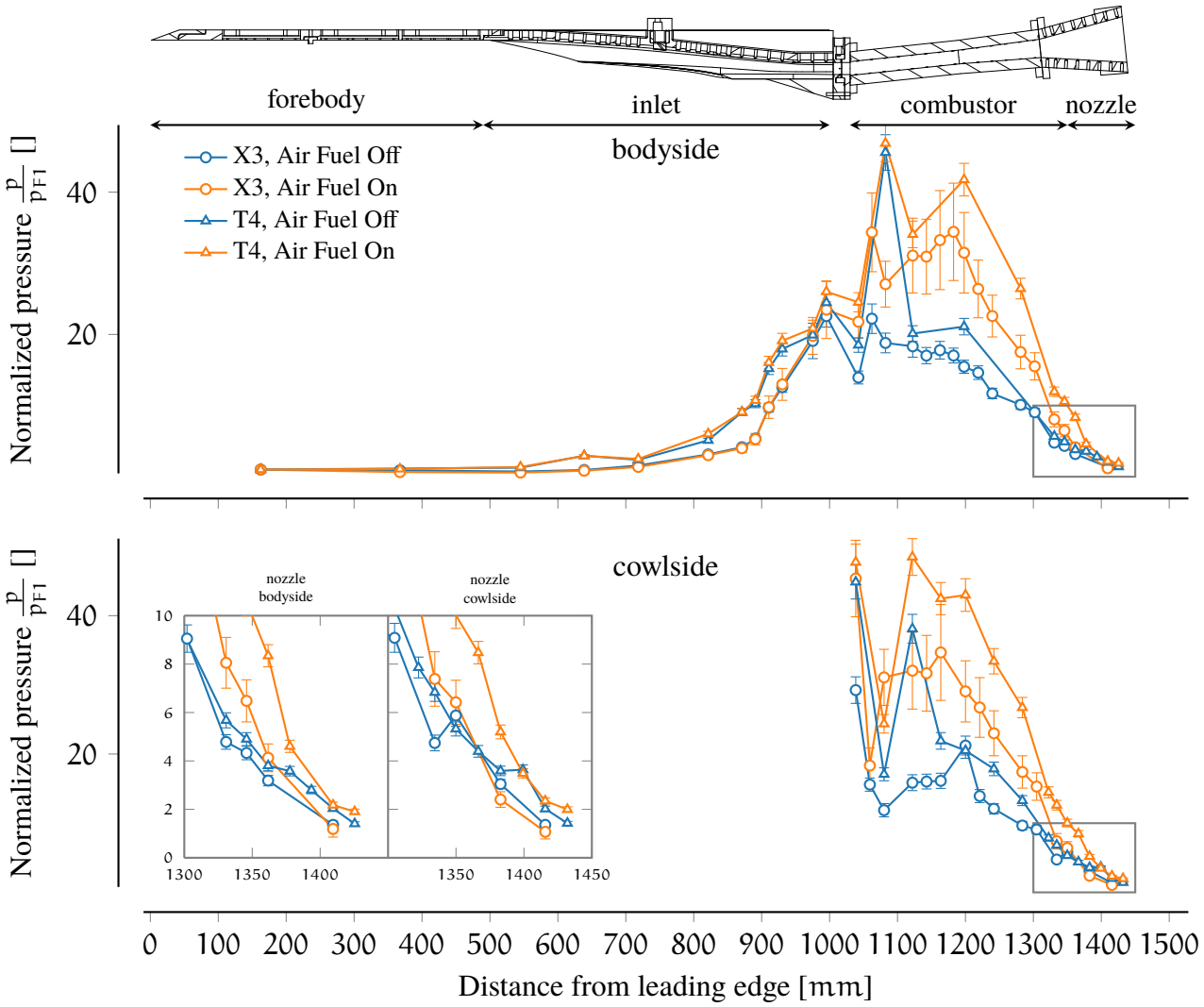

Figure 7.18: Comparison of experimental pressure distributions for combustor-only injection scheme, X3 nominal condition and T4 Landsberg's experiments. X3 experiments: $\phi = 0.62$. T4 experiments: $\phi = 0.91$. Uncertainty for T4 experiments calculated as 5.5 % [87].

Figure 7.18 illustrates a comparison of air, fuelled and unfuelled experiments from the current X3 dataset and Landsberg T4 dataset, for a combustor-only injection scheme. Albeit the amount of sensors employed in Landsberg's experiments was reduced, it can be noted that the produced fuel-on pressure rise is significantly bigger in the T4 experiments.

In the inlet, a significant pressure rise in the Landsberg T4 experiments is noted, which has not been observed in the present experiments, nor in the experiments of Barth. Landsberg investigated the issue, but no clear reasons were identified. The inlet pressure rise of Landsberg's experiments is believed to have significant effects on the engine internal flow dynamics, to the point that a more insightful comparison cannot be carried out. Additionally, it is noted that the amount of fuel injected differs, so that a conclusive answer cannot be drawn from this set of data.

7.5.4 Comparison with prior experiments: combined injection scheme

Combined injection experiments were carried out by both Landsberg and Barth, and experimental comparisons are shown in Figs. 7.19 and 7.20. For both the comparisons, there is a slight difference in equivalence ratio but, considering the uncertainties associated with them (see Section 10.6 and in Barth [83] and Landsberg [87]) they are statistically similar to each other. With respect to the considerations of model degradation that were discussed in the previous sections, it is necessary to point out that, for comparison of fuel-on experiments, they have a reduced importance, as globally the pressure rise induced by the combustion is significantly greater than the changes induced by the model geometry variations.

The experimental data of Landsberg present a very significant pressure rise that does not match the data of Barth, despite both studies testing the engine in the same configuration, facility, and almost at equal freestream condition. As noticed for the previous combustor-only injection comparison, there is a significant increase in pressure during the fuelled shots.

The comparison with Barth's data, which is believed to be more relevant as equivalence ratios are closer, shows that normalised pressures levels for both fuelled and unfuelled experiments are very similar. It is noted that in the final section of the engine, the pressure is consistently lower in the X3 experiments, on both the cowlside and bodyside of the engine.

Despite the small difference in equivalence ratios, a quantitative, but simplified analysis can be carried out as follows. The "thrust potential" of each experiment can be evaluated by integrating the experimental pressures on the thrust producing surfaces, i.e. the second part of the combustor and the nozzle (as they both are slightly diverging). The experimental pressures were assumed to be representative as average measurements of the actual circumferential pressures. To account for shot to shot variation, and changes in flow conditions across different experiments, the pressure is normalised prior to the integrations, thus obtaining a pseudo-gross thrust coefficient:

$$\overline{C_{T\,gross}} = \frac{1}{A_0} \int_S p_N \vec{t} \cdot dA \tag{7.1}$$

where p_N is the normalised pressure trace, $\vec{t}$ is a unit vector aligned with the direction of thrust, S is all of the thrust generating surfaces (i.e. $x > 1182\,mm$ from the leading edge), and A_0 a reference area. It is noted that a classic gross thrust coefficient normalises by dynamic pressure, which, however, cannot accurately be known for each of the X3 experiments, as only a reference nominal condition can be established (see Chapter 5). Once this pseudo-thrust coefficient can be estimated, the unfuelled amount can be subtracted, and estimates compared.

Calculations of the pseudo-gross thrust coefficients show Barth's coefficient is 1.67 times higher than the one calculated for the X3 experiments. Given the overall fuel equivalence ratio match and similar overall pressure level, this lower thrust coefficient is an indication that the engine is burning less effectively in the more chemically correct expansion tube flows. This is consistent with the fact that

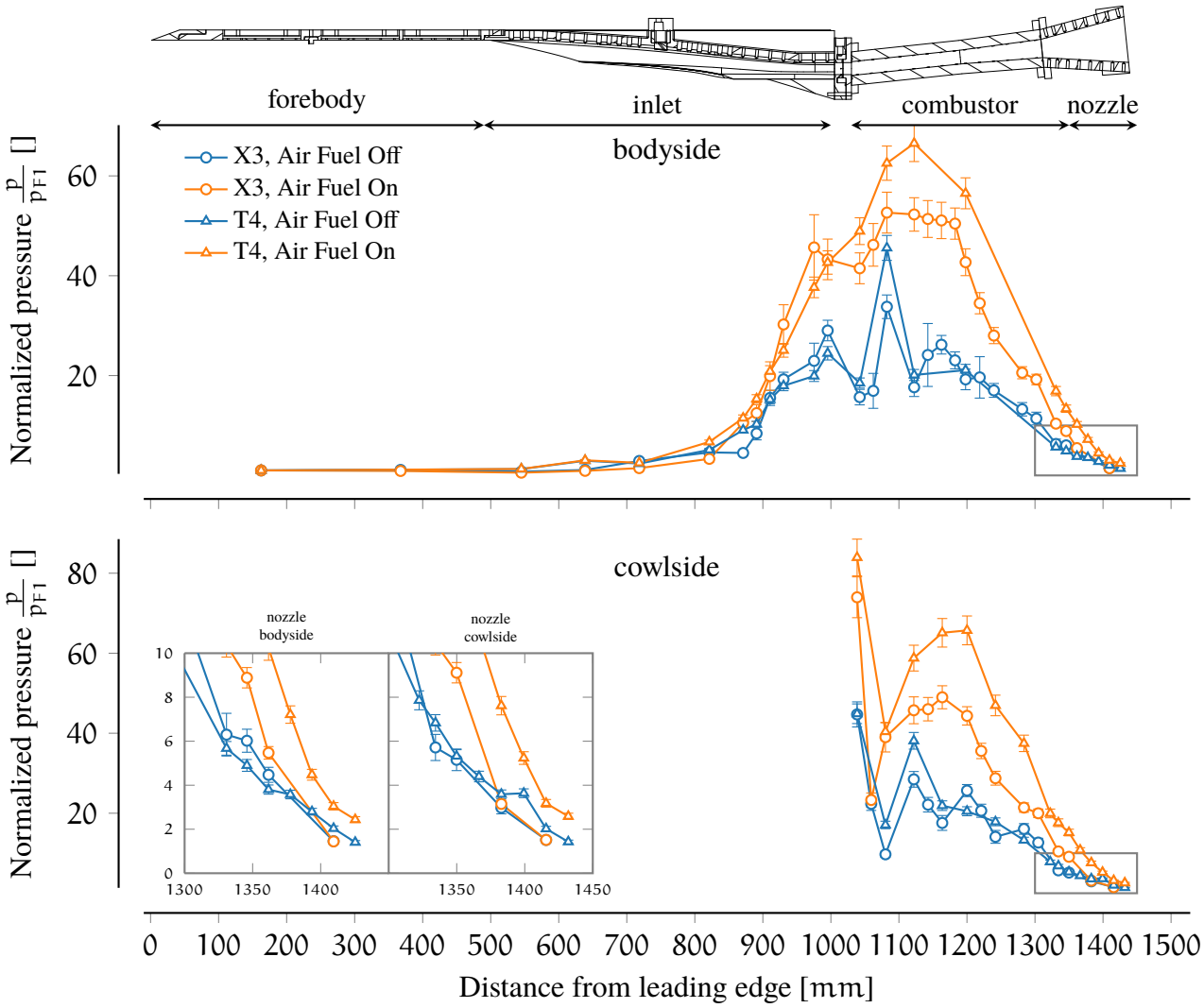

Figure 7.19: Comparison of experimental pressure distributions for combined injection scheme,X3 nominal condition and T4 Landsberg experiments. X3 experiments: $\phi = 1.05$. T4 experiments: $\phi = 1.23$. Uncertainty for T4 experiments calculated as 5.5 % [87].

reflected shock tunnels, especially at these required high Mach number enthalpies, can have significant levels of dissociated oxygen and NO in the freestream flow (see Sections 2.7.2 and 2.8.3) that enhance combustion processes.

Previous studies by Chinitz et al. [28] noted that NO is a good catalyst for air-hydrogen reactions and that the effective heat of combustion of hydrogen in atomic oxygen is about 104 % higher than in O_2, so that this "chemistry problem is significant at about Mach 10-14 tests conditions" [28, pag. 8]. However, the author did not calculate the effect on combustion efficiency, and therefore, engine gross thrust. Boyce et al. [244] attempted mass spectrometric measurements of the freestream composition in T4 in a total enthalpy range between 2.5 MJ kg^{-1} to 13 MJ kg^{-1} and total pressure in the range between 12 MPa to 40 MPa, using a Mach 6 nozzle, and found good agreement with numerical predictions. However, the experimental campaign of Barth employed a Mach 10 nozzle and required a stagnation pressure of 90 MPa, at which no direct measurements have been done yet. Barth [83], assuming

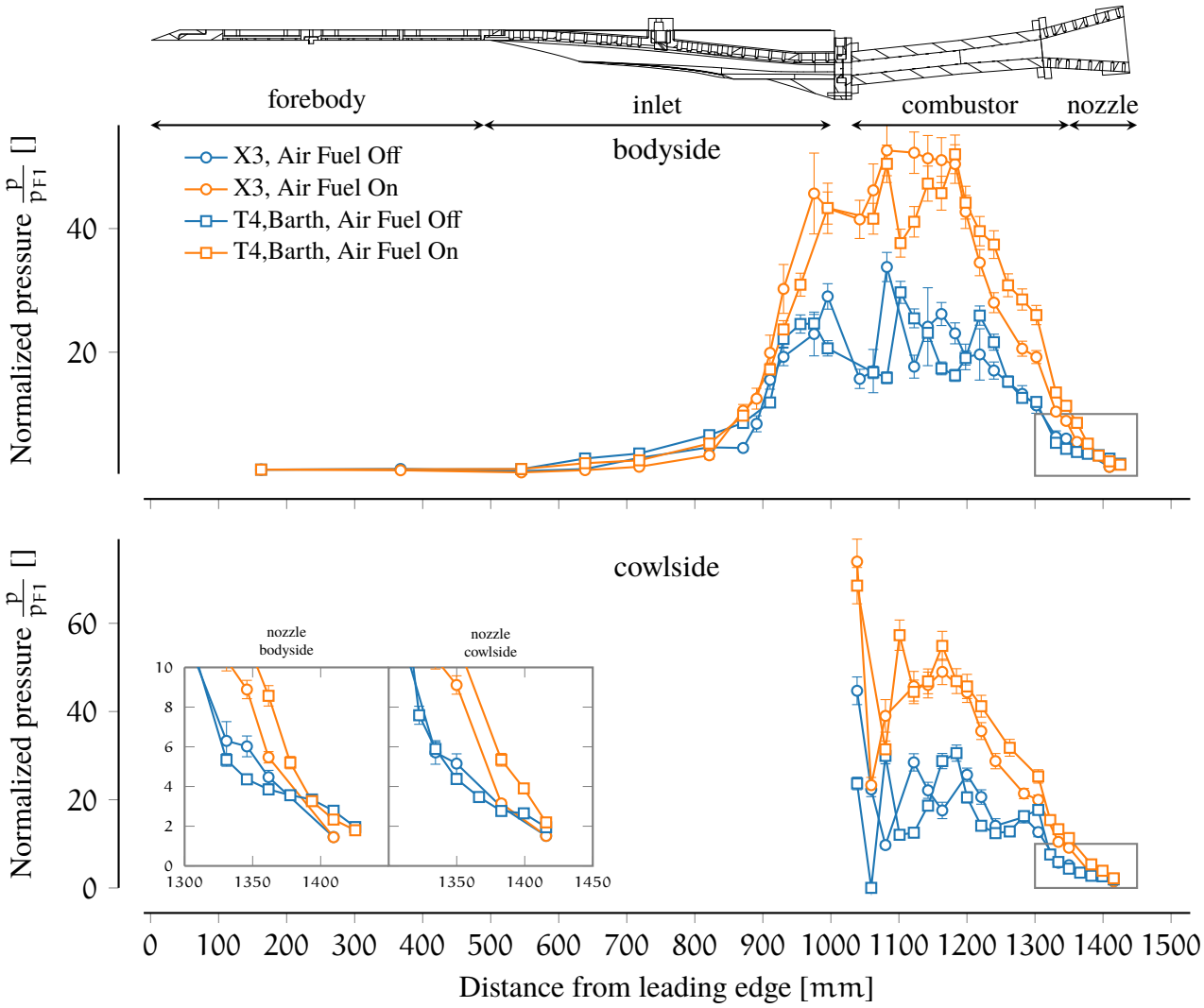

Figure 7.20: Comparison of experimental pressure distributions for combined injection scheme, X3 nominal condition and T4 Barth experiments. X3 experiments: $\phi = 1.05$. T4 experiments: $\phi = 1.1$. Uncertainty for T4 experiments calculated as 2.2 % [83].

that the numerical prediction for O and NO are correct, carried out a CFD comparison of tunnel and flight conditions. The flight condition maintained all the same freestream properties, but NO and O were removed from the inflow. He noted that the flow structures inside the engines changed when simulating the flight as the initial ignition location changes. Pressure levels from the flight simulation were reduced, confirming that the tunnel gas composition was enhancing the combustion process.

Calculations of the gross-thrust coefficient ratio for these two simulations gives 1.17, to be compared with 1.7, between X3 and T4 experiments. However, it is recalled that the experimental comparison is carried out with similar but not identical freestream properties, and slightly different equivalent ratios. More experiments are recommended to establish a more accurate comparison. In any case, this is an indication that the performance is reduced, and that expansion tube flows, despite the uncertainties associated with the unsteadiness of the flows, are able to produce freestream chemistry that are more representative of the flight conditions.

7.6 EFFECTS OF SCALING

A comparison of the experimental data across the nominal CONDITION x3s506 and pressure-scaled CONDITION x3s582 is shown in Fig. 7.21, where unfuelled and fuelled/air experiments are compared. It is reiterated that CONDITION x3s582 is a direct scaling of the nominal condition, and the only difference in the freestream properties is postulated to be a doubling of freestream static pressure.

The normalised pressure traces show that the fuel-off experiments follow similar trends at higher pressure, albeit the experiments at the nominal conditions exhibit higher normalised pressure levels. The position of the shock is also shifted slightly backwards. The same behaviour was observed in the comparison carried out by Sancho Ponce [119] for two-dimensional scramjet Mach 10 experiments. If there was a discrepancy in Mach number, this might explain the difference, but it is not expected to be the cause in this case. If equal Mach numbers are assumed, it can be reasoned that the increased Reynolds number produces thinner boundary layers, thus reducing the engine compression ratio. This could manifest as decreased normalised pressure levels.

While, from a high level perspective, it can be reasoned that increased freestream static pressure, and the consequential Reynolds number increase would theoretically increase combustion performance as turbulent mixing is augmented [63], the interaction of the mixture mixing lengths and reaction times can lead to different flow regimes with unexpected behaviours [245, 246]. In the specific case of the REST engine experiments, the comparison of the fuelled experiments indicates that the pressure levels of the nominal condition are higher than the scaled conditions, with a pseudo-gross thrust coefficient ratio of 1.10 between the nominal and the scaled experiments, indicating a reduced combustion efficiency. A 10 % difference in fuel equivalence ratio is noted. However, it is possible that an increase in pressure has an effect on the mixing of the hydrogen/fuel mixture. Indeed, the injection scheme of Barth was "tailored" to take advantage of the local features of the unscaled flow field, which are not guaranteed to scale when doubling the pressure.

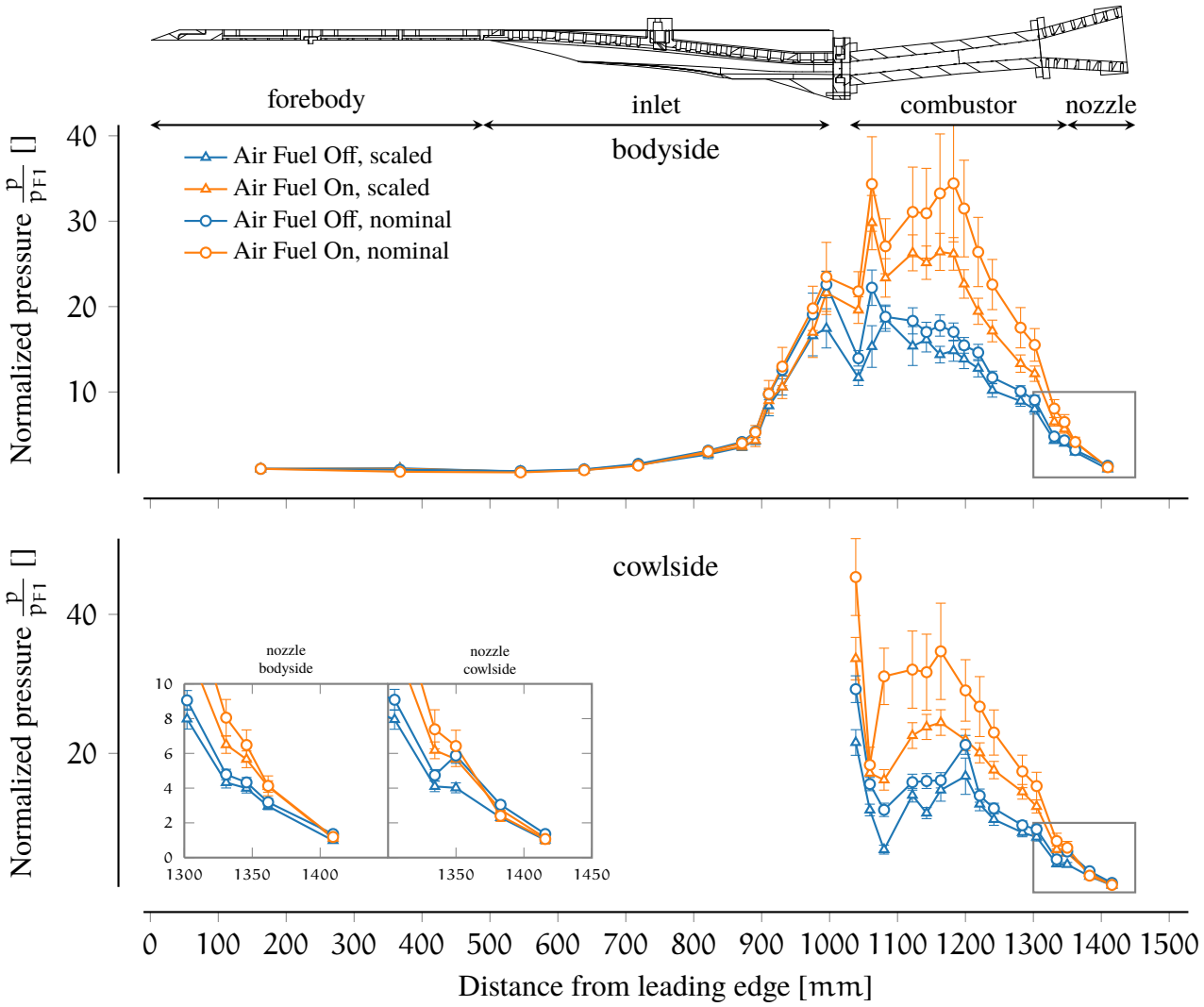

Figure 7.21: Experimental pressure distributions: comparison of pressure-scaled and nominal flow conditions fuel on and fuel off. Data averaged over a test duration of 450 µs. Error bars represent standard deviation from mean.

7.7 SUMMARY

Both nominal and pressure-length scaled conditions have shown significant and robust combustion. When adopting the combined injection scheme, engine unstarts have been noted and are attributed to the acceleration tube gas igniting the pre-fuelled hydrogen. A proposed helium substitution for the acceleration tube gas has been shown to allow consistent and repeatable engine operation, and robust combustion during the test time has occurred.

Comparisons to steady state CFD simulation have shown that, notwithstanding uncertainties associated with the changing freestream condition, the X3 experiments closely match the pressure levels and flow structures that are present in the numerical data. The observed differences can be attributed to

discrepancies between the CFD internal flow path geometry and the actual experimental test engine due to wear and erosion from previous test campaigns in the T4 RST.

The data, compared to previous experimental results in T4, have shown slightly decreased pressure levels at similar equivalence-ratios. Normalised gross thrust estimates indicate that the engine has reduced efficiency compared to the tests carried out in reflected shock tunnels. Although there are discrepancies in the equivalence ratios, these results are thought to reflect the fact that reflected shock tunnel flows, especially at high Mach number enthalpies, can enhance the combustion processes. Further studies are required to reduce the uncertainties related to the estimation of equivalence ratios, to then allow comparison at exactly matched fuel ratios for a conclusive finding.

With these experiments, expansion tubes have been shown to generate flows at the desired total enthalpies and total pressures for scramjet testing beyond Mach 10, and that consistent, and compatible data can be produced with high Mach number scramjet testing. Pressure-length scaled results have shown interesting results, highlighting that the pressure-scaled tests can play an important role in improving the understanding of scramjet performance. As such, high total pressure capabilities, and consequently expansion tubes remain an essential asset.

The next and final chapter concludes the body of this thesis, and presents an overview of the key findings. Recommendations for further work are also discussed, through which improved scramjet testing at high Mach number can be carried out.

8 CONCLUSIONS

Hypersonics ground testing still remains of fundamental importance for the development of scramjet technology. Compared to other propulsion systems, scramjet flight experiments are extremely complex and expensive, and numerical tools are still limited in their modelling capabilities. At the same time, capabilities to ground-test scramjets at high Mach number at replicated flight conditions, prior to this study, were severely lacking.

In this context, the objective of this thesis was to test a three-dimensional, high Mach number scramjet engine, at the fully replicated Mach 12 flight conditions and to show that it can reliably operate at these design conditions. In order to achieve this goal, a new ground testing capability has been established with the X3 expansion tube. The primary objective of the thesis was successfully achieved, allowing a number of scientific developments to be completed.

The X3 expansion tube is successfully able to generate an approximate Mach 12 scramjet condition for test times up to 1.3 ms. Nominal and pressure-scaled conditions were designed. The conditions have nominal Mach number of 11.14, temperature of 308 K and speed of 3.9 $\mathrm{km\,s^{-1}}$. The unscaled condition has a freestream pressure of 607 Pa, corresponding to a dynamic pressure of 52 Pa. The scaled condition has a freestream pressure of 1210 Pa, corresponding to a dynamic pressure of 104 Pa. The flow condition design adopted a mixed experimental-analytical approach, which allowed, in a single iteration, to achieve experimental results extremely close to the required flow condition. The discrepancy to the target Mach number was caused by the development of excessive boundary layers in the acceleration tube. Further flow refinement required hardware modification (shortening of the acceleration tube) that could not be carried out within the timeline of this project.

A new Mach 12 hypersonic nozzle has been designed, manufactured and tested, producing core flow up to 400 mm. The target Mach number and the model sizes required a new nozzle. Classic nozzle design methods are unable to cope with the thick hypersonic boundary layers that characterise expansion tube flows, so that a coupled RANS solver with a parallel Nelder-Mead algorithm has been adopted instead. The use of a parallel optimiser allowed coverage of a significant part of the solution space, which otherwise would be impossible to carry out considering the required nozzle size for X3 expansion tube. The optimised design produced a 2.8 m long 573 mm diameter nozzle, for an area ratio of 9.85 The nozzle exit profile showed that a theoretical core flow of 360 mm can be achieved. Some discrepancies were observed in the experimental results, due to the choice of using a steady inflow for the nozzle design. However, the nozzle has produced an experimental core flow of 400 mm for the nominal condition.

A hybrid approach has been developed to simulate and characterise large-scale expansion tube flows. Building on previous studies, combined shock tube quasi-one-dimensional simulations and acceleration tube axisymmetric RANS simulations produced flow estimates that matched with the experimental shock speeds and wall pressure measurements. An optimisation routine, coupled with the shock tube lagrangian solver, L1D, allowed automatic tuning of the L1D simulations parameters to closely replicate the shock tube experimental data. The CFD axisymmetric simulation showed good agreement with experimental wall pressure measurements and shock speeds. Additionally, time accurate shock-angle measurements, carried out with a schlieren imagining technique, and edge detection algorithms allowed Mach number measurements, which also proved to be consistent with numerical predictions. Pitot pressure measurements, on the other hand, have shown a discrepancy that could not be reconciliated with the rest of the dataset. They were consistently lower than numerical prediction and analytical estimates. However, they were still able to give indication of core flow sizes and test times.

The Mach 12 scramjet has shown successful and robust combustion in full-freestream testing The engine has been tested, for the first time, at the nominal 52 kPa dynamic pressure and at the pressure-scaled flow condition in full-freestream testing. Both combustor-only and the combined-injection scheme showed to reliably achieve combustion. The test times were sufficient to reach a relatively steady flow, and a consistent segment of the test time of ~400 μs was used in all experiments. The combined injection scheme, as predicted, presented the highest combustion efficiencies levels. Pressure-length scaled experiments, despite the difference in equivalence ratio, showed reduced levels of combustion, attributable to the increased Reynolds number. These are, to the author's best knowledge the first experiments in which a Mach 12 scramjet engine has been tested at correctly-scaled full flight conditions.

A helium substitution has been shown to facilitate the starting process of the engine. Initial experiments with the combined injection scheme evidenced repeated engine unstarts. It was supposed that the hot accelerator gas was igniting the pre-fuelled hydrogen in the inlet, creating a disturbance leading to inability of the engine to start. The use of helium in the accelerator gas, replacing air, was then proposed and tested. For this helium substitution, filling pressures need to be opportunely calculated to replicate the desired flow condition. Experiments showed the desired agreement, and fuelled experiments demonstrated that the use of helium is effective in avoiding the engine unstarts.

X3 unfuelled experimental data is consistent with equivalent data carried out in the T4 reflected shock tunnel, and in good agreement with steady state simulations. Previous experimental data was obtained by testing the engine in semi-freejet mode. Comparison of centreline pressure data, despite the experimental uncertainties of both sets of data, indicates very good agreement in the unfuelled experiments. Numerical steady state RANS simulations match the normalised measured pressure levels in the experiments. However, experimental data indicates a forward shift of the first shock inside the combustor, which is not observed in the numerical data. Analysis shows that a similar behaviour was present in the immediately previous experimental campaign, but not earlier. Therefore, it is assumed that gradual erosion and degradation in the experimental model was responsible for this mismatch. Overall, the com-

parison confirms that, notwithstanding the uncertainties of the freestream properties in expansion tubes, these experiments can be related to steady state flows and are an important prediction and analysis tool.

The X3 experimental data indicates reduced combustion levels compared to previous tests carried out in reflected shock tunnels. A comparison with fuelled experiments obtained in the T4 reflected shock tunnel shows good agreement, but considering the similar equivalence ratios, normalised gross thrust coefficients indicate that less thrust is generated in the X3 experiments. This is compatible with the presence of dissociated oxygen and NO in reflected shock tunnel flows, albeit further studies are required to verify this claim, considering the uncertainties in the equivalence ratios and the small experimental dataset.

In summary, this thesis has shown that expansion tubes in general, and X3 specifically, can generate a nominal Mach 12 flow condition of sufficient core flow sizes and test time for scramjet testing. Furthermore, as part of this project, several tests of the Mach 12 REST engine have been carried out, which have shown, for the first time, that the engine is fully operational at the correctly scaled design conditions.

This new established capability is of fundamental importance for studying high Mach number scramjet engines, since no other kind of ground test facility currently operating is able to replicate the total pressure and the total enthalpies required for the pressure-scaled full flight conditions of Mach 12 scramjets and above. Moreover, the X3 expansion tube is one of few expansion tubes in the world with driver performance and size able to produce the correct flow condition and sufficient test times for scramjet testing.

Several challenges remain to be addressed, which could not be tackled within the thesis time-frame, and many more emerged in the meantime. All of them can be undertaken in the future, and they will be detailed in the next section.

8.1 RECOMMENDATIONS FOR FUTURE WORK

A number of recommendations for future work are presented and discussed here. They cover both suggestions to improve methods, but also ideas for future experiments.

8.1.1 Expansion tube flows

Investigate facility modifications to improve flow conditions. Nozzle inlet measurements have shown that a thick boundary layer develops up to the nozzle centreline, so that no clearly identifiable core flow is present. Additionally, a significant shock speed attenuation takes place in the last section of the acceleration tube. The two phenomena are likely to be correlated and are responsible for off-design

operation of the Mach 12 nozzle. The removal of the last section of the acceleration tube, which is 4 m long, would potentially solve both problems, and restore an on-design inflow condition, thus likely producing a higher Mach number at nozzle exit.

Moreover, it is well-known that only the last part of the shock tube gas is actually sufficiently processed by the unsteady expansion to be used as test gas. Additionally, the shock tube, operated in its long configuration, contains an area change at the secondary diaphragm. The interaction of the shock tube length, and area change with the facility performance has not been investigated yet, and contextually to an eventual acceleration tube shortening, an investigation into the shock tube geometries could be carried out.

Effects of the driver wave processes Whilst not investigated in this thesis, it is recommended that study the wave processes generated by the piston motion be studied, how they interact with the facility geometry and interfere with the test gas. The adopted 100 % Argon and 60 % Argon driver conditions have shown that very strong acoustic waves are generated in the compression tube, causing a non-ideal diaphragm opening process, which possibly influence the test gas in the shock tube.

Investigate the use of the heavyweight piston. The use of the lightweight piston for this project was dictated by the fact that its development occurred in parallel. By sharing the piston, simplified operation and reduced turnaround times were possible. Additionally, it was considered that the increased hold times given by the lightweight piston would be beneficial for steadier test flows. However, the strong waves generated in the driver may suggest that this is not an optimal configuration. The use of the 200 kg piston would require higher helium percentages and lower compression ratios, and if its performance were sufficient, it could potentially reduce the strength of the acoustic waves and improve the rupturing process.

Develop improved techniques for Pitot pressure measurements. Discrepancies between the Pitot pressure measurements and the rest of the experimental data represent a significant issue to be solved. The harsh test environment, impulsive heat loads, diaphragm fragments and vibrations are long-standing problems that affect these measurements and limit diagnostics options. While increasing computational capabilities allows for more and more accurate numerical models, they cannot reliably be compared with the present Pitot pressure measurements. The mechanical and aerodynamic effects need to be understood and quantified.

Investigate the use of non-intrusive techniques for freestream property estimations. A significant part of this thesis was dedicated to the estimation of freestream properties, by means of a hybrid numerical and experimental approach, as direct measurements are not able to give a complete and time accurate estimation of the freestream properties. Considering the harsh environment of expansion tube flows, the author recommends investigating non-intrusive optical techniques, such as TDLAS, alternative to Pitot pressure measurements, which would allow an estimation of pressure, temperature and velocity. This could potentially reduce the uncertainties of the freestream properties.

Improved numerical techniques for facility simulations. The size of the facility makes numerical simulations extremely expensive. Additionally, grid density is a balance between accuracy and simulation time. However, a low grid resolution is responsible for shock smearing and dissipation, and

boundary layers are not accurately modelled. More refined turbulence models can be adopted, but their computational cost has to be reduced. Future studies can investigate how to improve the performance of the simulation codes currently in use, and look to the use of adaptive-techniques for localised mesh-refinements, to be able to capture all the flow features and reduce computational costs to carry out full facility simulation, including piston dynamics in the EILMER3 code, or its successor, EILMER3

8.1.2 Hypersonic nozzles design and operation

Transition measurements in the Mach 12 nozzle. The wall sensor mounts of the Mach 12 nozzle can host up to two sensors per location, and both heat transfer measurements and pressure can be taken simultaneously. The state of the boundary layer, and its laminar/turbulent status in a hypersonic nozzle, have not been studied in detail and are not yet understood. Indeed, nozzle designs methods often assume either a laminar or a turbulent boundary layer, however, a transitioning boundary layer could lead to significantly different nozzle design.

Incorporate transient inflows for nozzle design. The most important simplifying assumption for the nozzle design was the use of a steady state inflow. Remarkable improvements could be potentially achieved if a transient inflow was adopted in the nozzle design. This work, however, considering expansion tube sizes, is subordinated to improved performances for numerical flow solvers.

Investigate non-circular nozzle design. Axisymmetric nozzles have the advantage of only requiring axisymmetric simulations, and allowing for simplified manufacturing processes. However, these nozzles have the undesirable effects of focusing waves on the nozzle centreline, potentially increasing flow disturbances in the test gas. The use of a shape-transition nozzle, from circular to quasi-rectangular, would remove the issue. Additionally, advances in composite manufacturing processes would allow for this type of design to be manufactured.

8.1.3 Experimental models and scramjet tests

Improved heat transfer measurements techniques for expansion tube flows. Heat transfer measurements in the engine forebody have shown to be particularly challenging to carry out. The thin film heat transfer gauges adopted in this thesis, while able to give fast response times, were extremely sensitive to debris impact, and a significant number of them got damaged during the experiments. The development of more robust gauges is highly recommended.

Longer forebodies. Core flow size analysis indicates that forebodies of increased length can be used, compared to the one used in the T4 reflected shock tunnel (in the author's opinion, in first

approximation, forebodies of ~1 m could fit the nozzle core diamond). This should facilitate transition to turbulence, allowing the use of less-intrusive boundary layer trips.

Increased number of sensors and heat transfer models within the experimental engine. Due to the limitation in the data acquisition system, the engine was not run at full diagnostic capacity. Additionally, even at full capacity, discrete locations can hide some flow features within the data. It is also noted that sensors are located on the engine centreline, so that these offer no insight into the physics happening on the engine side walls. A greater sensor density and more varied locations would allow extraction of more information from the experiments. Finally, the experiments carried out in this thesis did not include heat transfer measurements inside the engine. The addition of heat transfer measurements would give further insight onto the engine internal flow physics.

Improvement in the mechanical design of the REST class engines. Discrepancies found in unfuelled experiments can be attributed to design flaws and erosion, due to wear and tear in the engine after more than 120 experiments carried out in 4 experimental campaigns and two different facilities. REST class inlets have a fully three-dimensional shape, but it would be highly desirable to allow for replaceable leading edges, as their bluntness was significantly increased in the last part of the experiments. Additionally, the inlet is currently machined in two halves, and pressure measurement cavities sit right in the middle. Misalignment, plastic deformation and other loads can enlarge the gap between the two halves, making experimental measurements non-ideal. Revised inlet design, avoiding the location of pressure sensors at the split-line is highly recommended.

Take advantage of the steady gradient in the freestream properties of expansion tube flows to test engines at off-design condition. If accurate models for the expansion tube flow condition can be developed and/or accurate measurements of freestream properties can be carried out, it could be possible to use the under-expanded test gas (at lower Mach number and higher pressure) to explore the behaviour of the engine operating in off-design condition. For example, an accelerator engine could potentially be tested at a varying Mach number, with high Mach number carried out in the usual test window and lower Mach numbers later in the experiments.

The author believes that the newly-established high Mach number testing capabilities have a significant potential for the development of hypersonic scramjet vehicles, and for a more affordable access to space that is worth pursuing.

BIBLIOGRAPHY

[1] D. E. Gildfind, C. M. James, P. Toniato, and R. G. Morgan. "Performance considerations for expansion tube operation with a shock-heated secondary driver". In: *Journal of Fluid Mechanics* 777 (July 2015), pp. 364–407. DOI: 10.1017/jfm.2015.349 (cit. on pp. vii, 32, 33, 39, 40, 50, 66, 69).

[2] P. Toniato, D. Gildfind, P. A. Jacobs, and R. G. Morgan. "Extension of the X3 expansion tube capabilities for Mach 12 scramjet testing: flow condition development and nozzle optimization". In: *20th Australasian Fluid Mechanics Conference*. Australasian Fluid Mechanics Society. Perth, Western Australia, Australia, 2016 (cit. on p. vii).

[3] P. Toniato, D. Gildfind, P. A. Jacobs, and R. G. Morgan. "Optimisation and design of a fully instrumented Mach 12 nozzle for the X3 expansion tube". In: *31th International Symposium on Shock Waves*. Nagoya, Japan: Springer, July 10, 2017 (cit. on pp. vii, 77).

[4] P. Toniato, D. E. Gildfind, C. M. Jacobs, and R. Morgan. "Development of a new Mach 12 scramjet operating capability in the X3 expansion tube". In: *7th Asia-Pacific International Symposium on Aerospace Technology (APISAT)* (Cairns). Nov. 26–29, 2015 (cit. on pp. vii, 9).

[5] P. Toniato, D. E. Gildfind, A. Andrianatos, and R. G. Morgan. "Full Free-stream Mach 12 Scramjet Testing in Expansion Tubes". In: *2018 Applied Aerodynamics Conference*. American Institute of Aeronautics and Astronautics, June 2018. DOI: 10.2514/6.2018-3818 (cit. on pp. vii, 169).

[6] C. M. James, D. R. Smith, C. McLean, R. G. Morgan, S. W. Lewis, and P. Toniato. "Improving High Enthalpy Expansion Tube Condition Characterisation Using High Speed Imagery". In: *2018 Aerodynamic Measurement Technology and Ground Testing Conference*. American Institute of Aeronautics and Astronautics, June 2018. DOI: 10.2514/6.2018-3805 (cit. on p. viii).

[7] K. G. Bowcutt and T. R. Smith. "Responsive ad Affordable Launch of Small Satellites: A reusable Air-breathing concept". In: *AIAA Reinventing Space Conference* (Los Angeles, USA). RS-2012-5001. AIAA. Los Angeles, May 7–10, 2012 (cit. on pp. 1, 3, 11).

[8] M. K. Smart and M. R. Tetlow. "Orbital Delivery of Small Payloads Using Hypersonic Airbreathing Propulsion". In: *Journal of Spacecraft and Rockets* 46.1 (Jan. 2009), pp. 117–125. DOI: 10.2514/1.38784 (cit. on pp. 1, 3, 11).

[9] D. Preller and M. Smart. "SPARTAN: Scramjet Powered Accelerator for Reusable Technology AdvaNcement". In: *Proceedings of the 12th Reinventing Space Conference*. Springer International Publishing, Dec. 2016, pp. 139–147. DOI: 10.1007/978-3-319-34024-1_11 (cit. on pp. 1, 10, 12, 20).

[10] W. H. Heiser and D. T. Pratt. *Hypersonic Airbreathing Propulsion*. AIAA Textbooks Series pt. 1. American Institute of Aeronautics and Astronautics, 1994. DOI: 10.2514/4.470356 (cit. on pp. 1, 2, 15, 18, 19).

[11] J. C. Turner and M. K. Smart. "Mode Change Characteristics of a Three-Dimensional Scramjet at Mach 8". In: *Journal of Propulsion and Power* 29.4 (July 2013), pp. 982–990. DOI: 10.2514/1.b34569 (cit. on pp. 2, 20).

[12] J. D. Anderson. *Hypersonic and high-temperature gas dynamics*. 2nd ed. Reston, Va: American Institute of Aeronautics and Astronautics, 2006 (cit. on p. 2).

[13] P. J. Waltrup. "Upper Bounds on the Flight Speed of Hydrocarbon-Fueled Scramjet-Powered Vehicles". In: *Journal of Propulsion and Power* 17.6 (Nov. 2001), pp. 1199–1204. DOI: 10.2514/2.5895 (cit. on p. 2).

[14] L. Doherty. "An experimental investigation of an airframe integrated three-dimensional scramjet engine at a Mach 10 flight condition". PhD thesis. University of Queensland, 2015. DOI: 10.14264/uql.2014.382 (cit. on pp. 2, 10, 24, 161, 162).

[15] K. G. Bowcutt, A. Paull, D. J. Dolvin, and M. Smart. "HIFIRE: An International collaboration to advance the science and technology of hypersonic flight. HIFiRE ICAS 2012 von Karman lecture". In: *28th Internationa Congress of the Aeronautical Sciences*. 2012. URL: http://www.icas.org/ICAS_ARCHIVE/ICAS2012/PAPERS/998.PDF (cit. on pp. 3, 14).

[16] E. H. Hirschel and C. Weiland. *Selected Aerothermodynamic Design Problems of Hypersonic Flight Vehicles*. Springer Berlin Heidelberg, 2009. DOI: 10.1007/978-3-540-89974-7 (cit. on p. 3).

[17] R. Barthelemy. "The National Aero-Space Plane program". In: *Maintainablity of Aerospace Systems Symposium*. American Institute of Aeronautics and Astronautics, July 1989. DOI: 10.2514/6.1989-5053 (cit. on p. 3).

[18] D. Preller and M. K. Smart. "Scramjets for Reusable Launch of Small Satellites". In: *20th AIAA International Space Planes and Hypersonic Systems and Technologies Conference* (Glasgow, Scotland). American Institute of Aeronautics and Astronautics (AIAA), July 6–9, 2015. DOI: 10.2514/6.2015-3586 (cit. on pp. 3, 11–13).

[19] K. W. Flaherty, K. M. Andrews, and G. W. Liston. "Operability Benefits of Airbreathing Hypersonic Propulsion for Flexible Access to Space". In: *Journal of Spacecraft and Rockets* 47.2 (Mar. 2010), pp. 280–287. DOI: 10.2514/1.43750 (cit. on pp. 3, 12).

[20] L. Marshall, C. Bahm, G. Corpening, and R. Sherrill. "Overview With Results and Lessons Learned of the X-43A Mach 10 Flight". In: *AIAA/CIRA 13th International Space Planes and Hypersonics Systems and Technologies Conference*. American Institute of Aeronautics and Astronautics, May 2005. DOI: 10.2514/6.2005-3336 (cit. on pp. 3, 13, 15).

[21] M. K. Smart. "Design of Three-Dimensional Hypersonic Inlets with Rectangular-to-Elliptical Shape Transition". In: *Journal of Propulsion and Power* 15.3 (May 1999), pp. 408–416. DOI: 10.2514/2.5459 (cit. on pp. 4, 16, 20).

[22] T. Jazra, D. Preller, and M. K. Smart. "Design of an Airbreathing Second Stage for a Rocket-Scramjet-Rocket Launch Vehicle". In: *Journal of Spacecraft and Rockets* 50.2 (Mar. 2013), pp. 411–422. DOI: 10.2514/1.a32381 (cit. on pp. 4, 12, 13, 16).

[23] M. V. Suraweera and M. K. Smart. "Shock-Tunnel Experiments with a Mach 12 Rectangular-to-Elliptical Shape-Transition Scramjet at Offdesign Conditions". In: *Journal of Propulsion and Power* 25.3 (May 2009), pp. 555–564. DOI: 10.2514/1.37946 (cit. on pp. 4, 21, 23, 29, 154).

[24] D. Wise and M. Smart. "Forced Transition of Hypervelocity Boundary Layers". In: *18th AIAA/3AF International Space Planes and Hypersonic Systems and Technologies Conference*. American Institute of Aeronautics and Astronautics, Sept. 2012. DOI: 10.2514/6.2012-5866 (cit. on pp. 4, 17, 152, 153, 230).

[25] R. W. Bilger, S. B. Pope, K. N. C. Bray, and J. F. Driscoll. "Paradigms in turbulent combustion research". In: *Proceedings of the Combustion Institute* 30.1 (Jan. 2005), pp. 21–42. DOI: 10.1016/j.proci.2004.08.273 (cit. on p. 5).

[26] Z. Gao, C. Jiang, and C.-H. Lee. "On the laminar finite rate model and flamelet model for supersonic turbulent combustion flows". In: *International Journal of Hydrogen Energy* 41.30 (Aug. 2016), pp. 13238–13253. DOI: 10.1016/j.ijhydene.2016.06.013 (cit. on p. 5).

[27] R. J. Bakos, M. Tamagno, O. Rizkalla, M. V. Pulsonetti, W. Chinitz, and J. I. Erdos. "Hypersonic Mixiing and Combustion Studies in the Hypulse Facility". In: *Journal of Propulsion and Power* 8.4 (July 1992), pp. 900–906. DOI: 10.2514/3.23567 (cit. on pp. 5, 36).

[28] W. Chinitz, J. I. Erdos, O. Rizkalla, G. Y. Anderson, and D. M. Bushnell. "Facility opportunities and associated stream chemistry considerations for hypersonic air-breathing propulsion". In: *Journal of Propulsion and Power* 10.1 (Jan. 1994), pp. 6–17. DOI: 10.2514/3.23705 (cit. on pp. 5, 17, 25, 26, 30, 31, 189).

[29] E. T. Curran. "Scramjet engines: the first forty years". In: *Journal of Propulsion and Power* 17.6 (2001), pp. 1138–1148. DOI: 10.2514/2.5875 (cit. on p. 10).

[30] D. E. Gildfind. "Development of high total pressure scramjet flow conditions using the X2 expansion tube". PhD thesis. University of Queensland, 2012. 453 pp. URL: https://espace.library.uq.edu.au/view/UQ:282684 (cit. on pp. 11, 13, 26, 27, 31, 33, 36, 39, 45, 49, 52, 112, 146).

[31] D. L. Kors. "Design considerations for combined air breathing-rocket propulsion systems". In: *2nd International Aerospace Planes Conference*. American Institute of Aeronautics and Astronautics, Oct. 1990. DOI: 10.2514/6.1990-5216 (cit. on p. 11).

[32] *Commercial Space Transportation Forecasts*. English. FAA Commercia Space Transportation (AST) and Commercial Space Transportation Advisory Committee (COMSTAC), Jan. 2018. URL: https://www.faa.gov/about/office_org/headquarters_offices/ast/media/2018_AST_Compendium.pdf (cit. on pp. 11, 12).

[33] P. L. Moses, K. A. Bouchard, R. F. Vause, S. Z. Pinckney, L. W. Taylor III, S. M. Ferlemann, C. P. Leonard, J. S. Robinson, J. G. Martin, D. H. Petley, and J. L. Hunt. "An airbreathing launch vehicle design with turbine-based lowspeed propulsion and dual mode scramjet high-speed propulsion". In: *9th International Space Planes and Hypersonic Systems and Technologies Conferences* (Nortfolk, USA). American Institute of Aeronautics and Astronautics, Nov. 1, 1999. DOI: 10.2514/6.1999-4948 (cit. on p. 11).

[34] Z. Rosenberg. *Hypersonic X-51 programme ends in success*. English. Ed. by F. Global. May 3, 2013. URL: http://www.flightglobal.com/news/articles/hypersonic-x-51-programme-ends-in-success-385481/ (cit. on pp. 11, 14).

[35] E. C. Semple. “Trajectory and Performance of an Expendable Scramjet Powered Launcher”. In: *The Institution of Engineers, Australia, Seventh National Space Engineering Symposium, Canberra, 21-26 Sep*. 1992 (cit. on p. 12).

[36] K. Bowcutt, M. Gonda, T. Ralston, and S. Hollowell. “Performance, Economic, and Operational Drivers of Reusable Launch Vehicles”. In: *38th AIAA/ASME/SAE/ASEE Joint Propulsion Conference and Exhibit*. American Institute of Aeronautics and Astronautics, July 2002. DOI: 10.2514/6.2002-3901 (cit. on p. 12).

[37] M. R. Tetlow and C. J. Doolan. “Comparison of Hydrogen and Hydrocarbon-Fueled Scramjet Engines for Orbital Insertion”. In: *Journal of Spacecraft and Rockets* 44.2 (Mar. 2007), pp. 365–373. DOI: 10.2514/1.24739 (cit. on pp. 12, 15).

[38] A. Kumar, J. P. Drummond, C. R. McClinton, and J. L. Hunt. “Research in Hypersonic Airbreathing Propulsion at the NASA Langley Research Center”. In: *ISABE-2001:Fifteenth International Symposium on Airbreathing Engines,* (Bangalore, India). Sept. 2–2, 2001. URL: https://ntrs.nasa.gov/archive/nasa/casi.ntrs.nasa.gov/20020011010.pdf (cit. on p. 12).

[39] R. Voland, A. Auslender, M. Smart, A. Roudakov, V. Semenov, and V. Kopchenov. “CIAM/NASA Mach 6.5 scramjet flight and ground test”. In: *9th International Space Planes and Hypersonic Systems and Technologies Conference*. American Institute of Aeronautics and Astronautics, Nov. 1999. DOI: 10.2514/6.1999-4848 (cit. on p. 13).

[40] C. McClinton. “X-43 - Scramjet Power Breaks the Hypersonic Barrier: Dryden Lectureship in Research for 2006”. In: *44th AIAA Aerospace Sciences Meeting and Exhibit*. American Institute of Aeronautics and Astronautics, 2006. DOI: 10.2514/6.2006-1 (cit. on p. 13).

[41] B. News, ed. *Revolutionary jet engine tested*. Mar. 25, 2006. URL: http://news.bbc.co.uk/2/hi/science/nature/4832254.stm (cit. on p. 13).

[42] “Data from HyShot III launch undergoes analysis”. In: *Jane’s Defence Weekly* MAR. (2006), pp. 633–634 (cit. on p. 13).

[43] T. Hiraiwa, K. Ito, S. Sato, S. Ueda, K. Tani, S. Tomioka, and T. Kanda. “Recent progress in scramjet/-combined cycle engines at JAXA, Kakuda space center”. In: *Acta Astronautica* 63.5-6 (Sept. 2008), pp. 565–574. DOI: 10.1016/j.actaastro.2008.04.011 (cit. on p. 13).

[44] S. Walker, F. Rodgers, A. Paull, and D. V. Wie. “HyCAUSE Flight Test Program”. In: *International Space Planes and Hypersonic Systems and Technologies Conferences*. American Institute of Aeronautics and Astronautics, Apr. 2008. DOI: 10.2514/6.2008-2580 (cit. on p. 13).

[45] K. R. Jackson, M. R. Gruber, and S. Buccellato. “Mach 6–8+ Hydrocarbon-Fueled Scramjet Flight Experiment: The HIFiRE Flight 2 Project”. In: *Journal of Propulsion and Power* 31.1 (Jan. 2015), pp. 36–53. DOI: 10.2514/1.b35350 (cit. on pp. 13, 14).

[46] T. J. Juliano, D. Adamczak, and R. L. Kimmel. “HIFiRE-5 Flight Test Results”. In: *Journal of Spacecraft and Rockets* 52.3 (May 2015), pp. 650–663. DOI: 10.2514/1.a33142 (cit. on p. 13).

[47] M. Suraweera. *HIFiRE 7 Flight Test Update*. English. Apr. 29, 2015. URL: http://www.academia.edu/12150581/HIFiRE_7_Flight_Test_Update_-_29_April_2015 (visited on 09/17/2015) (cit. on pp. 14, 23).

[48] J. Hank, J. Murphy, and R. Mutzman. "The X-51A Scramjet Engine Flight Demonstration Program". In: *15th AIAA International Space Planes and Hypersonic Systems and Technologies Conference*. American Institute of Aeronautics and Astronautics, 2008. DOI: 10.2514/6.2008-2540 (cit. on p. 14).

[49] Z. Rosenberg. *Second X-51 hypersonic flight ends prematurely*. English. Ed. by F. Global. June 15, 2011. URL: http://www.flightglobal.com/news/articles/second-x-51-hypersonic-flight-ends-prematurely-358056/ (cit. on p. 14).

[50] Z. Rosenberg. *August failure of Boeing X-51 likely due to fin, resonance*. English. Ed. by F. Global. Oct. 11, 2012. URL: http://www.flightglobal.com/news/articles/august-failure-of-boeing-x-51-likely-due-to-fin-resonance-378080/ (cit. on p. 14).

[51] *Queensland Hypersonic Testing Facility*. Research rep. University of Queensland, 2013. URL: http://hypersonics.mechmining.uq.edu.au/filething/get/1172/2013_%20Annual%20Report_final.pdf (cit. on p. 14).

[52] G. Y. Anderson. "Combustion in High-Speed Flow". English. In: *Combustion in High-Speed Flows*. Ed. by J. Buckmaster, T. Jackson, and A. Kumar. Vol. 1. ICASE/LaRC Interdisciplinary Series in Science and Engineering. Springer Netherlands, 1994. Chap. Hypersonic Combustion — Status and Directions, pp. 19–51. DOI: 10.1007/978-94-011-1050-1_2 (cit. on pp. 14, 25, 28, 30).

[53] P. Kutschenreuter. "Supersonic flow combustors". In: *Scramjet propulsion*. Ed. by E. T. Curran and S. Murthy. American Institute of Aeronautics and Astronautics (AIAA), Jan. 2001, pp. 513–568. DOI: 10.2514/5.9781600866609.0513.0568 (cit. on pp. 15, 16, 19).

[54] M. J. Lewis. "Significance of Fuel Selection for Hypersonic Vehicle Range". In: *Journal of Propulsion and Power* 17.6 (Nov. 2001), pp. 1214–1221. DOI: 10.2514/2.5866 (cit. on p. 15).

[55] M. B. Colket and L. J. Spadaccini. "Scramjet Fuels Autoignition Study". In: *Journal of Propulsion and Power* 17.2 (Mar. 2001), pp. 315–323. DOI: 10.2514/2.5744 (cit. on p. 15).

[56] P. Puri, F. Ma, J.-Y. Choi, and V. Yang. "Ignition characteristics of cracked JP-7 fuel". In: *Combustion and Flame* 142.4 (Sept. 2005), pp. 454–457. DOI: 10.1016/j.combustflame.2005.06.001 (cit. on p. 15).

[57] Z. Denman. "Supersonic combustion of hydrocarbon fuels in a three-dimensional Mach 8 scramjet". PhD thesis. DOI: 10.14264/uql.2018.8 (cit. on pp. 15, 166, 229–231).

[58] D. M. Van Wie. "Scramjet inlets". In: *Scramjet propulsion*. Ed. by E. T. Curran and S. Murthy. American Institute of Aeronautics and Astronautics (AIAA), Jan. 2001, pp. 513–568. DOI: 10.2514/5.9781600866609.0513.0568 (cit. on pp. 16, 17, 20).

[59] T. W. Drayna, I. Nompelis, and G. V. Candler. "Hypersonic Inward Turning Inlets: Design and Optimization". In: *44th AIAA Aerospace Sciences Meeting and Exhibit* (Reno, USA). American Institute of Aeronautics and Astronautics (AIAA), Jan. 9–12, 2006. DOI: 10.2514/6.2006-297 (cit. on p. 16).

[60] D. M. Van Wie and S. Molder. "Applications of Busemann inlet designs for flight at hypersonic speeds". In: *Aerospace Design Conference* (Irvine, USA). American Institute of Aeronautics and Astronautics (AIAA), Feb. 1992. DOI: 10.2514/6.1992-1210 (cit. on p. 16).

[61] M. K. Smart. "How Much Compression Should a Scramjet Inlet Do?" In: *AIAA Journal* 50.3 (Mar. 2012), pp. 610–619. DOI: 10.2514/1.j051281 (cit. on p. 16).

[62] A. Kantrowitz and C. D. Donaldson. *Preliminary Investigation of Supersonic Diffusers*. Tech. rep. NACA-WR-L-713, NACA-ACR-L5D20. National Advisory Committee for Aeronautics. Langley Aeronautical Lab.; Langley Field, VA, United States, 1945. URL: https://ntrs.nasa.gov/archive/nasa/casi.ntrs.nasa.gov/19930093667.pdf (cit. on p. 17).

[63] C. Segal. *The scramjet engine*. Processes and Characteristics. Vol. 25. Cambridge aerospace series. Cambridge University Press, 2009. 253 pp. DOI: 10.1017/cbo9780511627019 (cit. on pp. 17, 191).

[64] G. Y. Anderson. "An examination of injector/combustor design effects on scramjet perfomance". In: *2nd International Symposium on Air Breathing Engines, Proceedings* (Sheffield, UK). Mar. 24, 1974, p. 15 (cit. on p. 17).

[65] M. K. Smart. "Scramjets". In: *Advances on Propulsion Technology for High-Speed Aircraft*. Vol. Educational Notes RTO-EN-AVT-150. Paper 9. NATO Research & Technology Organisation, Oct. 2007, pp. 9–38. DOI: 10.1017/s0001924000004796 (cit. on pp. 17, 18, 21).

[66] S. Beckel, J. Garrett, and C. Gettinger. "Technologies for Robust and Affordable Scramjet Propulsion". In: *14th AIAA/AHI Space Planes and Hypersonic Systems and Technologies Conference* (Canberra, Australia). American Institute of Aeronautics and Astronautics (AIAA), Nov. 6–9, 2006. DOI: 10.2514/6.2006-7980 (cit. on pp. 17, 18).

[67] R. Portz and C. Segal. "Penetration of Gaseous Jets in Supersonic Flows". In: *AIAA Journal* 44.10 (Oct. 2006), pp. 2426–2429. DOI: 10.2514/1.23541 (cit. on p. 18).

[68] S. D. Stouffer, N. R. Baker, D. P. Capriotti, and G. B. Northam. "Effects of compression and expansion ramp fuel injector configuration on scramjet combustion and heat transfer". In: *31st Aerospace Sciences Meeting*. American Institute of Aeronautics and Astronautics, Jan. 1993. DOI: 10.2514/6.1993-609 (cit. on p. 18).

[69] R. G. Morgan, A. Paull, N. A. Morris, and R. J. Stalker. *Further shock tunnel studies of scramjet phenomena*. Research rep. NASA-CR-179937. NASA, 1986. URL: https://ntrs.nasa.gov/search.jsp?R=19870003109 (cit. on p. 18).

[70] J. Odam and A. Paull. "Radical Farming in Scramjets". In: *New Results in Numerical and Experimental Fluid Mechanics VI*. Ed. by C. Tropea, S. Jakirlic, H.-J. Heinemann, R. Henke, and H. Hönlinger. 96 vols. Notes on Numerical Fluid Mechanics and Multidisciplinary Design (NNFM). Springer Science + Business Media, 2008, pp. 276–283. DOI: 10.1007/978-3-540-74460-3_34 (cit. on pp. 18, 19).

[71] J. M. Donohue and J. C. McDaniel. "Complete three-dimensional multiparameter mapping of a supersonic ramp fuel injector flowfield". In: *AIAA Journal* 34.3 (Mar. 1996), pp. 455–462. DOI: 10.2514/3.13089 (cit. on p. 18).

[72] A. Kumar, D. M. Bushnell, and M. Y. Hussaini. "Mixing augmentation technique for hypervelocity scramjets". In: *Journal of Propulsion and Power* 5.5 (Sept. 1989), pp. 514–522. DOI: 10.2514/3.23184 (cit. on p. 18).

[73] G. Y. Anderson, C. R. McClinton, and J. P. Weidner. "Scramjet Performance". In: *Progress in Astronautics and Aeronautics*. Ed. by E. T. Curran and S. N. B. Murthy. American Institute of Aeronautics and Astronautics, Jan. 2001, pp. 369–446. DOI: 10.2514/5.9781600866609.0369.0446 (cit. on pp. 18, 25, 31).

[74] M. McGilvray. "Scramjet testing at high enthalpies in expansion tube facilities". PhD thesis. University of Queensland, 2008. URL: http://espace.library.uq.edu.au/view/UQ:155369 (cit. on pp. 18, 19, 25, 27, 31, 37, 38, 40–43, 87).

[75] K. Tanimizu, D. J. Mee, R. J. Stalker, and P. A. Jacobs. "Drag force on quasi-axisymmetric scramjets at various flight Mach numbers: theory and experiment". In: *Shock Waves* 19.2 (2009), pp. 83–93. DOI: 10.1007/s00193-009-0194-x (cit. on p. 18).

[76] D. W. Riggins. "Evaluation of Performance Loss Methods for High-Speed Engines and Engine Components". In: *Journal of Propulsion and Power* 13.2 (Mar. 1997), pp. 296–304. DOI: 10.2514/2.5162 (cit. on p. 19).

[77] G. Y. Anderson, A. Kumar, and J. I. Erdos. "Progress in Hypersonic Combustion Technology with Computation and Experiment". In: *AIAA 2nd International Aerospace Planes Conference,* (Orlando, USA). AIAA-90-5254. American Institute of Aeronautics and Astronautics (AIAA), 1990. DOI: 10.2514/6.1990-5254 (cit. on p. 19).

[78] M. V. Suraweera, D. J. Mee, and R. J. Stalker. "Skin Friction Reduction in Hypersonic Turbulent Flow by Boundary Layer Combustion". In: *43rd AIAA Aerospace Sciences Meeting and Exhibit* (Reno, NV). AIAA-2005-613. Jan. 10–13, 2005. DOI: 10.2514/6.2005-613 (cit. on p. 19).

[79] D. J. Hunt. "Supersonic combustion in inlet-fuelled busemann-like axisymmetric scramjet flow paths". PhD thesis. The University of Queensland, 2014. 251 pp. DOI: 10.14264/uql.2014.194 (cit. on p. 19).

[80] J. L. Kerrebrock. "Some readily quantifiable aspects of scramjet engine performance". In: *Journal of Propulsion and Power* 8.5 (Sept. 1992), pp. 1116–1122. DOI: 10.2514/3.23600 (cit. on p. 19).

[81] R. J. Stalker. "Control of Hypersonic Turbulent Skin Friction by Boundary- Layer Combustion of Hydrogen". In: *Journal of Spacecraft and Rockets* 42.4 (July 2005), pp. 577–587. DOI: 10.2514/1.8699 (cit. on p. 21).

[82] D. Wise. "Experimental investigation of a three dimensional scramjet engine at hypervelocity conditions". PhD thesis. University of Queensland, 2015, p. 197. DOI: 10.14264/uql.2015.465 (cit. on pp. 21–24, 151–154, 159, 161, 164, 170, 173, 175).

[83] J. E. Barth. "Mixing and combustion enhancement in a Mach 12 shape-transitioning scramjet engine". PhD thesis. The University of Queensland, 2014. 349 pp. DOI: 10.14264/uql.2014.614 (cit. on pp. 22–24, 151, 153, 155, 164, 166, 169, 172, 181, 185, 188–190).

[84] J. E. Barth, V. Wheatley, and M. K. Smart. "Streamwise porthole fuel injection for boundary-layer combustion inside a scramjet engine". In: *28th International Congress of the Aeronautical Sciences (ICAS 2012)*. Brisbane: International Council of the Aeronautical Sciences (ICAS), Sept. 23–28, 2012, p. 8. URL: http://www.icas.org/ICAS_ARCHIVE/ICAS2012/PAPERS/379.PDF (cit. on p. 22).

[85] L. J. Doherty, M. K. Smart, and D. J. Mee. "Experimental Testing of an Airframe Integrated 3-D Scramjet at True Mach 10 Flight Conditions". In: *19th AIAA International Space Planes and Hypersonic Systems and Technologies Conference* (Atlanta, USA). American Institute of Aeronautics and Astronautics (AIAA), June 16–20, 2014. DOI: 10.2514/6.2014-2930 (cit. on pp. 23, 29).

[86] M. J. Robinson, J. Martinez Schramm, and K. Hannemann. "Design and implementation of an internal stress wave force balance in a shock tunnel". In: *CEAS Space Journal* 1.1-4 (Aug. 2010), pp. 45–57. DOI: 10.1007/s12567-010-0003-5 (cit. on p. 23).

[87] W. Landsberg. "Improving performance of high Mach number scramjets: fuelling strategies and combustor design". PhD thesis. DOI: 10.14264/uql.2018.467 (cit. on pp. 23, 24, 151, 154, 159, 160, 166, 167, 169, 175, 181, 183, 185–189, 230).

[88] J. I. Erdos and R. J. Bakos. "Prospects for a quiet hypervelocity shock-expansion tunnel". In: *25th Plasmadynamics and Lasers Conference* (Colorado, USA). Fluid Dynamics and Co-located Conferences. American Institute of Aeronautics and Astronautics, June 20, 1994. DOI: 10.2514/6.1994-2500 (cit. on pp. 24, 87).

[89] D. M. Bushnell. "Hypersonic Ground Test Requirements". In: *Progress in Astronautics and Aeronautics*. American Institute of Aeronautics and Astronautics, Jan. 2002, pp. 1–15. DOI: 10.2514/5.9781600866678.0001.0015 (cit. on p. 25).

[90] M. V. Pulsonetti. "Scaling Laws for Scramjets". PhD. Brisbane, Australia: The University of Queensland, Department of Mechanical Engineering, 1997 (cit. on pp. 25, 54).

[91] M. V. Pulsonetti. *Experimental Methods for a Scramjet Scaling Study*. Departmental Report 7/95. University of Queensland, Department of Mechanical Engineering, 1995 (cit. on p. 25).

[92] F. Schloegel. "Combustion scaling laws for Inlet-fueled scramjets". PhD thesis. The University of Queensland, 2013. 460 pp. DOI: 10.14264/uql.2014.124 (cit. on p. 25).

[93] F. K. Lu and D. E. Marren. "Principles of Hypersonic Test Facility Development". In: *Progress in Astronautics and Aeronautics*. American Institute of Aeronautics and Astronautics, Jan. 2002, pp. 17–27. DOI: 10.2514/5.9781600866678.0017.0027 (cit. on p. 27).

[94] K. Hannemann, K. Itoh, D. J. Mee, and H. G. Hornung. "Free Piston Shock Tunnels HEG, HIEST, T4 and T5". In: *Experimental Methods of Shock Wave Research*. Springer International Publishing, Nov. 2015, pp. 181–264. DOI: 10.1007/978-3-319-23745-9_7 (cit. on pp. 27, 29, 30).

[95] B. S. Stewart. "Predicted scramjet testing capabilities of the proposed RHYFL-X expansion tube". PhD thesis. 2004. URL: https://espace.library.uq.edu.au/view/UQ:267592 (cit. on pp. 27, 28, 52, 88).

[96] D. M. Bushnell. "Mixing and Combustion Issues in Hypersonic Air-Breathing Propulsion". English. In: *Combustion in High-Speed Flows*. Ed. by J. Buckmaster, T. Jackson, and A. Kumar. Vol. 1. ICASE-/LaRC Interdisciplinary Series in Science and Engineering. Springer Netherlands, 1994, pp. 3–16. DOI: 10.1007/978-94-011-1050-1_1 (cit. on p. 28).

[97] K. Fischer and K. Rock. "Calculated Effects of Nitric Oxide Flow Contamination on Scramjet Performance". In: *31st Joint Propulsion Conference and Exhibit*. AIAA, July 10–12, 1995. DOI: 10.2514/6.1995-2524 (cit. on p. 28).

[98] S. Thomas, J. Lee, J. Stephens, R. Hostler, and W. V. Kamp. "The Mothball, Sustainment, and Proposed Reactivation of the Hypersonic Tunnel Facility (HTF) at NASA Glenn Research Center Plum Brook Station". In: *27th AIAA Aerodynamic Measurement Technology and Ground Testing Conference*. American Institute of Aeronautics and Astronautics, June 2010. DOI: 10.2514/6.2010-4533 (cit. on p. 28).

[99] J. D. Anderson. *Modern Compressible Flow: With Historical Perspective*. Aeronautical and Aerospace Engineering Series. McGraw-Hill Education, 2003. DOI: 10.1036/0070016739 (cit. on pp. 28, 33, 34, 82).

[100] R. G. Morgan. "Chapter 4.3 - Shock Tubes and Tunnels: Facilities, Instrumentation, and Techniques". In: *Handbook of Shock Waves*. Ed. by G. Ben-Dor, O. Igra, and T. Elperin. Burlington: Academic Press, 2001, pp. 603–622. DOI: 10.1016/B978-012086430-0/50014-2. (Cit. on pp. 28, 34, 35, 39–41, 69).

[101] S. P. Sharma and C. Park. "Operating characteristics of a 60- and 10-cm electric arc-driven shock tube. I - The driver. II - The driven section". In: *Journal of Thermophysics and Heat Transfer* 4.3 (July 1990), pp. 259–265. DOI: 10.2514/3.175 (cit. on p. 28).

[102] R. Morgan. "A review of the use of expansion tubes for creating superorbital flows". In: *35th Aerospace Sciences Meeting and Exhibit* (Jan. 1997). DOI: 10.2514/6.1997-279 (cit. on p. 28).

[103] A. Hertzberg, W. E. Smith, H. S. Glick, and W. Squire. *Modifications of the shock tube for the generation of hypersonic flow*. Tech. rep. 55-15. Cornell Aeronautical Laboratory, Inc., 1955 (cit. on pp. 28, 29, 78).

[104] R. G. Morgan. "Chapter 4.2 - Shock Tubes and Tunnels: Facilities, Instrumentation, and Techniques". In: *Handbook of Shock Waves*. Ed. by G. Ben-Dor, O. Igra, and T. Elperin. Burlington: Academic Press, 2001, pp. 587–601. DOI: 10.1016/B978-012086430-0/50013-0. (Cit. on p. 29).

[105] K. Itoh, S. Ueda, T. Komuro, K. Sato, M. Takahashi, H. Miyajima, H. Tanno, and H. Muramoto. "Improvement of a free piston driver for a high-enthalpy shock tunnel". English. In: *Shock Waves* 8.4 (Aug. 1998), pp. 215–233. DOI: 10.1007/s001930050115 (cit. on pp. 29, 31).

[106] R. J. Stalker. "A study of the free-piston shock tunnel." In: *AIAA Journal* 5.12 (Dec. 1967), pp. 2160–2165. DOI: 10.2514/3.4402 (cit. on pp. 29, 30).

[107] C. Stalker, R. G. Morgan, and R. I. Tanner. "Raymond John Stalker 1930–2014". In: *Historical Records of Australian Science* 27.1 (2016), p. 70. DOI: 10.1071/hr15012 (cit. on p. 29).

[108] M. Holden. "Studies of scramjet performance in the LENS facilities". In: *36th AIAA/ASME/SAE/ASEE Joint Propulsion Conference and Exhibit* (Las Vegas, USA). American Institute of Aeronautics and Astronautics (AIAA), July 17–19, 2000. DOI: 10.2514/6.2000-3604 (cit. on pp. 29, 30).

[109] D. Marren and F. Lu, eds. *Advanced Hypersonic Test Facilities*. American Institute of Aeronautics and Astronautics, Jan. 2002. DOI: 10.2514/4.866678 (cit. on p. 29).

[110] R. J. Stalker, A. Paull, D. J. Mee, R. G. Morgan, and P. A. Jacobs. "Scramjets and shock tunnels—The Queensland experience". In: *Progress in Aerospace Sciences* 41.6 (Aug. 2005), pp. 471–513. DOI: 10.1016/j.paerosci.2005.08.002. (Cit. on p. 29).

[111] A. Paull and R. J. Stalker. "Scramjet Testing, Facility and Instrumentation". In: *Progress in Astronautics and Aeronautics*. Ed. by E. T. Curran and S. N. B. Murthy. American Institute of Aeronautics and Astronautics, Jan. 2001, pp. 5–7. DOI: 10.2514/5.9781600866609.0369.0446 (cit. on p. 29).

[112] R. G. Morgan. "Private communications". 2018 (cit. on p. 30).

[113] K. Itoh, S. Ueda, H. Tanno, T. Komuro, and K. Sato. "Hypersonic aerothermodynamic and scramjet research using high enthalpy shock tunnel". In: *Shock Waves* 12.2 (Aug. 2002), pp. 93–98. DOI: 10.1007/s00193-002-0147-0 (cit. on p. 30).

[114] M. Takahashi, T. Komuro, K. Sato, M. Kodera, H. Tanno, and K. Itoh. "Effect of Combustor Shape on Scramjet Characteristics at Hypervelocity Condition over Mach 10 Flight". In: *14th International Space Planes and Hypersonic Systems and Technologies Conferences* (Canberra, Australia). American Institute of Aeronautics and Astronautics, Nov. 7–8, 2006. DOI: 10.2514/6.2006-8024 (cit. on p. 30).

[115] H. Tanno, T. Komuro, K. Sato, and K. Itoh. "Free-flight aerodynamic test of elliptic cone in Shock Tunnel". In: *20th AIAA International Space Planes and Hypersonic Systems and Technologies Conference* (Glasglow, Scotland). American Institute of Aeronautics and Astronautics (AIAA), July 6–9, 2015. DOI: 10.2514/6.2015-3655 (cit. on p. 30).

[116] B. Zhixian, Z. Bingbing, Z. Hao, C. Xing, S. Junmou, L. Chen, and S. Riming. "Experiments and Computations on the Compression Process in the Free Piston Shock Tunnel FD21". In: *5th International Conference on Experimental Fluid Mechanics*. Munich, Germany, 2018. URL: https://athene-forschung.rz.unibw-muenchen.de/doc/124228/124228.pdf (cit. on p. 30).

[117] Y. Liu, Y. Wang, C. Yuan, C. Luo, and Z. Jiang. "Aerodynamic force and moment measurement of 10 half-angle cone in JF12 shock tunnel". In: *Chinese Journal of Aeronautics* 30.3 (June 2017), pp. 983–987. DOI: 10.1016/j.cja.2017.02.008 (cit. on p. 30).

[118] H. G. Hornung. "28th Lanchester Memorial Lecture — Experimental real-gas hypersonics". In: 92.920 (Dec. 1988), pp. 379–389. DOI: 10.1017/s0001924000016511 (cit. on pp. 31, 57).

[119] J. Sancho Ponce. "Scramjet testing at high total pressure". PhD thesis. St Lucia: University of Queensland, 2016. DOI: 10.14264/uql.2016.71 (cit. on pp. 31, 38, 40–42, 47, 191, 227).

[120] J. I. Erdos. "Combustion in High-Speed Flow". In: ed. by J. Buckmaster, T. L. Jackson, and A. Kumar. Springer Science + Business Media, 1994. Chap. Recent Experiments on Hypersonic Combustion in an Expansion Tube Test Facility, pp. 53–91. DOI: 10.1007/978-94-011-1050-1_3 (cit. on p. 31).

[121] C. M. James. "Radiation from Simulated Atmospheric Entry into the Gas Giants". PhD thesis. University of Queensland, 2018 (cit. on pp. 33, 131, 227).

[122] R. G. Morgan and R. J. Stalker. "Double diaphragm driven free piston expansion tube". In: *Proceedings of the 18th International Symposium on Shock waves*. Ed. by K. Takayama. 1992, pp. 1031–1038 (cit. on pp. 33, 38, 40).

[123] R. L. Trimpi. *A preliminary theoretical study of the expansion tube: a new device for producing high-enthalpy short-duration hypersonic gas flows*. Tech. rep. NASA, 1962, p. 29. URL: https://ntrs.nasa.gov/archive/nasa/casi.ntrs.nasa.gov/19620002505.pdf (cit. on pp. 34, 40).

[124] H. Mirels. "Test Time in Low-Pressure Shock Tubes". In: *The Physics of Fluids* 6.9 (1963), pp. 1201–1214. DOI: 10.1063/1.1706887 (cit. on pp. 36, 49).

[125] R. E. Duff. "Shock-Tube Performance at Low Initial Pressure". In: *Physics of Fluids* 2.2 (1959), p. 207. DOI: 10.1063/1.1705910 (cit. on p. 36).

[126] H. Mirels. "Shock Tube Test Time Limitation Due to Turbulent-Wall Boundary Layer". In: *AIAA Journal* 2.1 (Jan. 1964), pp. 84–93. DOI: 10.2514/3.2218 (cit. on pp. 36, 49).

[127] A. Ben-Yakar and R. K. Hanson. "Characterization of Expansion Tube Flows for Hypervelocity Combustion Studies". In: *Journal of Propulsion and Power* 18.4 (July 2002), pp. 943–952. DOI: 10.2514/2.6021 (cit. on pp. 36, 37).

[128] M. McGilvray, J. M. Austin, M. Sharma, P. A. Jacobs, and R. G. Morgan. "Diagnostic modelling of an expansion tube operating condition". In: *Shock Waves* 19.1 (2009), pp. 59–66. DOI: 10.1007/s00193-009-0187-9 (cit. on p. 36).

[129] D. E. Gildfind, P. A. Jacobs, R. G. Morgan, W. Y. K. Chan, and R. J. Gollan. "Scramjet test flow reconstruction for a large-scale expansion tube, Part 2: axisymmetric CFD analysis". In: *Shock Waves* (Nov. 2017). DOI: 10.1007/s00193-017-0786-9 (cit. on pp. 36, 41, 66, 86, 98, 121, 139, 140, 142).

[130] O. Rizkalla, R. J. Bakos, W. Chinitz, M. V. Pulsonetti, and J. I. Erdos. "Use of an Expansion Tube to Examine Scramjet Combustion at Hypersonic Velocities". In: *AIAA/ASME/SAE/ASEE 25th Joint Propulsion Conference* (Monterey, USA). American Institute of Aeronautics and Astronautics, July 10–12, 1989. DOI: 10.2514/6.1989-2536 (cit. on p. 36).

[131] R. J. Bakos, R. G. Morgan, S. L. Tuttle, G. M. Kelly, A. Paull, J. M. Simmons, R. J. Stalker, M. V. Pulsonetti, D. R. Buttsworth, G. A. J. Allen, N. R. Ward, K. Skinner, A. J. Neely, and R. M. Krek. *Shock Tunnel Studies of Scramjet Phenomena - Supplement 7*. NASA Contractor Report NASA-CR-191572. NASA, Dec. 1993. URL: https://ntrs.nasa.gov/archive/nasa/casi.ntrs.nasa.gov/19940019040.pdf (cit. on p. 36).

[132] R. J. Bakos, A. Castrogiovanni, J. Calleja, L. Nucci, and J. I. Erdos. "Expansion of the scramjet ground test envelope of the Hypulse facility". In: *Space Plane and Hypersonic Systems and Technology Conference* (Norfolk, USA). American Institute of Aeronautics and Astronautics (AIAA), Nov. 18–22, 1996. DOI: 10.2514/6.1996-4506 (cit. on p. 37).

[133] C. Y. Tsai and R. J. Bakos. "Mach 7-21 flight Simulation in the HYPULSE Shock Tunnel". In: *23rd International Symposium on Shock Waves* (Forth Worth, USA). July 2001 (cit. on p. 37).

[134] R. S. M. Chue, R. J. Bakos, C. Y. Tsai, and A. Betti. "Design of a shock-free expansion tunnel nozzle in HYPULSE". In: *Shock Waves* 13.4 (Dec. 2003), pp. 261–270. DOI: 10.1007/s00193-003-0215-0 (cit. on pp. 37, 79, 81).

[135] R. C. Rogers, A. T. Shih, C. Y. Tsai, and R. O. Foelsche. "Scramjet tests in a shock tunnel at flight Mach 7, 10, and 15 conditions". In: *37th Joint Propulsion Conference and Exhibit* (Salt Lake City,USA). American Institute of Aeronautics and Astronautics, July 8–11, 2001. DOI: 10.2514/6.2001-3241 (cit. on p. 37).

[136] N. E. Hass, A. T. Shih, and R. C. Rogers. "Mach 12 & 15 Scramjet Test Capabilities of the HYPULSE Shock-Expansion Tunnel". In: *43rd AIAA Aerospace Sciences Meeting and Exhibit* (Reno, Nevada). American Institute of Aeronautics and Astronautics (AIAA), Jan. 10–13, 2005. DOI: 10.2514/6.2005-690 (cit. on p. 37).

[137] R. Bakos and J. Erdos. "HYPULSE: A Versatile Hypersonic Research Facility. 11th International Workshop on Shock Tube Technology". Oral presentation. Goettingen, Germany, 2016 (cit. on p. 37).

[138] A. Dufrene, M. MacLean, R. Parker, T. Wadhams, and M. Holden. "Characterization of the New LENS Expansion Tunnel Facility". In: *48th AIAA Aerospace Sciences Meeting Including the New Horizons Forum and Aerospace Exposition*. American Institute of Aeronautics and Astronautics, Jan. 2010. DOI: 10.2514/6.2010-1564 (cit. on p. 37).

[139] F. Orley, C. L. Strand, V. A. Miller, F. Oerley, M. Gamba, N. Adams, and G. Iaccarino. "A Study of Expansion Tube Gas Flow Conditions for Scramjet Combustor Model Testing". In: *42nd AIAA Fluid Dynamics Conference and Exhibit* (New Orleans, USA). American Institute of Aeronautics and Astronautics (AIAA), June 25–28, 2012. DOI: 10.2514/6.2012-3264 (cit. on p. 37).

[140] A. Dufrene, M. Sharma, and J. M. Austin. "Design and Characterization of a Hypervelocity Expansion Tube Facility". In: *Journal of Propulsion and Power* 23.6 (Nov. 2007), pp. 1185–1193. DOI: 10.2514/1.30349 (cit. on p. 37).

[141] Y. M. Abul-Huda and M. Gamba. "Design and Characterization of the Michigan Hypersonic Expansion Tube Facility (MHExT)". In: *53rd AIAA Aerospace Sciences Meeting* (Kissimmee, Florida). American Institute of Aeronautics and Astronautics (AIAA), Jan. 5, 2015. DOI: 10.2514/6.2015-1785 (cit. on p. 37).

[142] M. McGilvray, R. M. Kirchhartz, and T. Jazra. "Comparison of Mach 10 Scramjet Measurements from Different Impulse Facilities". In: *AIAA Journal* 48.8 (Aug. 2010), pp. 1647–1651. DOI: 10.2514/1.J050025 (cit. on p. 38).

[143] B. D. Henshall. "The Use of Multiple Diaphragms in Shock Tubes". In: *A.R.C. Technical Report C.P. No. 291. Ministry of Supply, Aeronautical Research Council* (1956) (cit. on p. 38).

[144] R. J. Stalker and D. L. Plumb. "Diaphragm-type Shock Tube for High Shock Speeds". In: *Nature* 218.5143 (May 1968), pp. 789–790. DOI: 10.1038/218789a0 (cit. on p. 38).

[145] A. J. Neely and R. G. Morgan. "The Superorbital Expansion Tube concept, experiment and analysis". In: *Aeronautical Journal* 98.973 (Mar. 1994), pp. 97–105. DOI: 10.1017/s0001924000050107 (cit. on p. 40).

[146] C. G. Miller. "Operational Experience in the Langley Expansion Tube With Various Test Gases". In: *AIAA Journal* 16.3 (Mar. 1978), pp. 195–196. DOI: 10.2514/3.60877 (cit. on pp. 40, 78).

[147] C. G. Miller and J. J. Jones. "Development and performance of the NASA Langley research center expansion tube/tunnel, a hypersonic-hypervelocity real-gas facility". In: *Shock tubes and waves*. Sydney, Australia, 1983 (cit. on p. 40).

[148] A. Paull, R. Stalker, and I. Stringer. "Experiments on an expansion tube with a free piston driver". In: *15th Aerodynamic Testing Conference*. American Institute of Aeronautics and Astronautics, May 1988. DOI: 10.2514/6.1988-2018 (cit. on p. 40).

[149] A. Paull and R. J. Stalker. "Test flow disturbances in an expansion tube". In: *Journal of Fluid Mechanics* 245.1 (1992), pp. 493–521. DOI: 10.1017/S0022112092000569 (cit. on pp. 40, 41, 66, 67, 69, 75, 78).

[150] P. A. Jacobs. "Numerical Simulation of Transient Hypervelocity Flow in an Expansion Tube". In: *Computers Fluids* 23.1 (Jan. 1994), pp. 77–101. DOI: 10.1016/0045-7930(94)90028-0 (cit. on pp. 40, 134).

[151] A. Paull. "Noise Reduction in Argon Driven Expansion Tubes". English. In: *Shock Waves @ Marseille I*. Ed. by R. Brun and L. Dumitrescu. 1992. Springer Berlin Heidelberg, 1995, pp. 209–214. DOI: 10.1007/978-3-642-78829-1_33 (cit. on pp. 41, 60, 67).

[152] M. McGilvray, R. G. Morgan, and P. A. Jacobs. "Scramjet experiments in an expansion tunnel: evaluated using a quasi-steady analysis technique". In: *AIAA journal* 48.8 (Aug. 2010), pp. 1635–1646. DOI: 10.2514/1.J050024 (cit. on pp. 41, 42, 158, 181).

[153] D. E. Gildfind, R. G. Morgan, and P. A. Jacobs. "Expansion Tubes in Australia". In: *Experimental Methods of Shock Wave Research*. Springer International Publishing, Nov. 2015, pp. 399–431. DOI: 10.1007/978-3-319-23745-9_13 (cit. on p. 43).

[154] R. Morgan. "Development of X3, a superorbital expansion tube". In: *Aerospace Sciences Meetings* (Reno, USA). American Institute of Aeronautics and Astronautics, Jan. 10–13, 2001. DOI: 10.2514/6.2000-558 (cit. on p. 43).

[155] M. P. Scott, R. G. Morgan, and P. A. Jacobs. "A New Single Stage Driver for the X2 Expansion Tube". In: *43rd AIAA Aerospace Sciences Meeting and Exhibit* (Reno, USA). American Institute of Aeronautics and Astronautics (AIAA), Jan. 10–13, 2005. DOI: 10.2514/6.2005-697 (cit. on pp. 43, 52).

[156] A. G. Dann, R. G. Morgan, D. E. Gildfind, C. M. Jacobs, M. McGilvray, and F. Zander. "Upgrade of the X3 Super-orbital Expansion Tube". In: *18th Australasian Fluid Mechanics Conference* (Launcheston, Australia). Ed. by P. A. Brandner and B. W. Pearce. Australasian Fluid Mechanics Society, Dec. 3–7, 2012. URL: http://people.eng.unimelb.edu.au/imarusic/proceedings/18/126%20-%20Dann.pdf (cit. on pp. 43, 44, 55).

[157] M. P. Scott. "Development and modelling of expansion tubes". PhD thesis. University of Queensland, 2007. URL: https://espace.library.uq.edu.au/view/UQ:158451 (cit. on pp. 44, 79, 81, 98, 103).

[158] M. H. Davey. "A hypersonic nozzle for the X3 expansion tube". MA thesis. St Lucia: University of Queensland, 2006. URL: https://espace.library.uq.edu.au/view/UQ:348514 (cit. on pp. 44, 80).

[159] D. E. Gildfind, J. Sancho, and R. G. Morgan. "High Mach Number Scramjet Test Flows in the X3 Expansion Tube". In: *29th International Symposium on Shock Waves 1*. Springer International Publishing, 2015, pp. 373–378. DOI: 10.1007/978-3-319-16835-7_58 (cit. on p. 44).

[160] D. E. Gildfind, R. G. Morgan, and J. Sancho. "Design and commissioning of a new lightweight piston for the X3 Expansion Tube". English. In: *29th International Symposium on Shock Waves 1* (Madison, USA). Ed. by R. Bonazza and D. Ranjan. Madison, WI, United States: Springer International Publishing, July 17–19, 2013, pp. 367–372. DOI: 10.1007/978-3-319-16835-7_57 (cit. on pp. 45, 56).

[161] A. Andrianatos, D. E. Gildfind, and R. G. Morgan. "Driver Condition Development for High Enthalpy Operation of the X3 Expansion Tube". In: *31st International Symposium on Shock Waves*. 2017 (cit. on pp. 45, 52, 55–57, 59).

[162] D. E. Gildfind and R. G. Morgan. "A new sliding joint to accommodate recoil of a free-piston-driven expansion tube facility". In: *Shock Waves* 26.6 (Dec. 2015), pp. 825–833. DOI: 10.1007/s00193-015-0609-9 (cit. on p. 45).

[163] B. J. McBride and S. Gordon. *Computer Program for Calculation of Complex Chemical Equilibrium Compositions and Applications: II. Users Manual and Program Description*. NASA Reference Publication NASA RP 1311. NASA Lewis Research Center, Cleveland, OH, 1996 (cit. on pp. 49, 166).

[164] C. M. James, D. E. Gildfind, R. G. Morgan, S. W. Lewis, E. J. Fahy, and T. J. McIntyre. "On the Current Limits of Simulating Gas Giant Entry Flows in an Expansion Tube". In: *20th AIAA International Space Planes and Hypersonic Systems and Technologies Conference* (Glasgow, Scotland). American Institute of Aeronautics and Astronautics (AIAA), July 6–9, 2015. DOI: 10.2514/6.2015-3501 (cit. on p. 49).

[165] D. G. Goodwin, H. K. Moffat, and R. L. Speth. *Cantera: An Object-oriented Software Toolkit for Chemical Kinetics, Thermodynamics, and Transport Processes*. http://www.cantera.org. Version 2.2.0. 2017. DOI: 10.5281/zenodo.170284 (cit. on p. 49).

[166] D. E. Gildfind, P. A. Jacobs, R. G. Morgan, W. Y. K. Chan, and R. J. Gollan. "Scramjet test flow reconstruction for a large-scale expansion tube, Part 1: quasi-one-dimensional modelling". In: *Shock Waves* 28.4 (Nov. 2017), pp. 877–897. DOI: 10.1007/s00193-017-0785-x (cit. on pp. 50, 132, 135).

[167] P. A. Jacobs. "Quasi-one-dimensional modeling of a free-piston shock tunnel". In: *AIAA Journal* 32.1 (Jan. 1994), pp. 137–145. DOI: 10.2514/3.11961 (cit. on p. 52).

[168] P. A. Jacobs. *Shock Tube Modelling with L1d*. Tech. rep. Department of Mechanical Engineering, The University of Queensland, 1998 (cit. on p. 52).

[169] D. E. Gildfind, R. G. Morgan, P. A. Jacobs, and M. McGilvray. "Production of High-Mach-Number Scramjet Flow Conditions in an Expansion Tube." In: *AIAA Journal* 52 (2014), pp. 162–177. DOI: 10.2514/1.J052383 (cit. on pp. 53, 56).

[170] T. Parks and J. McClellan. "Chebyshev Approximation for Nonrecursive Digital Filters with Linear Phase". In: *IEEE Transactions on Circuit Theory* 19.2 (1972), pp. 189–194. DOI: 10.1109/tct.1972.1083419 (cit. on pp. 54, 118, 158).

[171] *U.S. Standard Atmosphere, 1976*. Tech. rep. NOAA-S/T-76-1562. NOAA, 1976 (cit. on p. 54).

[172] D. E. Gildfind, C. M. James, and R. G. Morgan. "Free-piston driver performance characterisation using experimental shock speeds through helium". In: *Shock Waves* 25.2 (Jan. 2015), pp. 169–176. DOI: 10.1007/s00193-015-0553-8 (cit. on p. 57).

[173] D. C. Stone. "Application of median filtering to noisy data". In: *Canadian Journal of Chemistry* 73.10 (Oct. 1995), pp. 1573–1581. DOI: 10.1139/v95-195 (cit. on pp. 69, 118).

[174] J. J. Rast. *The design of flat-scored high-pressure diaphragm for use in shock tunnels and gas guns*. Tech. rep. NAVAL ORDNANCE LAB WHITE OAK MD, 1961. URL: http://www.dtic.mil/dtic/tr/fulltext/u2/653285.pdf (cit. on p. 72).

[175] A. Hertzberg. "A Shock Tube Method of Generating Hypersonic Flows". In: *Journal of the Aeronautical Sciences* 18.12 (Dec. 1951), pp. 803–804. DOI: 10.2514/8.2124 (cit. on p. 78).

[176] L. B. Callis and R. L. Trimpi. *A perfect-gas analysis of the expansion tunnel, a modification to the expansion tube*. Tech. rep. R-223. Langley Research Center. NASA, 1965. URL: https://ntrs.nasa.gov/archive/nasa/casi.ntrs.nasa.gov/19650010885.pdf (cit. on p. 78).

[177] L. B. Callis. *A theoretical study of the effect on expansion-tube performance of area changes at primary and secondary diaphragm stations*. Tech. rep. NASA-TN-D-3303. NASA, 1966. URL: https://ntrs.nasa.gov/archive/nasa/casi.ntrs.nasa.gov/19660009026.pdf (cit. on p. 78).

[178] L. B. Callis. *An analysis of supersonic flow phenomena in conical nozzles by a method of characteristics*. Tech. rep. NASA-TN-D-3550. NASA, 1966. URL: https://ntrs.nasa.gov/archive/nasa/casi.ntrs.nasa.gov/19660024682.pdf (cit. on p. 78).

[179] G. D. Norfleet, J. Lacey, J. John, and J. D. Whitfield. *Results of an experimental investigation of the performance of an expansion tube*. Tech. rep. AD0628628. Arnold Engineering Development Center, 1966. URL: http://www.dtic.mil/dtic/tr/fulltext/u2/628628.pdf (cit. on p. 78).

[180] I. Leyva. "Study of the addition of a divergent nozzle to an expansion tube for increasing test time". In: *25th Plasmadynamics and Lasers Conference*. American Institute of Aeronautics and Astronautics, June 1994. DOI: 10.2514/6.1994-2533 (cit. on p. 78).

[181] O. Sudnitsin. "Design and Testing of Expansion Tube with Area Change". MA thesis. University of Queensland, 2000 (cit. on p. 78).

[182] J. J. Korte. "Flow quality of hypersonic wind-tunnel nozzles designed using computational fluid dynamics". In: *Journal of Spacecraft and Rockets* 32.4 (July 1995), pp. 569–580. DOI: 10.2514/3.26655 (cit. on p. 78).

[183] J. J. Korte. "Aerodynamic design of axisymmetric hypersonic wind-tunnel nozzles using a least-squares/parabolized Navier-Stokes procedure". In: *Journal of Spacecraft and Rockets* 29.5 (Sept. 1992), pp. 685–691. DOI: 10.2514/3.11511 (cit. on pp. 78, 82).

[184] F. Shope. "Contour design techniques for super/hypersonic wind tunnel nozzles". In: *24th AIAA Applied Aerodynamics Conference*. American Institute of Aeronautics and Astronautics (AIAA), June 2006. DOI: 10.2514/6.2006-3665 (cit. on p. 79).

[185] R. J. Bakos, J. Calleja, J. I. Erdos, A. Auslender, M. Sussman, and G. Wilson. "Design, calibration and analysis of a tunnel mode of operation for the HYPULSE facility". In: (New Orleans, USA). American Institute of Aeronautics and Astronautics (AIAA), June 17, 1996. DOI: 10.2514/6.1996-2194 (cit. on p. 79).

[186] C. S. Craddock. "Computational optimization of scramjets and shock tunnel nozzles". PhD thesis. University of Queensland, 1999. URL: https://espace.library.uq.edu.au/view/UQ:157835 (cit. on pp. 79, 84, 99).

[187] M. Holden. "Experimental Studies in the LENS Shock Tunnel and Expansion Tunnel to Examine Real-Gas Effects in Hypervelocity Flows". In: *42nd AIAA Aerospace Sciences Meeting and Exhibit*. American Institute of Aeronautics and Astronautics, Jan. 2004. DOI: 10.2514/6.2004-916 (cit. on p. 79).

[188] I. Nompelis, G. Candler, M. Holden, and T. Wadhams. "Numerical Simulation of High-Enthalpy Experiments in the LENS X Expansion Tube Facility". In: *42nd AIAA Aerospace Sciences Meeting and Exhibit*. American Institute of Aeronautics and Astronautics, Jan. 2004. DOI: 10.2514/6.2004-1000 (cit. on p. 79).

[189] W. Y. K. Chan, P. A. Jacobs, M. K. Smart, S. Grieve, C. S. Craddock, and L. J. Doherty. "Aerodynamic Design of Nozzles with Uniform Outflow for Hypervelocity Ground-Test Facilities". In: *Journal of Propulsion and Power* (Sept. 2018), pp. 1–12. DOI: 10.2514/1.b36938 (cit. on pp. 80, 83–85).

[190] R. J. Gollan and P. A. Jacobs. "About the formulation, verification and validation of the hypersonic flow solver Eilmer". In: *Int. J. Numer. Meth. Fluids* 73.1 (Mar. 2013), pp. 19–57. DOI: 10.1002/fld.3790 (cit. on pp. 80, 82).

[191] G. Candler and J. Perkins. "Effects of vibrational nonequilibrium on axisymmetric hypersonic nozzle design". In: *29th Aerospace Sciences Meeting*. American Institute of Aeronautics and Astronautics, Jan. 1991. DOI: 10.2514/6.1991-297 (cit. on p. 82).

[192] D. Lee and M. Wiswall. "A Parallel Implementation of the Simplex Function Minimization Routine". In: *Comput Econ* 30.2 (June 2007), pp. 171–187. DOI: 10.1007/s10614-007-9094-2 (cit. on pp. 82–84, 236).

[193] L. Doherty, Y. K. W. Chan, F. Zander, P. A. Jacobs, R. J. Gollan, and R. M. Kirchhartz. *NENZF-r: Non-Equilibrium Nozzle Flow, Reloaded. A User Guide*. Tech. rep. School of Mechanical and Mining Engineering. The University of Queensland, Nov. 2011 (cit. on pp. 82, 131).

[194] D. Thévenin and G. Janiga, eds. *Optimization and Computational Fluid Dynamics*. Springer Berlin Heidelberg, 2008. DOI: 10.1007/978-3-540-72153-6 (cit. on p. 83).

[195] J. A. Nelder and R. Mead. "A Simplex Method for Function Minimization". In: *The Computer Journal* 7.4 (Jan. 1965), pp. 308–313. DOI: 10.1093/comjnl/7.4.308 (cit. on p. 83).

[196] H. Wei, W. Y. K. Chan, P. A. Jacobs, and R. G. Morgan. "Computational optimisation and analysis of a truncated hypersonic nozzle for X3 expansion tunnel." In: *Proceedings of the 19th Australasian Fluid Mechanics Conference*. (Melbourne, Australia). Ed. by H. Chowdhury and F. Alam. RMIT University, Dec. 2014 (cit. on pp. 88, 93).

[197] J. Korte, A. Kumar, D. Singh, and J. White. "CAN-DO, CFD-based Aerodynamic Nozzle Design and Optimization programfor supersonic/hypersonic wind tunnels". In: *17th Aerospace Ground Testing Conference*. American Institute of Aeronautics and Astronautics, July 1992. DOI: 10.2514/6.1992-4009 (cit. on p. 89).

[198] R. N. Gupta, J. M. Yos, R. A. Thompson, and K.-P. Lee. "A review of reaction rates and thermodynamic and transport properties for an 11-species air model for chemical and thermal nonequilibrium calculations to 30000 K". In: (1990). URL: https://ntrs.nasa.gov/archive/nasa/casi.ntrs.nasa.gov/19900017748.pdf (cit. on p. 89).

[199] B. Baldwin and H. Lomax. "Thin-layer approximation and algebraic model for separated turbulent-flows". In: *16th Aerospace Sciences Meeting*. American Institute of Aeronautics and Astronautics (AIAA), Jan. 1978. DOI: 10.2514/6.1978-257 (cit. on pp. 89, 139).

[200] D. Wilcox. "Formulation of the k-omega Turbulence Model Revisited". In: *45th AIAA Aerospace Sciences Meeting and Exhibit*. American Institute of Aeronautics and Astronautics (AIAA), Jan. 2007. DOI: 10.2514/6.2007-1408 (cit. on p. 89).

[201] F. Stern, R. Wilson, and J. Shao. "Quantitative V&V of CFD simulations and certification of CFD codes". In: *International Journal for Numerical Methods in Fluids* 50.11 (2006), pp. 1335–1355. DOI: 10.1002/fld.1090 (cit. on pp. 100, 166).

[202] P. J. Roache. "Perspective: A Method for Uniform Reporting of Grid Refinement Studies". In: *Journal of Fluids Engineering* 116.3 (1994), p. 405. DOI: 10.1115/1.2910291 (cit. on p. 100).

[203] R. G. Morgan and D. E. Gildfind. "X3 reflected shock tunnel for extended flow duration". In: *Asia-Pacific International Symposium on Aerospace Technology APISAT* (Shanghai, China). Shanghai, China: Science Direct, Sept. 24–26, 2014 (cit. on p. 103).

[204] M. McGilvray, P. A. Jacobs, R. G. Morgan, R. J. Gollan, and C. M. Jacobs. "Helmholtz Resonance of Pitot Pressure Measurements in Impulsive Hypersonic Test Facilities". In: *AIAA Journal* 47.10 (Oct. 2009), pp. 2430–2439. DOI: 10.2514/1.42543 (cit. on p. 112).

[205] D. E. Gildfind. *Pitot Cap, Four Hole Swirl Type, Drawing Number X2-PIT-001-1*. Tech. rep. University of Queensland, 2011. URL: https://espace.library.uq.edu.au/view/UQ:322502 (cit. on p. 113).

[206] D. E. Gildfind. *15 Deg Pitot Cone, 8 Hole, Drawing Number X2-PIT-003-1*. Tech. rep. University of Queensland, 2011. URL: https://espace.library.uq.edu.au/view/UQ:322450 (cit. on p. 113).

[207] P. A. Czysz. *Correlation of Wind Tunnel Blockage Data*. English. Tech. rep. ASD-TDR-63-230. Directorate of Engineering Test, Aeronaultical Systems Divisions, 1963. DOI: 10.21236/ad0407689. (Cit. on p. 114).

[208] C. Leys, C. Ley, O. Klein, P. Bernard, and L. Licata. "Detecting outliers: Do not use standard deviation around the mean, use absolute deviation around the median". In: *Journal of Experimental Social Psychology* 49.4 (July 2013), pp. 764–766. DOI: 10.1016/j.jesp.2013.03.013 (cit. on p. 118).

[209] F. R. Hampel. "The Influence Curve and its Role in Robust Estimation". In: *Journal of the American Statistical Association* 69.346 (June 1974), pp. 383–393. DOI: 10.1080/01621459.1974.10482962 (cit. on p. 118).

[210] P. J. Rousseeuw and C. Croux. "Alternatives to the Median Absolute Deviation". In: *Journal of the American Statistical Association* 88.424 (Dec. 1993), pp. 1273–1283. DOI: 10.1080/01621459.1993.10476408 (cit. on p. 118).

[211] V. A. Miller, M. Gamba, M. G. Mungal, and R. K. Hanson. "Secondary Diaphragm Thickness Effects and Improved Pressure Measurements in an Expansion Tube". In: *AIAA Journal* 52.2 (Feb. 2014), pp. 451–456. DOI: 10.2514/1.j052767 (cit. on p. 121).

[212] G. S. Settles. *Schlieren and Shadowgraph Techniques*. Springer Berlin Heidelberg, 2001. DOI: 10.1007/978-3-642-56640-0 (cit. on p. 125).

[213] S. J. Laurence and S. Karl. "An improved visualization-based force-measurement technique for short-duration hypersonic facilities". In: *Experiments in Fluids* 48.6 (Nov. 2009), pp. 949–965. DOI: 10.1007/s00348-009-0780-9 (cit. on p. 126).

[214] J. Canny. "A Computational Approach to Edge Detection". In: *IEEE Transactions on Pattern Analysis and Machine Intelligence* PAMI-8.6 (Nov. 1986), pp. 679–698. DOI: 10.1109/tpami.1986.4767851 (cit. on p. 126).

[215] G. E. P. Box and K. B. Wilson. "On the Experimental Attainment of Optimum Conditions". In: *Springer Series in Statistics*. Springer New York, 1992, pp. 270–310. DOI: 10.1007/978-1-4612-4380-9_23 (cit. on p. 136).

[216] R. G. Regis and C. A. Shoemaker. "Constrained Global Optimization of Expensive Black Box Functions Using Radial Basis Functions". In: *Journal of Global Optimization* 31.1 (Jan. 2005), pp. 153–171. DOI: 10.1007/s10898-004-0570-0 (cit. on pp. 136, 237).

[217] P. Knysh and Y. Korkolis. "Blackbox: A procedure for parallel optimization of expensive black-box functions". In: *CoRR* abs/1605.00998 (2016). arXiv: 1605.00998. URL: http://arxiv.org/abs/1605.00998 (cit. on pp. 136, 237, 238).

[218] B. Wheatley. "Tunable Diode Laser Absorption Spectroscopy of Aerospace Flows". PhD thesis. DOI: 10.14264/uql.2017.1050 (cit. on p. 150).

[219] H. Johnson, C. Alba, G. Candler, M. MacLean, T. Wadhams, and M. Holden. "Boundary-Layer Stability Analysis of the Hypersonic International Flight Research Transition Experiments". In: *Journal of Spacecraft and Rockets* 45.2 (Mar. 2008), pp. 228–236. DOI: 10.2514/1.31878 (cit. on p. 152).

[220] A. G. Dann. *The Manufacturing of Thin Film Heat Transfer Gauges. Technical report*. Tech. rep. 2013 (cit. on p. 159).

[221] M. Hayne. *The manufacture and mounting of thin film gauges for heat transfer.* Tech. rep. Division of Mecechanical Engineering, The University (cit. on p. 159).

[222] C. Miller. "Comparison of Thin-Film Resistance Heat-Transfer Gages With Thin-Skin Transient Calorimeter Gages in Conventional Hypersonic Wind Tunnels". In: *NASA Scientific and Technical Information Branch*, NASA Technical Memorandum 83197 (1981) (cit. on p. 159).

[223] D. Schultz and T. Jones. *Heat-Transfer Measurements in Short-Duration Hypersonic Facilities*. AGARD-AG-165. North Atlantic Treaty Organization Advisory Group for Aerospace Research and Development, 1973 (cit. on p. 159).

[224] S. A. Razzaqi, W. Y. K. Chan, and M. K. Smart. *Ground Testing of the HIFiRE 7 Scramjet at 75% Scale - Fuel Injector Calibration*. Tech. rep. UQHF7–2014/06. University of Queensland, 2014 (cit. on pp. 161, 163, 230).

[225] I. Nompelis, T. W. Drayna, and G. V. Candler. "Development of a Hybrid Unstructured Implicit Solver for the Simulation of Reacting Flows Over Complex Geometries". In: *34th AIAA Fluid Dynamics Conference and Exhibit*. AIAA Paper 2004-2227. Portland, Oregon, 2004. DOI: 10.2514/6.2004-2227 (cit. on p. 165).

[226] H. B. Johnson, T. W. Drayna, I. Nompelis, and G. V. Candler. *US3D Manual*. Manual. Department of Aerospace Enginer and Mechanics, University of Minnesota, 2014 (cit. on p. 165).

[227] R. W. MacCormack and G. V. Candler. "The solution of the Navier-Stokes equations using Gauss-Seidel line relaxation". In: *Computers & Fluids* 17.1 (Jan. 1989), pp. 135–150. DOI: 10.1016/0045-7930(89)90012-1 (cit. on p. 166).

[228] M. J. Wright, G. V. Candler, and D. Bose. "Data-Parallel Line Relaxation Method for the Navier-Stokes Equations". In: *AIAA Journal* 36.9 (Sept. 1998), pp. 1603–1609. DOI: 10.2514/2.586 (cit. on p. 166).

[229] M. J. Wright, G. V. Candler, and M. Prampolini. "Data-parallel lower-upper relaxation method for the Navier-Stokes equations". In: *AIAA Journal* 34.7 (July 1996), pp. 1371–1377. DOI: 10.2514/3.13242 (cit. on p. 166).

[230] P. R. Spalart and S. R. Allmaras. "A One-Equation Turbulence Model for Aerodynamic Flows". In: *La Recherche Aérospatiule* 5.5 (1994) (cit. on p. 166).

[231] S. Catris and B. Aupoix. "Density corrections for turbulence models". In: *Aerospace Science and Technology* 4.1 (Jan. 2000), pp. 1–11. DOI: 10.1016/s1270-9638(00)00112-7 (cit. on p. 166).

[232] F. R. Menter. "Two-Equation Eddy-Viscosity Turbulence Models for Engineering Applications". In: *AIAA Journal* 32.8 (1994), pp. 1598–1605. DOI: 10.2514/3.12149 (cit. on p. 166).

[233] J. L. Gomez. "Numerical and experimental investigation of hypersonic streamwise vortices and their effect on mixing". PhD thesis. DOI: 10.14264/uql.2018.190 (cit. on p. 166).

[234] R. M. Gehre, V. Wheatley, R. R. Boyce, D. M. Peterson, and S. Brieschenk. "Reynolds-Averaged Navier-Stokes And Wall-Modelled Large-Eddy Simulations of Sonic Hydrogen Injection into Hypersonic Crossflow". In: *Proceedings of the 18th Australasian Fluid Mechanics Conference*. Launceston, Australia, 2012 (cit. on p. 166).

[235] C. J. Jachimowski. *An Analysis of Combustion Studies in Shock Expansion Tunnels and Reflected Shock Tunnels*. Technical Report NASA TP-3224. NTRS: 19920019131. Hampton, VA, United States: NASA Langley Research Center, 1992. URL: https://ntrs.nasa.gov/archive/nasa/casi.ntrs.nasa.gov/19920019131.pdf (cit. on p. 166).

[236] P. D. C. PDC. *Gridpro Software - Automatic Multiblock Grid Generation System*. Version 6.5. White Plains, NY, 2015. URL: http://www.gridpro.com (cit. on p. 166).

[237] C. J. Roy. "Grid Convergence Error Analysis for Mixed-Order Numerical Schemes". In: *AIAA Journal* 41.4 (Apr. 2003), pp. 595–604. DOI: 10.2514/2.2013 (cit. on p. 166).

[238] M. V. Suraweera, Y. Moule, and M. K. Smart. *On-Design Tests of the M12REST Scramjet in the T4 Shock Tunnel*. Tech. rep. Unpublished. School of Mechanical and Mining Engineering, The University of Queensland, 2009 (cit. on p. 170).

[239] C. Fureby. "LES of a Multi-burner Annular Gas Turbine Combustor". In: *Flow, Turbulence and Combustion* 84.3 (Oct. 2009), pp. 543–564. DOI: 10.1007/s10494-009-9236-9 (cit. on p. 172).

[240] P. A. Jacobs, R. C. Rogers, E. H. Weidner, and R. D. Bittner. "Flow establishment in a generic scramjet combustor". In: *Journal of Propulsion and Power* 8.4 (July 1992), pp. 890–899. DOI: 10.2514/3.23566 (cit. on p. 172).

[241] R. C. Rogers and E. H. Weidner. "Scramjet fuel-air mixing establishment in a pulse facility". In: *Journal of Propulsion and Power* 9.1 (Jan. 1993), pp. 127–133. DOI: 10.2514/3.11494 (cit. on p. 172).

[242] J. E. Barth, V. Wheatley, and M. K. Smart. "Effects of Hydrogen Fuel Injection in a Mach 12 Scramjet Inlet". In: *AIAA Journal* 53.10 (Oct. 2015), pp. 2907–2919. DOI: 10.2514/1.j053819 (cit. on pp. 175, 179).

[243] J. L. Shinn and C. G. Miller III. *Experimental perfect-gas study of expansion-tube flow characteristics*. Tech. rep. NASA-TP-1317. NASA, 1978. URL: https://ntrs.nasa.gov/archive/nasa/casi.ntrs.nasa.gov/19790006156.pdf (cit. on p. 176).

[244] R. R. Boyce, M. Takahashi, and R. J. Stalker. "Mass spectrometric measurements of the freestream composition in the T4 free-piston shock-tunnel". In: *Shock Waves* 14.5-6 (Oct. 2005), pp. 359–370. DOI: 10.1007/s00193-005-0275-4 (cit. on p. 189).

[245] M. K. Smart and R. J. Stalker. "Scramjet Combustion Processes". In: *High Speed Propulsion: Engine Design - Integration and Thermal Management*. EN-AVT-185-11. 2010. URL: https://www.sto.nato.int/publications/STO%20Educational%20Notes/RTO-EN-AVT-185/EN-AVT-185-11.pdf (cit. on p. 191).

[246] R. G. Morgan, A. Paull, R. J. Stalker, P. A. Jacobs, N. A. Morris, I. Stringer, and C. P. Brescianini. *Shock Tunnel Studies of Scramjet Phenomena*. NASA Contractor Report NASA-CR-181721. NASA, Sept. 1988 (cit. on p. 191).

[247] D. J. Mee. *Uncertainty analysis of conditions in the test section of the T4 shock tunnel*. Tech. rep. 1993/04. The University of Queensland, 1993 (cit. on p. 225).

[248] P. G. Hoel. *Introduction to Mathematical Statistics*. John Wiley & Sons, Inc., Jan. 17, 1984. 448 pp. URL: https://www.ebook.de/de/product/3635796/paul_gerhard_hoel_hoel_introduction_to_mathematical_statistics.html (cit. on p. 226).

[249] P. J. Bickel and D. A. Freedman. "Some Asymptotic Theory for the Bootstrap". In: *The Annals of Statistics* 9.6 (Nov. 1981), pp. 1196–1217. DOI: 10.1214/aos/1176345637 (cit. on p. 226).

[250] K. Holmström, N.-H. Quttineh, and M. M. Edvall. "An adaptive radial basis algorithm (ARBF) for expensive black-box mixed-integer constrained global optimization". In: *Optimization and Engineering* 9.4 (Feb. 2008), pp. 311–339. DOI: 10.1007/s11081-008-9037-3 (cit. on p. 237).

[251] M. D. McKay, R. J. Beckman, and W. J. Conover. "A Comparison of Three Methods for Selecting Values of Input Variables in the Analysis of Output from a Computer Code". In: *Technometrics* 21.2 (May 1979), p. 239. DOI: 10.2307/1268522 (cit. on p. 237).

[252] P. Knysh and Y. P. Korkolis. "Identification of the post-necking hardening response of rate- and temperature-dependent metals". In: *International Journal of Solids and Structures* 115-116 (June 2017), pp. 149–160. DOI: 10.1016/j.ijsolstr.2017.03.012 (cit. on p. 238).

9 SCRAMJET N2 EXPERIMENTS

This appendix presents results of the scramjet N2 experiments. Indeed, the experiments with the Mach 12 REST engine were also carried out using itnrogen as the test gas, both with and without hydrogen injection. The goal was to suppress combustion and to separate the effects of the pressure rise due to the injection of hydrogen from the rise due to the combustion of hydrogen. However, the N2 test flow has shown to be not directly comparable to the air one —being faster— so that the normalised pressure traces in air and N2 do not line up with each other. If the test flows were similar, they would be expected to overlap. This is likely due to the difference in ratio of specific heats, speed of sound and density (a difference of about 3 % to 4 % in the gas post primary shock conditions between air and nitrogen). These differences are amplified in the unsteady expansion process in the acceleration tube, and in the nozzle expansion. Additionally, viscous effects in the acceleration tube, may significantly differ for the nitrogen flow condition. For future studies, the author recommends using helium as a fuel-substitute matching the fuel momentum flux ratio, and keeping the test gas as air. The N2 experiment plots are reported here in this appendix for completeness.

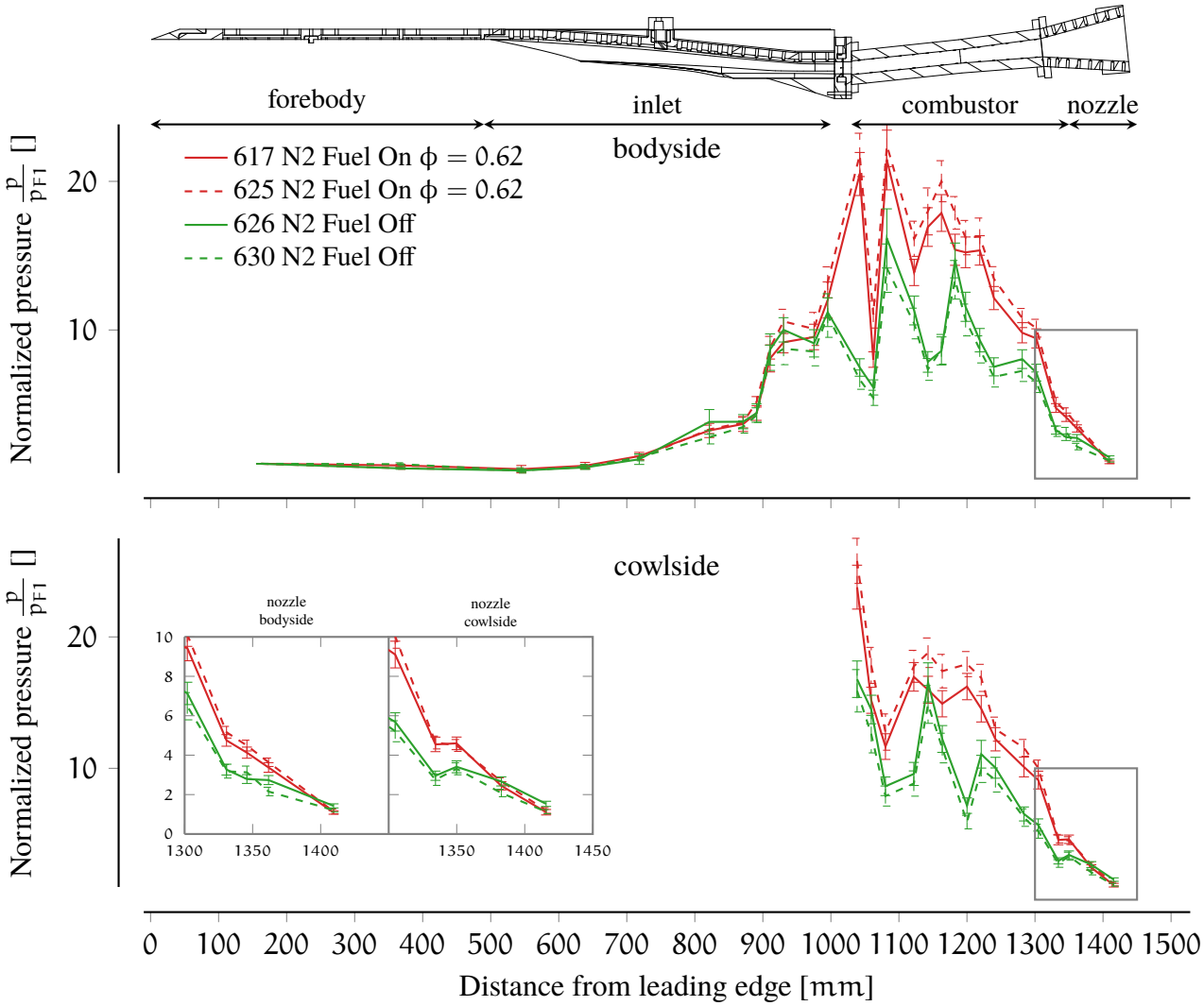

Figure 9.1: *Combustion suppressed experiments*: experimental pressure distributions for combustor-only injection. Data averaged over a test duration of 400 µs. Error bars represent standard deviation from mean.

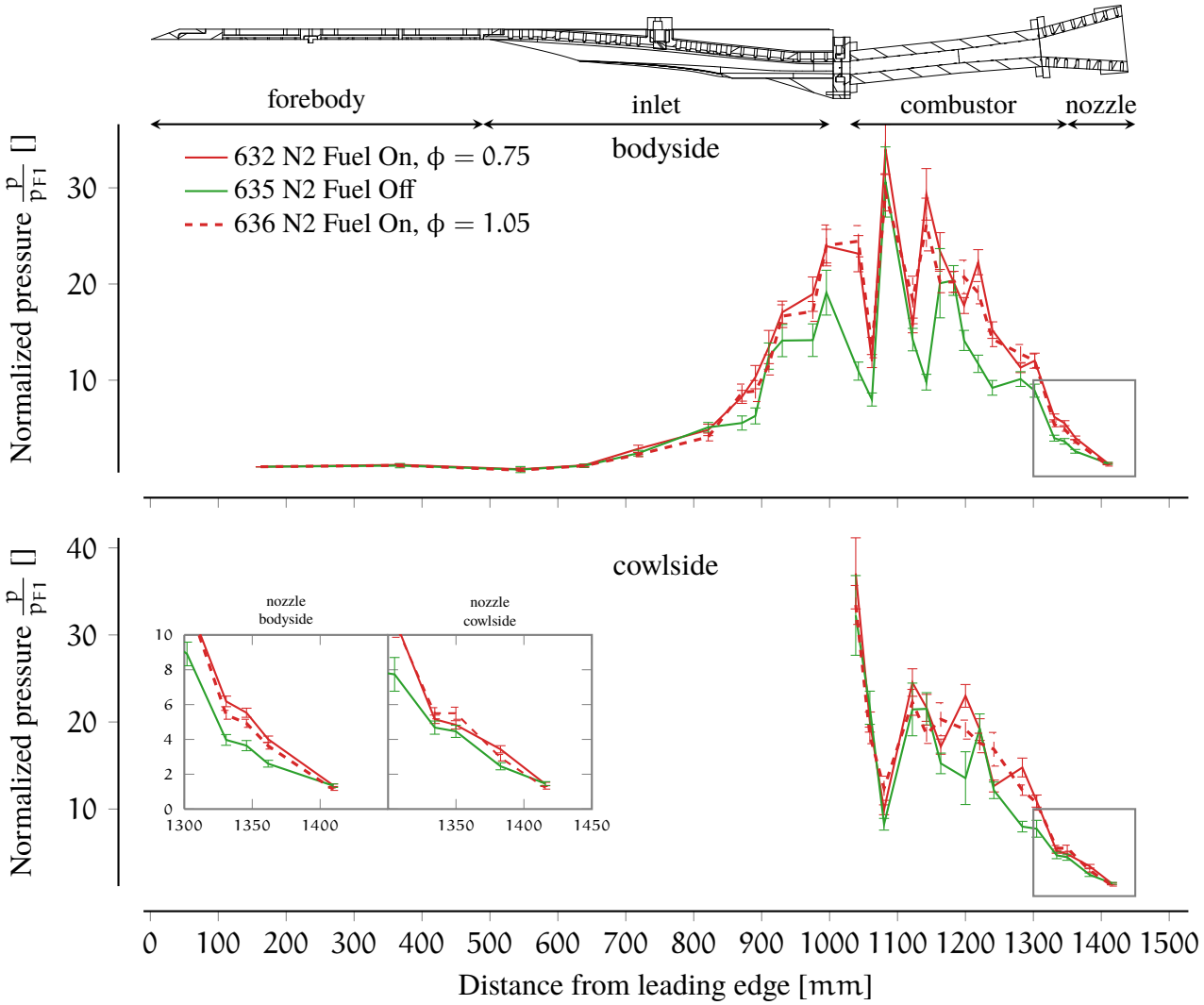

Figure 9.2: *Combustion suppressed experiments*: Experimental pressure distributions for combined injection with a helium acceleration tube. Data averaged over a test time of 500 µs. Error bars represent standard deviation from mean.

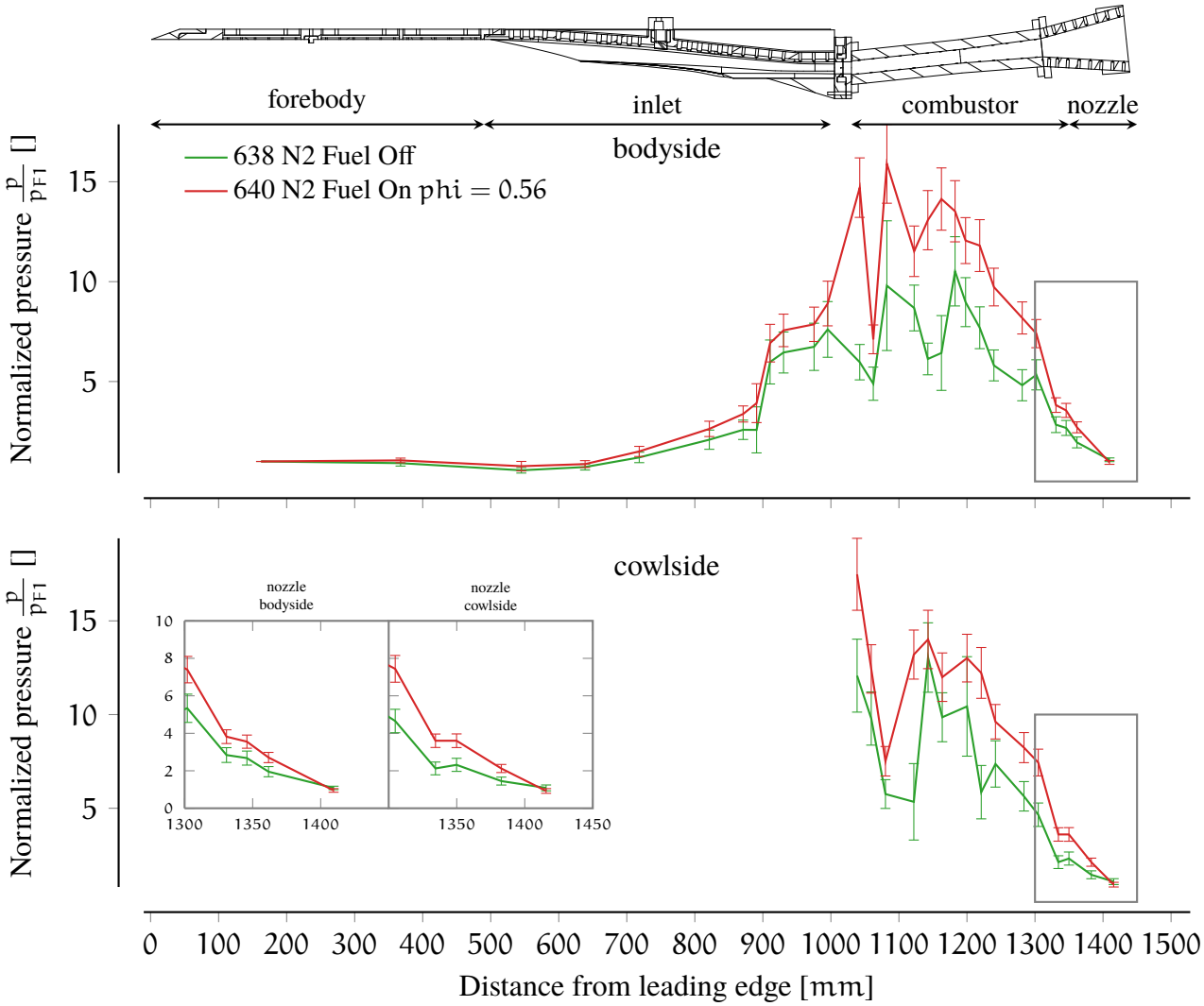

Figure 9.3: *Combustion suppressed experiments*: experimental pressure distributions for combustor-only injection, **pressure-scaled condition** and $\phi = 0.56$. Data averaged over a test time of 450 µs. Error bars represent standard deviation from mean.

10 UNCERTAINTY ANALYSIS

This appendix presents the uncertainty analysis carried out for the experimental measurements of this thesis.

10.1 THEORY

In this section we briefly discuss the theory underlying the uncertainty analysis of this section, which is based on the framework presented by Mee [247].

Any derived quantity F is a function of the fundamental quantities ψ_i:

$$F = f(\psi_1, \psi_2, \ldots, \psi_n) \tag{10.1}$$

A classical approach for the determination of uncertainties ([247]) is based on a first-order Taylor expansion of the function f. Each primary variable ψ_i has an associated uncertainty and is expressed as $\psi_i = \psi_{i,true} + \delta\psi_i$. The effect of the uncertainty $\delta\psi_i$ on the uncertainty of F can be written as:

$$(\delta F)_i = \left(\frac{\partial F}{\partial \psi_i}\right) \delta\psi_i \tag{10.2}$$

The total uncertainty can be reduced to a sum of root mean squares, if the fundamental quantities are uncorrelated and normally distributed:

$$\delta F = \sqrt{(\delta F)_1^2 + (\delta F)_2^2 + \ldots + (\delta F)_n^2} \tag{10.3}$$

Relative uncertainty in each fundamental quantity is simply:

$$X_{\psi_i} = \frac{\delta_{\psi_i}}{\psi_i} \tag{10.4}$$

and the relative uncertainty in the derived quantities is then expressed as:

$$X_F = \frac{\delta F}{F} \tag{10.5}$$

so that the relative uncertainty of the derived quantity can be expressed as:

$$X_F = \sqrt{\left[(X_F)_{\psi_1}\right]^2 + \left[(X_F)_{\psi_2}\right]^2 + \ldots + \left[(X_F)_{\psi_n}\right]^2} \tag{10.6}$$

with $(X_F)_{\psi_i}$ defined as:

$$(X_F)_{\psi_i} = \left(\frac{\partial X_F}{\partial X_{\psi_i}}\right) X_{\psi_i} \tag{10.7}$$

10.2 FLOW CONDITION UNCERTAINTY ESTIMATION

Experimental measurements are insufficient to completely establish the freestream properties, and CFD has been used to estimate the approximate flow condition. Complete and successful flow determination in expansion tubes remains a challenge, especially in the case of a large-scale facility like X3. An open problem, which in some aspects is even more difficult than the transient CFD simulations of expansion tube flows, is the determination of the uncertainties associated with the flow properties. In this section, a simplified bootstrapping approach is proposed, along with simplifying assumptions and associated limitations, and results are presented.

With respect to the theory presented in the previous section, considering the case of the X3 expansion tube, the fundamental quantities are filling pressures and temperatures of the different sections, as well as the rupture pressure of the primary diaphragm. The derived variables are the nozzle exit gas freestream properties.

The approach above described is limited by the following facts:

- The distribution of the primary variables is not known.
- The function F relating these fundamental and derived quantities cannot be expressed analytically.
- The freestream properties vary across the test time.

A solution to the first point is the use of a bootstrapping method that can be adopted without any assumption on the distribution of the random input variables (excluding some pathological cases) [248, 249]. With this method, rather than relying on the calculation of the partial derivative of the function f, the input variables are randomly perturbed, observing the resulting variation in the derived quantities. If a significant number of evaluations of the function f are done, then the error in the estimation of the variability is proportional to $\frac{1}{\sqrt{2*(n-1)}}$.

Concerning the second bullet point, CFD simulations, treated as "black box" functions, would allow estimation the $\frac{\partial F}{\partial \psi_i}$ via numerical differentiation. However, the computational cost of such an approach is well outside the available capabilities.

An alternative model for the function f is the analytical approach presented in Sections 2.9.1 and 3.3.1, previously used to estimate the required filling pressures to achieve the desired nozzle inlet inflow. As previously discussed, the model is fundamentally limited in the fact that it does not take into account many effects experimentally observed, such as thick boundary layers, shock speed attenuation, radially non-uniform inflow and time-variable steady pressure gradient. The model can be augmented, as has been done in other codes [121], with empirical loss factors (to reproduce shock speed attenuation) and expansion factors (to reproduce the effective amount of expansion that occurs into the nozzle), however, it fails to give an adequate representation of the experimental quantities.

Notwithstanding this, the analytical model is the only way to effectively estimate freestream property uncertainties. It is postulated that, although the mean value is not considered correct, the calculated uncertainties will nevertheless be a good estimated of uncertainties of CFD-obtained freestream properties. In other words, the analytical model is selected as the black-box function to estimate these uncertainties around the mean flow properties that have been calculated via CFD simulations per Section 5.8.2 and Table 5.3. The approach for the uncertainties' calculation is similar to the one adopted by Sancho Ponce [119].

The first two bullet points were related to the experimental shot-to-shot variability. However, the test time variation needs to be included in the uncertainty estimation. To do so, it is simply postulated that the test-time variation is *independent* of the shot-to-shot variation, estimated via the aforementioned bootstrapping method. It is a reasonable assumption, considering the steady pressure gradient is mainly due to the facility configuration, and does not relate to the filling parameters, as observed across a diverse range of flow condition in Section 5.8.2. The total variability can be then expressed as the square root of the single squared deviation as:

$$\delta F = \sqrt{\delta^2_{\text{shot}} + \delta^2_{\text{time}}} \tag{10.8}$$

where δ^2_{shot} is the uncertainty estimated via the bootstrapping method of function f simulated using the analytical model, and δ^2_{time} is the test-time variation estimated in the CFD simulations.

The uncertainties in the primary variables of the facility are presented in Table 10.1. The pressure filling errors are significantly higher than the pressure gauges accuracy, so that the gauge uncertainties can be neglected. The temperature is assumed to be a uniform distribution, representing the fact that experiments took place at different times of the day and across several months spanning all seasons (although considering this, it is noted that the temperature is relatively stable in the laboratory). The rupture pressure is assumed to be a normal distribution with significant variability.

Two analytical models, differing in the values of loss factors, have been prepared, in which the loss factors are tuned to match as closely as possible the flow properties of Table 5.3. Each model was run 5000 times, and then, as safety margin, for each derived property, the largest uncertainty was selected. Table 10.2 includes the estimates, indicated as δ_{shot}. The temporal variation column is calculated from

Table 10.1: CONDITION x3s506 sources of uncertainties and relative random distribution.

	value	relative standard deviation	distribution
p_{driver}	49.0 kPa	1.0 %	normal
T_{driver}	298 K	1.6 %	uniform
p_4	17.5 MPa	5.0 %	normal
p_1	22.7 kPa	10 %	normal
T_1	298 K	1.6 %	uniform
p_5	22.7 kPa	15 %	normal
T_5	298 K	1.6 %	uniform

Table 10.2: CONDITION x3s506 Freestream flow properties: CFD and uncertainties. δ_{time} is the absolute standard deviation across the test time, δ_{shot} the relative shot-to-shot uncertainty calculated in Section 10.2, and $\delta_{total} = \sqrt{\delta_{time}^2 + (value \cdot \delta_{shot}/100)^2}$. T is temperature, p pressure, v velocity, M Mach number, P_p Pitot pressure,H_0 nominal total enthalpy, P_0 nominal total pressure, q nominal dynamic pressure, h is equivalent flight altitude.

	value	δ_{time}	δ_{shot}[%]	δ_{total}	unit
T	308	21.0	3.9	24	K
p	607	123.0	10.0	138	Pa
v	3911	129.0	1.6	143	$m\,s^{-1}$
M	11.1	0.7	2.1	0.7	
P_p	95 610	7020.0	6.3	9280	Pa
H_0	6.0				$MJ\,kg^{-1}$
P_0	223.3				MPa
q	52.7				kPa
h	34.6				km

the total variation in the test time on the centreline during the CFD simulations and the experimental measurements.

It is noted that there is non-negligible uncertainty in static and dynamic pressure, particularly due to the transient pressure rise across the test time. However, as outlined in Chapter 6, a quasi-steady normalisation routine has been adopted, so that the error could be accounted for.

As a conclusive note, the author is well-aware that the approach is essentially limited by the underlying analytical model, and more detailed uncertainty quantifications for the expansion would require a significant advance in the modelling techniques at his disposal.

10.3 PCB PRESSURE MEASUREMENTS

Nozzle inlet and nozzle exit rake pressure measurements were carried out with pressure sensors and the manufacturer sensitivity was adopted, as the sensors were brand-new and used for the first time for the experiments of this thesis. According to the specification, the nominal uncertainty is 1 %.

10.4 SCRAMJET WALL PRESSURE MEASUREMENTS

The scramjet wall pressure measurements were carried out with Kulite sensors with maximum pressure ranges of 10 psi, 25 psi, 50 psi, 100 psi and 500 psi. These sensors are absolute pressure sensors and are calibrated in-situ, with reference to an absolute, known atmospheric and vacuum pressures. Intermediate pressures were also recorded and the excellent linearity of the sensor across its range was confirmed. Atmospheric pressure was measured by reference to a nearby weather station (which has been assumed to be high-accuracy), and the vacuum pressure by a Varian Gauge CDG500-1 torr. Ultimate vacuum pressure in the X3 test section was in the range 2 Pa to 4 Pa. The sensitivity is simply calculated as:

$$S_K = \frac{V_{atm} - V_{vac}}{P_{atm} - P_{vac}}, \tag{10.9}$$

with V indicating measured raw voltage and P pressure. In this case, it is possible to directly use the perturbation method, as the expression of the sensitivity is known:

$$\delta F = \sqrt{\left(\frac{\partial F_1}{\partial \psi_1}\delta\psi_1\right)^2 + \left(\frac{\partial F_2}{\partial \psi_2}\delta\psi_2\right)^2 + \ldots + \left(\frac{\partial F_n}{\partial \psi_n}\delta\psi_n\right)^2} \tag{10.10}$$

Kulite sensors exhibit an offset, i.e at 0 Pa their voltage is non- zero. At very low-pressures (forebody pressure measurements), the offset needs to be accounted for in the pressure estimate. However, its impact on the pressure uncertainty is negligible and therefore it has not been included. The uncertainties relative to the fundamental quantities are shown in Table 10.3.

Table 10.3: Relative uncertainties of the measured quantities for Kulite pressure sensor calibrations [57].

Quantity	Relative uncertainty X_F, %	
Voltage measurement at atmospheric pressure	$X_{V_{atm}}$	±1.%
Voltage measurement at vacuum	$X_{V_{vac}}$	±1.%
Atmospheric pressure from UQ Weather *	$X_{p_{atm}}$	±0.5%
Vacuum pressure reading	$X_{p_{vac}}$	±2.%

* http://ww2.gpem.uq.edu.au/UQweather/

The largest uncertainty obtained across the whole set of probes was 3.51 %, and as a conservative measures, it was assumed to apply for to the Kulite sensors.

10.5 HEAT TRANSFER MEASUREMENT UNCERTAINTIES

An in-depth analysis of the thin-film heat transfer gauge uncertainty analysis is reported by Wise and Smart [24]. A table summarising the discussion is shown in Table 10.4 with the calculated uncertainty. The total uncertainty is evaluated using the classic perturbation method.

Table 10.4: uncertainties of measured quantities for heat transfer gauges. Taken and modified from [87].

Source	Forebody
Nickel film	—
SiO2 film	±5.0%
Quartz thermal properties	±1.5%
Calibration	±2.5%
Voltage reading	±0.5%
Total uncertainty	±5.8%

10.6 FUEL CALIBRATION

The fuel calibration was carried out in accordance with the approach used by Razzaqi et al. [224], as the setup was essentially the same, along with use of the same type of gauges. In the case of hydrogen fuel, it is possible to directly estimate uncertainties using the perturbation method, as an analytical formula for the discharge coefficient can be derived as shown in Section 6.3.1. Relative uncertainties of the primary variables are presented in Table 10.5. The reader is reminded that the change in temperature in the plenum was assumed to be negligible, and the initial temperature of the Ludwieg tube was assumed to be equal to the measured ambient temperature. Prior to these experiments, the Ludwieg tube volume was calculated by measuring the change in pressure of the gas contained in the tube after it was released into a reference volume. Plenum and Ludwieg tube pressures were measured using Kulite pressure sensors, thus the previously calculated uncertainty was adopted (3.51 %). All the other required properties have an assumed uncertainty as per [57, 224]. The injector area uncertainty is relatively high due to the high erosion levels that the injectors underwent during high total pressure experiments, due to the correspondingly high hydrogen gas pressures that were used.

Following from the parameters of Table 10.5, with the definition of discharge coefficient carried out in Section 6.3.2, calculations show that the uncertainty for the discharge coefficient is 8.4 % and for the equivalence ratio 18.2 %.

Table 10.5: Relative uncertainties of measured quantities related to fuelling conditions. Modified from [57].

Quantity	Relative uncertainty	X_F [%]
Plenum pressure	p_{plenum}	3.5
Plenum temperature	T_{plenum}	1.0
Initial Ludwieg tube pressure	$p_{LT,i}$	3.5
Final Ludwieg tube pressure	$p_{LT,f}$	3.5
Initial Ludwieg tube temperature	$T_{LT,i}$	1.0
Ludwieg tube volume	V_{LT}	0.4
Injector area	A	2.0

11 TESTS SUMMARY

In this appendix, the shots discussed in this thesis are enumerated. Each shot configuration is presented. Each table groups a set of experiments, although there are overlapping experiments used in multiple discussions.

Res.		X3 reservoir
CT		X3 compression tube
SD		X3 secondary driver
ST		X3 shock tube
AT		X3 acceleration tube
p_{fill}	MPa or kPa	Static pressure of gas within reservoir, compression tube, secondary driver, shock tube and acceleration tube
Ar	%	Volume fraction of argon in primary driver gas
He	%	Volume fraction of helium in primary driver gas
Test gas	Air or N2	Gas within shock tube
SD gas	-	Gas within secondary driver
AT Air	%	Volume fraction of air in Acceleration tube
AT He	%	Volume fraction of helium in Acceleration tube
Diaph.	mm	Primary diaphragm thickness. Diaphragm are scored at 0.3 mm
Or.plate	mm	Selected orifice plate
Short ST	-	Selected shock tube configuration for the test. Short : diaphragm at secondary station. Long: diaphragm at tertiary station
Long ST	-	
Cone head	-	Selected impact pressure probe type
Flat head	-	
Swept ramp trip	-	Selected boundary layer trip
Diamond trip	-	
$p_{Ludwieg}$	kPa	Ludwieg tube fill pressure
inlet	%	Inlet fuel split
combustor	%	Combustor fuel split
T_{fuel}	K	Fuel temperature

Table 11.1: Nozzle inlet Pitot pressure measurements. Tunnel operating conditions.

	Res.	CT			SD		ST				AT			Facility	
Shot	p_{fill}	p_{fill}	Ar	He	p_{fill}	SD	p_{fill}	Test	Short	Long	p_{fill}	Air	He	Diaph.	Or. plate
-	MPa	kPa	%	%	kPa	gas	kPa	gas	ST	ST	kPa	%	%	mm	mm
573	6.7	49.0	100	-	-	-	22.7	Air	x		58.0	100	-	3mm	-
574	6.7	49.0	100	-	-	-	22.7	Air	x		58.0	100	-	3mm	-
575	6.7	49.0	100	-	-	-	22.7	Air		x	58.0	100	-	3mm	-
576	6.7	49.0	100	-	-	-	22.7	Air		x	58.0	100	-	3mm	-
577	6.7	49.0	100	-	100.0	He	22.7	Air	-	-	58.0	100	-	3mm	-
578	6.7	49.0	100	-	100.0	He	22.7	Air	-	-	58.0	100	-	3mm	-
579	6.7	49.0	100	-	100.0	He	22.7	Air	-	-	58.0	100	-	3mm	-
580	6.7	49.0	100	-	100.0	He	22.7	Air	-	-	58.0	100	-	3mm	-
581	6.7	49.0	100	-	200.0	He	22.7	Air	-	-	58.0	100	-	3mm	-
582	6.7	49.0	40	60	-	-	45.5	Air		x	118.0	100	-	3mm	164.7
583	6.7	49.0	40	60	-	-	45.5	Air		x	118.0	100	-	3mm	164.7
584	6.7	49.0	40	60	100.0	He	45.5	Air	-	-	118.0	100	-	3mm	164.7
585	6.7	49.0	40	60	100.0	He	45.5	Air	-	-	118.0	100	-	3mm	164.7

Table 11.2: Nozzle exit Pitot pressure experiments. Tunnel operating conditions.

	Res.	CT			ST		AT			Facility		Probe type	
Shot	p_{fill}	p_{fill}	Ar	He	p_{fill}	Test	p_{fill}	Air	He	Diaph.	Or. plate	Cone	Flat
-	MPa	kPa	%	%	kPa	gas	kPa	%	%	mm	mm	head	head
586	6.7	49.0	100	-	22.7	Air	58.0	100	-	3mm	-	x	
587	6.7	49.0	100	-	22.7	Air	58.0	100	-	3mm	-	x	
588	6.7	49.0	40	60	45.5	Air	118.0	100	-	3mm	164.7	x	
589	6.7	49.0	40	60	45.5	Air	118.0	100	-	3mm	164.7	x	
590	6.7	49.0	100	-	22.7	Air	58.0	100	-	3mm	-		x
591	6.7	49.0	100	-	22.7	Air	58.0	100	-	3mm	-		x
592	6.7	49.0	40	60	45.5	Air	118.0	100	-	3mm	164.7		x
593	6.7	49.0	40	60	45.5	Air	118.0	100	-	3mm	164.7		x
594	6.7	49.0	100	-	22.7	Air	58.0	100	-	3mm	-		x
595	6.7	49.0	100	-	22.7	Air	58.0	100	-	3mm	-		x
601	6.7	49.0	100	-	22.7	Air	58.0	100	-	3mm	-		x
602	6.7	49.0	100	-	22.7	Air	58.0	100	-	3mm	-		x

Table 11.3: 30° wedge shock angle schlieren experiments. Tunnel operating conditions.

	Res.	CT			ST		AT			Facility	
Shot	p_{fill}	p_{fill}	Ar	He	p_{fill}	Test	p_{fill}	Air	He	Diaph.	Or. plate
-	MPa	kPa	%	%	kPa	gas	kPa	%	%	mm	mm
602	6.7	49.0	100	-	22.7	Air	58.0	100	-	3mm	-
603	6.7	49.0	100	-	22.7	Air	58.0	100	-	3mm	-
604	6.7	49.0	100	-	22.7	Air	58.0	100	-	3mm	-
605	6.7	49.0	100	-	22.7	Air	58.0	100	-	3mm	-

Table 11.4: Boundary layer transition experiments. Tunnel operating conditions and selected boundary layer trip.

	Res.	CT			ST		AT			Facility		Trip	
Shot	p_{fill}	p_{fill}	Ar	He	p_{fill}	Test	p_{fill}	Air	He	Diaph.	Or. plate	Swept	7 mm diamond
-	MPa	kPa	%	%	kPa	gas	kPa	%	%	mm	mm	ramp	trip
606	6.7	49.0	100	-	22.7	Air	58.0	100	-	3mm	-	x	
607	6.7	49.0	100	-	22.7	Air	58.0	100	-	3mm	-	x	
608	6.7	49.0	100	-	22.7	Air	58.0	100	-	3mm	-	x	
609	6.7	49.0	100	-	22.7	Air	58.0	100	-	3mm	-	x	
610	6.7	49.0	100	-	22.7	Air	58.0	100	-	3mm	-	x	
611	6.7	49.0	100	-	22.7	Air	58.0	100	-	3mm	-	x	
612	6.7	49.0	100	-	22.7	Air	58.0	100	-	3mm	-	x	
613	6.7	49.0	100	-	22.7	Air	58.0	100	-	3mm	-	x	
614	6.7	49.0	100	-	22.7	Air	58.0	100	-	3mm	-		x
615	6.7	49.0	100	-	22.7	Air	58.0	100	-	3mm	-		x
616	6.7	49.0	100	-	22.7	Air	58.0	100	-	3mm	-		x
617	6.7	49.0	100	-	22.7	N2	58.0	100	-	3mm	-		x
618	6.7	49.0	100	-	22.7	N2	58.0	100	-	3mm	-		x

Table 11.5: Scramjet experiments.Tunnel operating conditions and fuelling parameters

	Res.	CT			ST		AT			Facility		Fuel condition			
Shot	p_{fill}	p_{fill}	Ar	He	p_{fill}	Test	p_{fill}	Air	He	Diaph.	Or. plate	$p_{Ludwieg}$	inlet	comb	T_{fuel}
-	MPa	kPa	%	%	kPa	gas	kPa	%	%	mm	mm	kPa	%	%	K
610	6.7	49.0	100	-	22.7	Air	58.0	100	-	3mm	-	3200.0	31	69	297.65
611	6.7	49.0	100	-	22.7	Air	58.0	Air	-	3mm	-	3200.0	25	75	297.45
612	6.7	49.0	100	-	22.7	Air	58.0	Air	-	3mm	-	2474.0	27	73	296.35
613	6.7	49.0	100	-	22.7	Air	58.0	Air	-	3mm	-	-	-	-	-
614	6.7	49.0	100	-	22.7	Air	58.0	Air	-	3mm	-	3200.0	25	75	297.05
615	6.7	49.0	100	-	22.7	Air	58.0	Air	-	3mm	-	2450.0	20	80	296.55
616	6.7	49.0	100	-	22.7	Air	58.0	Air	-	3mm	-	2651.0	0	100	296.71
617	6.7	49.0	100	-	21.9	N2	58.0	Air	-	3mm	-	2640.0	0	100	296.65
624	6.7	49.0	100	-	22.7	Air	58.0	Air	-	3mm	-	2649.0	0	100	296.45
625	6.7	49.0	100	-	21.9	N2	58.0	Air	-	3mm	-	2472.0	0	100	296.15
626	6.7	49.0	100	-	21.9	N2	58.0	Air	-	3mm	-	-	-	-	-
627	6.7	49.0	100	-	22.7	Air	319.0	0.63	99.37	3mm	-	2468.0	24	76	296.05
629	6.7	49.0	100	-	22.7	Air	58.0	Air	-	3mm	-	-	-	-	-
630	6.7	49.0	100	-	21.9	N2	58.0	Air	-	3mm	-	-	-	-	-
631	6.7	49.0	100	-	22.7	Air	309.2	0.97	99.03	3mm	-	2498.0	24	76	295.65
632	6.7	49.0	100	-	21.9	N2	309.4	0.93	99.07	3mm	-	2649.0	23	73	296.05
633	6.7	49.0	100	-	22.7	Air	311.4	0.8	99.2	3mm	-	-	-	-	-
634	6.7	49.0	100	-	22.7	Air	309.2	0.65	99.35	3mm	-	3200.0	24	76	296.15
635	6.7	49.0	100	-	21.9	N2	313.1	0.74	99.26	3mm	-	-	-	-	-
636	6.7	49.0	100	-	21.9	N2	312.6	0.82	99.18	3mm	-	3200.0	25	75	296.95
637	6.7	49.0	40	60	45.5	Air	118.0	100	-	3mm	164.7	-	-	-	-
638	6.7	49.0	40	60	44.8	N2	118.0	100	-	3mm	164.7	-	-	-	-
639	6.7	49.0	40	60	45.5	Air	118.0	100	-	3mm	164.7	4025.0	0	100	295.35
640	6.7	49.0	40	60	44.8	N2	118.0	100	-	3mm	164.7	4025.0	0	100	296.2

12 OPTIMISATION ALGORITHMS

12.1 LEE-WISWALL OPTIMISATION ALGORITHM

The algorithm selected for the optimisation of the Mach 12 nozzle is a parallel version of the classic Nelder-Mead, due to Lee and Wiswall [192]. Below, a description of the algorithm is presented.

The goal is to find the minimum of a function $f(\mathbf{x})$ where $\mathbf{x} \in \mathbb{R}^n$. Let's assume a degree of parallelisation $\mathbf{p}$ (that does not necessarily correspond to the number of processors available). We assume that $n >= p$.

1. Let's create an initial simplex of size $n+1$ evaluated at the points $\mathbf{x_0}, \mathbf{x_1}, \ldots, \mathbf{x_n}$. Sort all the points of the simplex from best to worst, and without loss of generality we can write:$f(\mathbf{x_1}) \leqslant f(\mathbf{x_2}) \leqslant \cdots \leqslant f(\mathbf{x_n}+\mathbf{1}))$.
2. Calculate the centroid of the best $n-p$ points $\mathbf{x_0}, \mathbf{x_1}, \ldots, \mathbf{x_{n-p}}$ defined as:

$$\mathbf{x_c} = \frac{1}{n}\sum_{j=0}^{n-p} \mathbf{x_j}$$

   The worse $\mathbf{p}$ points $\mathbf{x_{n-p+1}}, \mathbf{x_{n-p+2}}, \ldots, \mathbf{x_n}$ are reflected: $\mathbf{x_j^R} = \mathbf{x_c} + \alpha(\mathbf{x_c} - \mathbf{x_j})$, where $\alpha \geqslant 0$ The p reflected points are then evaluated in parallel. If $p = 1$ the step is identical to the classical Nelder-Mead approach.
3. For each processor, i.e. for each $j = n-p+1, n-p+2, \ldots, n$ a new point is returned as follows. Each processor follows a routine that is independent of the other, but equivalent to what is done in the classical Nelder-Mead.

Case 1 if $f(\mathbf{x_j^R}) \leqslant f(\mathbf{x_0})$ then we continue in the same direction by calculating the "expansion point" $\mathbf{x_j^E} = \mathbf{x_j^R} + \alpha(\mathbf{x_j^R} - \mathbf{x_c})$. If $f(\mathbf{x_j^E}) \leqslant f(\mathbf{x_0})$ the processor return the point x_j^E, otherwise it returns x_j^R.

Case 2 if $f(\mathbf{x_j^R}) \not\leqslant f(\mathbf{x_0})$ but $f)\mathbf{x_j^R}) \leqslant f(\mathbf{x_{j-1}})$ the processor returns x_j^R. Note that when a processor falls into case 2, and any of the other falls into case 1 or case 3, it will sit idle to wait for the other processors to finish.

Case 3 if $f(\mathbf{x_j^R}) \not\leqslant f(\mathbf{x_{j-1}})$. If $f(\mathbf{x_j^R}) \leqslant f(\mathbf{x_j})$ we define $\bar{\mathbf{x}_j} = \mathbf{x_j^R}$, otherwise $\bar{\mathbf{x}_j} = \mathbf{x_j}$. We then calculate the contraction point $\mathbf{x_j^C} = \beta * (\mathbf{x_c} + \bar{\mathbf{x}_j} = \mathbf{x_j^R})$ the processors calculate the "contraction point" $\mathbf{x_j^C} = \mathbf{x_j^R} + \alpha(\mathbf{x_j^R} - \mathbf{x_c})$. If $f(\mathbf{x_j^C}) \leqslant f(\bar{\mathbf{x}_j})$ then the processor returns $\mathbf{x_j^C}$ otherwise it returns $\bar{\mathbf{x}_j}$.

4. The p processors return p points x_j^*. If for any processor, Case 1 or Case 2 applies, or if Case 3 applied and $x_j^* = x_j^C$, then the points $x_0, x_1, \ldots, x_{n-p}, x_{n-p+1}^*, x_{n-p+2}^*, \ldots, x_n^*$ define a new simplex, which is an improvement over the one at Step 2. Otherwise, if none of the conditions above apply, the entire simplex shrinks towards the best point x_0, giving the new simplex as $x_0, (\tau x_0 + (1-\tau) * x_1), (\tau x_0 + (1-\tau) * x_2), \ldots, (\tau x_0 + (1-\tau) * x_{n-p+1}^*), \ldots, (\tau x_0 + (1-\tau) * x_n^*)$, with $0 < \tau < 1$ a chosen parameter. Once the new simplex is formed and sorted by its objective function values, the algorithm, if not converged by an opportune criterion, returns to step 2 and iterates until convergence.

12.2 KNYSH-KORKOLIS ALGORITHM

The algorithm proposed by Knysh and Korkolis [217] is described below. It is specifically developed and suited for the optimisation of expensive black-box functions, and adopted for the optimisation of the tuning parameters of the L1D facility simulations.

This algorithm is a modified CORS algorithm (Constrained Optimisation using Response Surfaces), originally developed by Regis and Shoemaker [216]. A cubic radial basis function (RBF) is used as originally proposed by Holmström et al. [250]. Considering that the goal is to optimise an objective function $f(x)$, where $x \in \mathbb{R}^d$, the response surface function (RSF) $s_n(x)$, estimated through n sampled points, is defined as:

$$s_n(x) = \sum_{i=1}^{n} \lambda_i \phi\left(\|\mathbb{T}(x - x_i\|)\right) + b^T x + a \tag{12.1}$$

where $\phi(r) = r^3$ is a cubic function, λ_i, b, a are coefficients that are determined by fitting all points x_i where the function has been evaluated, $\|x\|$ is the euclidean norm, and $\mathbb{T}$ is a space scaling operator described below. The RBF as defined is then a good approximation of the objective function and it is able to estimate its value at arbitrary points. Then, rather than looking for the minimum of the objective function, the minimum of the surrogate RSF is sought. The algorithm iterates with the newly found minimum, with increasing accuracy, until the global minimum is found.

In more detail, the procedure can be divided in four steps:

1 INITIAL RESCALING OF THE VARIABLES All the variables are normalised in the range $[0, 1]$. Initial sampling of the variable space: a Latin hypercube [251] is built in the d-dimensional space to initialise the RBF without the need of a uniform grid, which would be too expensive to evaluate.

2 FUNCTION VALUES RESCALING If extremely high values for the objective functions are found, to avoid decreasing the quality of the RBF approximating the objective function, only a portion

of the samples with the lowest values are kept, while all the other samples are discarded. The rescaled function is defined as follows:

$$f* = \begin{cases} \frac{f}{t}, & \text{if } f < t \\ 1, & \text{if } f \geqslant t \end{cases} \tag{12.2}$$

where t is a threshold value which is set by the user.

3 SPACE RESCALING If a minimum is located at the bottom of a "valley", the fit response-surface might not be a good description, and a linear operator $\mathbb{T}$ is introduced in Eq. (12.1). After the initial $s_n(\mathbf{x})$ is constructed assuming $\mathbb{T} = \mathbb{I}$ (identity operator), the obtained $s_n(\mathbf{x})$ is evaluated at a large number of points. Then, a certain fraction of the points is kept, according to their RBF values. Then if C is the covariance matrix of the selected points, and α_i, m_i are respectively the eigenvalues and eigenvectors of the matrix C, the scaling operator is constructed as:

$$\mathbb{T} = \begin{pmatrix} \frac{m_1}{\sqrt{\alpha_1}} \\ \frac{m_2}{\sqrt{\alpha_2}} \\ \vdots \\ \frac{m_d}{\sqrt{\alpha_2}} \end{pmatrix} \tag{12.3}$$

Finally, $s_n(\mathbf{x})$ is reconstructed by reapplying Eq. (12.1)

4 SUBSEQUENT ITERATIONS The search for the objective function minimum is carried out with a modified CORS algorithm. At every iteration, the optimum of the current $s_n(\mathbf{x})$ is sought in the parameter space, with the constraint that any solution cannot be inside any ball of radius r around any of the already existing points $\mathbf{x}_i$. r is defined such that it decreases in every iteration:

$$r = \left(\rho_0 \left(\frac{m-i}{m-1} \right)^p \frac{1}{\nu_1 (n+i-1)} \right)^{\frac{1}{d}} \tag{12.4}$$

with ρ_0 an initial ball density, and p the rate of decay, m is the total number of iterations, i the current number of iteration, and ν_1 the volume of a unitary d-dimensional sphere (see [217] for further details). The newly discovered "minimum" of $s_n(\mathbf{x})$ is added to the set of $\mathbf{x}_i$ and then $s_n(\mathbf{x})$ is re-evaluated.

The process is iterated for m iterations (excluding the first initial variable rescaling). The algorithm has been validated for a variety of test cases and used to optimise the response of FE (finite-element) models [252].

The most significant advantage is that the algorithm is easily parallelisable up to hundreds of processors, and its accuracy and rate of convergence are proportional to the number of parallel function evaluations.

13 MACH 12 NOZZLE TECHNICAL DRAWINGS

In the following section all the technical drawings relating to the Mach 12 nozzle and associated instrumentation have been included.

REVISION HISTORY			
REV	DESCRIPTION	DATE	APPROVED
0	Nozzle__collar update	5/07/2018 4:33:16 PM	

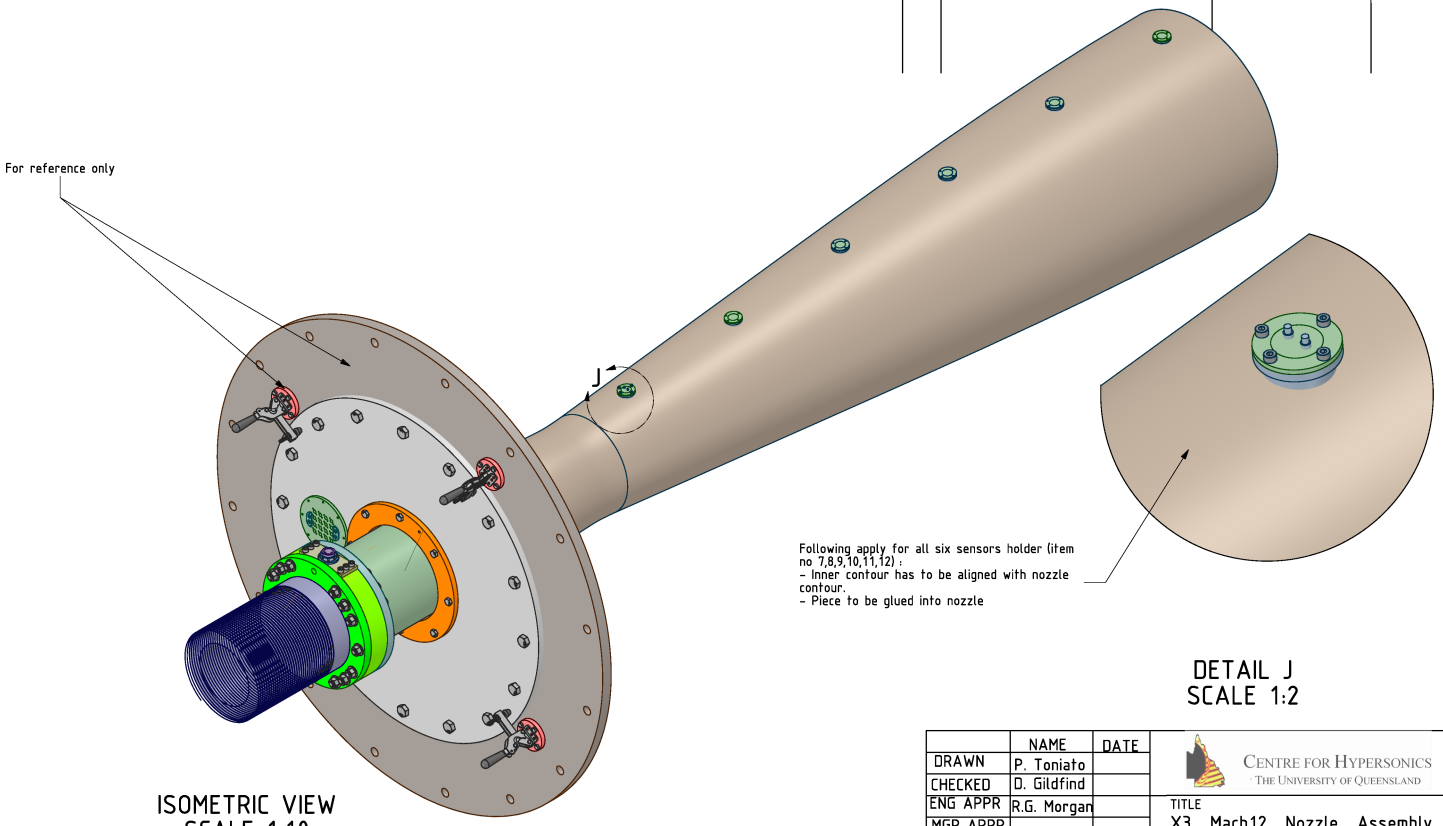

ISOMETRIC VIEW
SCALE 1:10

DETAIL J
SCALE 1:2

	NAME	DATE
DRAWN	P. Toniato	
CHECKED	D. Gildfind	
ENG APPR	R.G. Morgan	
MGR APPR		

UNLESS OTHERWISE SPECIFIED
DIMENSIONS ARE IN MILLIMETERS
ANGULAR TOLERANCE ±1.0°
DIMENSIONAL TOLERANCE
X: ± 1mm, X.X: ± 0.1mm, X.XX: ± 0.05mm

CENTRE FOR HYPERSONICS
THE UNIVERSITY OF QUEENSLAND

TITLE
X3__Mach12__Nozzle__Assembly

SIZE	DWG NO	REV
A3	X3__M12__Nozzle__0000__2	0

Filename: X3__M12__Nozzle__0000__2.pdf

SCALE 1:10	WEIGHT: n/a	SHEET 1

REVISION HISTORY			
REV	DESCRIPTION	DATE	APPROVED
0	Nozzle__collar update	5/07/2018 3:44:57 PM	

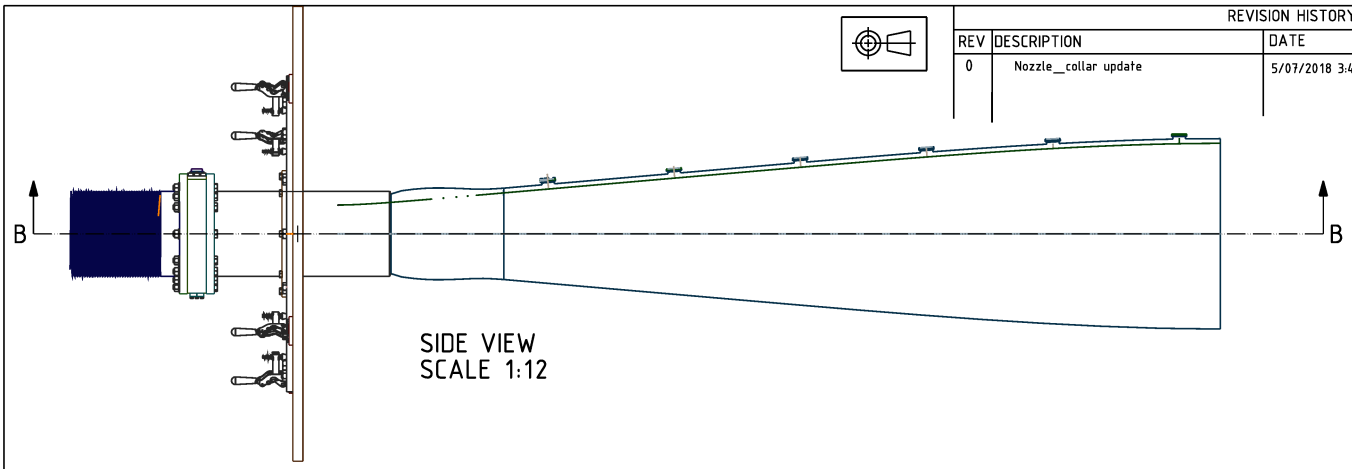

SIDE VIEW
SCALE 1:12

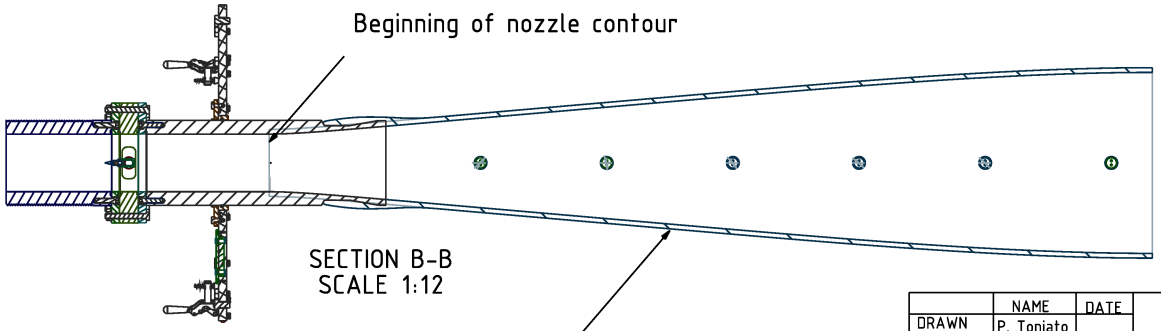

SECTION B-B
SCALE 1:12

Nozzle to be made externally by winding around nozzle collar

	NAME	DATE
DRAWN	P. Toniato	
CHECKED	D. Gildfind	
ENG APPR	R.G. Morgan	
MGR APPR		

UNLESS OTHERWISE SPECIFIED
DIMENSIONS ARE IN MILLIMETERS
ANGULAR TOLERANCE ±1.0°
DIMENSIONAL TOLERANCE
X: ± 1mm, X.X: ± 0.1mm, X.XX: ± 0.05mm

TITLE
X3__Mach12__Nozzle__Assembly

SIZE	DWG NO	REV
A3	X3__M12__Nozzle__0000__2	0

Filename: X3__M12__Nozzle__0000__2.pdf

SCALE 1:12	WEIGHT: n/a	SHEET 2

REVISION HISTORY			
REV	DESCRIPTION	DATE	APPROVED
2	Nozzle__collar Nozzle__collar update	28/07/2017 3:19:36 PM	

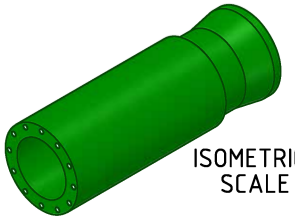

ISOMETRIC VIEW
SCALE 1:10

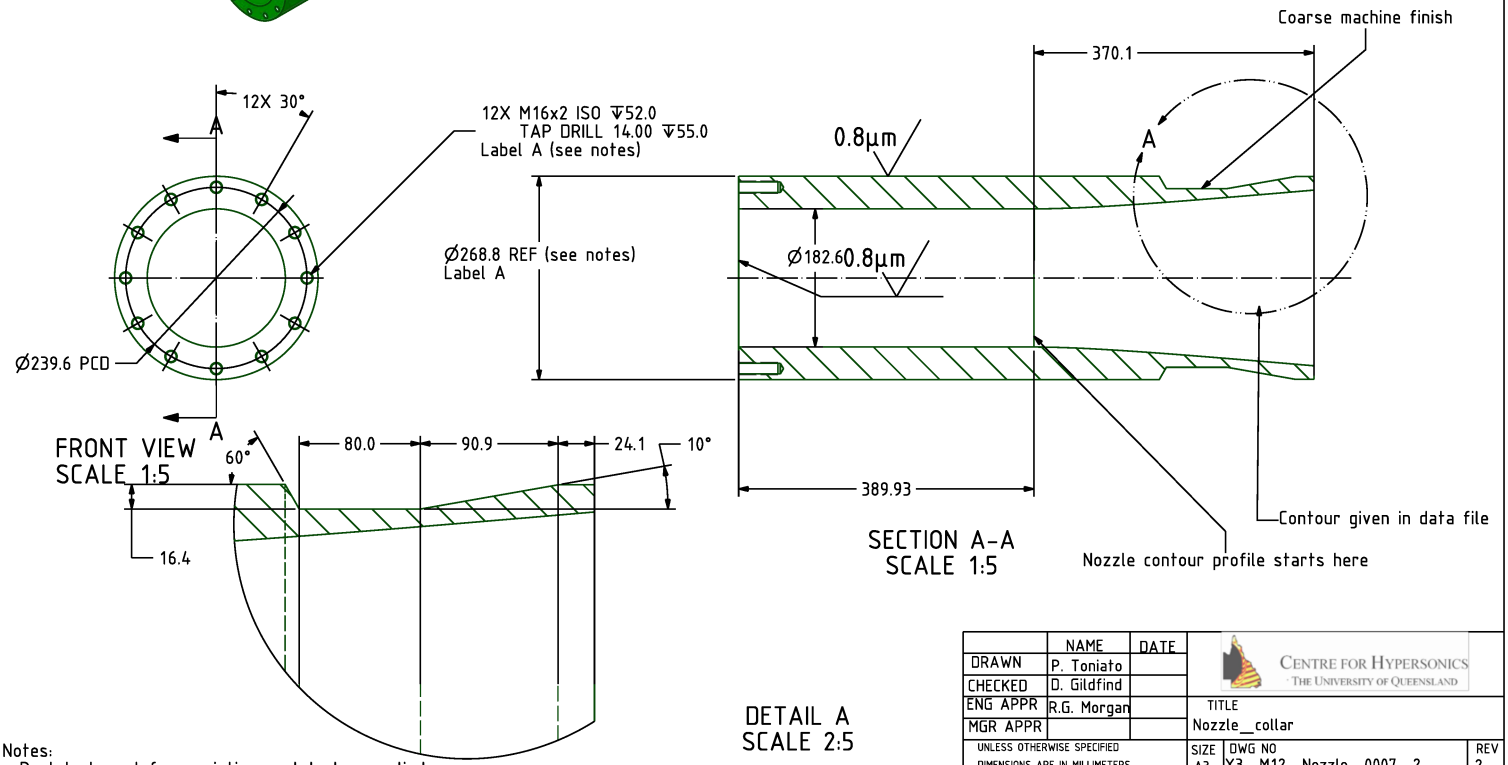

DETAIL A
SCALE 2:5

Notes:
- Part to be cut from existing part to be supplied
- Holes labelled A to be aligned with holes labelled A of part Downstream__flange
- External surface to be machined to appropiate constant diameter until surface roughness is achieved

	NAME	DATE
DRAWN	P. Toniato	
CHECKED	D. Gildfind	
ENG APPR	R.G. Morgan	
MGR APPR		

UNLESS OTHERWISE SPECIFIED
DIMENSIONS ARE IN MILLIMETERS
ANGULAR TOLERANCE ±1.0°
DIMENSIONAL TOLERANCE
X: u 1mm, X.X: u 0.1mm, X.XX: u 0.05mm

CENTRE FOR HYPERSONICS
THE UNIVERSITY OF QUEENSLAND

TITLE: Nozzle__collar

SIZE	DWG NO	REV
A3	X3__M12__Nozzle__0007__2	2

Filename: X3__M12__Nozzle__0007__2.pdf

SCALE 1:5 | WEIGHT: n/a | SHEET 1

REVISION HISTORY			
REV	DESCRIPTION	DATE	APPROVED
		28/07/2017 3:19:37 PM	

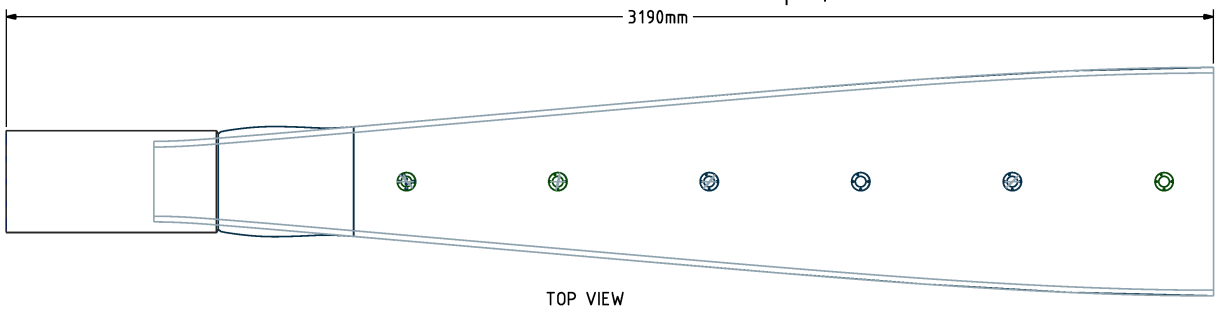

TOP VIEW

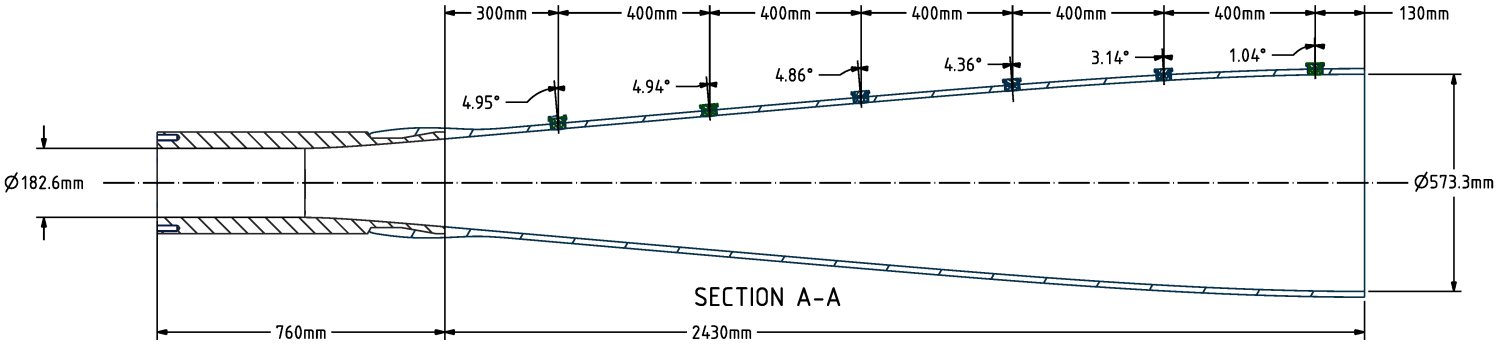

SECTION A-A

	NAME	DATE
DRAWN	P. Toniato	
CHECKED	D. Gildfind	
ENG APPR	R.G. Morgan	
MGR APPR		

UNLESS OTHERWISE SPECIFIED
DIMENSIONS ARE IN MILLIMETERS
ANGULAR TOLERANCE ±1.0°
DIMENSIONAL TOLERANCE
X: u 1mm, X.X: u 0.1mm, X.XX: u 0.05mm

TITLE: Mach 12 nozzle wound assembly

SIZE	DWG NO	REV
A3	X3__M12__Nozzle__0008__2	

Filename:

SCALE 1:10 | WEIGHT: n/a | SHEET

CONFIG B: Pcb__mount__flange with pcb__rake__assembly configuration (in config B)

REVISION HISTORY			
REV	DESCRIPTION	DATE	APPROVED
1	Bottom part of pcb__mount__flange modified	8/03/2016 3:21:16 PM	

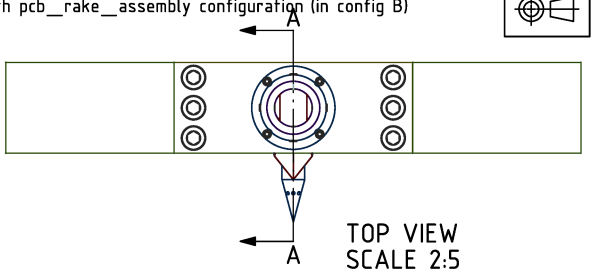

TOP VIEW
SCALE 2:5
CONFIG B

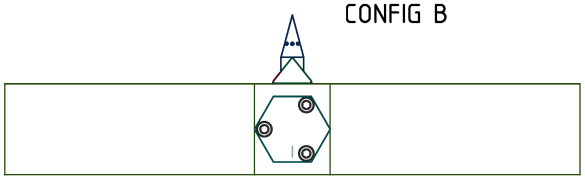

BOTTOM VIEW
SCALE 2:5
CONFIG B

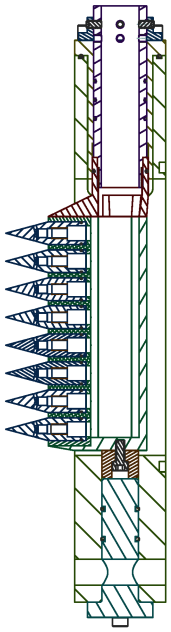

SECTION A-A
SCALE 2:5
CONFIG B

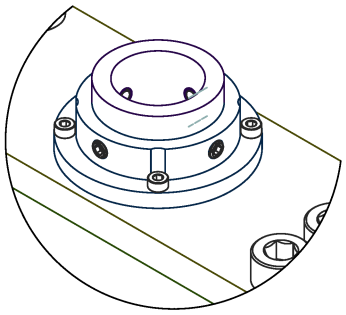

DETAIL G
SCALE 1:1
CONFIG B

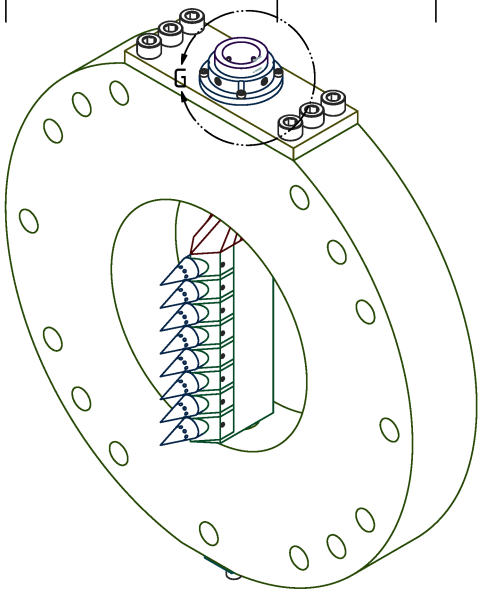

ISOMETRIC VIEW
SCALE 2:5
CONFIG B

	NAME	DATE
DRAWN	P. Toniato	
CHECKED	D. Gildfind	
ENG APPR	R.G. Morgan	
MGR APPR		

UNLESS OTHERWISE SPECIFIED
DIMENSIONS ARE IN MILLIMETERS
ANGULAR TOLERANCE ±1.0°
DIMENSIONAL TOLERANCE
X: ± 1mm, X.X: ± 0.1mm, X.XX: ± 0.05mm

TITLE: Pcb__mount__assembly

SIZE	DWG NO	REV
A3	X3__M12__Nozzle__0100__1	1

Filename: X3__M12__Nozzle__0100__1.pdf

SCALE 2:5	WEIGHT: n/a	SHEET 2

REVISION HISTORY			
REV	DESCRIPTION	DATE	APPROVED
0		22/02/2016 4:55:36 PM	

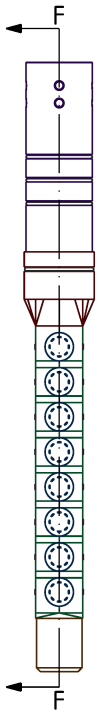

FRONT VIEW
SCALE 1:2
CONFIG A

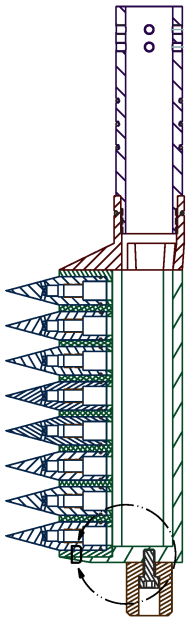

SECTION F-F
SCALE 1:2
CONFIG A

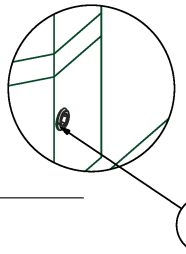

DETAIL A
SCALE 2:1

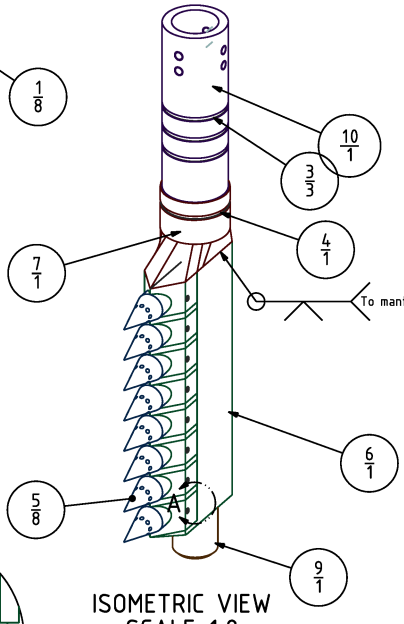

ISOMETRIC VIEW
SCALE 1:2
CONFIG A

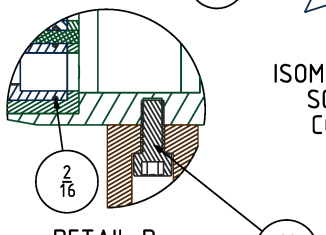

DETAIL D
SCALE 1:1
CONFIG A

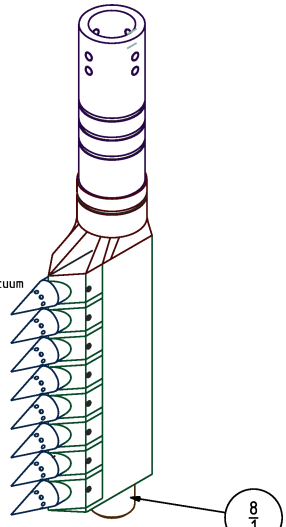

ISOMETRIC VIEW
SCALE 1:2
CONFIG B

	NAME	DATE
DRAWN	P. Toniato	
CHECKED	D. Gildfind	
ENG APPR	R.G. Morgan	
MGR APPR		

UNLESS OTHERWISE SPECIFIED
DIMENSIONS ARE IN MILLIMETERS
ANGULAR TOLERANCE ±1.0°
DIMENSIONAL TOLERANCE
X: ± 1mm, X.X: ± 0.1mm, X.XX: ± 0.05mm

CENTRE FOR HYPERSONICS
THE UNIVERSITY OF QUEENSLAND

TITLE: Pcb__rake__assembly

SIZE	DWG NO	REV
A3	X3__M12__Nozzle__0200__0	0

Filename: X3__M12__Nozzle__0200__0.pdf

SCALE 1:2	WEIGHT: n/a	SHEET 1

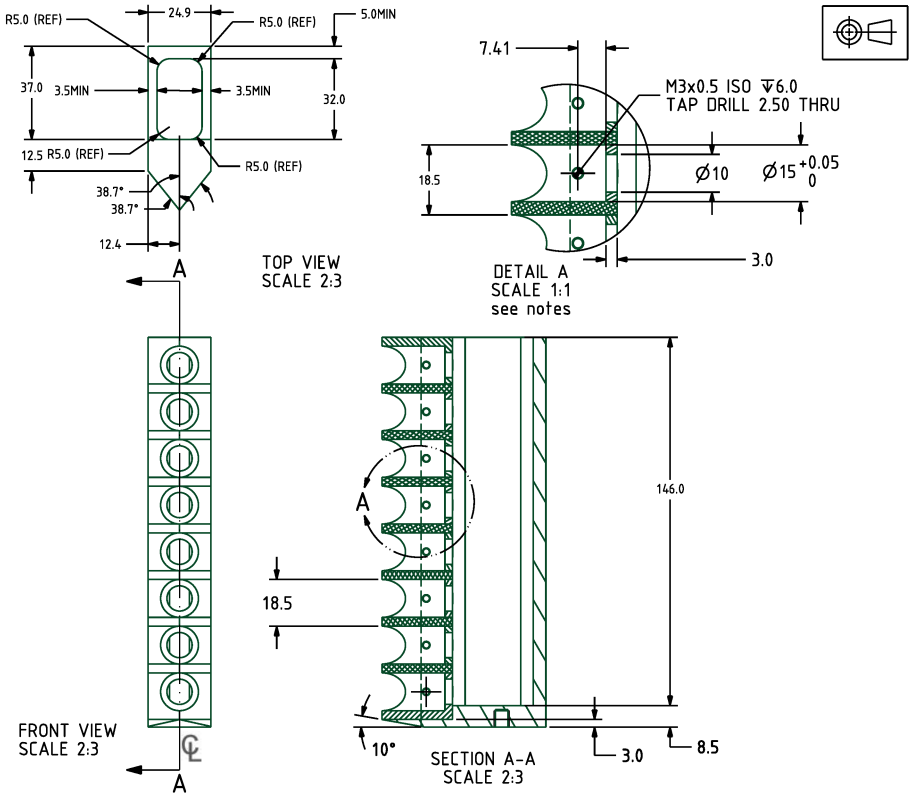

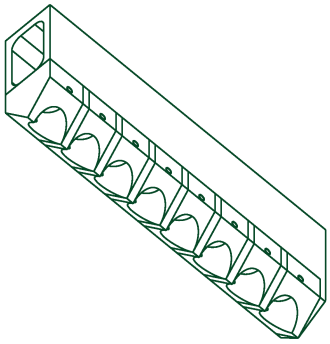

ISOMETRIC VIEW

Notes:
Repeat DETAIL A 8 times with equal spacing

REVISION HISTORY			
REV	DESCRIPTION	DATE	APPROVED
0	Pcb__rake	19/02/2016 2:59:53 PM	

	NAME	DATE
DRAWN	P. Toniato	
CHECKED	D. Gildfind	
ENG APPR	R.G. Morgan	
MGR APPR		

UNLESS OTHERWISE SPECIFIED
DIMENSIONS ARE IN MILLIMETERS
ANGULAR TOLERANCE ±1.0°
DIMENSIONAL TOLERANCE
X: ± 1mm, X.X: ± 0.1mm, X.XX: ± 0.05mm

CENTRE FOR HYPERSONICS
THE UNIVERSITY OF QUEENSLAND

TITLE: Pcb__rake

SIZE	DWG NO	REV
A3	X3__M12__Nozzle__0201__0	0

Filename: X3__M12__Nozzle__0201__0.pdf

SCALE 2:3 | WEIGHT: n/a | SHEET 1

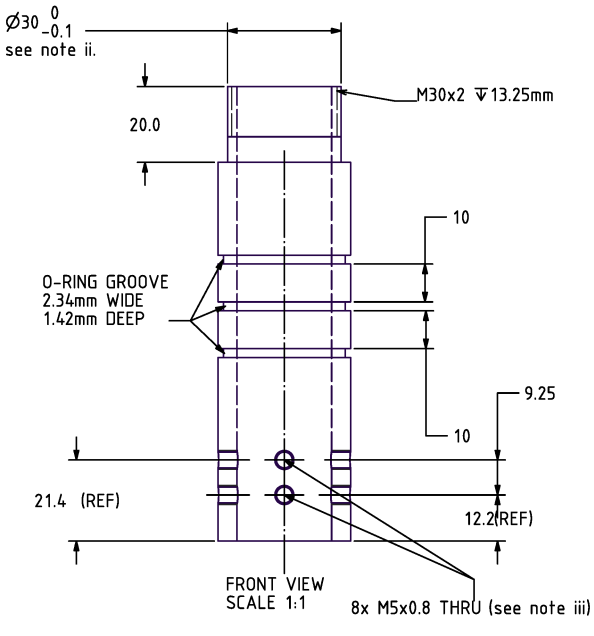

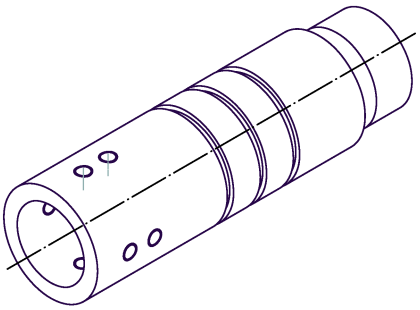

ISOMETRIC VIEW
SCALE 1:1

REVISION HISTORY			
REV	DESCRIPTION	DATE	APPROVED
0	pcb__rake__connector	19/02/2016 5:54:00 PM	

Notes
i. Hole in part pcb__rake__mount
ii. Hole in part pcb__rake__adaptor2
iii. DO NOT DRILL holes until whole Pcb__mount__assembly has been assembled (DWG X3__M12__Nozzle__0100).
Holes to be aligned with holes in pcb__rake__support__connector

	NAME	DATE
DRAWN	P. Toniato	
CHECKED	D. Gildfind	
ENG APPR	R.G. Morgan	
MGR APPR		

UNLESS OTHERWISE SPECIFIED
DIMENSIONS ARE IN MILLIMETERS
ANGULAR TOLERANCE ±1.0°
DIMENSIONAL TOLERANCE
X: ± 1mm, X.X: ± 0.1mm, X.XX: ± 0.05mm

CENTRE FOR HYPERSONICS
THE UNIVERSITY OF QUEENSLAND

TITLE: pcb__rake__connector

SIZE	DWG NO	REV
A3	X3__M12__Nozzle__0203__0	0

Filename: X3__M12__Nozzle__0203__0.pdf

SCALE 1:1 | WEIGHT: n/a | SHEET 1

REVISION HISTORY			
REV	DESCRIPTION	DATE	APPROVED
0	pcb__rake__adaptor	19/02/2016 3:38:40 PM	

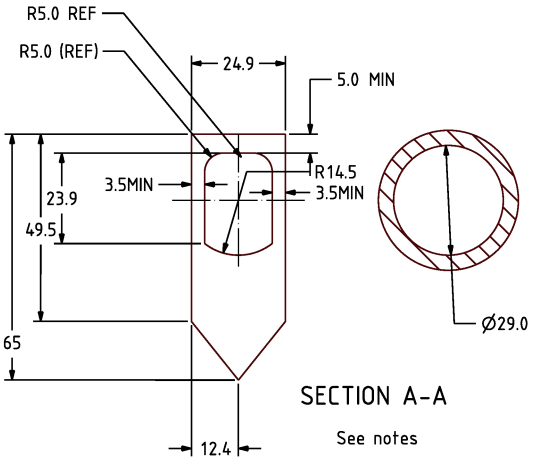

SECTION A-A

See notes

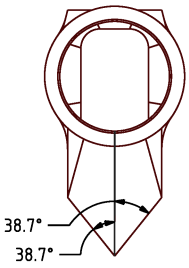

TOP VIEW
SCALE 1:1

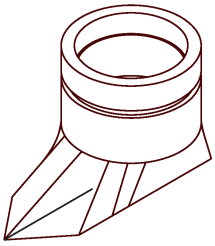

ISOMETRIC VIEW
SCALE 1:1

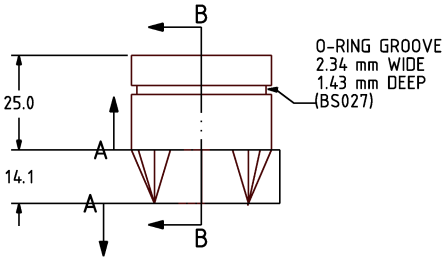

FRONT VIEW
SCALE 1:1

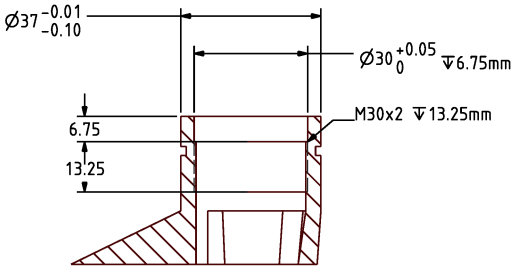

SECTION B-B

	NAME	DATE
DRAWN	P. Toniato	
CHECKED	D. Gildfind	
ENG APPR	R.G. Morgan	
MGR APPR		

UNLESS OTHERWISE SPECIFIED
DIMENSIONS ARE IN MILLIMETERS
ANGULAR TOLERANCE ±1.0°
DIMENSIONAL TOLERANCE
X: u 1mm, X.X: u 0.1mm, X.XX: u 0.05mm

CENTRE FOR HYPERSONICS
THE UNIVERSITY OF QUEENSLAND

TITLE: pcb__rake__adaptor

SIZE	DWG NO	REV
A3	X3__M12__Nozzle__0204__0	0

Filename: X3__M12__Nozzle__0204__0.pdf

SCALE 1:1 | WEIGHT: n/a | SHEET 1

i. SECTION A-A: transition from rectangular (left) to circular shape to be realised in 14.1mm.
Maintain generic streamlined external shape and generic internal shape.
ii. Shaft (to be screwed in) from part pcb__rake__connector

REVISION HISTORY			
REV	DESCRIPTION	DATE	APPROVED
0	Pcb__conehead	19/02/2016 6:16:20 PM	

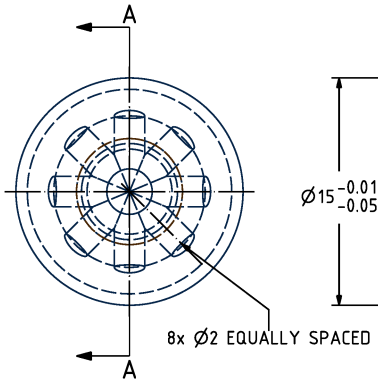

FRONT VIEW
SCALE 4:1

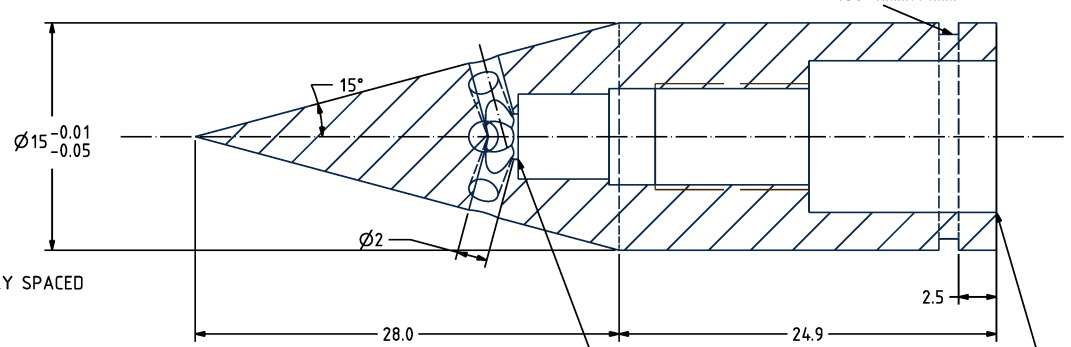

SECTION A-A
SCALE 4:1

Drill Ø3mm hole to 1mm nominal depth.
Ensure that hole fully penetrates into cavity formed by 8x intersecting Ø2mm holes

PCB FLUSH INSTALLATION
Ø5.61±.05 x 31.59 ↧
⌴Ø6.35 -.00+0.13 x 25.59 ↧
M7 x 0.75-6H x 22.54
⌴Ø10.0↧ x 12.44 ↧ 12.38

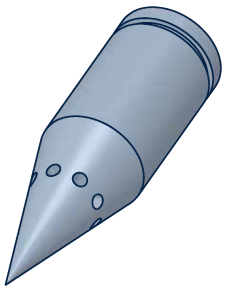

ISOMETRIC VIEW
SCALE 2:1

	NAME	DATE
DRAWN	P. Toniato	
CHECKED	D. Gildfind	
ENG APPR	R.G. Morgan	
MGR APPR		

UNLESS OTHERWISE SPECIFIED
DIMENSIONS ARE IN MILLIMETERS
ANGULAR TOLERANCE ±1.0°
DIMENSIONAL TOLERANCE
X: u 1mm, X.X: u 0.1mm, X.XX: u 0.05mm

CENTRE FOR HYPERSONICS
THE UNIVERSITY OF QUEENSLAND

TITLE: Pcb__conehead

SIZE	DWG NO	REV
A3	X3__M12__Nozzle__0207__0	0

Filename: X3__M12__Nozzle__0207__0.pdf

SCALE 4:1 | WEIGHT: n/a | SHEET 1

REVISION HISTORY			
REV	DESCRIPTION	DATE	APPROVED
0		22/02/2016 4:55:36 PM	

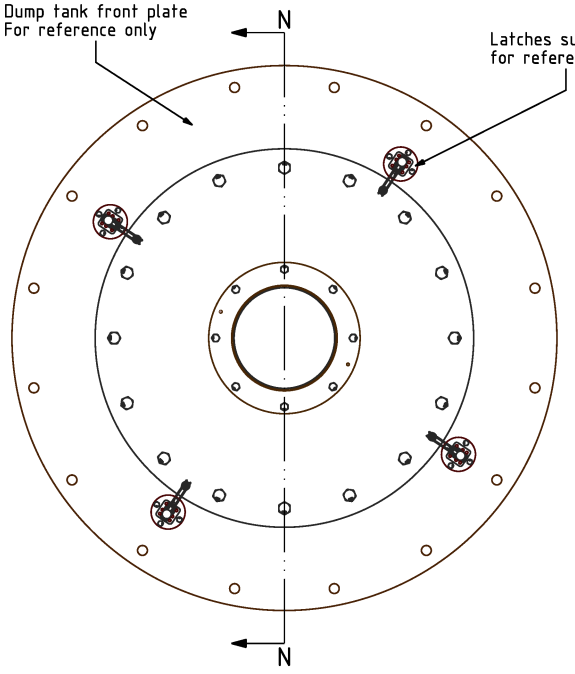

FRONT VIEW
SCALE 1:10

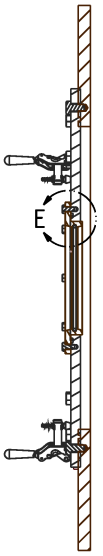

SECTION N-N
SCALE 1:10

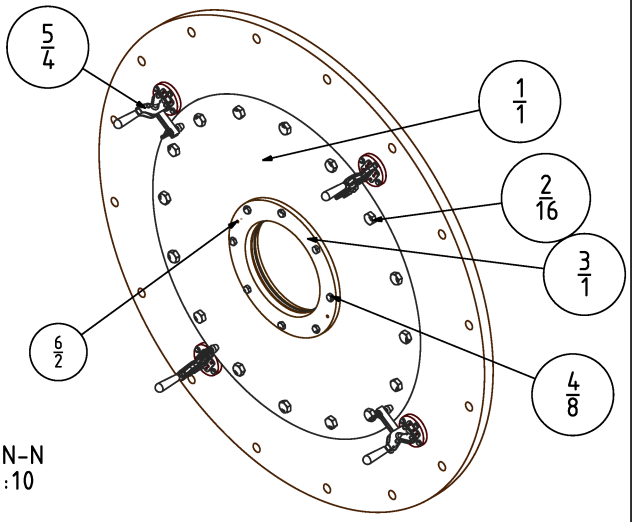

ISOMETRIC VIEW
SCALE 1:10

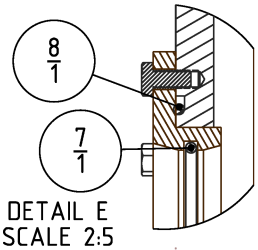

DETAIL E
SCALE 2:5

	NAME	DATE
DRAWN	P. Toniato	
CHECKED	D. Gildfind	
ENG APPR	R.G. Morgan	
MGR APPR		

UNLESS OTHERWISE SPECIFIED
DIMENSIONS ARE IN MILLIMETERS
ANGULAR TOLERANCE ±1.0°
DIMENSIONAL TOLERANCE
X: ± 1mm, X.X: ± 0.1mm, X.XX: ± 0.05mm

CENTRE FOR HYPERSONICS
THE UNIVERSITY OF QUEENSLAND

TITLE: Dump tank assembly

SIZE	DWG NO	REV
A3	X3_M12_Nozzle_0300_0	0

Filename: X3_M12_Nozzle_0300_0.pdf

SCALE 1:10 | WEIGHT: n/a | SHEET 1

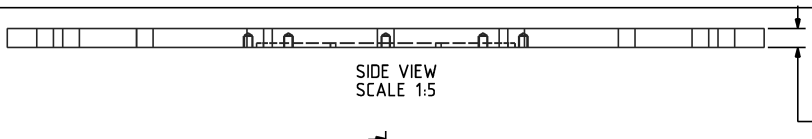

SIDE VIEW
SCALE 1:5

REVISION HISTORY			
REV	DESCRIPTION	DATE	APPROVED
0	Aluminium_front_plate	22/02/2016 11:46:52 AM	

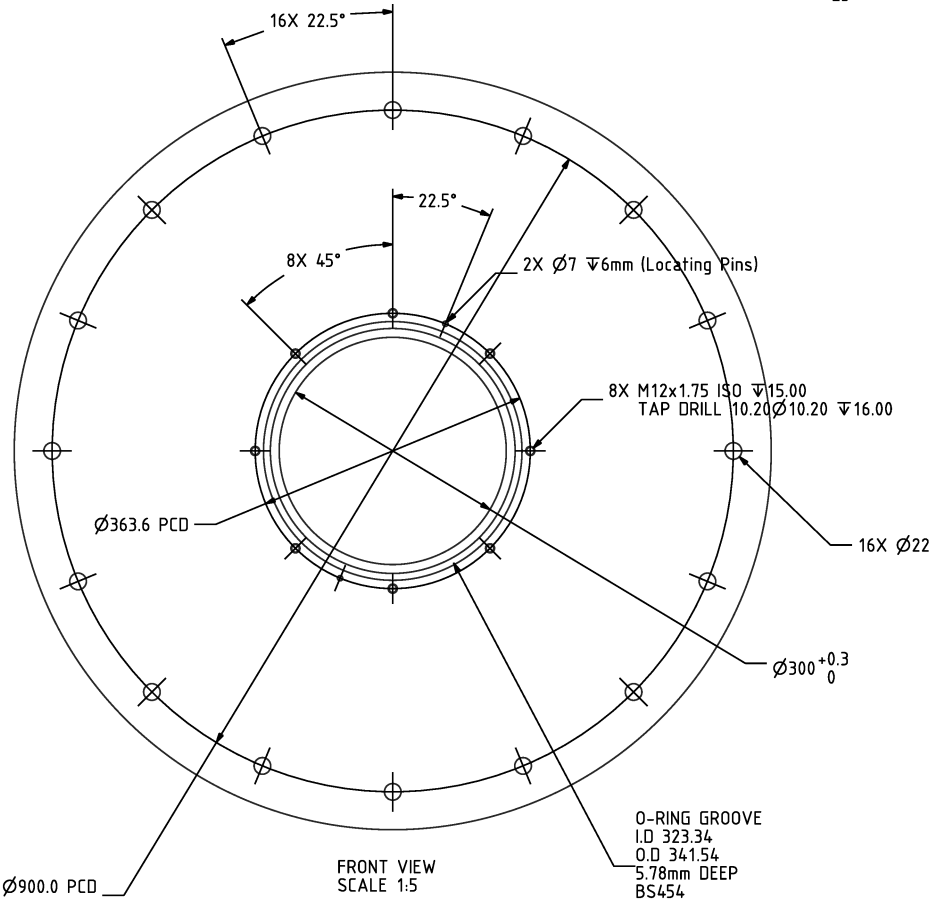

FRONT VIEW
SCALE 1:5

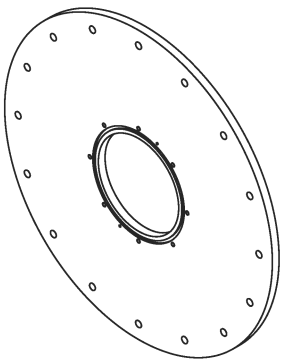

ISOMETRIC VIEW
SCALE 1:10

	NAME	DATE
DRAWN	P. Toniato	
CHECKED	D. Gildfind	
ENG APPR	R.G. Morgan	
MGR APPR		

UNLESS OTHERWISE SPECIFIED
DIMENSIONS ARE IN MILLIMETERS
ANGULAR TOLERANCE ±1.0°
DIMENSIONAL TOLERANCE
X: ± 1mm, X.X: ± 0.1mm, X.XX: ± 0.05mm

CENTRE FOR HYPERSONICS
THE UNIVERSITY OF QUEENSLAND

TITLE: Aluminium_front_plate

SIZE	DWG NO	REV
A3	X3_M12_Nozzle_0304_0	0

Filename: X3_M12_Nozzle_0304_0.pdf

SCALE 1:5 | WEIGHT: n/a | SHEET 1

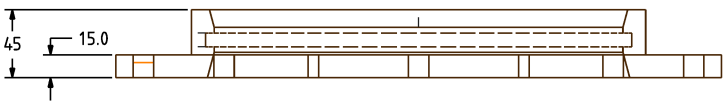

SIDE VIEW
SCALE 2:5

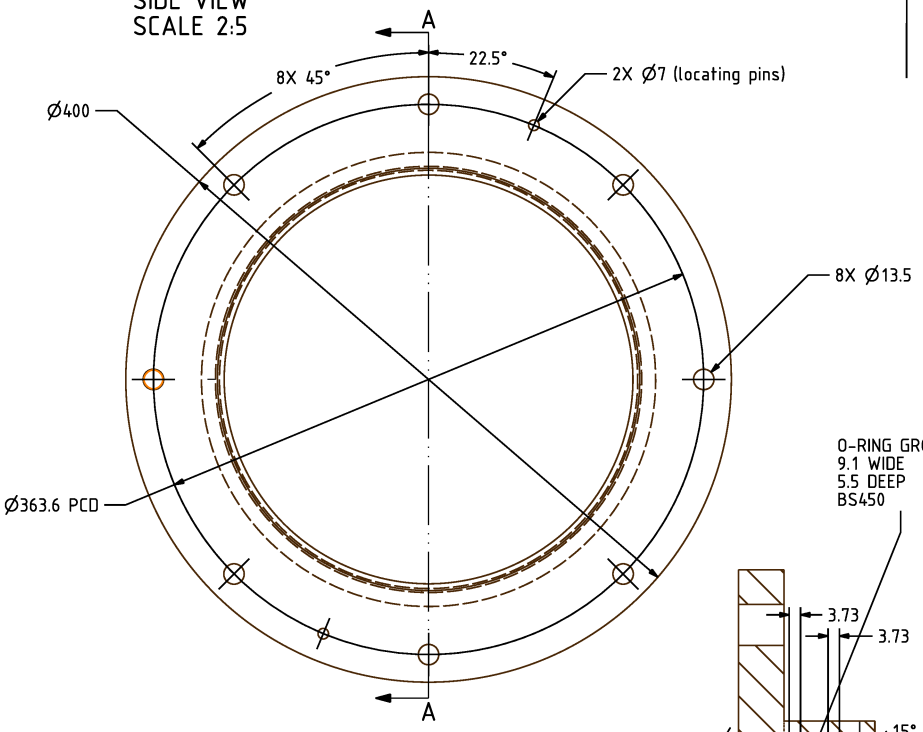

FRONT VIEW
SCALE 2:5

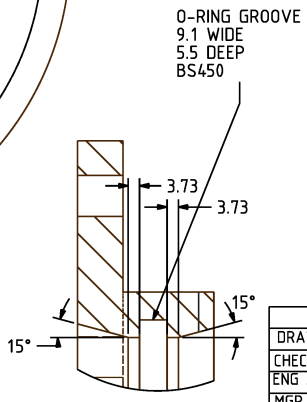

DETAIL A
SCALE 4:5

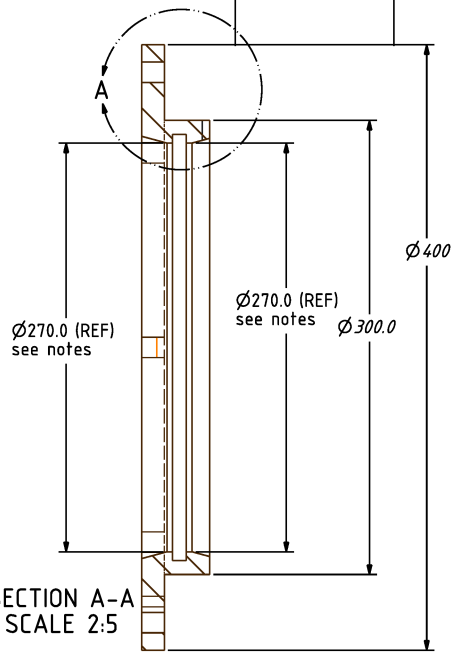

SECTION A-A
SCALE 2:5

REVISION HISTORY			
REV	DESCRIPTION	DATE	APPROVED
0	Dump tank sliding seal	22/02/2016 11:34:34 AM	

Note
-Holes to be aligned with holes labelled A in part *dump_tank_plate*
-Make internal diameter dimensions to dimension labelled A in part Nozzle_collar, (dwg X3_M12_nozzle_0007_0) plus 0.16mm and tollerances +0.02,-0.02

	NAME	DATE
DRAWN	P. Toniato	
CHECKED	D. Gildfind	
ENG APPR	R.G. Morgan	
MGR APPR		

UNLESS OTHERWISE SPECIFIED
DIMENSIONS ARE IN MILLIMETERS
ANGULAR TOLERANCE ±1.0°
DIMENSIONAL TOLERANCE
X: u 1mm, X.X: u 0.1mm, X.XX: u 0.05mm

CENTRE FOR HYPERSONICS
THE UNIVERSITY OF QUEENSLAND

TITLE: Dump tank sliding seal

SIZE	DWG NO	REV
A3	X3_M12_Nozzle_0305_0	0

Filename: X3_M12_Nozzle_0305_0.pdf

SCALE 2:5 | WEIGHT: n/a | SHEET 1

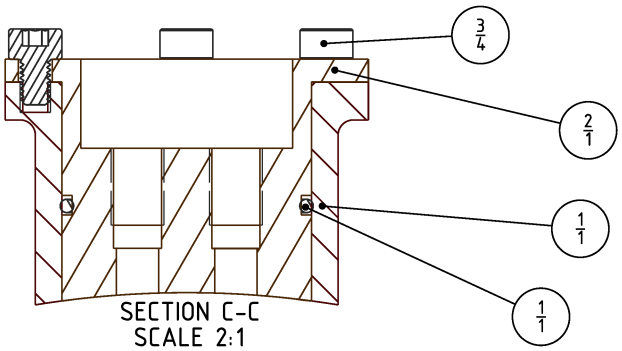

SECTION C-C
SCALE 2:1
CONFIG A

REVISION HISTORY			
REV	DESCRIPTION	DATE	APPROVED
0		22/02/2016 5:06:10 PM	

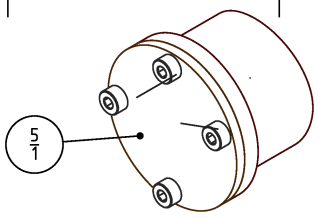

ISOMETRIC VIEW
SCALE 1:1
CONFIG B

ITEM NO.	PART NAME	PART NUMBER	MATERIAL	QTY
1	Instrumentation_adaptor_1	X3_M12_Nozzle_0501_0	Stainless Steel	1
2	Instrumentation_insert_1	X3_M12_Nozzle_0504_0	Stainless Steel	1
3	M4x0.7mm 6mm long	N/A	High tensile steel	4
4	O-Ring BS015	N/A	Nitrile	1
5	Plug_1	X3_M12_Nozzle_0505_0	Stainless Steel	1

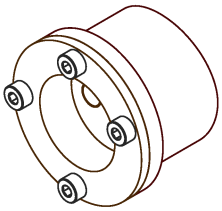

ISOMETRIC VIEW
SCALE 1:1
CONFIG A

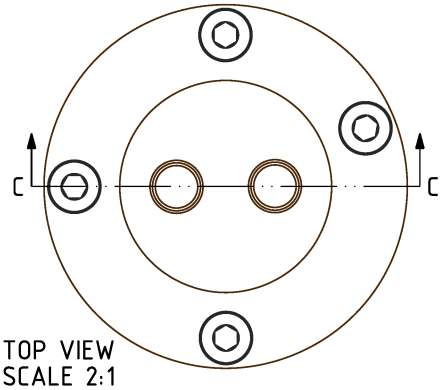

TOP VIEW
SCALE 2:1
CONFIG A

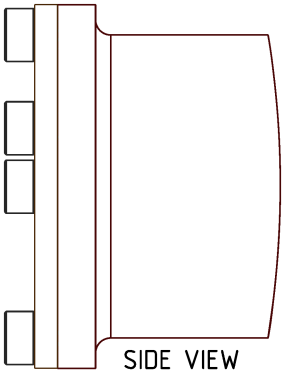

SIDE VIEW
SCALE 2:1
CONFIG A

	NAME	DATE
DRAWN	P. Toniato	
CHECKED	D. Gildfind	
ENG APPR	R.G. Morgan	
MGR APPR		

UNLESS OTHERWISE SPECIFIED
DIMENSIONS ARE IN MILLIMETERS
ANGULAR TOLERANCE ±1.0°
DIMENSIONAL TOLERANCE
X: u 1mm, X.X: u 0.1mm, X.XX: u 0.05mm

CENTRE FOR HYPERSONICS
THE UNIVERSITY OF QUEENSLAND

TITLE: Nozzle_sensor_holder_1

SIZE	DWG NO	REV
A3	X3_M12_Nozzle_0500_0	0

Filename: X3_M12_Nozzle_0500_0.pdf

SCALE 2:1 | WEIGHT: n/a | SHEET 1

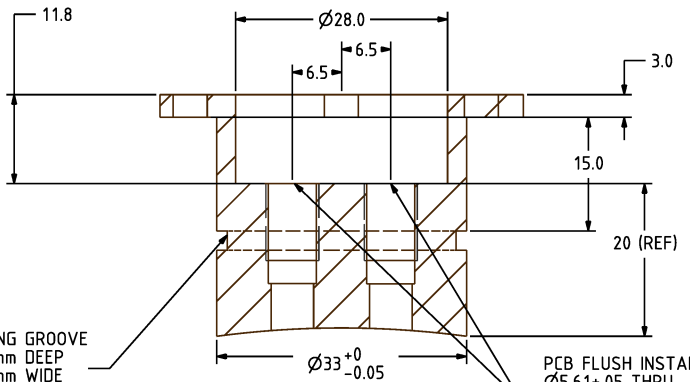

SECTION A-A
SCALE 2:1

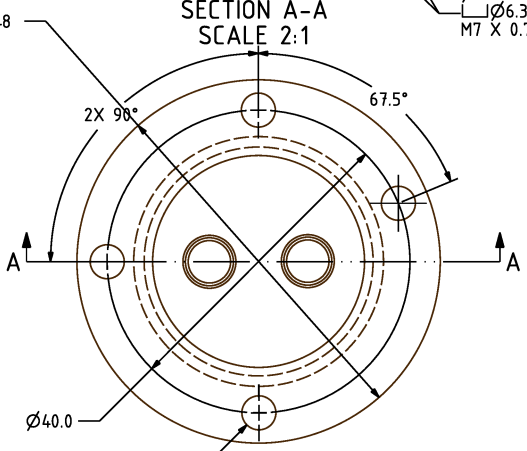

TOP VIEW
SCALE 2:1

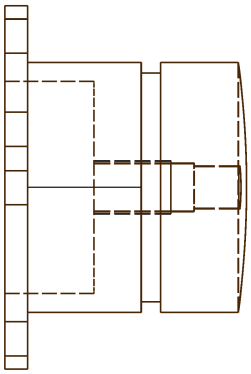

SIDE VIEW
SCALE 2:1

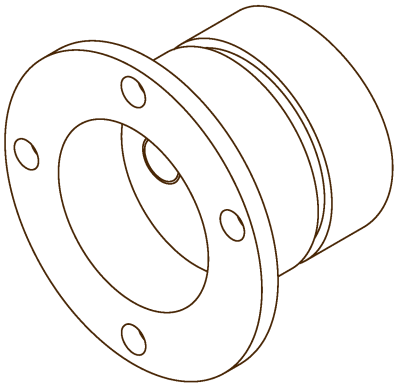

ISOMETRIC VIEW
SCALE 2:1

REVISION HISTORY			
REV	DESCRIPTION	DATE	APPROVED
0		18/02/2016 4:58:08 PM	

	NAME	DATE
DRAWN	P. Toniato	
CHECKED	D. Gildfind	
ENG APPR	R.G. Morgan	
MGR APPR		

UNLESS OTHERWISE SPECIFIED
DIMENSIONS ARE IN MILLIMETERS
ANGULAR TOLERANCE ±1.0°
DIMENSIONAL TOLERANCE
X: u 1mm, X.X: u 0.1mm, X.XX: u 0.05mm

CENTRE FOR HYPERSONICS
THE UNIVERSITY OF QUEENSLAND

TITLE: Instrumentation_insert_1

SIZE	DWG NO	REV
A3	X3_M12_nozzle_0504_0	0

Filename: X3_M12_nozzle_0504_0.pdf

SCALE 2:1 | WEIGHT: n/a | SHEET 1

Notes:
Bottom surface to be supplied: see 3D CAT STP file x3_M12_Nozzle_0504_0.stp (and aligned with *Instrumentation_adaptor_1* bottom surface)
Bottom surface orientation to be preserved with respect to other part elements

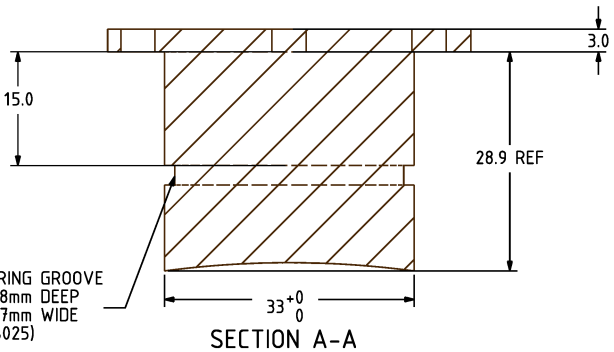

SECTION A-A
SCALE 2:1

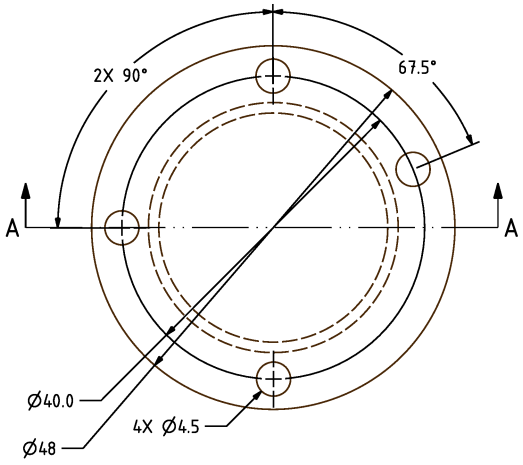

TOP VIEW
SCALE 2:1

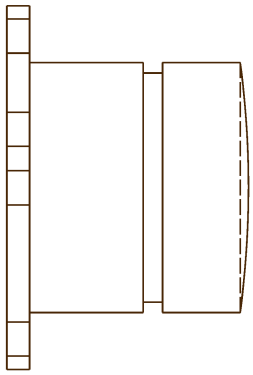

SIDE VIEW
SCALE 2:1

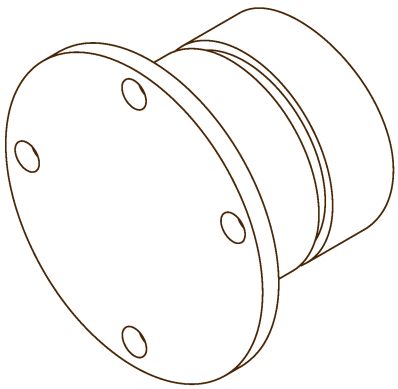

ISOMETRIC VIEW
SCALE 2:1

REVISION HISTORY			
REV	DESCRIPTION	DATE	APPROVED
0		18/02/2016 3:24:38 PM	

	NAME	DATE
DRAWN	P. Toniato	
CHECKED	D. Gildfind	
ENG APPR	R.G. Morgan	
MGR APPR		

UNLESS OTHERWISE SPECIFIED
DIMENSIONS ARE IN MILLIMETERS
ANGULAR TOLERANCE ±1.0°
DIMENSIONAL TOLERANCE
X: u 1mm, X.X: u 0.1mm, X.XX: u 0.05mm

CENTRE FOR HYPERSONICS
THE UNIVERSITY OF QUEENSLAND

TITLE: Plug_1

SIZE	DWG NO	REV
A3	X3_M12_nozzle_0505_0	0

Filename: X3_M12_nozzle_0505_0.pdf

SCALE 2:1 | WEIGHT: n/a | SHEET 1

Notes:
Bottom surface to be supplied: see 3D CAT STP file x3_M12_Nozzle_0505_0.stp (and aligned with *Instrumentation_adaptor_1* bottom surface)
Bottom surface orientation to be preserved with respect to other part elements